A Near-field Wireless Power Transfer System with Planar Split-ring Loops for Medical Implants

Thesis submitted in accordance with the requirements of the

University of Liverpool

for the degree of Doctor in Philosophy

by

Jingchen Wang

July 2019

I would like to dedicate this thesis to my beloved parents and husband.

Declaration

I hereby declare that except where specific reference is made to the work of others, the contents of this dissertation are original and have not been submitted in whole or in part for consideration for any other degree or qualification in this, or any other University. This dissertation is the result of my own work and includes nothing which is the outcome of work done in collaboration, except where specifically indicated in the text.

Jingchen Wang

Abstract

With the continuous progress in science and technology, a myriad of implantable medical devices (IMDs) have been invented aimed at improving public health and wellbeing. One of the main problems with these devices is their limited battery lifetime. This results in otherwise unnecessary surgeries to replace depleted batteries leading to excessive medical expenses. Wireless power transfer (WPT), as a promising technology, could be used to remedy this. Wireless power technologies, both through the transfer of transmitted radio frequency (RF) power or the harvesting of RF energy from the ambient environment and its subsequent conversion to useable electrical energy, are emerging as important features for the future of electronic devices in general and have attracted an upsurge in research interest. Unfortunately, the path to realising this wire free charging dream is paved with many thorns and there still exist critical challenges to be addressed. This thesis aims to deal with some of these challenges, developing an efficient WPT system for IMDs.

The work begins with a comprehensive study of currently applied methods of WPT, which broadly fall into two categories: far-field (radiative) WPT and near field (non-radiative) WPT. The review includes a brief history of WPT, comparisons between current methodologies applied and a comprehensive literature review. Magnetic resonance coupling (MRC) WPT is emphasised due to its advantages for the desired application making it the technology of choice for system development. Design of an MRC-WPT system requires an understanding of the performance of the four basic topologies available for the MRC method. Following an investigation of these, it is found that series primary circuits are generally most suitable for WPT and that the choice of a series or parallel secondary circuit is dependent on the relative size of the load impedance. Importantly, design parameters must be optimised to avoid the phenomena of frequency splitting to simultaneously obtain maximum power transfer efficiency（PTE) and load power.

The use of printed spiral coils (PSCs) as inductors in the construction of WPT circuits for IMDs, which can save space and be integrated with other circuit boards, is then investigated. The challenges and issues of PSCs present for WPT mainly relate to maintaining an inductive characteristic at frequencies in the Medical Implant Communication Service (MICS) band and to maximising the PTE between primary and secondary circuits. Investigations of PSC design parameters are performed to obtain inductive characteristics at high frequencies and the split-ring loop is proposed to increase the Quality factor relative to that offered by the PSC, which is shown to enhance WPT performance. To simplify the necessary resonating circuit configuration for MRC-WPT, a self-resonating split-ring loop with a series inductor-capacitor characteristic has been developed. A pair of these self-resonators has been adopted into a series primary-series secondary WPT system operating at high frequency. This is different to traditional planar self-resonators, which offer parallel self-resonance characteristics that are less desirable due to their reduced system power insertion as a parallel primary resonator.

Finally, a system for implantable devices is developed using the split-ring loop in consideration of the effects of body tissues, whose dielectric characteristics have a significant influence on WPT performance. Due concern is also paid to human safety from radiated RF power. A series resonating split-ring loop for transmitting power is formed at the desired frequency through the addition of a lumped element capacitor. A single loop as a receiving resonator with a low Specific Absorption Rate (SAR), is designed to allow greater transmit power to be used in comparison to previous work, whilst satisfying the relevant standards relating to human safety. A rectifier circuit is also designed to convert the received RF energy into useable electrical energy allowing the realisation of the proposed WPT system.

In a nutshell, this thesis places emphasis on solutions to overcome challenges relating to the use of MRC-WPT for IMDs. An efficient near-field WPT system for such devices is successfully demonstrated and should have profound significance to pushing forward the future development of this topic.

Key Words: wireless power transfer, magnetic resonance coupling, implantable medical devices, planar split-ring loops, self-resonant coils.

Acknowledgements

Thinking of the fleeting last four years of memorable and hard-working doctoral studies, gratitude fills my heart to allow me to fully appreciate everyone who has supported me and everything that has made me stronger. Firstly, I would like to express my great appreciation, from deep in my heart, for my principal supervisor Prof. Eng Gee Lim, who provided me with this precious and extraordinary opportunity to test myself at the highest level. Your academic guidance and help have enlightened me, allowing me to explore the right way to perform research and enabling me to grow from a fresh graduate student into a professional researcher. I have learned from you both academically and personally. I am grateful for your cultivation of my research, along with my life and career. Your support and encouragement have been a driving force giving me the impetus to continuously move forward when confronted by difficulties and obstacles. It is my great honour to be one of your PhD students and I wish that I have repaid the faith you showed in me. Secondly, I would like to thank my second supervisor Prof. Yi Huang for showing me rigorous methods of scholarly research activity and pushing my studies forward. I am very grateful that you directed my investigations, from theory into practice, from the perspective of systemic and logical thinking. Thanks for your significant instruction and advice which were key stones along my research road. Thirdly, I would like to show my sincere gratitude to my third supervisor Dr. Mark Paul Leach for his scrupulous tutorials, especially with my English. Thank you very much for helping me to improve my English from making ambiguous statements to offering fluent communication. Thanks to your meticulous and repetitive revisions, I have achieved obvious progress in my English writing. I greatly appreciate your affectionate sympathy and solicitude, like the sunshine in the winter, alleviating my sadness and sorrow when I encountered frustration. Your spirit of striving for perfection and strong sense of responsibility set a marvellous example for me. Finally, I am grateful to my fourth supervisor, Dr. Zhao Wang, whose attitude towards desiring deeper insight into scientific knowledge increasingly infects. You taught me to be a realistic engineer and academic with a pragmatic awareness. I will always treasure your illumination and impartment.

In addition, thanks are due to Dr. Jiafeng Zhou for insightful comments during group meetings when I was in Liverpool and in my annual reviews. Dr. Jinling Zhang, also for beneficial feedback during the annual reviews. Thanks to Dr. Derek Gray for sharing related research information and measurement opinions.

Special thanks must be paid to my brilliant and lovely colleagues and friends, particularly to Dr. Chaoyun Song, Dr. Zhihao Tian, Dr. Haochuan Jiang, Dr. Zhuang Yuan, Dr. Xiaotong Xu, Mr. Rui Pei, Ms. Wenzhang Zhang, Ms. Yujie Liu, Ms. Zhenzhen Jiang, Ms. Xiaoyi Wu, Ms. Jinhong Luo, Ms. Ying Cheng, Ms. Na Li, Mr. Bing Han and Mr. Hao Zhang for many fruitful discussions and joyful moments.

None of this would have been possible without the unselfish love of my parents who brought me up with no expectation of reward. I feel indebted to my parents for their understanding and company, for helping me persist in accomplishing my goal. Additionally, I would like to show my gratitude to my husband Mr. Mao who always stands by my side emboldening me and giving me the confidence to succeed. It is you that has created a life full of delight and happiness with which I am content to enjoy. I am very thankful for everything that you have done for me including your longstanding compatibility, concession, patience and encouragement.

Last, but not least, the department of Electrical Engineering and Electronics of the University of Liverpool and the department of Electrical and Electronic Engineering of Xi’an Jiaotong-Liverpool University are gratefully acknowledged for their support.

Publications

Journal Publications

[1] **J. Wang**, M. P. Leach, E. G. Lim, Z. Wang, Z. Jiang, R. Pei, and Y. Huang, "A conformal split-ring loop as a self-resonator for wireless power transfer," *IEEE Access*, pp. 1-1, 2019, doi: 10.1109/ACCESS.2019.2918640.

[2] **J. Wang**, M. Leach, E. G. Lim, Z. Wang, and Y. Huang, "Investigation of magnetic resonance coupling circuit topologies for wireless power transmission," *Microwave and Optical Technology Letters,* vol. 0, no. 0, 2019/02/27 2019, doi: 10.1002/mop.31803.

[3] **J. Wang**, M. Leach, E. G. Lim, Z. Wang, R. Pei, and Y. Huang, "An implantable and conformal antenna for wireless capsule endoscopy," *IEEE Antennas and Wireless Propagation Letters*, vol. 17, no. 7, pp. 1153-1157, 2018, doi: 10.1109/LAWP.2018.2836392.

[4] Z. Jiang, Z. Wang, M. Leach, Y. Huang, E. G. Lim, **J. Wang**, and R. Pei, "Wideband loop antenna with split-ring resonators for wireless medical telemetry," *IEEE Antennas and Wireless Propagation Letters,* vol. 18, no. 7, pp. 1415-1419, 2019, doi: 10.1109/LAWP.2019.2918501.

Conference Publications

[1] **J. Wang**, M. Leach, E. G. Lim, Z. Wang, and Y. Huang, "Wireless power transfer using resonance coupling method for implantable applications," *in 2018 IEEE International Symposium on Antennas and Propagation & USNC/URSI National Radio Science Meeting*, 8-13 July 2018 2018, pp. 2557-2558, doi: 10.1109/APUSNCURSINRSM.2018.8609288.

[2] Y. Shi, Z. Jiang, S. Lam, M. Leach, **J. Wang**, and E. G. Lim, "Multi-GHz microstrip transmission lines realised by screen printing on flexible substrates," *in 2017 IEEE Electrical Design of Advanced Packaging and*

Systems Symposium (EDAPS), 14-16 Dec. 2017 2017, pp. 1-3, doi: 10.1109/EDAPS.2017.8277038.

[3] R. Pei, **J. Wang**, M. Leach, Z. Wang, S. Lee, and E. G. Lim, "Wearable antenna design for bioinformation," *in 2016 IEEE Conference on Computational Intelligence in Bioinformatics and Computational Biology (CIBCB)*, 5-7 Oct. 2016, pp. 1-4, doi: 10.1109/CIBCB.2016.7758129.

Contents

List of Abbreviations

AC	Alternating Current
ADS	Advanced Design System
CST	Computer Simulation Technology
DC	Direct Current
EIRP	Effective Isotropic Radiated Power
EMC	Electromagnetic Compatibility
EMI	Electromagnetic Interference
EMR	Electromagnetic Radiation
EV	Electric Vehicle
FCC	Federal Communications Commission
GSM	Global System for Mobile Communications
GMD	Geometric Mean Distance
HFSS	High Frequency Structure Simulator
Im	Imaginary Part
IMD	Implantable Medical Device
ISM	Industrial Scientific and Medical
LC	Inductor-Capacitor
LCR	Inductor Capacitor Resistor
LED	Light Emitting Diode
LoS	Line of Sight
MRC	Magnetic Resonance Coupling

MPE	Maximum Permissible Exposure
MPT	Microwave Power Transmission
MedRadio	Medical Device Radiocommunication
MICS	Medical Implant Communication Service
PCB	Printed Circuit Board
PIFA	Planar Inverted F Antenna
PP	Parallel primary and Parallel secondary
PS	Parallel primary and Series secondary
PSC	Printed Spiral Coil
PTE	Power Transfer Efficiency
Q-factor	Quality Factor
Re	Real Part
RF	Radio Frequency
RFID	Radio Frequency Identification
RMS	Root Mean Square
RX	Receiver
SAR	Specific Absorption Rate
SMA	Subminiature Version A
SPS	Solar Power Satellite
SS	Series primary and Series secondary
SP	Series primary and Parallel secondary
TV	Television
TX	Transmitter

UHF	Ultra High Frequency
VNA	Vector Network Analyser
WBAN	Wireless Body Area Network
WiTricity	Wireless Electricity
WPT	Wireless Power Transfer
WSN	Wireless Sensor Network

List of Figures

List of Tables

Chapter 1 Introduction

1.1 History of Wireless Power Transfer

Electrical power is indispensable and essential to modern life, used to provide convenience and comfort. Many items considered vital to our daily lives require electrical energy and even new smart cities are designed around the concept of energy usage, as shown in Fig.1-1. Traditional power generation methods such as burning coal, are based on fuels with limited resources. More recently sustainable energy sources including solar, wind and radio frequency energy have been used to generate electrical power promoting environmental protection.

Wireless power transfer (WPT) technology, in which radiated electromagnetic waves are used to convey power from one location to another, has become of increasing interest to the scientific community, it can be applied in applications where it is not feasible to provide continuous power to devices such as aerial drones commonly used for example to assist in disasters to detect and pinpoint survivors. WPT also provides convenience, allowing consumer devices such as electric vehicles, mobile/portable devices and implantable medical devices (IMDs) to be powered wirelessly, overcoming battery life limitations and avoiding umbilical cables, as shown in Fig. 1-2.

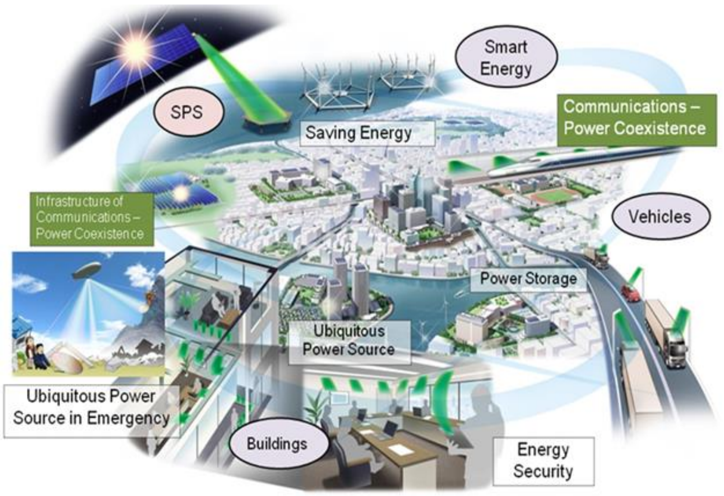

Fig. 1-1. A wireless power society [1].

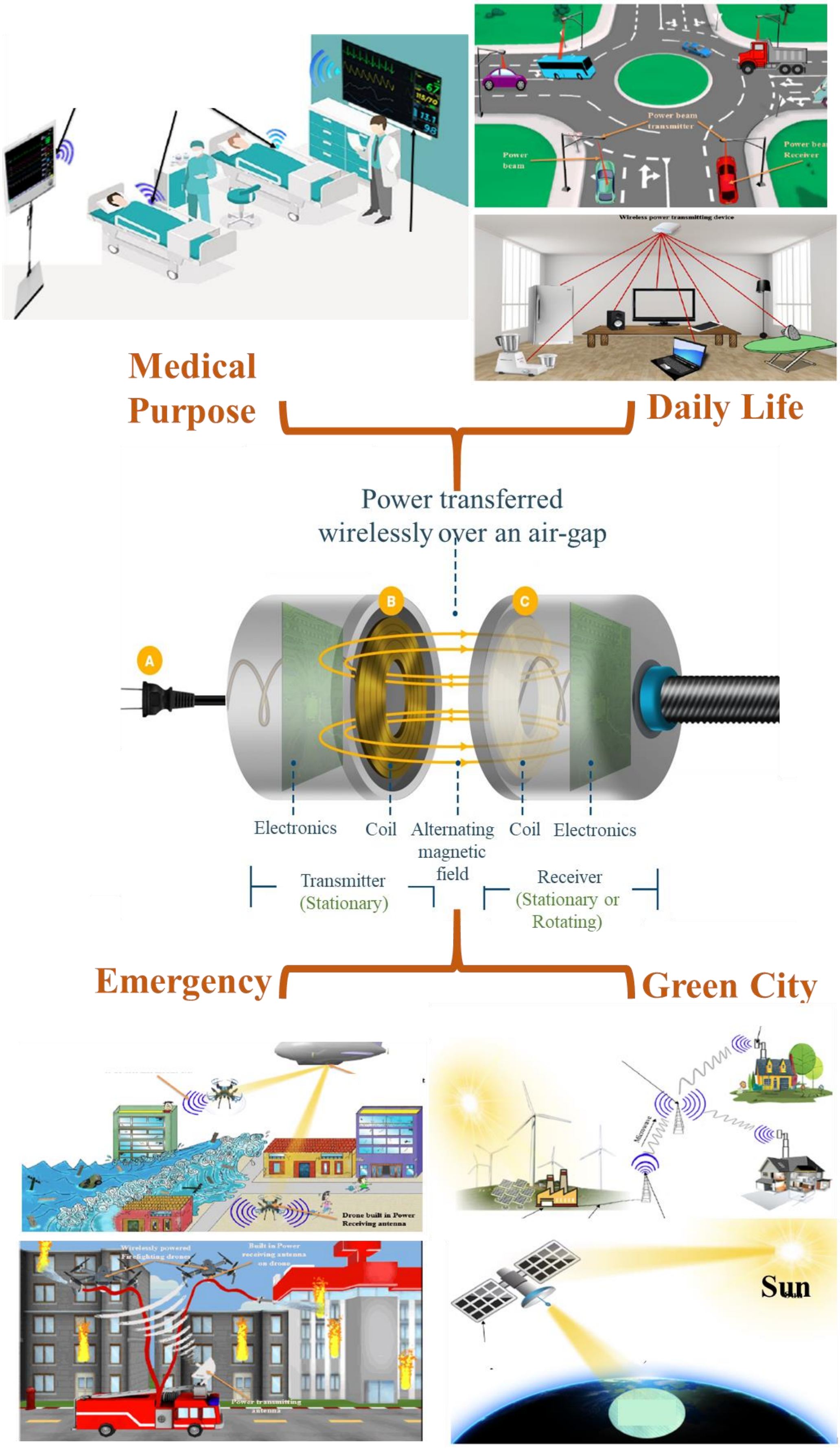

Fig. 1-2. Wireless power transfer technology for diverse applications [2, 3].

Wireless power transfer is not a new concept, its theoretical foundation originated in 1819 when H. C. Oersted discovered that a magnetic field could be created by an electric current [4]. The modelling of the basic properties of magnetic fields was then explored leading to the formulation of several laws of physics: Ampere’s Law, Biot-Savart’s Law and Faraday’s Law. Maxwell’s equations, the keystone of electromagnetics, were derived in 1864 to portray the characteristics of reciprocal transformations i.e. that a changing electric field can give rise to a magnetic field and conversely a changing magnetic field can give rise to an electric field [5]. These historic advancements established the theoretical foundation of electromagnetism and the development of WPT is based on these same theoretical foundations.

Heinrich Rudolf Hertz first confirmed the existence of electromagnetic radiation in 1888, by conducting an experiment in which oscillators connected with induction coils transmitted an electric spark over a tiny air gap and which could be observed to be received some distance away [6]. This experiment represented a technical breakthrough for WPT. Following this, the founder of alternating current (AC) electricity, Nikola Tesla, invented the “Tesla Coil” [7] in 1891 using an iron core in place of the air gap in Hertz’s experiment. He constructed the Wardenclyffe Tower [8] (shown in Fig. 1-3) in 1901 to realise wireless power transmission through the ionosphere. Even though his ideas about transmitting messages, telephony and even facsimile images across most of the Earth were not realised, his contributions to microwave technology as a milestone of electromagnetism provided the road map for further development of WPT.

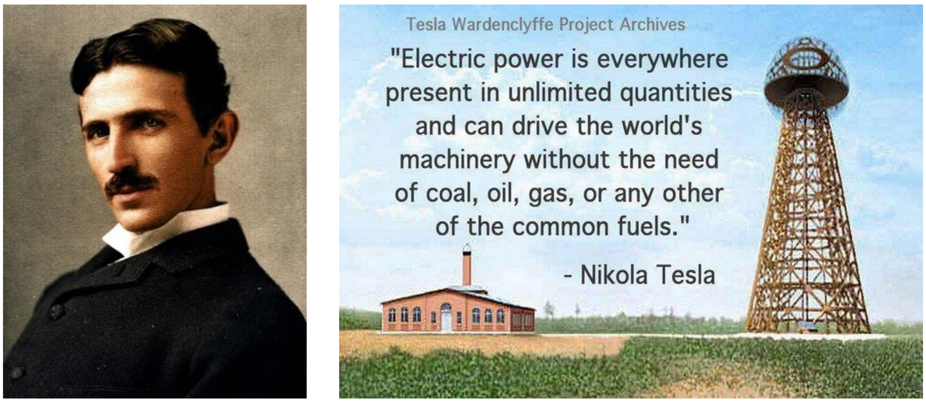

(a) **(b)**

Fig. 1-3. (a) Nikola Tesla and (b) His Wardenclyffe Project in Long Island, New York [9].

Another great leap forward for WPT occurred in 1964 when W.C. Brown demonstrated the practicality of microwave power transfer by powering a model helicopter (as shown in Fig. 1-4). This represented a practical achievement in relation to the conversion of microwaves into electricity through a rectenna [10].

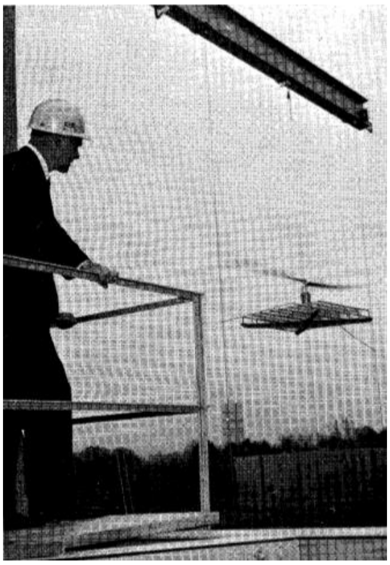

Fig. 1-4. Microwave-powered helicopter developed by W.C. Brown [10].

During that period, coupling based WPT (non-radiative or near-field WPT) did not attract much attention from researchers, thus it grew at a slower pace. Nevertheless, the emergence of portable electronic devices and the development of advanced technologies since the end of the last century has aroused an upsurge in wireless charging research of both far-field and near-field designs. Cota system [11], PRIMOVE [12] and Powercast [13] wireless rechargeable sensor systems, which are based on far-field wireless charging technology were commercialised at the beginning of the 20th century. The first published outstanding achievement for near-field WPT, WiTricity technology, was proposed by Kurs *et al* in 2007 [14]. This new approach was demonstrated in an experiment where power was transmitted to light a 60 W lamp over a distance of 2 m with an efficiency of 40% (shown in Fig. 1-5). The new method applied was called the magnetic resonance coupling (MRC) method. Since then, many researchers have investigated MRC-WPT for various applications such as electric vehicles (EVs)[15], portable or consumer devices [16-18] and LED lighting [19-21].

Fig. 1-5. Researchers in Massachusetts Institute of Technology and the demonstration of the Wirticity system [22].

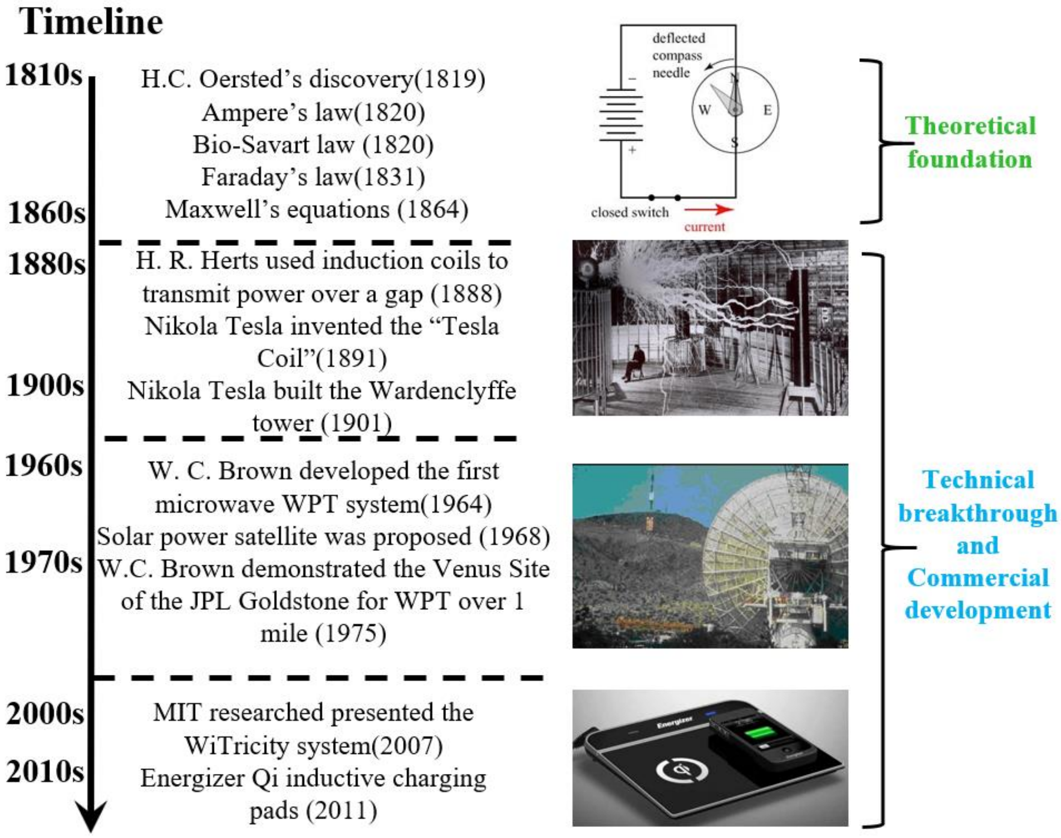

Fig. 1-6. A brief development progress of WPT technology.

A brief development history of WPT technology is depicted in Fig. 1-6. Above all, WPT technology can be mainly divided into two categories: far-field WPT (radiative) and near-field WPT (non-radiative). To be specific, far-field WPT can be sorted into directive radio frequency (RF) power beamforming and non-directive RF power beamforming [23, 24]. Near-field WPT can be classified into a further three approaches, namely inductive coupling [25], MRC [14] and capacitive coupling [26].

A comparison of these approaches for WPT is provided in Table 1-1, detailing types, advantages, disadvantages and typical applications.

Table 1-1: Comparison of different approaches for WPT techniques

Classification	**Far-field WPT (radiative)**		**Near-field WPT (non-radiative)**		
Approaches	Directive RF power beaming	Non-directive RF power beaming	Inductive coupling	Magnetic resonance coupling	Capacitive coupling
Types	Antennas / Antennas Arrays		Coils	Resonators	Metal plates
Effective charging distance	Dependent on frequency and power level, typically from several meters to kilometers		From a few millimeters to a few centimeters	From a few centimeters to a few meters	Up to a few millimeters
Frequency range	GHz		kHz-MHz	kHz-MHz	MHz
Advantages	Long transfer distance, Insensitive to misalignment		Safe for human, Simple complementation	High power transfer efficiency, No need of Line-of-Sight	Eddy current loss free
Disadvantages	Very low transfer efficiency and low conversion efficiency, Require Line-of-Sight, Not safe for human,		Short transfer distance, Very sensitive to misalignment	Sensitive to misalignment and driving frequency	High voltages
Applications	Solar power system, Ambient energy harvesting, Low-power wireless sensors		Electric toothbrush; Charging pad for cell phones, EV, Medical devices	EV; Portable /mobile devices, Medical devices,	Railway vehicles, Medical devices, EV

Generally, far-field WPT is used in applications such as ambient energy harvesting and low-power wireless sensors as it can achieve power transmission over a range of several metres to kilometres. Near-field WPT has wider application possibilities, such as electric vehicles, wearable/implantable electronic devices, mobile phones and laptops. Inductive coupling is based on electromagnetic induction between two coils. Magnetic resonance coupling is based on electromagnetic resonance between two resonators with same resonance frequency. Capacitive coupling delivers energy via electric fields formed between metal plates. Inductive coupling requires accurate alignment. Magnetic resonance coupling can have a relatively large transfer distance with high power transfer efficiency. Capacitive coupling is suitable for those applications where the transfer distance is less than 1 mm.

1.2 Research Motivation

Despite enjoying the modernisation that various electronic devices like mobile phones, laptops and computers bring to us, we still have to suffer from the inconvenience of an increasing number of chargers and charger wires to keep these devices functioning. In the contemporary world, health care is advancing at an astounding speed, for example offering patients IMDs for detecting and sensing in real time, the functioning of areas of the body that cannot be reached easily.

Cardiovascular diseases could be significantly reduced or prevented by the continuous real time monitoring of the heart rhythm and blood flow via sensors implanted in the body, as a kind of in-body wireless body area network (WBAN) [27, 28] application. Biomedical implantable devices [29, 30] offer promising solutions to the monitoring, diagnosis and treatment of various diseases helping to save and extend lives. A pacemaker is a treatment solution for cardiovascular diseases allowing a person with an abnormal heart rhythm to maintain a normal lifestyle [31]. Since the first artificial pacemaker was introduced in 1932, much has changed and will continue to do so in the future. The first implantable pacemaker was developed by Dr. Rune Elmqvist in 1958 and since then they have become smaller and lighter [32].

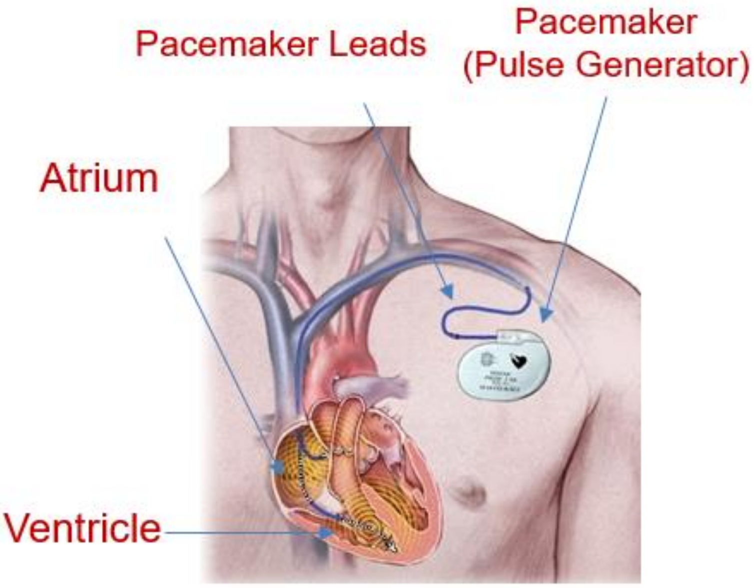

Fig. 1-7. Schematic of a double chamber pacemaker [33].

Functionally, a pacemaker with a typical size of 60 mm×42 mm×10 mm comprises at least three parts: an electrical pulse generator, a power source (battery), and an electrode (lead) system [34]. Generally, there are two types of pacemakers according to the number of electrodes: single chamber pacemakers and double chamber pacemakers [35]. A schematic of a double chamber pacemaker is shown in Fig. 1-7. A pacemaker utilises the energy stored in batteries to sense the heartbeat through electrodes implanted in the heart and to provide pacing pulses to the heart to stimulate normal sinus rhythm.

The power supply of choice for implantable devices is generally a battery, however, owing to their finite lifetime they present a significant limitation to device usage. Conventional operation relies heavily on continuous power supply from batteries. Battery capacity is closely related to battery size and for an implantable device it must be small limiting its application. Recently, WPT techniques have gained significant interest in many applications, especially for wearable and implantable medical devices, to address this power delivery issue [36]. With the aid of WPT, surgeries for replacing batteries can be avoided. However, there are still many challenges to be addressed in designing a WPT system for an implantable device, including: power transfer efficiency (PTE), power stability, size of receiver and accompanying circuitry.

This research aims to develop a WPT system for pacemakers. The system will include a transmitting coil, a receiving coil and an RF-to-DC conversion circuit. To gain higher PTE for medical implants, the following factors and issues should be taken into consideration and addressed in this work.

1) Circuit topology – The MRC method for WPT offers higher PTE and larger transfer distances in comparison to other techniques. However, the complex configuration of the matching circuits required makes the selection of transmitting and receiving resonator difficult [37, 38]. Furthermore, the impedance of the load on the WPT system militates the performance of the WPT link. Each circuit topology has its own characteristics, leading to different performance in relation to load power and PTE. Therefore, the choice of topology is application dependent in order to ensure maximum PTE and maximum load power. The effect of load size on different system topologies is important and forms a core investigation in this work.

2) Operating frequency – According to the regulations of the Federal

Communications Commission (FCC), the Medical Device Radiocomunications Service (MedRadio) is allocated in the 401-406, 413-419, 426-432, 438-444 and 451-457 MHz ranges [39]. To be compatible with other international frequency allocations, the 402-405 MHz frequency band is the Medical Implant Communication Service (MICS) band for medical implant apparatus in the performance of diagnostic or therapeutic functions (such as cardiac pacemakers and defibrillators) [40]. However, in many researches, lower frequencies (below 100 MHz) are chosen as the MRC-WPT operating frequency to decrease energy absorption by the human body, despite these frequencies being outside of those allowed for medical implant devices. Requirements on resonators with frequencies in the MICS band presents design challenges for the transmitting/receiving antennas and necessary matching networks. The design and matching of appropriate resonators form another significant area for investigation in this work.

3) Loss minimisation – Higher transmitting frequencies offer the potential for higher power transfer efficiencies; however, they can also produce more eddy current losses, tissue heating, and generate electromagnetic compatibility (EMC) issues in the electronic circuitry of the IMDs. Crucial factors for MRC-WPT are the Quality (Q) factors of the coils used for transmitting and receiving. The reason for this is that a high Q-factor can mitigate losses during power transmission, therefore enhancing PTE. This work involves the design of transmitting and receiving coils with high Q-factors for an implantable WPT system.

4) Safety issues – In order to prevent the hazardous heating of biological tissues, implantable systems must comply with the specific absorption rate (SAR) standards. The IEEE standard restricts the SAR averaged over any 1 g of tissue in the shape of a cube (1-g AVG SAR) to less than 1.6 W/kg or the SAR averaged over any 10 g of tissue in the shape of a cube (10-g AVG SAR) to less than 2 W/kg[41]. These regulations influence the maximum transmit power of the system. To ensure a high PTE, the receiver should minimise its SAR value in order to maximise the transmittable power and hence minimise charging time. Thus, design of a receiver that best satisfies the SAR regulations is another important area of investigation in this work.

1.3 Aim and Objectives

The main aim of this research is to develop an implantable WPT system with a high PTE and high allowable transmit power for pacemakers. This aim is expressed in terms of six objectives in order to provide a structured approach to the research.

1) To investigate the effects of different topologies of the primary and secondary circuits used in magnetic resonance coupled WPT.
2) To determine the criteria for the selection of a suitable circuit topology based on specific application requirements to maximise PTE and load power at a given frequency.
3) To develop a printed spiral coil with inductive characteristics at the desired frequency.
4) To develop a method of decreasing parasitic resistance and improving the *Q*-factor of printed spiral coils and planar loops using a split-ring loop.
5) To develop a self-resonator with series self-resonance at a desired frequency, which could be used as a transmitting or receiving resonator in a WPT circuit.
6) To develop a series-primary and parallel-secondary WPT system for charging a pacemaker with: series and parallel self-resonators and a rectifying circuit to convert RF energy to DC power.

1.4 Overview of the Thesis

This thesis is composed of seven chapters that focus on the design of a WPT system for implantable devices. Specifically, the research includes a theoretical analysis of MRC-WPT circuits, the design and optimisation of a WPT system and verification of the system by practical measurement. The thesis is organised as follows.

Chapter 1 provides the background of this work, including a brief history of the development of WPT, comparisons of WPT techniques, research motivation, aims and objectives and an overview of the thesis.

Chapter 2 provides fundamental knowledge and a detailed literature review of different techniques (far-field and near-field) for different WPT applications (in free space and in body tissues) to obtain a better understanding of the state-of-the-art in WPT designs, meanwhile recognising the issues and challenges to be overcome in this work.

Chapter 3 investigates the characteristics of different topologies of the MRC method for WPT. Experimental results are used to verify the theoretical analysis. The effects of load impedance on the performance of the wireless power link is demonstrated. Criteria for the avoidance of the phenomena of frequency splitting and enhancing PTE for a specific application are given.

Chapter 4 highlights the suitability of coils as a planar structure for a WPT system operating at high frequency. Meanwhile, an investigation of the characteristics of traditional planar spiral coils (PSCs) is conducted, including simulations and measurement. Thus, the limitations of traditional PSCs on PTE at high operating frequencies are clearly shown. This work paves the way towards tackling the challenges and drawbacks of traditional PSCs for WPT at higher operating frequencies.

Chapter 5 proposes a new structure for a planar split-ring loop with high Q-factor that decreases ohmic loss and enhances PTE, as well as allowing for increased power transfer distance. Furthermore, a novel self-resonator is designed as transmitter and receiver that allows the need for complex matching circuits to be avoided. The resonators parameters are swept and optimised to realise self-resonance at the chosen frequency. These could easily be applied to portable devices due to the self-contained circuit configuration. The structure of the self-resonator has a unique resonance characteristic and high PTE in comparison to a traditional planar coil, making it more suitable for WPT.

Chapter 6 proposes a WPT system with planar split-ring loops for IMDs, including a transmitting antenna, a receiving antenna and a rectifier for RF-to-DC conversion. The operating frequency of this WPT system is 403 MHz, which belongs to the MICS band and hence can be used for implantable devices without an individual license being issued by the FCC. The design process and optimisation of the WPT link between the transmitter and receiver are illustrated; enhancing the PTE and receiving power while satisfying SAR regulations. The configuration of a rectifying circuit is presented to convert the RF power to DC power. Measurements are conducted using minced pork to simulate body tissue allowing the practicality of this designed WPT system for IMDs (such as pacemakers) to be demonstrated.

Chapter 7, the final chapter, concludes this thesis and highlights the contributions of this work. Some future work in this research topic is also recommended.

1.5 References

[1] "Wireless Power Society Supported by WiPoT." [Online]. Available: http://www.wipot.jp/english/.

[2] "Wireless Power Transfer and Charging." [Online]. Available: http://www.designhmi.com/2015/04/16/wireless-power-transfer-and-charging/.

[3] F. Sumi, "Future with Wireless Power Transfer Technology," *Journal of Electrical & Electronic Systems,* vol. 07, no. 04, 2018, doi: 10.4172/2332-0796.1000279.

[4] B. Dibner, *Oersted and the discovery of electromagnetism*. New York: Blaisdell, 1962.

[5] J. C. Maxwell, *A Treatise on Electricity and Magnetism*. Clarendon press, 1873.

[6] D. Baird, R.I.G. Hughes, N. Alfred, *Heinrich Hertz: Classical Physicist, Modern Philosopher*. U.S.: Kluwer Academic Publishers, 1998.

[7] N. Tesla, "Apparatus for transmitting electrical energy," U.S. Patent Patent 1119 732, Dec., 1914.

[8] M. Cheney, *Tesla: Man Out of Time*. USA: Prentice-Hall, Inc., Englewood Cliffs, NJ, 1981.

[9] "Nikola Tesla Quotes on Life, Energy & Inventions to Inspired." [Online]. Available: https://cutelovequotesforher.org/nikola-tesla-quotes-on-life-energy-inventions/

[10] W. C. Brown, "The History of Power Transmission by Radio Waves," *IEEE Transactions on Microwave Theory and Techniques,* vol. 32, no. 9, pp. 1230-1242, 1984, doi: 10.1109/TMTT.1984.1132833.

[11] "Cota system." [Online]. Available: http://www.ossiainc.com.

[12] "PRIMOVE e-Mobility Solution." [Online]. Available:

http://primove.bombardier.com.

[13] "Powercast." [Online]. Available: http://www.powercastco.com.

[14] A. Kurs, A. Karalis, R. Moffatt, J. D. Joannopoulos, P. Fisher, and M. Soljacic, "Wireless power transfer via strongly coupled magnetic resonances," *Science,* vol. 317, no. 5834, pp. 83-6, Jul 6 2007, doi: 10.1126/science.1143254.

[15] S. Li and C. C. Mi, "Wireless Power Transfer for Electric Vehicle Applications,". *IEEE Journal of Emerging and Selected Topics in Power Electronics*, vol. 3, no. 1, pp. 4-17, 2015, doi:10.1109/JESTPE.20142319453.

[16] "Hands-on: Energizer Qi inductive charging pad." [Online]. Available: https://www.cnet.com/news/hands-on-energizer-qi-inductive-charging-pad/.

[17] N. Dobrostomat, G. Turcan, and M. Neag, "Wearable health monitors with TransferJet data communications and inductive power transfer," in *2014 International Semiconductor Conference (CAS)*, 13-15 Oct. 2014 2014, pp. 259-262, doi: 10.1109/SMICND.2014.6966453.

[18] O. Jonah, S. V. Georgakopoulos, and M. M. Tentzeris, "Wireless power transfer to mobile wearable device via resonance magnetic," in *WAMICON 2013*, 7-9 April 2013 2013, pp. 1-3, doi: 10.1109/WAMICON.2013.6572768.

[19] I. Cho, S. Kim, J. Moon, J. Yoon, W. Byun, and J. Choi, "Wireless power transfer system for LED display board by using 1.8 MHz magnetic resonant coils," in *2011 Electromagnetic Compatibility Symposium - Perth*, 9-11 Nov. 2011 2011, pp. 1-4.

[20] David W. Baarman, "Inductively powered lamp assembly," U.S. Patent USOO6917163B2, July 12, 2005.

[21] J. Wang and Q. Huang, "Wireless power transfer system in the LED lighting application," in *2015 12th China International Forum on Solid State Lighting (SSLCHINA)*, 2-4 Nov. 2015 2015, pp. 120-122, doi: 10.1109/SSLCHINA.2015.7360703.

[22] "'WiTricity' Wireless Electricity Technology demonstrated by MIT." [Online]. Available: http://www.techgadgets.in/wireless/2007/08/witricity-wireless-electricity-technology-demonstrated-by-mit/.

[23] S. Y. Hui, "Planar Wireless Charging Technology for Portable Electronic Products and Qi," *Proceedings of the IEEE,* vol. 101, no. 6, pp. 1290-1301, 2013, doi: 10.1109/JPROC.2013.2246531.

[24] Z. Popovic, "Cut the Cord: Low-Power Far-Field Wireless Powering," *IEEE*

Microwave Magazine, vol. 14, no. 2, pp. 55-62, 2013, doi: 10.1109/MMM.2012.2234638.

[25] S. L. Ho, J. Wang, W. N. Fu, and M. Sun, "A Comparative Study Between Novel Witricity and Traditional Inductive Magnetic Coupling in Wireless Charging," *IEEE Transactions on Magnetics,* vol. 47, no. 5, pp. 1522-1525, 2011, doi: 10.1109/TMAG.2010.2091495.

[26] F. Lu, H. Zhang, and C. Mi, "A Review on the Recent Development of Capacitive Wireless Power Transfer Technology," *Energies,* vol. 10, no. 11, 2017, doi: 10.3390/en10111752.

[27] Z. Liu, B. Liu, and C. W. Chen, "Joint Power-Rate-Slot Resource Allocation in Energy Harvesting-Powered Wireless Body Area Networks," *IEEE Transactions on Vehicular Technology,* vol. 67, no. 12, pp. 12152-12164, 2018, doi: 10.1109/TVT.2018.2872960.

[28] S. Sodagari, B. Bozorgchami, and H. Aghvami, "Technologies and Challenges for Cognitive Radio Enabled Medical Wireless Body Area Networks," *IEEE Access,* vol. 6, pp. 29567-29586, 2018, doi: 10.1109/ACCESS.2018.2843259.

[29] A. Kiourti and K. S. Nikita, "A Review of In-Body Biotelemetry Devices: Implantables, Ingestibles, and Injectables," *IEEE Transactions on Biomedical Engineering,* vol. 64, no. 7, pp. 1422-1430, 2017, doi: 10.1109/TBME.2017.2668612.

[30] G. Zheng, R. Shankaran, M. A. Orgun, L. Qiao, and K. Saleem, "Ideas and Challenges for Securing Wireless Implantable Medical Devices: A Review," *IEEE Sensors Journal,* vol. 17, no. 3, pp. 562-576, 2017, doi: 10.1109/JSEN.2016.2633973.

[31] W. V. Shi and M. Zhou, "Body Sensors Applied in Pacemakers: A Survey," *IEEE Sensors Journal,* vol. 12, no. 6, pp. 1817-1827, 2012, doi: 10.1109/JSEN.2011.2177256.

[32] S. A. P. Haddad, R. P. M. Houben, and W. A. Serdijin, "The evolution of pacemakers," *IEEE Engineering in Medicine and Biology Magazine,* vol. 25, no. 3, pp. 38-48, 2006, doi: 10.1109/MEMB.2006.1636350.

[33] "Pacemakers." [Online]. Available: http://www.solarstorms.org/SPacemakers.html.

[34] M. R. Neuman *et al.*, "Advances in Medical Devices and Medical Electronics," *Proceedings of the IEEE,* vol. 100, no. Special Centennial Issue, pp. 1537-1550,

2012, doi: 10.1109/JPROC.2012.2190684.

[35] P. Arzuaga, "Cardiac pacemakers: past, present and future," *IEEE Instrumentation & Measurement Magazine,* vol. 17, no. 3, pp. 21-27, 2014, doi: 10.1109/MIM.2014.6825384.

[36] C. Liu, C. Jiang, J. Song, and K. T. Chau, "An Effective Sandwiched Wireless Power Transfer System for Charging Implantable Cardiac Pacemaker," *IEEE Transactions on Industrial Electronics,* vol. 66, no. 5, pp. 4108-4117, 2019, doi: 10.1109/TIE.2018.2840522.

[37] Y. H. Sohn, B. H. Choi, E. S. Lee, G. C. Lim, G. Cho, and C. T. Rim, "General Unified Analyses of Two-Capacitor Inductive Power Transfer Systems: Equivalence of Current-Source SS and SP Compensations," *IEEE Transactions on Power Electronics,* vol. 30, no. 11, pp. 6030-6045, 2015, doi: 10.1109/TPEL.2015.2409734.

[38] W. Zhang and C. C. Mi, "Compensation Topologies of High-Power Wireless Power Transfer Systems," *IEEE Transactions on Vehicular Technology,* vol. 65, no. 6, pp. 4768-4778, 2016, doi: 10.1109/TVT.2015.2454292.

[39] "Medical Device Radiocommunications Service (MedRadio)," doi: https://www.fcc.gov/medical-device-radiocommunications-service-medradio.

[40] "Medical Implant Communications Service Frequency Table," doi: http://www.csgnetwork.com/micsfreqtable.html.

[41] "IEEE Standard for Safety Levels with Respect to Human Exposure to Electric, Magnetic, and Electromagnetic Fields, 0 Hz to 300 GHz," *IEEE Std C95.1-2019 (Revision of IEEE Std C95.1-2005/ Incorporates IEEE Std C95.1-2019/Cor 1-2019),* pp. 1-312, 2019, doi: 10.1109/IEEESTD.2019.8859679.

Chapter 2 Wireless Power Transfer Systems

2.1 Background

The development of wireless power transfer (WPT) technologies is advancing in two main directions: far-field (radiative) WPT and near-field (non-radiative or coupled-based) WPT.

2.1.1 Far-field Wireless Power Transfer

Far-field WPT is based on the transmission and receiving of radiated electromagnetic waves [1, 2], where a receiving antenna is placed a large separation distance of $R \geq 2D^2/\lambda$ (where D is the largest antenna dimension and λ is the operating wavelength) from the transmit antenna [3]. Initially, terrestrial far-field wireless energy transfer research was geared towards intentional long-range transmission of electromagnetic waves at radio frequencies (RF) [4].

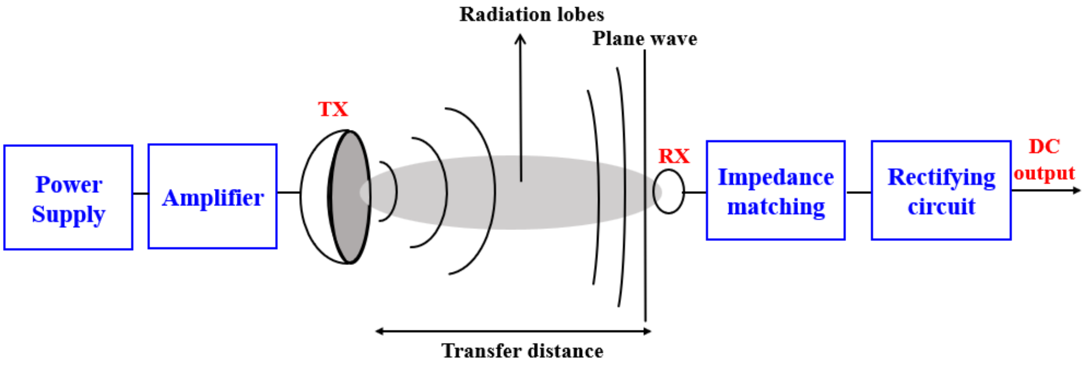

Fig. 2-1. Schematic of a far-field WPT system.

The architecture of a far-field WPT system is shown in Fig. 2-1. The power transmission starts with a power supply which is converted to RF energy via for example by magnetron, this is typically followed by an amplifier which can provide sufficient RF power for the transmitting antenna to send. After propagating over the antenna separation distance (typically through air), the RF/microwave signal is captured by the receiving antenna and rectified into electricity again through an RF-to-DC conversion using a rectifying circuit. The overall power transfer efficiency (PTE) of the far-field WPT system depends on various factors, such as the directivity and efficiency of the transmit and receive antennas, impedance mismatch losses and the RF-to-DC conversion efficiency.

2.1.2 Near-field Wireless Power Transfer

Near-field WPT schemes involve much shorter-range non-radiative energy interactions within electromagnetic fields. Energy may be transferred either through the magnetic or electrical fields in the vicinity of the excited field sources. It can be divided into three methods, namely inductive coupling, magnetic resonance coupling (MRC) and capacitive coupling, as discussed in the previous chapter.

2.1.2.1 Inductive Coupling Method

Inductive coupling works by magnetic field induction, that is to say, an alternating current in a primary/transmitting coil (connected to a source) generates a varying magnetic field that induces a voltage across the terminals of a secondary/receiving coil at the receiver (as shown in Fig. 2-2).

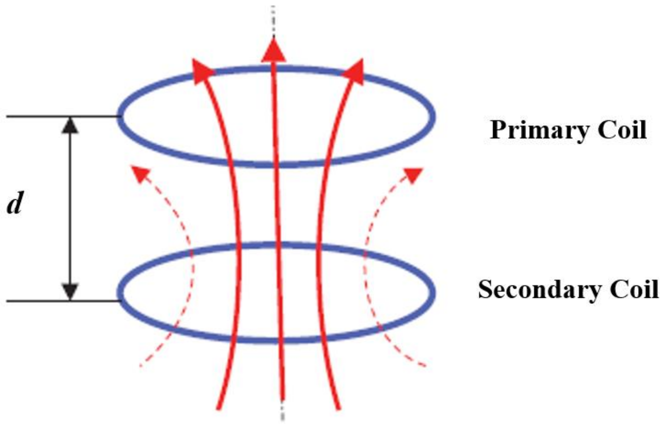

Fig. 2-2. Schematic of inductive coupling-based WPT [5].

The fundamental theories of inductive coupling-based WPT include the use of Biot-Savart's Law and Faraday's Law. Biot-Savart's Law is used to calculate the magnetic field **B,** produced by an arbitrary current distribution **I** [5]:

$$\mathbf{B} = \frac{\mu_0}{4\pi} \oint \frac{\mathbf{I} d\mathbf{l} \times \vec{r}}{\left|\vec{r}\right|^3} \tag{2.1}$$

where μ_0 is the vacuum permeability, **I** is the current in the transmitting coil, $d\mathbf{l}$ is a vector whose magnitude is the length of the differential element of the conducting wire, and $\vec{r}$ is the full displacement vector from the wire element to the point at which the field is being computed.

Faraday's Law [6] can then be used to calculate the induced voltage V_{Ind} over the receiver coil as the rate of magnetic field change through an effective surface area S by

$$V_{\mathrm{Ind}} = -\iint \frac{\partial \mathbf{B}}{\partial t} \bullet d\vec{s} \tag{2.2}$$

2.1.2.2 Magnetic Resonance Coupling Method

Resonance is a trend whereby one physical system in its natural frequency tends to absorb more energy from the environment. In other words, it is a phenomenon in which when one object vibrates it can cause another object with the same natural frequency to vibrate in phase. An example of this would be the sound of a tuning fork. Resonances can be formed to transfer energy [7]. In 2007, A. Kurs established the resonance energy transfer system, named WiTricity (Wireless electricity) based on electromagnetic coupled mode theory. The system was able to wirelessly transfer energy with up to 40% efficiency over distances in excess of 2 m [8].

The electromagnetic field is an energy field and can provide energy to power electrically driven apparatus. Electromagnetic waves contain energy, no matter whether there is a receiver or not. Therefore, use can be made of a non-radiative magnetic field (near-field) with a designed resonant frequency, by placing a resonator, such as an inductor-capacitor (LC) circuit, with the same resonant frequency in the field. Like the tuning fork, it will begin to resonate, and energy will be collected. As energy is stored in the resonating coil, the voltage across it will increase and as a result two systems with the same inherent resonant frequency will generate a strong magnetic field intensity (as shown in Fig. 2-3). The received energy can be used by the load after being converted via follow-up circuits [7]. The stronger the magnetic field the higher the transfer efficiency and also the greater the energy transfer distance can be.

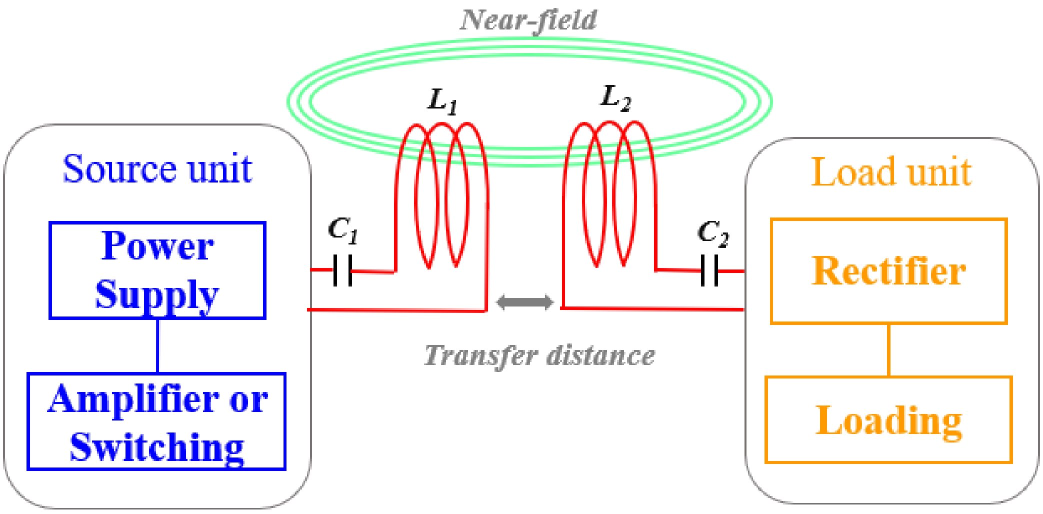

Fig. 2-3. Schematic diagram of energy transfer system via coupled magnetic resonance.

The energy supply of the source is provided by a power conversion module, inductor L_1 and capacitor C_1 constitute a resonant source, able to generate an alternating non-radiative magnetic field. The resonance frequency of the LC circuit is f_1. In theory, at f_1 the oscillation of the source resonant circuit is at its strongest and when f_2 (the resonance frequency of the secondary circuit) is equal to f_1, the value of the currents resonating in both coils is at its highest as well as the magnetic field intensity. Inductor L_2 and capacitor C_2 constitute the receiving resonant circuit, resonating due to the presence of an electromagnetic field and hence receiving energy. The receiving circuit must ensure $f_2 = f_1$, which is the necessary condition for energy transfer via MRC [9].

2.1.2.3 Capacitive Coupling Method

The capacitive coupling method delivers energy from transmitter to receiver mainly via electric field coupling rather than magnetic field coupling, thus possessing the ability to bypass metal materials existing in the transmission path, which is unlike the inductive coupling method [10].

Fig. 2-4 shows the schematic of a capacitive coupled based WPT system. The voltage excitation between the pair of external conductors (TX) generates extremely low currents, due to a high mutual impedance between them. However, when another pair of conductors (RX) are brought to close the loop, the mutual impedance reduces and draws current (I^+, I^-) from the source. In the process, the current drawn is mirrored to the load, thus powering it through this capacitive coupling. The impedance formed by the capacitive reactance between TX and RX is large even for very small separations between them (on the order of a few millimeters). Hence, the current drawn from the source is expected to be low, thus limiting the power transfer capability [11-13].

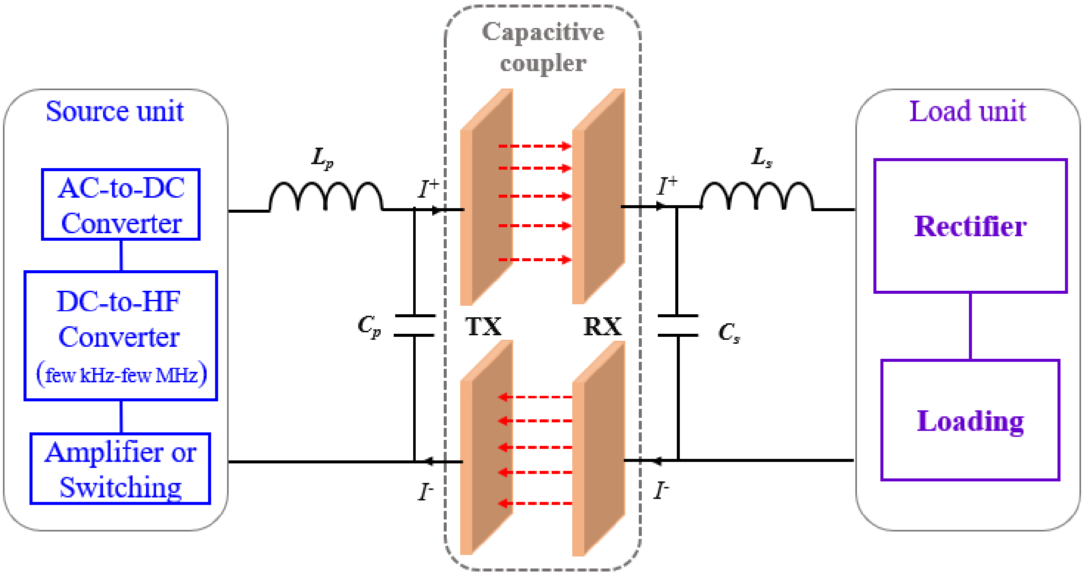

Fig. 2- 4. Schematic of a capacitive coupling based WPT system.

2.2 Studies of Wireless Power Transfer

Recently, there has been much research work investigating WPT for different applications. Three main applications are portable devices, electric vehicles and implantable devices. In this section, some recent designs of WPT used in free space and in body will be introduced.

2.2.1 Wireless Power Transfer in Free Space

Far-field charging systems can be realised through either non-directive RF radiation or directive RF beamforming [14]. Non-directive RF radiation can be conducted without line of sight and is less sensitive to the orientation and position of the receiver relative to the transmit antenna [15]. However, the resulting efficiency is relatively low. Low power wireless systems, such as wireless sensor networks (WSNs) [16] and Radio Frequency Identification (RFID) systems [17, 18] have become the most widely adopted applications for non-directive charging. A far-field wireless power charging system for low-power wireless sensors was proposed in [19] with low incident power density. It is suitable for low-duty cycle wireless sensors and applications sensing in environments where it is difficult or impossible to change batteries and where the exact position of the sensors might not be known.

Ambient RF energy harvesting as a non-directive charging method has also recently attracted a great deal of attention to harvest RF energy from TV broadcasts [20, 21], Global system for mobile communications (GSM) bands (900/1800) [22-24] and WiFi routers [25, 26] to charge low-power or ultra-low power sensors.

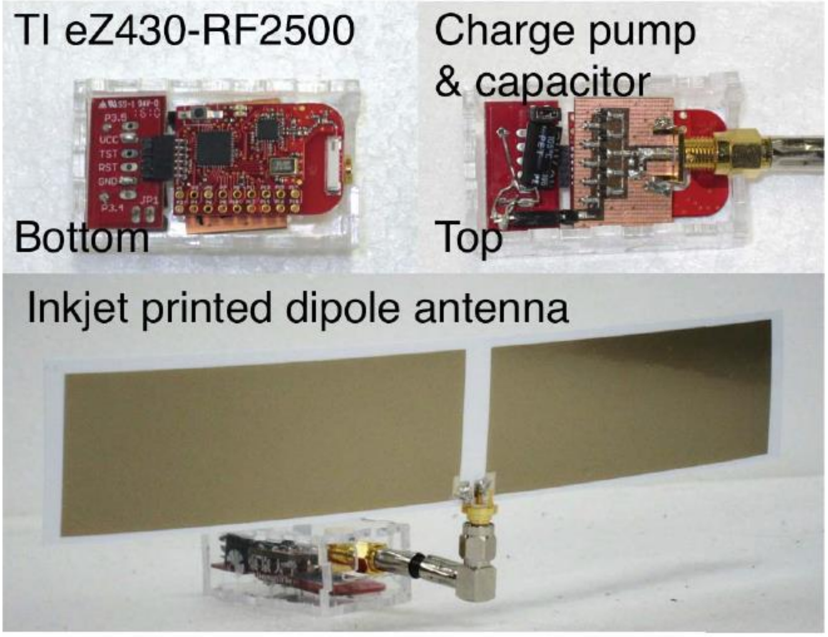

Fig. 2-5. Prototype of TV radiowave energy harvesting sensor node [27].

A prototype of an ambient RF energy harvesting sensor node is presented in Fig. 2-5, using scavenged energy from digital TV broadcasting signals. The charging system in Fig. 2-6 is made up of an inkjet-printed dipole antenna, 5-step modified Dickson charge pump with matching circuit, 100 µF capacitor and a Texas Instruments eZ430 RF-2500 sensor node with temperature sensor [27].

The RF power received by the dipole antenna from the broadcasting tower can be taken as the input to the rectifier, typical power levels are around -10 dBm, the RF-to-DC conversion efficiency at 540 MHz is 30% with a load of 50 kΩ. The efficiency is directly related to the input power as when the rectifier input level decreases to -15 dBm, the conversion efficiency is only 10% [27]. To increase the receiving power, a directional transmitting antenna and a directional Yagi antenna are used in [28]. The space between the transmitting antenna and receiving antenna is 90 cm, and an operating frequency of 433 MHz (industrial, scientific and medical (ISM) band) is used. The Yagi antenna can receive almost 4 mW and the RF-to-DC conversion efficiency can reach 39.1% in this case. Therefore, far-field WPT can operate over a large transfer distance, but only a small amount of power can be received in part due to a low conversion efficiency.

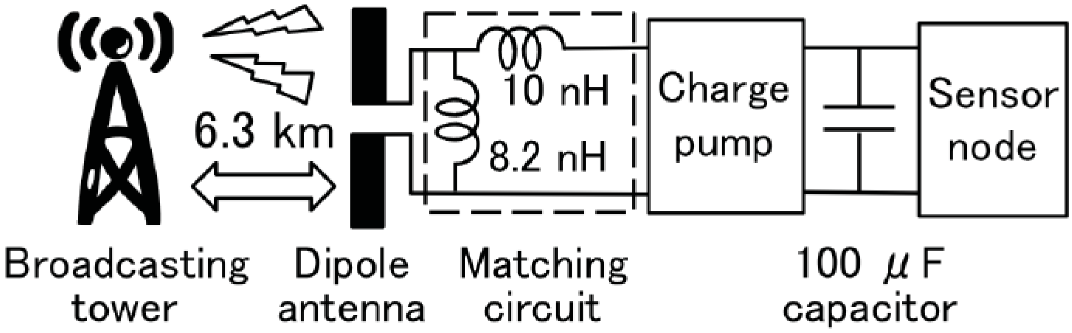

Fig. 2-6. Equivalent schematic of RF energy harvesting sensor nodes [27].

Near-field WPT is a promising technology for charging electric toothbrushes [29], portable devices (such as iPads, mobile phones and laptops) [30-32] and electric vehicles [33-35]. An inductive power transfer system with magnetic dipole type coils operating at 20 kHz is proposed in [36]. When the separation between the primary coil and secondary coil is 3 m, 4 m and 5 m, the primary-coil-to-load power transfer efficiencies are 29%, 16% and 8%, respectively.

An MRC system using U-coils (three coils) to replace the traditional two-coil method was illustrated in [37] in order to further improve PTE, which can be seen in Fig. 2-7. The PTE can reach 66% over a transfer distance of 1 m at an operating frequency of 85 kHz.

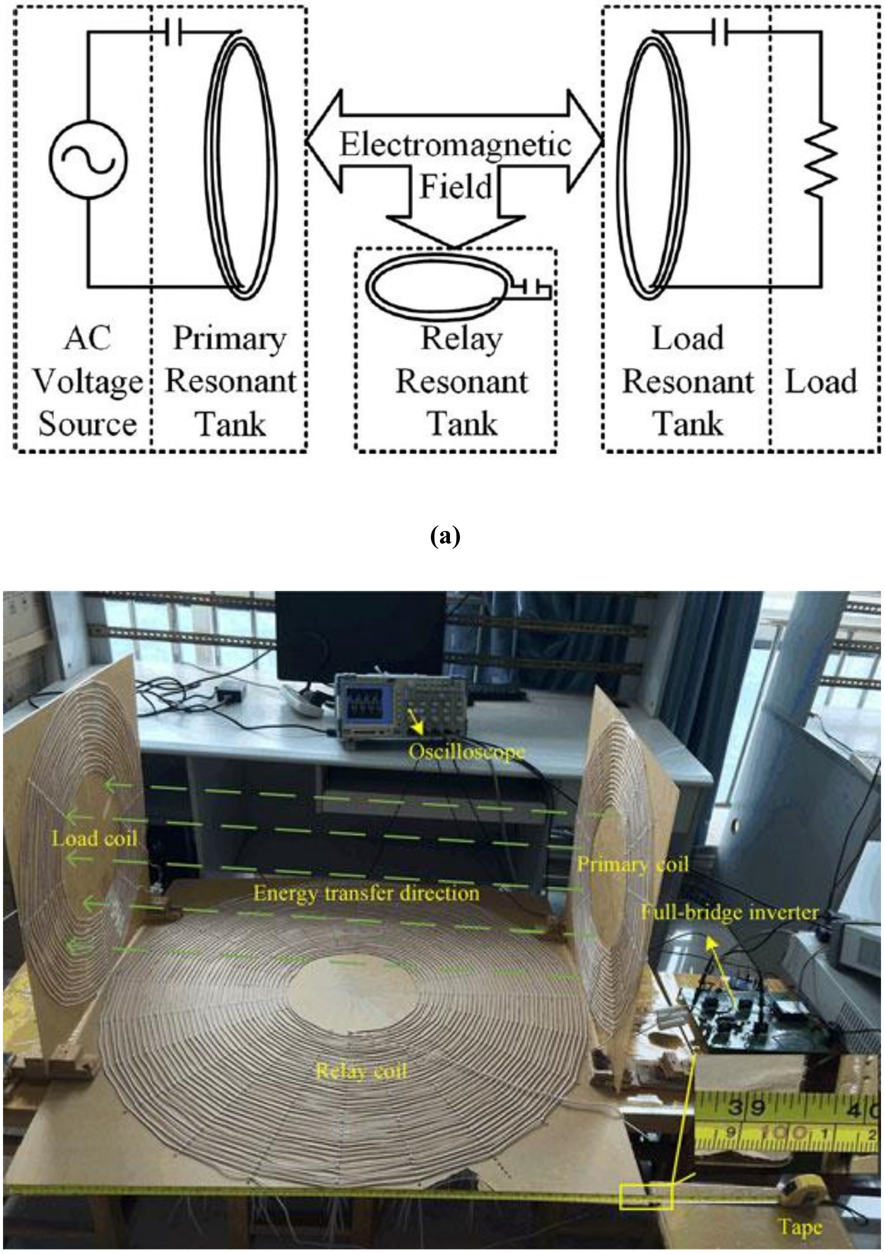

(a)

(b)

Fig. 2-7. (a) Equivalent schematic and (b) practical setup of U-coil WPT system [37].

Capacitive coupled WPT is suitable for stationary charging of electric vehicles. A capacitively coupled wireless EV charging system using a conformal bumper docking station allows for simple mechanical implementation and avoids the pitfalls associated with alignment and air-gap maintenance [38]. A photo of a capacitive coupling WPT system is depicted in Fig. 2-8. This method requires the air gap between transmitter and receiver to be as small as possible (<1 mm). In this case, the PTE can reach 90%

at an operating frequency of 530 kHz.

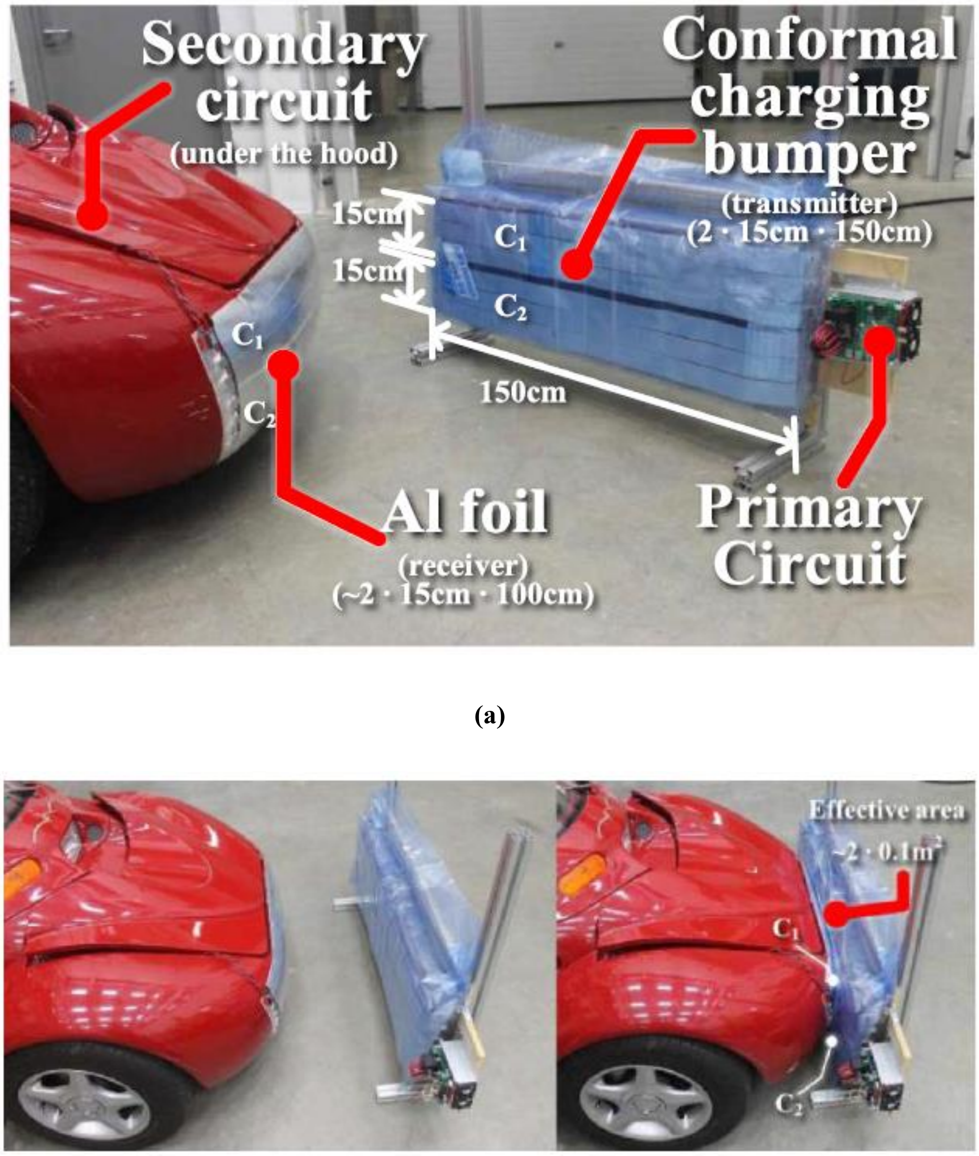

(a)

(b)

Fig. 2-8. Photos of Corbin Sparrow approaching and docked with the conformal bumper charging station. (a) Corbin Sparrow charging system, car-left, station-right. (b) Corbin Sparrow approaching and docked with the charging station [38].

These methods for WPT have their own advantages and disadvantages. However, the PTE and transfer distance remain the two most significant challenges for improvement.

2.2.2 Wireless Power Transfer for Implantable Applications

2.2.2.1 Effect of the Body on Wireless Power Transfer Performance

WPT offers the possibility of charging implantable medical devices (IMDs), overcoming issues of limited battery life and avoiding the inconvenience of wires and surgeries. Unlike free space, the human body has frequency dependent loss. Different body tissues have different characteristics of permittivity and conductivity at different frequencies [39]. Human safety is the most significant factor which needs to be taken into account through consideration of SAR.

For far-field WPT, the transmit antenna is usually optimised for free space, while the receive antenna is placed inside the body surrounded by tissues. The Federal Communications Commission (FCC) limits the maximum transmit output power in the ISM bands, to 30 dBm (1 W). Besides, the maximum effective isotropic radiated power (EIRP) should be less than 36 dBm (4 W). The EIRP for a wireless power link can be expressed by equation (2.3), the transmitted power P_T is adjusted to balance the gain G_T of the transmit antenna and impedance mismatch losses L_{imp} (as described in equation (2.4)) to keep the EIRP under acceptable limits [40].

$$[EIRP]_{dBm} = [P_T]_{dBm} + [G_T]_{dB} - [L_{imp}]_{dB} \tag{2.3}$$

$$[L_{imp}](dB) = -10\log(1-|\tau|^2) \tag{2.4}$$

where τ is the appropriate reflection coefficient.

As an example, the maximum permissible exposure (MPE) limit for uncontrolled exposure to an intentional radiator operating at a 2.4 GHz is 10 W/m^2. The power flux density W_f at a transfer distance from the transmitter is provided by [41]

$$[W_f](W/m^2) = \frac{EIRP}{4\times\pi\times d^2} \le 10 \quad (W/m^2) \tag{2.5}$$

The minimum transfer distance [42] can be obtained from equation (2.5) when the EIRP of the transmit antenna is fixed. Furthermore, maximum specific absorption rate (SAR) values are limited to protect patient safety.

For inductive coupling and MRC based near-field WPT, inductors or coils play a critical role in the power transmission process. Implantable printed spiral coils (PSCs) are implemented on organic, ceramic or silicon substrates and coated by an insulator such as Parylene or silicone [43]. Compared to the PSCs in air, they are surrounded by body tissues and fluids that have high permittivities, which significantly increases the parasitic capacitance of the PSCs when implanted [44, 45]. Body tissues include skin, fat, muscle, blood and bone, however body tissues will be considered here as a single homogeneous layer for simplicity. Fig. 2-9 shows the equivalent modelling of the parasitic capacitance generated by a multilayer material surrounding an implanted PSC. The total equivalent parasitic capacitance of the implanted PSC [46, 47] can be calculated by (2.6)

$$C_{eq} = C_0 + C_1 + C_2 + C_3 + C_4 + C_5 + C_6 \qquad (2.6)$$

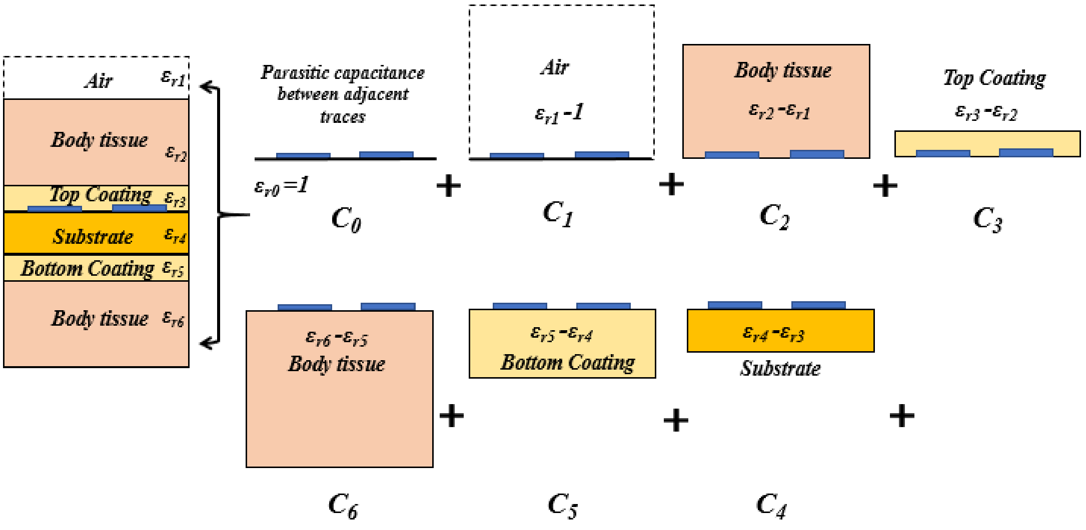

Fig. 2-9. Equivalent modelling of the parasitic capacitance generated by multilayer material surrounding of the implanted PSCs.

Capacitive coupling based WPT typically has a high frequency of operation (tens or hundreds of MHz) to increase PTE. Tissue losses in body base applications would therefore be significant. In capacitive WPT, tissue losses are the main source of loss and hence highest goal in terms of design. This is closely followed by ensuring SAR requirements are met. As shown in Fig. 2-10(a), a pair of metallic patches with an effective area (A) has been separated by a tissue layer [48]. Upon power transmission through these capacitances, conduction currents lead to losses in the tissue and ohmic losses in the patches [49]. These tissue losses R_T and conductor losses R_C can be modelled as equivalent loss resistances in series with the capacitance of the patches C_{eq}. The self-inductance L_{self} of the lead wires and patches can be added as series inductors, as shown in Fig. 2-10(b). PTE increases with effective area but decreases with the distance of separation. The PTE of the capacitive coupling link is highly sensitive to the separation between the transmitter and receiver due to the weakness of capacitive coupling (few millimeters separation). Therefore, body tissues have a great influence on PTE.

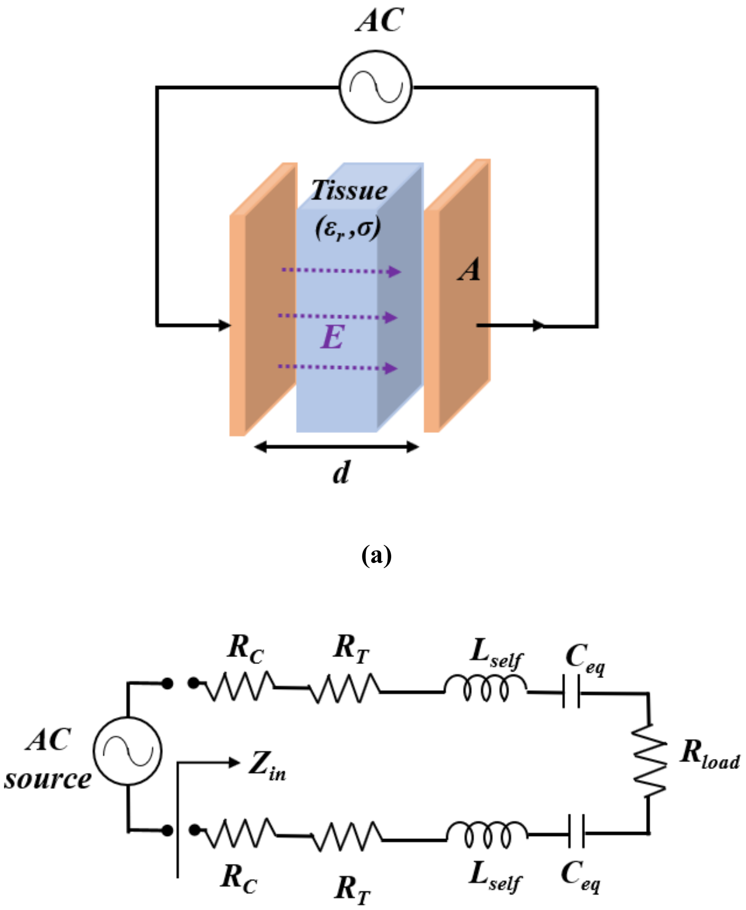

(a)

(b)

Fig. 2-10. Schematic of near-field capacitive coupling between two metallic patches; (b) Equivalent modelling of the link with tissue losses and conductor losses.

2.2.2.2 Implantable Wireless Power Transfer Systems

A far-field WPT system for implantable devices is proposed in [50], including horn antenna and implantable rectenna (implantable antenna integrated with a rectifier). The overall dimension of the implantable rectenna is 8 mm×4 mm×1.9 mm, which is shown in Fig. 2-11.

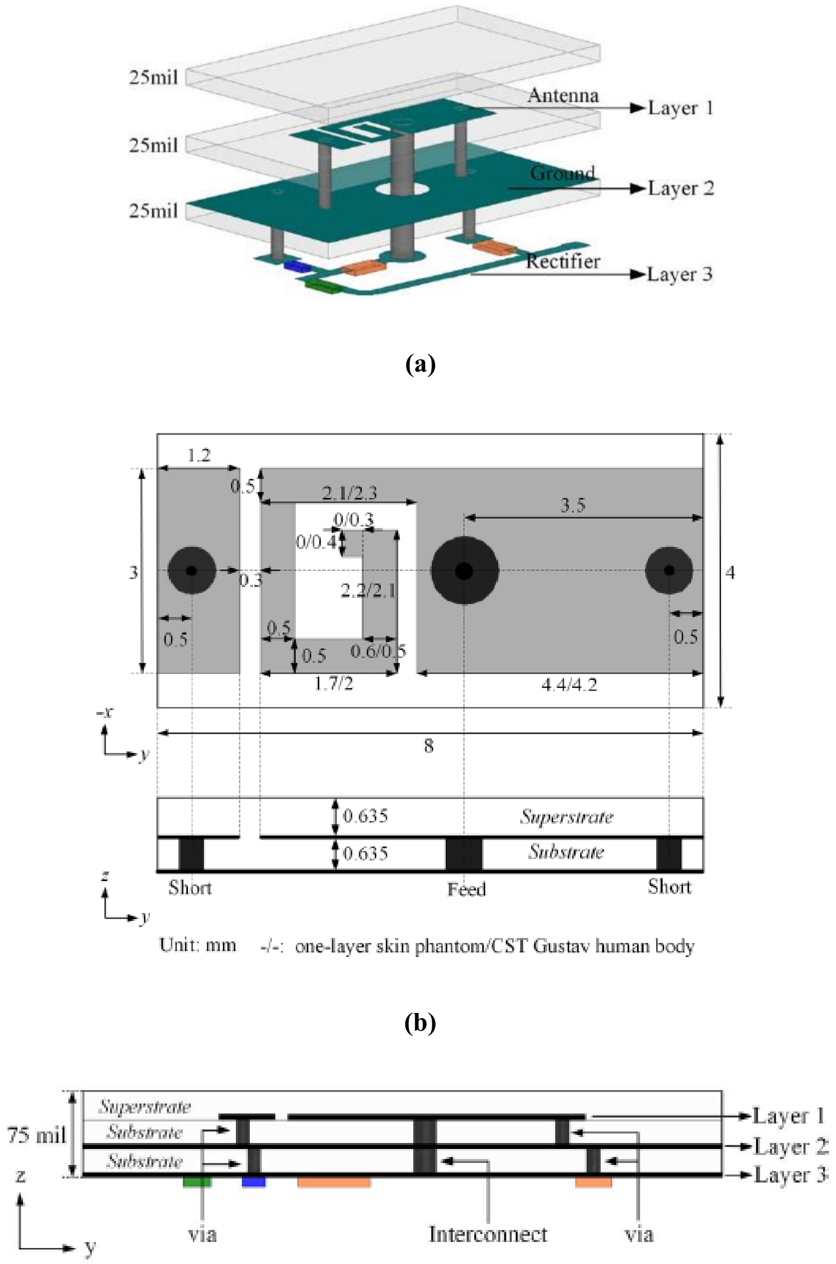

(a)

(b)

(c)

Fig. 2-11. Configurations for implanted rectenna. (a) Geometry; (b) Top view (Unit: mm); (c) Side view [50].

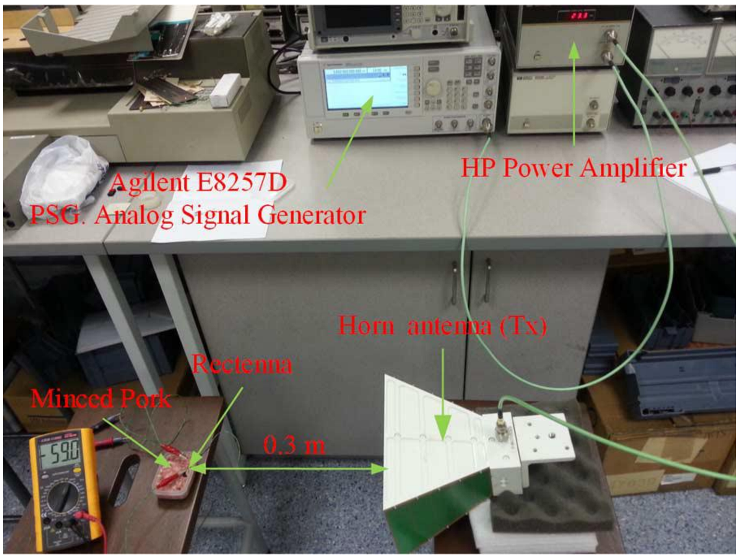

Fig. 2-12. Measurement setup for far-field WPT [50].

Fig. 2-12 illustrates the measurement setup used for far-field WPT, where the designed implanted rectenna is in the minced pork and the horn antenna is placed at a distance of 0.3 m away from the edge of the pork. The maximum input power to the horn antenna is 24.3 dBm (269 mW). At 2.51 GHz, the DC output voltage is 0.12 V across a load of 3.25 kΩ. Thus, the received power is 4.4 µW and the overall PTE (PTE and conversion efficiency) is only 0.0016%.

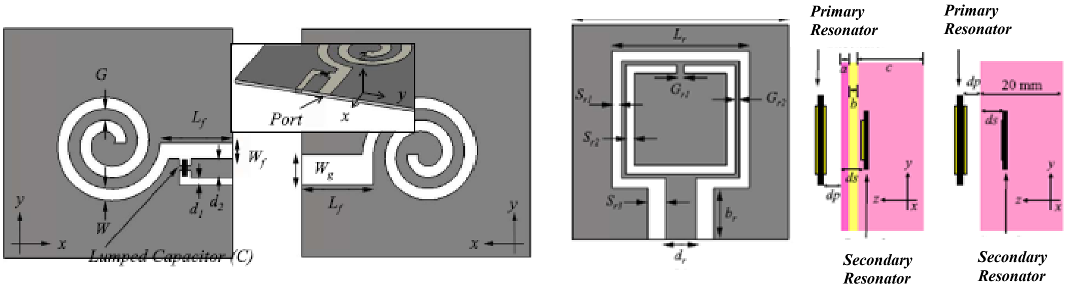

(a) (b) (c) (d)

Fig. 2-13. Geometry of the primary resonator. (a) Front and back view. (b) Geometry of the secondary resonator. Configurations adopted in full-wave simulations. (c) Three-tissue-layer model (skin–fat–muscle) with $dp = ds = 5$ mm, $a = b = 2$ mm and c = 16 mm. (d) Homogeneous model with $dp = ds = 5$ mm [51].

An inductive link for charging pacemakers operating at 403 MHz (in the MICS band) was proposed and simulated in [51]. The primary resonator consisted of two spirals printed on the top and bottom face of an Arlon substrate with dimensions 30 mm × 30 mm and a square split-ring resonator (14.9 mm × 14.9 mm) as the secondary resonator implanted at a depth of 5 mm in a layer of muscle, below layers of skin and fat, both approximately 2 mm thick (as shown in Fig. 2-13). This WPT system has a maximum measured transfer efficiency of around 7.4% when the distance between two resonators is 6.5 mm. As the distance increases to 10 mm, the measured transfer efficiency falls to around 5.24% with a 10-g average SAR of less than 1.08 W/kg), which is within the limits set out in the IEEE/FCC standard (2 W/kg).

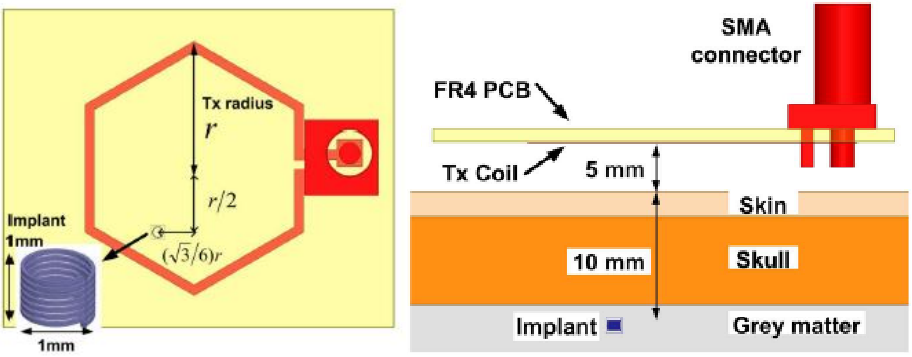

(a) (b)

Fig. 2-14. HFSS simulation model used for wireless link optimisation. (a) Top view. (b) Side view [52].

An inductive WPT link for millimetre-size biomedical implants at 200 MHz was proposed in [52]. An HFSS simulation model was used to determine its performance and is shown in Fig. 2-14. The radii of the transmit coil with 1 turn and receive coil with 7 turns were 12 mm and 0.5 mm respectively. The measured PTE with 12 mm transmit to receive separation at 200 MHz was 1.02% in air and 0.56% in tissue.

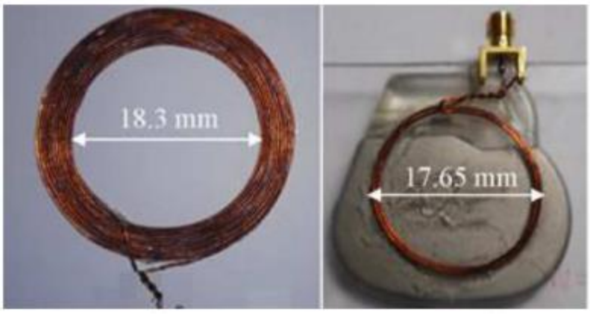

(a) (b)

Fig. 2-15. Demonstrator configuration. (a) Fabricated primary coil. (b) Secondary coil and pacemaker case [53].

A WPT charging system for active implantable and medical devices and pacemakers was proposed in [53] to address issues of limited battery life. The WPT system utilised is based on MRC with one on-body primary coil and one in-body secondary coil (as shown in Fig. 2-15). The system has been analysed by a co-simulation method using a numerical tool for the time-harmonic magnetic field calculations and an equivalent circuit to predict coil currents and voltages at 300 kHz. The number of turns for the primary and secondary coils were 10 and 4, respectively. The compensation topology of primary-secondary circuit is series-parallel with a separation of 5 mm. The numerical and measured PTEs were 82% and 78% respectively.

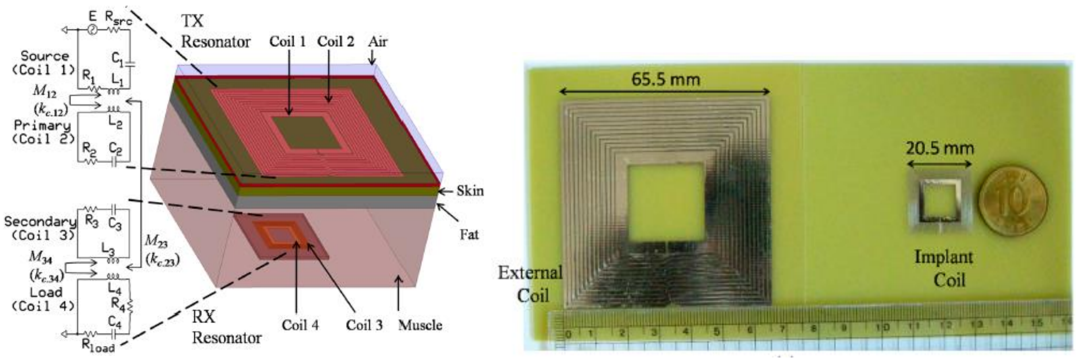

(a) **(b)**

Fig. 2-16. (a) Simplified physical and electrical configuration of a fully planar WPT in a human tissue medium; (b) Fabrication of square PSCs [54].

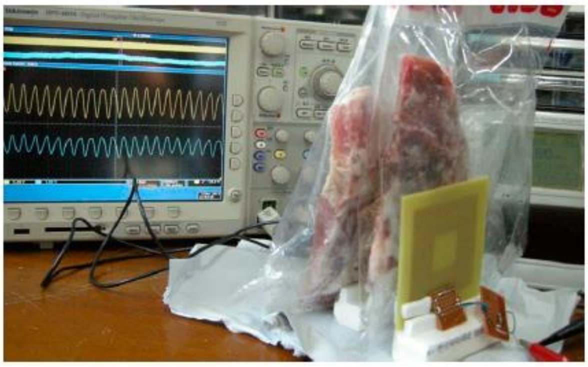

Fig. 2-17. Measurement setup of the proposed wireless power link for implantable device [54].

A fully planar wireless power link based on the MRC method for implantable devices is proposed in [54] at an operating frequency of 13.56 MHz using square printed spiral coils (PSCs). The system includes source coil, primary coil, secondary coil and load coil (as shown in Fig. 2-16(a)). The dimension of the primary coil is 65.5 mm×65.5 mm and the dimension of secondary coil is 20.5 mm×20.5 mm. All coils are printed on FR-4 substrate which has a relative permittivity of ε_r=4.4, as shown in Fig. 2-16(b). The separation between primary coil and secondary coil is 10 mm. 10 mm of beef muscle tissue is placed between the primary and secondary coils and a further 20 mm of beef muscle tissue is placed behind the secondary coil; the measurement setup is shown in Fig. 2-17. The measured PTE was 35.4%.

A capacitive coupling based WPT link operating at 4 MHz was designed for stent-based biomedical implants [55]. The transmitting plates had a size of 80 mm x 30 mm and the receiver consisted of two 40 mm long stents made from nitinol, as shown in Fig. 2-18. When the transfer distance between the transmitter and the receiver is 15 mm, the measured PTE is 2.6% for an input power of 53 mW, whereas, the measured PTE decreases to only 0.98% as the transfer distance enlarges to 30 mm.

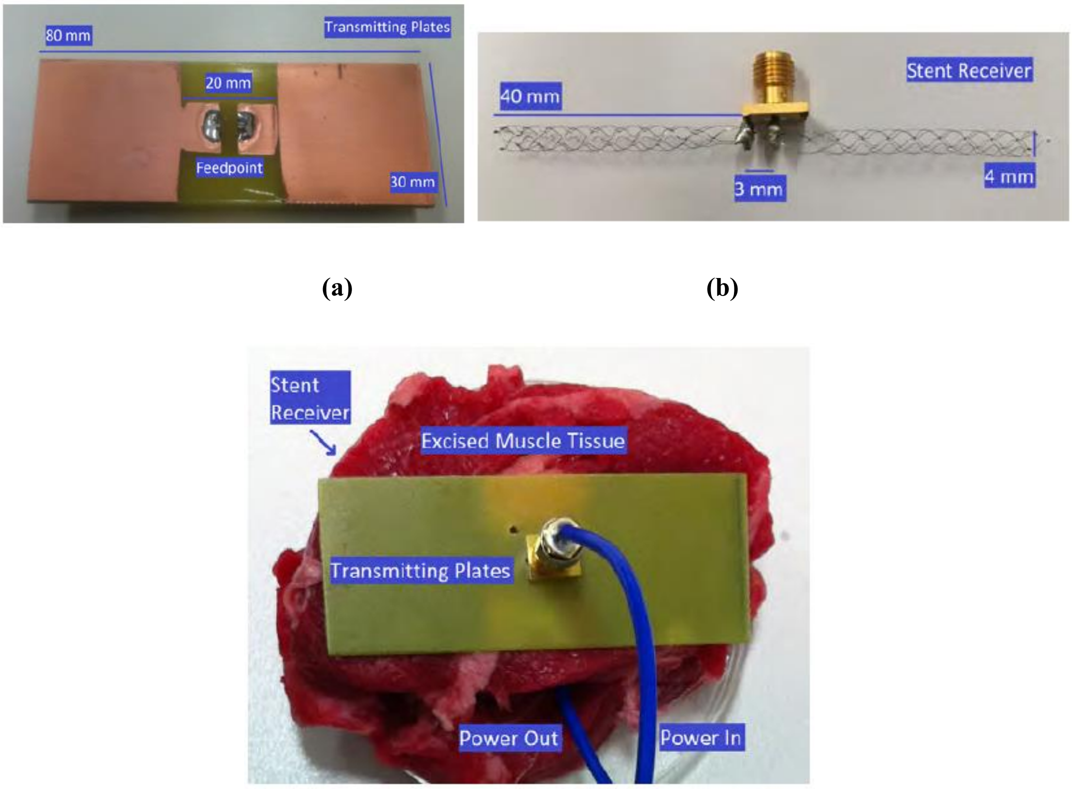

(a) **(b)**

(c)

Fig. 2-18. Fabrications of (a) the transmitting plate and (b) the stent receiver; (c) measurement setup [55].

Far-field WPT can support larger transfer distances to but provides very low PTE. It is most suitable for sensors with low-power consumption. Furthermore, taking safety limitations into consideration, the use of far-field WPT for implantable applications would require a low transmit power, which would in turn lead to received powers in the range of µW. Near-field WPT has recently attracted more attention owing to its advantages of high PTE, which is necessary for portable/electronic devices and wearable e/implantable equipment. However, owing to the consideration of human safety and the loss from the absorption of body tissues, PTE and transfer distance should be further enhanced for implantable devices.

2.3 Summary

In this chapter, both far-field and near-field WPT have been introduced, including fundamental knowledge and study cases. Far-field WPT has two main domains: one is non-directive RF radiation; the other is directive RF radiation. Near-field WPT has three approaches, namely inductive coupling, MRC and capacitive coupling.

Far-field WPT as a radiative technique can conduct power transmission over a range from several metres to kilometres. However, far-field WPT is dangerous to humans due to its radiative characteristics, which is a crucial factor when dealing with implantable devices. SAR regulations limit the transmit power and hence the RF power received by an antenna is only in the range of µW or several mW due to low antenna efficiency. That brings further challenges to the rectifier design and decreases the RF-to-DC conversion efficiency. Therefore, far-field WPT is commonly used for wireless sensor networks, which have low-power consumption and are situated in remote environments.

Compared with far-field WPT, near-field WPT as a non-radiative technique has wider application possibilities, such as electric vehicles, mobile phones, portable and wearable electronic devices. Firstly, inductive coupling is based on electromagnetic induction between two coils. The coupling efficiency between the two coils is exponentially inversely proportional to the transfer distance, which leads to very short transfer distances, on the order of a few millimetres to a few centimetres. Hence, the most important issue is to design coils with a high *Q*-factor to diminish the loss in the coils and enhance coupling strength. Secondly, MRC is based on electromagnetic resonance between two resonators with same resonance frequency. This method allows for greater transfer distances between the two resonators, up to several metres. Thirdly, capacitive coupling delivers power via electric field from one metal plate to another metal plate. This requires consideration of electromagnetic interference (EMI) effects and due to the high voltages used enhanced safety requirements. The physical limitations on the air gap between two capacitive coupling plates leans to those applications whose gap length is less than 1 mm.

For implantable applications, WPT is a promising and valuable technique to overcome the limitation of battery life. The effect of the human body on the wireless power link and safety considerations must be accounted for. The main challenges are related to PTE and transfer distance, especially for high operating frequencies.

All approaches for WPT have their own merits and demerits. According to the overview, the MRC method is more suitable for implantable applications due to its higher PTE. However, WPT systems working in the Medical Implants Communication Service (MICS) band from 402 MHz to 405 MHz have seldom been researched. As received power is proportional to the rate of change of the incident magnetic field, choosing a higher carrier frequency improves power transfer. In contrast, electromagnetic energy absorption in human tissues increases with frequency for implantable applications. Enlarging delivered power to implants at higher frequencies under the condition of human safety becomes a focus in this work. Furthermore, the design of a rectifier to convert RF to DC power also plays a critical role in wireless power transmission. A planar configuration of transmitting and receiving resonators integrated with conversion circuits would be the optimal solution. The planar configuration of resonators, however, will be significantly affected by the dielectric characteristics of the human body. These challenges will be tackled as part of this work.

2.4 References

[1] A. A. Eteng, S. K. A. Rahim, C. Y. Leow, S. Jayaprakasam, and B. W. Chew, "Low-power near-field magnetic wireless energy transfer links: A review of architectures and design approaches," (in English), *Renew Sust Energ Rev,* vol. 77, pp. 486-505, Sep 2017, doi: 10.1016/j.rser.2017.04.051.

[2] D. Belo, D. C. Ribeiro, P. Pinho, and N. B. Carvalho, "A Selective, Tracking, and Power Adaptive Far-Field Wireless Power Transfer System," *IEEE Transactions on Microwave Theory and Techniques,* vol. 67, no. 9, pp. 3856-

3866, 2019, doi: 10.1109/TMTT.2019.2913653.

[3] K. Agarwal, R. Jegadeesan, Y. Guo, and N. V. Thakor, "Wireless Power Transfer Strategies for Implantable Bioelectronics," *IEEE Reviews in Biomedical Engineering,* vol. 10, pp. 136-161, 2017, doi: 10.1109/RBME.2017.2683520.

[4] X. Lu, P. Wang, D. Niyato, D. I. Kim, and Z. Han, "Wireless Charging Technologies: Fundamentals, Standards, and Network Applications," *IEEE Communications Surveys & Tutorials,* vol. 18, no. 2, pp. 1413-1452, 2016, doi: 10.1109/COMST.2015.2499783.

[5] X. Mou and H. Sun, "Wireless Power Transfer: Survey and Roadmap," in *2015 IEEE 81st Vehicular Technology Conference (VTC Spring)*, 11-14 May 2015 2015, pp. 1-5, doi: 10.1109/VTCSpring.2015.7146165.

[6] J. D. Kraus, D.A., Fleisch, *Electromagnetics with applications*. William C Brown Pub, 1999.

[7] Z. Chunbo, L. Kai, Y. Chunlai, M. Rui, and C. Hexiao, "Simulation and experimental analysis on wireless energy transfer based on magnetic resonances," in *2008 IEEE Vehicle Power and Propulsion Conference*, 3-5 Sept. 2008 2008, pp. 1-4, doi: 10.1109/VPPC.2008.4677400.

[8] A. Kurs, A. Karalis, R. Moffatt, J. D. Joannopoulos, P. Fisher, and M. Soljacic, "Wireless power transfer via strongly coupled magnetic resonances," *Science,* vol. 317, no. 5834, pp. 83-6, Jul 6 2007, doi: 10.1126/science.1143254.

[9] O. Jonah and S. V. Georgakopoulos, "Wireless Power Transfer in Concrete via Strongly Coupled Magnetic Resonance," *IEEE Transactions on Antennas and Propagation,* vol. 61, no. 3, pp. 1378-1384, 2013, doi: 10.1109/TAP.2012.2227924.

[10] C. Liu, A. P. Hu, B. Wang, and N. C. Nair, "A Capacitively Coupled Contactless Matrix Charging Platform With Soft Switched Transformer Control," *IEEE Transactions on Industrial Electronics,* vol. 60, no. 1, pp. 249-260, 2013, doi: 10.1109/TIE.2011.2172174.

[11] J. Dai and D. C. Ludois, "A Survey of Wireless Power Transfer and a Critical Comparison of Inductive and Capacitive Coupling for Small Gap Applications," *IEEE Transactions on Power Electronics,* vol. 30, no. 11, pp. 6017-6029, 2015, doi: 10.1109/TPEL.2015.2415253.

[12] A. M. Jawad, R. Nordin, S. K. Gharghan, H. M. Jawad, and M. Ismail,

"Opportunities and Challenges for Near-Field Wireless Power Transfer: A Review," *Energies,* vol. 10, no. 7, 2017, doi: 10.3390/en10071022.

[13] D. Kim, A. Abu-Siada, and A. Sutinjo, "State-of-the-art literature review of WPT: Current limitations and solutions on IPT," *Electric Power Systems Research,* vol. 154, pp. 493-502, 2018, doi: 10.1016/j.epsr.2017.09.018.

[14] H. J. Visser and R. J. M. Vullers, "RF Energy Harvesting and Transport for Wireless Sensor Network Applications: Principles and Requirements," *Proceedings of the IEEE,* vol. 101, no. 6, pp. 1410-1423, 2013, doi: 10.1109/JPROC.2013.2250891.

[15] S. Kim *et al.*, "Ambient RF Energy-Harvesting Technologies for Self-Sustainable Standalone Wireless Sensor Platforms," (in English), *Proceedings of the Ieee,* vol. 102, no. 11, pp. 1649-1666, Nov 2014, doi: 10.1109/Jproc.2014.2357031.

[16] E. Falkenstein, D. Costinett, R. Zane, and Z. Popovic, "Far-Field RF-Powered Variable Duty Cycle Wireless Sensor Platform," *IEEE Transactions on Circuits and Systems II: Express Briefs,* vol. 58, no. 12, pp. 822-826, 2011, doi: 10.1109/TCSII.2011.2173964.

[17] A. P. Sample, D. J. Yeager, P. S. Powledge, A. V. Mamishev, and J. R. Smith, "Design of an RFID-Based Battery-Free Programmable Sensing Platform," *IEEE Transactions on Instrumentation and Measurement,* vol. 57, no. 11, pp. 2608-2615, 2008, doi: 10.1109/TIM.2008.925019.

[18] D. D. Donno, L. Catarinucci, and L. Tarricone, "An UHF RFID Energy-Harvesting System Enhanced by a DC-DC Charge Pump in Silicon-on-Insulator Technology," *IEEE Microwave and Wireless Components Letters,* vol. 23, no. 6, pp. 315-317, 2013, doi: 10.1109/LMWC.2013.2258002.

[19] Z. Popović, E. A. Falkenstein, D. Costinett, and R. Zane, "Low-Power Far-Field Wireless Powering for Wireless Sensors," *Proceedings of the IEEE,* vol. 101, no. 6, pp. 1397-1409, 2013, doi: 10.1109/JPROC.2013.2244053.

[20] M. Piñuela, P. D. Mitcheson, and S. Lucyszyn, "Ambient RF Energy Harvesting in Urban and Semi-Urban Environments," *IEEE Transactions on Microwave Theory and Techniques,* vol. 61, no. 7, pp. 2715-2726, 2013, doi: 10.1109/TMTT.2013.2262687.

[21] R. J. Vyas, B. B. Cook, Y. Kawahara, and M. M. Tentzeris, "E-WEHP: A Batteryless Embedded Sensor-Platform Wirelessly Powered From Ambient

Digital-TV Signals," *IEEE Transactions on Microwave Theory and Techniques,* vol. 61, no. 6, pp. 2491-2505, 2013, doi: 10.1109/TMTT.2013.2258168.

[22] C. Song, Y. Huang, J. Zhou, and P. Carter, "Improved Ultrawideband Rectennas Using Hybrid Resistance Compression Technique," *IEEE Transactions on Antennas and Propagation,* vol. 65, no. 4, pp. 2057-2062, 2017, doi: 10.1109/TAP.2017.2670359.

[23] S. Shen, C. Chiu, and R. D. Murch, "A Dual-Port Triple-Band L-Probe Microstrip Patch Rectenna for Ambient RF Energy Harvesting," *IEEE Antennas and Wireless Propagation Letters,* vol. 16, pp. 3071-3074, 2017, doi: 10.1109/LAWP.2017.2761397.

[24] B. L. Pham and A. Pham, "Triple bands antenna and high efficiency rectifier design for RF energy harvesting at 900, 1900 and 2400 MHz," in *2013 IEEE MTT-S International Microwave Symposium Digest (MTT)*, 2-7 June 2013 2013, pp. 1-3, doi: 10.1109/MWSYM.2013.6697364.

[25] C. Song, Y. Huang, P. Carter, J. Zhou, S. D. Joseph, and G. Li, "Novel Compact and Broadband Frequency-Selectable Rectennas for a Wide Input-Power and Load Impedance Range," *IEEE Transactions on Antennas and Propagation,* vol. 66, no. 7, pp. 3306-3316, 2018, doi: 10.1109/TAP.2018.2826568.

[26] K. Niotaki, S. Kim, S. Jeong, A. Collado, A. Georgiadis, and M. M. Tentzeris, "A Compact Dual-Band Rectenna Using Slot-Loaded Dual Band Folded Dipole Antenna," *IEEE Antennas and Wireless Propagation Letters,* vol. 12, pp. 1634-1637, 2013, doi: 10.1109/LAWP.2013.2294200.

[27] R. Shigeta *et al.*, "Ambient RF Energy Harvesting Sensor Device With Capacitor-Leakage-Aware Duty Cycle Control," *IEEE Sensors Journal,* vol. 13, no. 8, pp. 2973-2983, 2013, doi: 10.1109/JSEN.2013.2264931.

[28] S. Percy, C. Knight, F. Cooray, and K. Smart, "Supplying the power requirements to a sensor network using radio frequency power transfer," *Sensors (Basel),* vol. 12, no. 7, pp. 8571-85, 2012, doi: 10.3390/s120708571.

[29] "Oral-B Triumph with SmartGuide ProfessionalCare 9910 Electric Toothbrush," 2007. [Online]. Available: https://the-gadgeteer.com/2007/08/09/oral_b_triumph_9910/.

[30] "Splashpower Charger Lets You Charge Wirelessly, Lose That Wired Mess," 2008. [Online]. Available: https://gizmodo.com/splashpower-charger-lets-you-charge-wirelessly-lose-th-342384.

[31] "Dell readies laptops with wireless charging while Intel retreats from its development," 2016. [Online]. Available: https://www.zdnet.com/article/dell-readies-laptops-with-wireless-charging-while-intel-retreats-from-its-development/.

[32] H. Hoang, S. Lee, Y. Kim, Y. Choi, and F. Bien, "An adaptive technique to improve wireless power transfer for consumer electronics," *IEEE Transactions on Consumer Electronics,* vol. 58, no. 2, pp. 327-332, 2012, doi: 10.1109/TCE.2012.6227430.

[33] C. C. Mi, G. Buja, S. Y. Choi, and C. T. Rim, "Modern Advances in Wireless Power Transfer Systems for Roadway Powered Electric Vehicles," *IEEE Transactions on Industrial Electronics,* vol. 63, no. 10, pp. 6533-6545, 2016, doi: 10.1109/TIE.2016.2574993.

[34] S. Li and C. C. Mi, "Wireless Power Transfer for Electric Vehicle Applications," *IEEE Journal of Emerging and Selected Topics in Power Electronics,* vol. 3, no. 1, pp. 4-17, 2015, doi: 10.1109/JESTPE.2014.2319453.

[35] S. Y. Choi, B. W. Gu, S. Y. Jeong, and C. T. Rim, "Advances in Wireless Power Transfer Systems for Roadway-Powered Electric Vehicles," *IEEE Journal of Emerging and Selected Topics in Power Electronics,* vol. 3, no. 1, pp. 18-36, 2015, doi: 10.1109/JESTPE.2014.2343674.

[36] C. Park, S. Lee, G. Cho, and C. T. Rim, "Innovative 5-m-Off-Distance Inductive Power Transfer Systems With Optimally Shaped Dipole Coils," *IEEE Transactions on Power Electronics,* vol. 30, no. 2, pp. 817-827, 2015, doi: 10.1109/TPEL.2014.2310232.

[37] Z. Ye, Y. Sun, X. Dai, C. Tang, Z. Wang, and Y. Su, "Energy Efficiency Analysis of U-Coil Wireless Power Transfer System," *IEEE Transactions on Power Electronics,* vol. 31, no. 7, pp. 4809-4817, 2016, doi: 10.1109/TPEL.2015.2483839.

[38] J. Dai and D. C. Ludois, "Capacitive Power Transfer Through a Conformal Bumper for Electric Vehicle Charging," *IEEE Journal of Emerging and Selected Topics in Power Electronics,* vol. 4, no. 3, pp. 1015-1025, 2016, doi: 10.1109/JESTPE.2015.2505622.

[39] S. Gabriel, R. W. Lau, and C. Gabriel, "The dielectric properties of biological tissues: II. Measurements in the frequency range 10 Hz to 20 GHz," *Physics in Medicine and Biology,* vol. 41, no. 11, pp. 2251-2269, 1996/11/01 1996, doi:

10.1088/0031-9155/41/11/002.

[40] R. A. Bercich, D. R. Duffy, and P. P. Irazoqui, "Far-Field RF Powering of Implantable Devices: Safety Considerations," *IEEE Transactions on Biomedical Engineering,* vol. 60, no. 8, pp. 2107-2112, 2013, doi: 10.1109/TBME.2013.2246787.

[41] S. M. Asif, A. Iftikhar, J. W. Hansen, M. S. Khan, D. L. Ewert, and B. D. Braaten, "A Novel RF-Powered Wireless Pacing via a Rectenna-Based Pacemaker and a Wearable Transmit-Antenna Array," *IEEE Access,* vol. 7, pp. 1139-1148, 2019, doi: 10.1109/ACCESS.2018.2885620.

[42] A. N. Abdulfattah, C. C. Tsimenidis, B. Z. Al-Jewad, and A. Yakovlev, "Performance Analysis of MICS-Based RF Wireless Power Transfer System for Implantable Medical Devices," *IEEE Access,* vol. 7, pp. 11775-11784, 2019, doi: 10.1109/ACCESS.2019.2891815.

[43] M. R. Shah, R. P. Phillips, and R. A. Normann, "A study of printed spiral coils for neuroprosthetic transcranial telemetry applications," *IEEE Transactions on Biomedical Engineering,* vol. 45, no. 7, pp. 867-876, 1998, doi: 10.1109/10.686794.

[44] S. Gevorgian, H. Berg, H. Jacobsson, and T. Lewin, "Basic parameters of coplanar-strip waveguides on multilayer dielectric/semiconductor substrates. Part 2: Low permittivity superstrates," *IEEE Microwave Magazine,* vol. 4, no. 3, pp. 59-78, 2003, doi: 10.1109/MMW.2003.1237478.

[45] S. Gevorgian, H. Berg, H. Jacobsson, and T. Lewin, "Application notes - basic parameters of coplanar-strip waveguides on multilayer dielectric/semiconductor substrates, Part 1: high permittivity superstrates," *IEEE Microwave Magazine,* vol. 4, no. 2, pp. 60-70, 2003, doi: 10.1109/MMW.2003.1201599.

[46] U. Jow and M. Ghovanloo, "Modeling and Optimization of Printed Spiral Coils in Air, Saline, and Muscle Tissue Environments," *IEEE Transactions on Biomedical Circuits and Systems,* vol. 3, no. 5, pp. 339-347, 2009, doi: 10.1109/TBCAS.2009.2025366.

[47] P. Pieters *et al.*, "Accurate modeling of high-Q spiral inductors in thin-film multilayer technology for wireless telecommunication applications," *IEEE Transactions on Microwave Theory and Techniques,* vol. 49, no. 4, pp. 589-599, 2001, doi: 10.1109/22.915431.

[48] R. Jegadeesan, K. Agarwal, Y. Guo, S. Yen, and N. V. Thakor, "Wireless Power Delivery to Flexible Subcutaneous Implants Using Capacitive Coupling," *IEEE Transactions on Microwave Theory and Techniques,* vol. 65, no. 1, pp. 280-292, 2017, doi: 10.1109/TMTT.2016.2615623.

[49] K. R. Foster, H. P. Schwan, "Dielectric properties of tissues and biological materials: a critical review," *Critical reviews in biomedical engineering,* vol. 17, no. 1, pp. 25-104, 1989.

[50] C. Liu, Y. Guo, H. Sun, and S. Xiao, "Design and Safety Considerations of an Implantable Rectenna for Far-Field Wireless Power Transfer," *IEEE Transactions on Antennas and Propagation,* vol. 62, no. 11, pp. 5798-5806, 2014, doi: 10.1109/TAP.2014.2352363.

[51] G. Monti, P. Arcuti, and L. Tarricone, "Resonant Inductive Link for Remote Powering of Pacemakers," *IEEE Transactions on Microwave Theory and Techniques,* vol. 63, no. 11, pp. 3814-3822, 2015, doi: 10.1109/TMTT.2015.2481387.

[52] D. Ahn and M. Ghovanloo, "Optimal Design of Wireless Power Transmission Links for Millimeter-Sized Biomedical Implants," *IEEE Transactions on Biomedical Circuits and Systems,* vol. 10, no. 1, pp. 125-137, 2016, doi: 10.1109/TBCAS.2014.2370794.

[53] T. Campi, S. Cruciani, F. Palandrani, V. D. Santis, A. Hirata, and M. Feliziani, "Wireless Power Transfer Charging System for AIMDs and Pacemakers," *IEEE Transactions on Microwave Theory and Techniques,* vol. 64, no. 2, pp. 633-642, 2016, doi: 10.1109/TMTT.2015.2511011.

[54] S. R. Khan and G. Choi, "Analysis and Optimization of Four-Coil Planar Magnetically Coupled Printed Spiral Resonators," *Sensors (Basel),* vol. 16, no. 8, Aug 3 2016, doi: 10.3390/s16081219.

[55] A. Aldaoud, J. Redoute, K. Ganesan *et al.*, "Near-Field Wireless Power Transfer to Stent-Based Biomedical Implants," *IEEE Journal of Electromagnetics, RF and Microwaves in Medicine and Biology,* vol. 2, no. 3, pp. 193-200, 2018, doi: 10.1109/JERM.2018.2833386.

Chapter 3 Magnetic Resonance Coupling Method for Wireless Power Transfer

In comparison to the inductive coupling approach, the magnetic resonant coupling (MRC) approach can transfer power over greater distances, on the order of meters, and offers significantly higher power transfer efficiencies. Furthermore, it is non-radiative, so it does not require line of sight and has been shown to be safe for human use [1]. MRC based wireless power transfer (WPT) is not visibly affected by the insertion of everyday objects or even humans between the source and the receiver. External objects only have a noticeable effect when they are placed within a few centimetres of the coils. Some materials such as aluminium foil, styrofoam, and human tissue, mostly shift the resonant frequency, which can in principle be easily corrected [2]. However, the MRC approach is sensitive to misalignment. The maximum charging distance can only be achieved when the source and receiving coils are aligned coaxially (along their axis) [3]. When the technology is extended to charge multiple devices, mutual coupling among various receiving coils and other objects may cause interference, and therefore careful tuning is necessary [4].

Nowadays, the MRC method has been widely used for WPT. Even though the WPT technique provides some advantages with respect to the aspects of research and commercial usage, the MRC approach, as a modernised method still has some theoretical issues and practical challenges, which need to be addressed and overcome [5-7]. In [8-10], secondary series-and parallel-compensated WPT circuits were compared to investigate the influence of load impedance on power transfer efficiency (PTE). However, sufficient practical verifications of the theory through published experimental results were not provided. Despite all four topologies of the WPT circuit being studied in [11-13], comparison between the four topologies was limited, with no criteria provided as to which topology was most appropriate for a given system. For example, literatures on design and optimisation of wireless power links showed that some studies used parallel-primary and parallel secondary circuits [14, 15]. Most references focus on series-primary and series-secondary circuits for WPT [16-18]. The phenomenon of frequency splitting [19-21] can easily appear when series-primary and series-secondary circuits are used for WPT and so should be considered in any such system design. To enhance PTE at certain frequencies, there are some techniques such as impedance matching [22, 23], high Q-factor coil designs [24, 25] and load optimisation [26, 27] that can be applied. However, the load cannot be optimised to enhance PTE because it is normally fixed. Therefore, it is necessary to focus on the design of suitable WPT systems with high PTE for fixed load applications.

In this chapter, comprehensive investigations of the four basic topologies for MRC-WPT have been performed, including theoretical analysis and experimental verification. From the viewpoint of the primary and secondary circuits, a detailed introduction and theoretical analysis of the four topologies for MRC-WPT is illustrated in Section 3.2. Solutions for the design of an optimal WPT system and a description of the experimental designs are provided in Section 3.3.1. Section 3.3.2 offers related experimental verifications and the investigation of the phenomenon of frequency splitting in terms of circuit parameters and PTE. Conclusions regarding MRC-WPT, including a comparison among the four topologies and selection of the most appropriate topology for a given system are highlighted in Section 3.4.

3.1 Theoretical Analysis of Topology

Resonance is a trend whereby a physical system subjected to its natural frequency, will tend to absorb energy at that frequency. In other words, it is a phenomenon in which, when one object vibrates it will cause another with the same resonant frequency to vibrate, such as sound of the correct frequency causing a tuning fork to vibrate. In this regard resonance can be used to transfer energy. Electromagnetic resonance is used widely in electromagnetic systems. The electromagnetic field itself is an energy field which can provide energy to electrically driven apparatus.

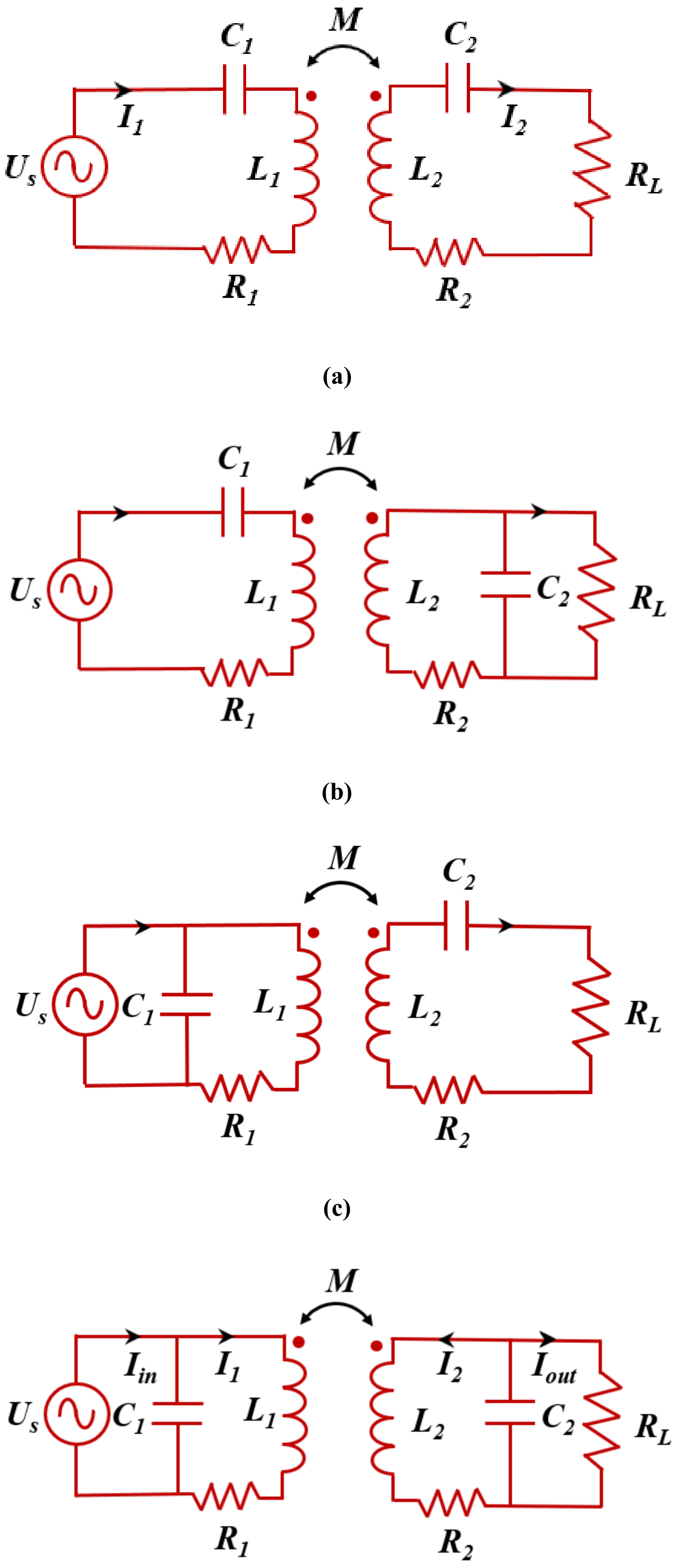

(a)

(b)

(c)

(d)

Fig. 3-1. (a) Series-Series (SS) circuit (b) Series-Parallel (SP) circuit (c) Parallel-Series (PS) circuit (d) Parallel-Parallel (PP) circuit.

A radiating electromagnetic wave contains energy, whether there is a receiver present or not, the energy of an electromagnetic wave is continuously consumed. A non-radiative magnetic field (near field) with a specific resonance frequency can be used as a source of power, when a resonator, such as an inductor-capacitor (LC) oscillating circuit with the same resonance frequency is present. Then the electromagnetic resonance will generate energy in the oscillating circuit and as the energy gathered increases, the voltage across the inductor will also increase. As a result, two systems with the same inherent resonant frequency can generate strong magnetic resonance together with a strong magnetic field intensity. The energy stored in the resonator can be used by a load after being appropriately converted by follow-up circuits [28].

MRC-WPT relies on a pair of resonant circuits with the same resonant frequency, one located at the transmitter and the other at the receiver. The circuits contain coils which are placed so as to be strongly coupled via non-radiative magnetic resonance induction, enabling longer distance power transmission than inductive coupling [29]. Resonating circuits can be constructed from inductors and capacitors in two topology types, series and parallel. Considering the need for a resonator in both the transmitter (primary circuit) and receiver (secondary circuit), there are four possible topologies of circuit for an MRC-WPT system (as shown in Fig. 3-1).

The electrical circuit used for the model consists of two separate coils of self-inductance L_1 and L_2 coupled by a mutual inductance M that describes the inductive coupling, depending on coil properties and the distance between the coils. R_1 and R_2 are the equivalent resistances modelling the losses in the primary and secondary coils, respectively. C_1 and C_2 represent capacitors used in tandem with the inductors to create resonance. R_L represents the load impedance. U_s represents the alternating current (AC) power supply voltage.

Each of these four topologies has advantages/disadvantages for use in the realisation of a wireless power transmission system. In terms of topology selection, theoretical analysis and experimental verifications are needed to determine the most suitable choice for a given WPT system. In this section, primary circuits and secondary circuits with different topologies will be analysed in terms of resonant frequency and PTE. The topologies are referred to by their parallel (P) or series (S) nature on the primary and secondary sides as SS, SP, PP and PS (as shown in Fig. 3-1).

3.1.1 Series Primary Circuits (SS and SP)

Topologies with a series primary circuit are first considered, i.e. SS and SP in Fig. 3-1(a) and 3-1(b) respectively. For the SS topology, the equivalent impedance of the secondary circuit [30] at the resonant angular frequency (ω_s), can be expressed as (3.1).

$$Z_{e1} = \frac{(\omega_s M)^2}{R_2 + R_L}, \quad \omega_s^2 = \frac{1}{L_2 C_2} \tag{3.1}$$

Similarly, if the secondary circuit is the parallel configuration and the capacitor is represented by C_{p2}, the equivalent impedance of the secondary circuit at the resonant angular frequency (ω_p), can be expressed as (3.2):

$$Z_{e2} = \frac{(\omega_p M)^2}{R_2 + \frac{L_2}{C_{p2} R_L}}, \quad \omega_p^2 = \frac{1}{L_2 C_{p2}} - \frac{1}{C_{p2}^2 R_L^2} \tag{3.2}$$

The power transfer performance depends on the equivalent impedance of the secondary circuit to that of the primary circuit at the resonant frequency [31]. If the equivalent impedance of the secondary circuit is larger, the PTE is higher. Hypothetically, the resonant frequencies are the same in both series and parallel secondary circuit configurations. In this case, the capacitance in the series secondary circuit must be different from that in the parallel secondary circuit for resonance to take place at the same frequency. Clearly, by comparing equations (3.1) and (3.2), when the load impedance R_L satisfies the condition in (3.3), a parallel secondary circuit configuration should be chosen, otherwise, the series configuration is more efficient.

$$R_L > \sqrt{\frac{L_2}{C_{p2}}} \tag{3.3}$$

3.1.2 Parallel Primary Circuits

Topologies with a parallel primary circuit are now considered i.e. PP and PS in Fig. 3-1(c) and 3-1(d) respectively.

In the case of the PP circuit topology, if the resistance of the inductors can be considered negligible so the circuit structure can be simplified, then the equivalent input impedance can be expressed as (3.4).

$$Z_{in} = \frac{(1-\omega^2 L_1 C_1)[R_L(1-\omega^2 L_2 C_2)+j\omega L_2]-\omega^2 M C_1\left(\omega^2 M C_2 R_L - j\omega M\right)}{\left(j\omega L_1\right)[R_L(1-\omega^2 L_2 C_2)+j\omega L_2]+\left(j\omega M\right)\left(\omega^2 M C_2 R_L - j\omega M\right)} \tag{3.4}$$

The precondition of the resonance phenomenon is that the imaginary part of the circuit input impedance goes to zero. If $L=L_1=L_2$ and $C=C_1=C_2$, then the imaginary part of Z_{in} can be expressed as (3.5):

$$\mathrm{Im}(Z_{in}) = \frac{\omega L\left[1-\omega^2(L^2-M^2)C/L\right]\left[(1-\omega^2 LC)^2 R_L{}^2-\omega^4 M^2 C^2 R_L{}^2+\omega^2 L^2-\omega^2 M^2\right]}{\left[\omega^2 L^2-\omega^2 M^2\right]^2+R_L{}^2\left[\omega L(1-\omega^2 LC)+\omega^3 M^2 C\right]^2} \tag{3.5}$$

The resonant frequency can be obtained by setting the imaginary part expressed in (3.5) to zero. This gives rise to:

$$f = \frac{1}{2\pi}\sqrt{\frac{L}{(L^2-M^2)C}} = \frac{1}{2\pi}\sqrt{\frac{1}{(1-k^2)LC}} \tag{3.6}$$

where k is the mutual coupling coefficient. Equation (3.6) shows that the resonant frequency is related to k. Furthermore, the parallel topology looks like an open circuit at resonance, which results in a low current supply in the primary and hence will lead to low power transfer and low load power.

3.1.3 Phenomenon of Frequency Splitting

Although the MRC-WPT method offers higher power transfer efficiencies than inductive coupling over larger distances, the phenomenon of frequency splitting can occur and lead to reduced performance.

For the SS topology, as shown in Fig. 3-1(a), I_1 and I_2 represent the currents in the primary and secondary coils respectively. If

$$X_1 = \omega L_1 - \frac{1}{\omega C_1} \tag{3.7}$$

and

$$X_2 = \omega L_2 - \frac{1}{\omega C_2} \tag{3.8}$$

then I_1 and I_2 can be expressed as:

$$I_1 = \frac{U_s(R_L + R_2 + jX_2)}{(R_1 + jX_1)(R_L + R_2 + jX_2) + \omega^2 M^2} \tag{3.9}$$

$$I_2 = \frac{j\omega M U_s}{(R_1 + jX_1)(R_L + R_2 + jX_2) + \omega^2 M^2} \tag{3.10}$$

The equivalent input impedance can then be expressed as:

$$Z_{in} = R_1 + jX_1 + \frac{\omega^2 M^2}{R_L + R_2 + jX_2} = R_1 + j(\omega L_1 - \frac{1}{\omega C_1}) + \frac{\omega^2 M^2}{R_L + R_2 + j(\omega L_2 - \frac{1}{\omega C_2})} \tag{3.11}$$

The phenomenon of resonance occurs, when the imaginary part of Z_{in} equals 0. Substituting for $L=L_1=L_2$, $C=C_1=C_2$, $\mathrm{Im}(Z_{in})$ can be expressed as:

$$\mathrm{Im}(Z_{in}) = \frac{(\omega L - \frac{1}{\omega C})\left[\left(R_L + R_2\right)^2 + (\omega L - \frac{1}{\omega C})^2 - (\omega M)^2\right]}{\left(R_L + R_2\right)^2 + (\omega L - \frac{1}{\omega C})^2} \tag{3.12}$$

The numerator of $\mathrm{Im}(Z_{in})$ can be separated into two factors making it easy to obtain one root for ω_0 of $(LC)^{-0.5}$ from the first factor. Equation (3.12) always has at least this one root, however other roots can also exist in the second factor which can be abbreviated as a two-variable linear equation:

$$y(\omega^2) = (L^2 - M^2)(\omega^2)^2 + \left[(R_2 + R_L)^2 - \frac{2L}{C}\right]\omega^2 + \frac{1}{C^2} \tag{3.13}$$

The angular frequency ω must be bigger than 0, which only happens when the conditions in (3.14) and (3.15) are met simultaneously.

$$\left(R_2+R_L\right)^2-\frac{2L}{C}\leq 0 \tag{3.14}$$

$$\Delta=\left[\left(R_2+R_L\right)^2-\frac{2L}{C}\right]^2-\frac{4(L^2-M^2)}{C^2}\geq 0 \tag{3.15}$$

Now two other resonance frequencies can be expressed as:

$$f_{1,2}^{'}=\frac{1}{2\pi}\sqrt{\frac{-\left[\left(R_2+R_L\right)^2-\frac{2L}{C}\right]\pm\sqrt{\Delta}}{2(L^2-M^2)}} \tag{3.16}$$

Table 3-1: Calculated resonance frequencies with different conditions in an SS circuit

Conditions		Resonance Frequencies
$\left(R_2+R_L\right)^2-\frac{2L}{C}\geq 0$		$f_1=\frac{1}{2\pi\sqrt{LC}}$
$\left(R_2+R_L\right)^2-\frac{2L}{C}<0$	$\Delta<0$	$f_1=\frac{1}{2\pi\sqrt{LC}}$
	$\Delta=0$	$f_1=\frac{1}{2\pi\sqrt{LC}}$ $f_2=\frac{1}{2\pi}\sqrt{\frac{-\left[\left(R_2+R_L\right)^2-\frac{2L}{C}\right]}{2(L^2-M^2)}}$
	$\Delta>0$	$f_1=\frac{1}{2\pi\sqrt{LC}}$ $f_{2,3}=\frac{1}{2\pi}\sqrt{\frac{-\left[\left(R_2+R_L\right)^2-\frac{2L}{C}\right]\pm\sqrt{\left[\left(R_2+R_L\right)^2-\frac{2L}{C}\right]^2-\frac{4(L^2-M^2)}{C^2}}}{2(L^2-M^2)}}$

For the SS circuit, when the load resistance is large enough, there is only one resonant frequency, which can be directly calculated from the inductance and capacitance as in (3.1). In this case, the equivalent impedance of the secondary circuit to that of the primary circuit is very small, resulting in low PTE. When the load resistance is small enough to meet the condition of equation (3.14), multiple resonant frequencies will appear, the values of which are related to the mutual inductance between the coils *M*. Several conditions can be summarised as shown in Table 3-1. From equation (3.15), when the mutual inductance is large, the value of Δ is greater than 0, making it easy to form multiple resonant frequencies. However, the PTE and load power do not reach their maximum potential at all of these resonant frequencies.

For the PP topology, as shown in Fig. 3-1(c), I_1 and I_2 represent the current in the primary and secondary coils respectively. Based on the dot convention, the current I_1 and I_2 can be expressed as [32]:

$$I_1 = \frac{V_s[R_L(1-\omega^2 L_2 C_2) + j\omega L_2]}{[R_s(1-\omega^2 L_1 C_1) + j\omega L_1][R_L(1-\omega^2 L_2 C_2) + j\omega L_2] - \left(\omega^2 M C_1 R_s - j\omega M\right)\left(\omega^2 M C_2 R_L - j\omega M\right)} \tag{3.17}$$

$$I_2 = \frac{V_s\left(\omega^2 M C_2 R_L - j\omega M\right)}{[R_s(1-\omega^2 L_1 C_1) + j\omega L_1][R_L(1-\omega^2 L_2 C_2) + j\omega L_2] - \left(\omega^2 M C_1 R_s - j\omega M\right)\left(\omega^2 M C_2 R_L - j\omega M\right)} \tag{3.18}$$

So the input current I_{in} and the output current I_{out} can be expressed as:

$$I_{in} = (1-\omega^2 L_1 C_1) I_1 - \omega^2 M C_1 I_2 \tag{3.19}$$

$$I_{out} = \frac{j\omega L_2 I_2 + j\omega M I_1}{R_L} \tag{3.20}$$

Then the equivalent input impedance can be expressed as:

$$Z_{eq} = \frac{(1-\omega^2 L_1 C_1)[R_L(1-\omega^2 L_2 C_2) + j\omega L_2] - \omega^2 M C_1\left(\omega^2 M C_2 R_L - j\omega M\right)}{[R_s(1-\omega^2 L_1 C_1) + j\omega L_1][R_L(1-\omega^2 L_2 C_2) + j\omega L_2] - \left(\omega^2 M C_1 R_s - j\omega M\right)\left(\omega^2 M C_2 R_L - j\omega M\right)} \tag{3.21}$$

Once again, the precondition of the resonance phenomenon is that the imaginary part of the input impedance goes to zero. In particular, if $L=L_1=L_2$, $C=C_1=C_2$, the imaginary part of Z_{eq} can be expressed as:

$$\mathrm{Im}(Z_{eq}) = \frac{\omega L\left[1-\omega^2(L^2-M^2)C/L\right]\left[(1-\omega^2LC)^2R_L{}^2-\omega^4M^2C^2R_L{}^2+\omega^2L^2-\omega^2M^2\right]}{\left[(1-\omega^2LC)^2R_LR_S-\omega^4M^2C^2R_LR_S-\omega^2L^2+\omega^2M^2\right]^2+(R_L+R_S)^2\left[\omega L(1-\omega^2LC)+\omega^3M^2C\right]^2} \tag{3.22}$$

It is easy to get one root from equation (3.22) of $\omega_0=\sqrt{\frac{L}{(L^2-M^2)C}}$, but whether there exist other roots must be determined from the following equation:

$$(1-\omega^2LC)^2R_L{}^2-\omega^4M^2C^2R_L{}^2+\omega^2L^2-(\omega M)^2=0 \tag{3.23}$$

Equation (3.23) can be abbreviated as a two-variable linear equation:

$$y(\omega^2)=C^2R_L{}^2(L^2-M^2)(\omega^2)^2+(L^2-M^2-2LCR_L{}^2)\omega^2+R_L{}^2=0 \tag{3.24}$$

According to the positive and real number requirement on the angular frequency ω, only when the following conditions are satisfied simultaneously, does this equation have at least one root.

$$L^2-M^2-2LCR_L{}^2\le 0 \tag{3.25}$$

$$\Delta=(L^2-M^2-2LCR_L{}^2)^2-4(L^2-M^2)C^2R_L{}^4\ge 0 \tag{3.26}$$

The resonance frequency can therefore be expressed as:

$$f_{1,2}^{'}=\frac{1}{2\pi}\sqrt{\frac{-(L^2-M^2-2LCR_L{}^2)\pm\sqrt{\Delta}}{2(L^2-M^2)C^2R_L{}^2}} \tag{3.27}$$

For the PP MRC-WPT system, the resonance frequency is affected not only by the LC circuit but also by the mutual inductance. When the load resistance is small enough, there is only one resonance frequency, which will be shifted by different mutual inductances. That is to say, the shift of resonance frequency may result from different distances (mutual inductances), which makes the WPT system unstable unless the resonators are fixed. As the mutual inductance decreases, the resonance frequency will approach the resonance frequency of the LC oscillating circuit, which is $1/\left(2\pi\sqrt{LC}\right)$, Additionally, the PP system has very strict requirements on mutual inductance. When the load resistance is very big, meeting the condition L^2-M^2-$2LCR_L{}^2 \leq 0$, multiple resonance frequencies will appear, and the value of those resonant frequencies is related to the mutual inductance. Several conditions are summarised as shown in Table 3-2.

Although the SS circuit is suitable for small loads, frequency splitting makes the topology difficult in application. Only when all parameters satisfy the condition $\Delta<0$, do both the PTE and the load power reach their maximums. Comparisons of the four topologies are provided in Table 3-3.

Table 3-2: Calculated resonance frequencies with different conditions in PP compensation circuit

Conditions		The resonance frequency
$L^2 - M^2 - 2LCR_L{}^2 > 0$		$f_1 = \frac{1}{2\pi}\sqrt{\frac{L}{(L^2 - M^2)C}}$
$L^2 - M^2 - 2LCR_L{}^2 \leq 0$	$\Delta < 0$	$f_1 = \frac{1}{2\pi}\sqrt{\frac{L}{(L^2 - M^2)C}}$
	$\Delta = 0$	$f_1 = \frac{1}{2\pi}\sqrt{\frac{L}{(L^2 - M^2)C}}$ $f_2 = \frac{1}{2\pi}\sqrt{\frac{-(L^2 - M^2 - 2LCR_L{}^2)}{2(L^2 - M^2)C^2R_L{}^2}}$
	$\Delta > 0$	$f_1 = \frac{1}{2\pi}\sqrt{\frac{L}{(L^2 - M^2)C}}$ $f_{2,3} = \frac{1}{2\pi}\sqrt{\frac{-(L^2 - M^2 - 2LCR_L{}^2) \pm \sqrt{(L^2 - M^2 - 2LCR_L{}^2)^2 - 4(L^2 - M^2)C^2R_L{}^4}}{2(L^2 - M^2)C^2R_L{}^2}}$

Table 3-3: Qualitative comparisons of the four topologies

Topologies	Features
SS	1. Transmit resonator is short circuit at resonance frequency; 2. Suitable for load impedances of less than $(L_2/C_2)^{0.5}$; 3. Large currents present in the circuits; 4. Problem of frequency splitting.
SP	1. Transmit resonator is open circuit at resonance frequency; 2. Suitable for load impedances larger than $(L_2/C_2)^{0.5}$; 3. Large voltage in the secondary circuit; 4. The compensated capacitance is related to the load.
PS	1. Transmit resonator is open circuit at resonance frequency; 2. Suitable for load impedances less than $(L_2/C_2)^{0.5}$; 3. Tiny current in the circuits; 4. Tiny load power; 5. The resonance frequency is affected by mutual inductance.
PP	1. Transmit resonator is open circuit at resonance frequency; 2. Suitable for load impedances larger than $(L_2/C_2)^{0.5}$; 3. Tiny current in the circuits; 4. Tiny load power; 5. The resonance frequency is affected by mutual inductance; 6. The compensated capacitance is related to the load and mutual inductance

3.2 Measurement Verification

3.2.1 Measurement Setup

Based on the theoretical analysis, solutions for designing an optimal WPT system are shown in Fig.3-2 for applications with a fixed load. Firstly, the load impedance needs to be defined for different applications. Secondly, the inductances and capacitances need to be determined based on the fixed load and finally the topology of secondary circuit for WPT needs to be considered. To compare the difference between the two topologies of primary circuit, experimental results need to be obtained. Finally, a WPT design is proposed with optimised parameters to gain high load power and PTE and avoid the phenomenon of frequency splitting.

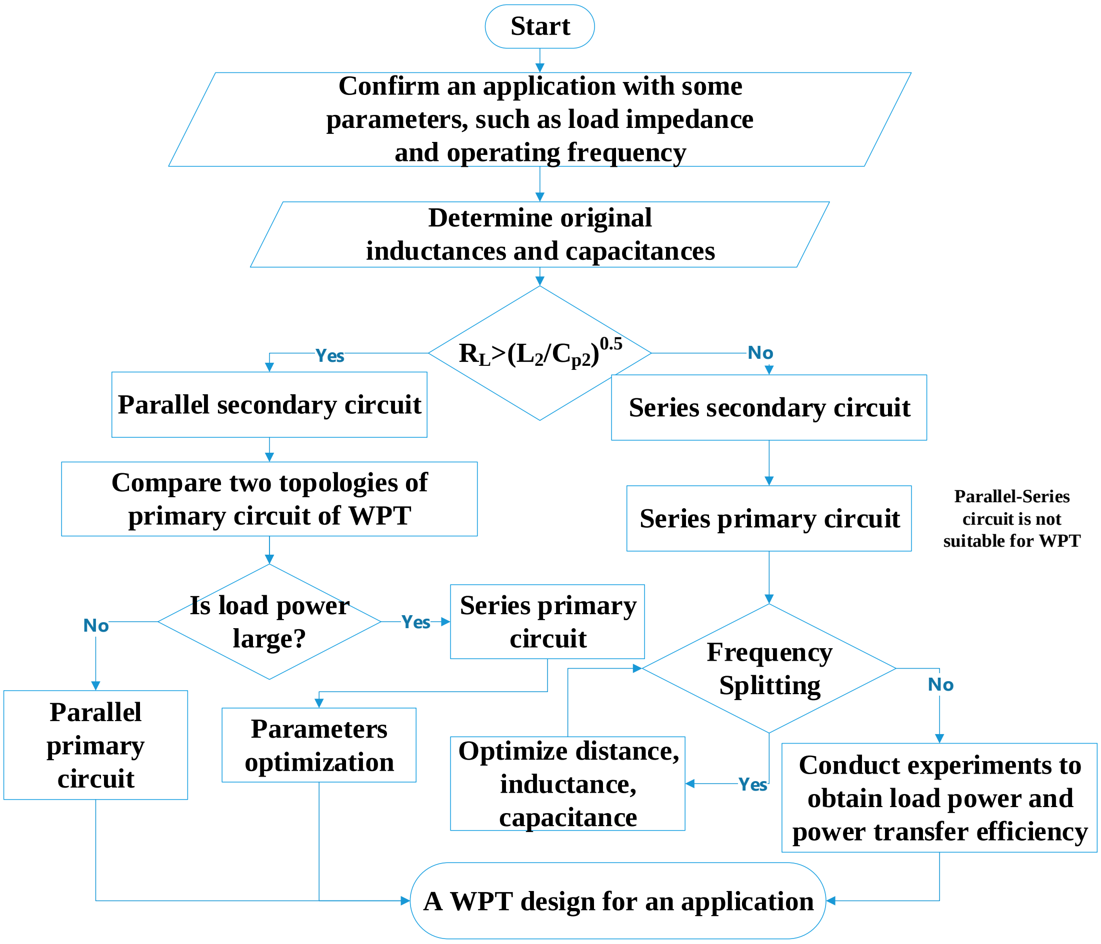

Fig. 3-2. Flow chart of a WPT system designing procedure.

To conduct experimental verification, two coils were manufactured to form inductors each with 10 turns and a radius of 5 cm. The inductance of the coils was measured to be 25.2 μH using a multi-frequency LCR meter. The resistance of the coils was measured to be 0.73 Ω. The distance between the two coils was fixed at 5 cm. The capacitances of the capacitors were calculated using the equations in [33] for WPT operation at 6.78 MHz, which is in an unlicensed band. The experimental setup is shown in Fig. 3-3. The root mean square (rms) value of the source voltage provided by the signal generator is 5 V_{rms}.

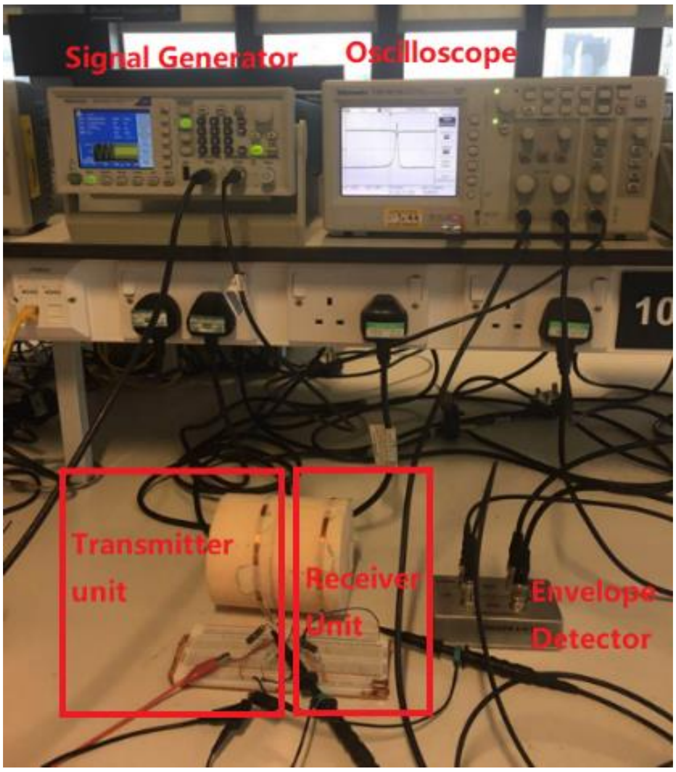

Fig. 3-3. Experimental setup of WPT circuit.

Output voltages (V_{out}) at the load and input voltage (U_s) were measured using an oscilloscope and the input current was measured using a multi-meter, allowing the load power (P_{load}) and input power (P_{in}) to be calculated. The PTE can then be calculated by (3.28).

$$\eta = \frac{P_{load}}{P_{in}} \times 100\% = \frac{V_{out}^{\ 2}}{R_L \mathbf{U_S} \mathbf{I_S}} \times 100\% \tag{3.28}$$

3.2.2 Measurement Results

3.2.2.1 Effect of Fixed Load

The SS and SP circuits for WPT were constructed as shown in Fig. 3-1(a) and 3-1(b). To investigate the influence of load impedance, the load was varied as: 100 Ω, 500 Ω, 1.6 kΩ, 5 kΩ and 10 kΩ, which represent the fixed load impedances of some sensors and electrical devices [34, 35].

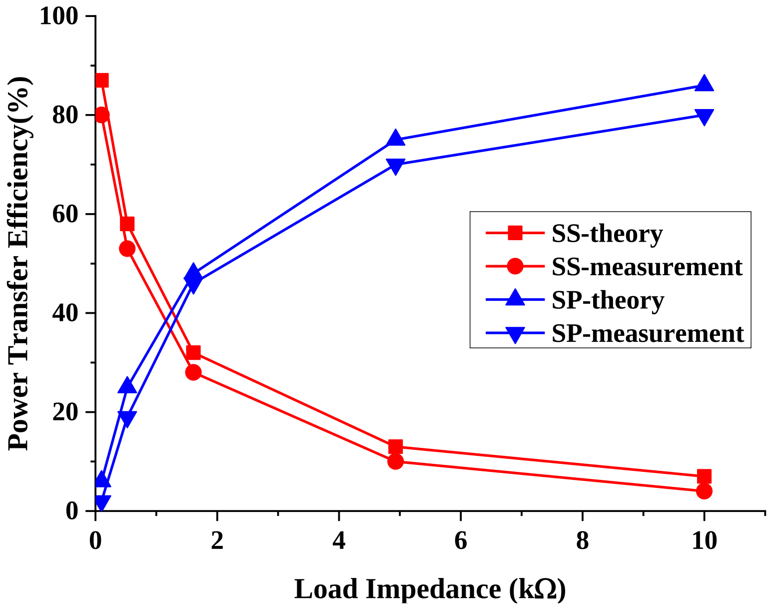

Fig. 3-4. Theoretical and experimental PTE against loads in SS and SP topologies.

From Fig. 3-4, it is seen that the experimental results show good agreement with the theoretical results for both the SS and SP topologies. When the load impedance is smaller than 1.6 kΩ, the PTE at 6.78 MHz in the SS topology is higher than that of the SP topology. However, when the load impedance is larger than 1.6 kΩ, the PTE in the SP topology is higher than that in the SS topology. What's more, the PTE reaches over 80% for small load impedances in the SS topology, whereas similar efficiencies are seen for large load impedances in the SP topology.

Therefore, a series secondary circuit is suitable for a system delivering power to a small load, whereas a parallel secondary circuit is suitable for a system delivering power to a large load in order to enhance PTE.

3.2.2.2 Load Power Comparisons

Using the experimental system as defined in Section II, with the distance set at 5 cm, the mutual inductance of the coils was measured to be M=2.115 μH. The theoretical resonant frequency of this WPT circuit shifts from 6.78 MHz to 6.83 MHz. For a load impedance of 5 kΩ a comparison of load power against frequency from theoretical and experimental results for PP and SP topologies is shown in Fig. 3-5. It can be seen from Fig. 3-5(a) that the power delivered to the load is only 0.33 μW at the resonant frequency in the PP topology, whereas the load power can reach 0.17 W at the resonance frequency in the SP topology as shown in Fig. 3-5(b).

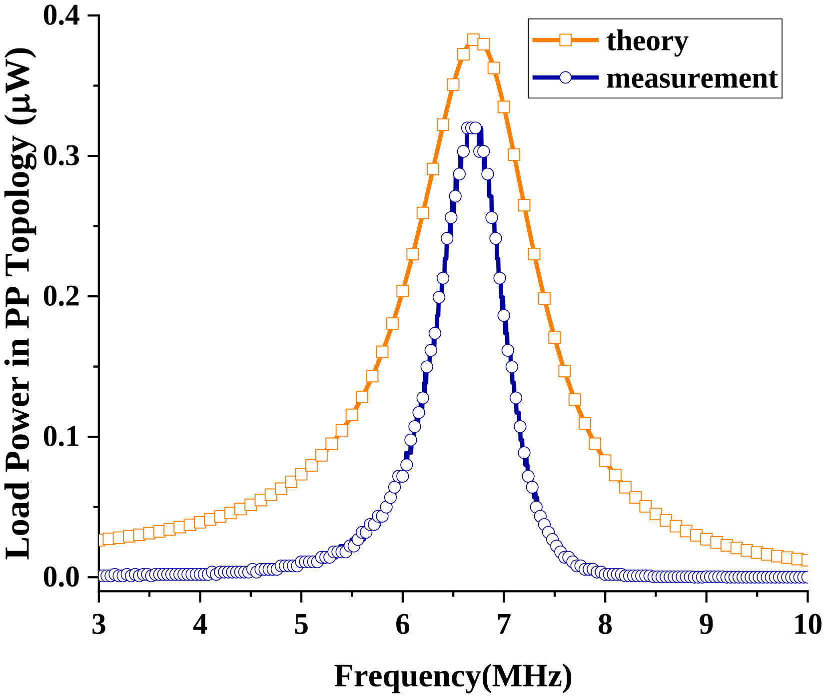

(a)

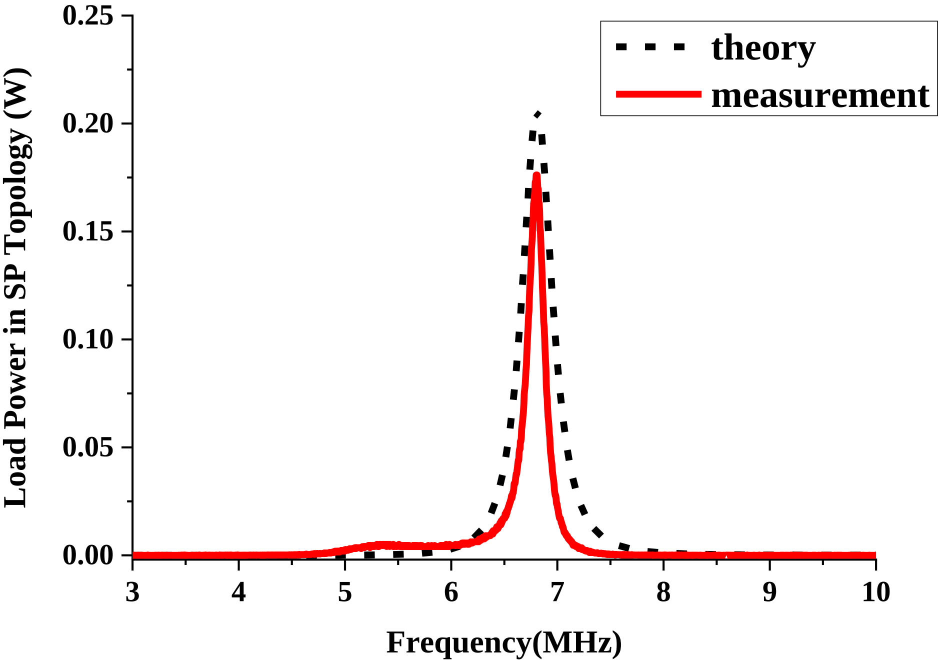

(b)

Fig. 3-5. Comparison of load power against frequency from theoretical and experimental results for (a) PP topology and (b) SP topology.

The parallel primary circuit provides a high PTE over a large distance, however the load power obtained is tiny, compared with that obtained from the series primary circuit. No matter whether the primary circuit is series or parallel, a series secondary circuit is suitable for small loads and a parallel secondary circuit is suitable for large loads. The theoretical analysis is similar to that shown in Section 3.2.1. Thus, the PS topology can obtain high PTE over a large distance only for a small load, but the load power is still extremely small. Therefore, it is more appropriate to use a series topology for the primary circuit of the WPT system to maximise load power and PTE.

The series primary circuit has been shown to transfer larger power, however, it is necessary to avoid the associated phenomenon of frequency splitting. This can result in high PTE but not maximised load power. In the following section, circuit theory and experiments are used to explain and demonstrate the frequency splitting phenomenon.

3.2.2.3 Optimisation

To gain maximum load power and maximum PTE at the same time, the influence of the coupling coefficient on the resonance frequency, load power and PTE should be investigated. The PTE of the SS topology can be calculated by:

$$\eta = \frac{P_{load}}{P_{in}} \times 100\% = \frac{I_2^{\,2} R_L}{\mathbf{U}_s \mathbf{I}_s} \times 100\% \tag{3.29}$$

Where, P_{in} and P_{load} represent the power provided by the source and output power in the load. I_s and I_{out} represent the input current phasor of the series primary and the effective output current through the load. $\boldsymbol{U_s}$ represents the source voltage phasor and R_L represents the load impedance. The trend of theoretical load power against coupling efficiency and frequency is shown in Fig. 3-6. It is worth noting that as the coupling coefficient k decreases, the load power firstly has two peaks at two resonant frequencies and then these two frequencies move together to become a single resonance frequency which is a critical coupling point. Afterwards, the load power only has one peak at the desired operating frequency. The PTE, however, only has one peak at the desired operating frequency no matter how the coupling efficient changes, which can be seen from Fig. 3-7.

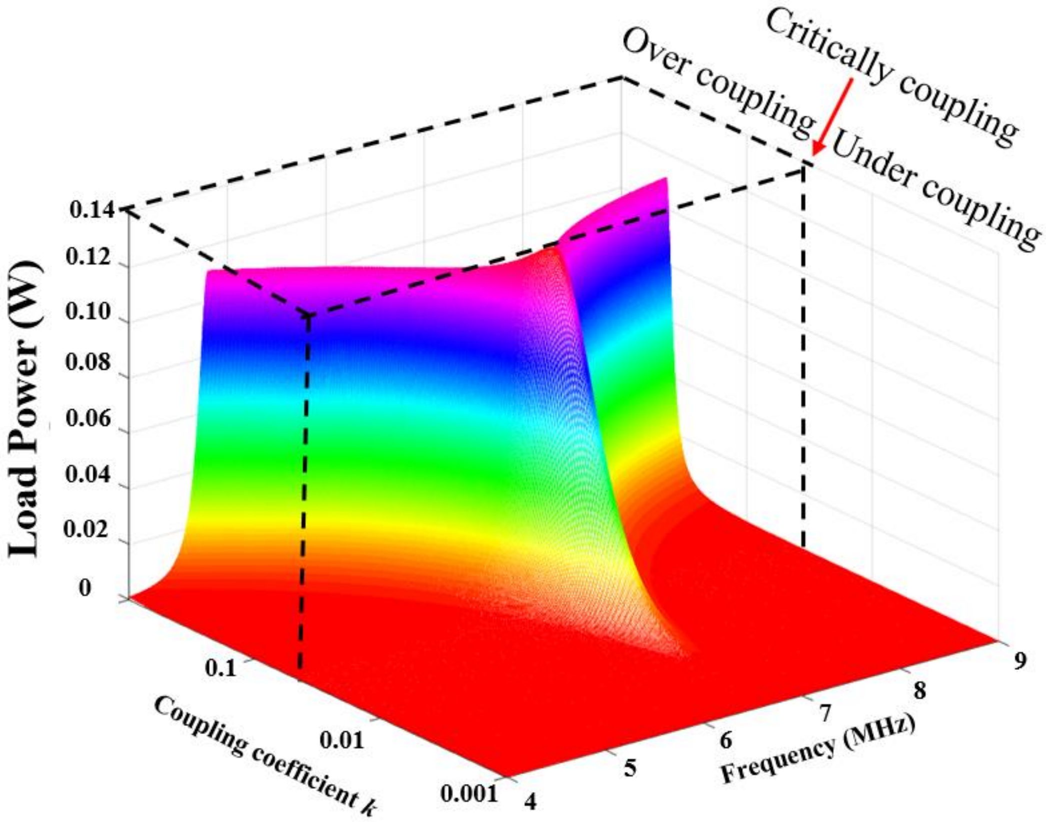

Fig. 3-6. Theoretical load power against coupling coefficient and frequency.

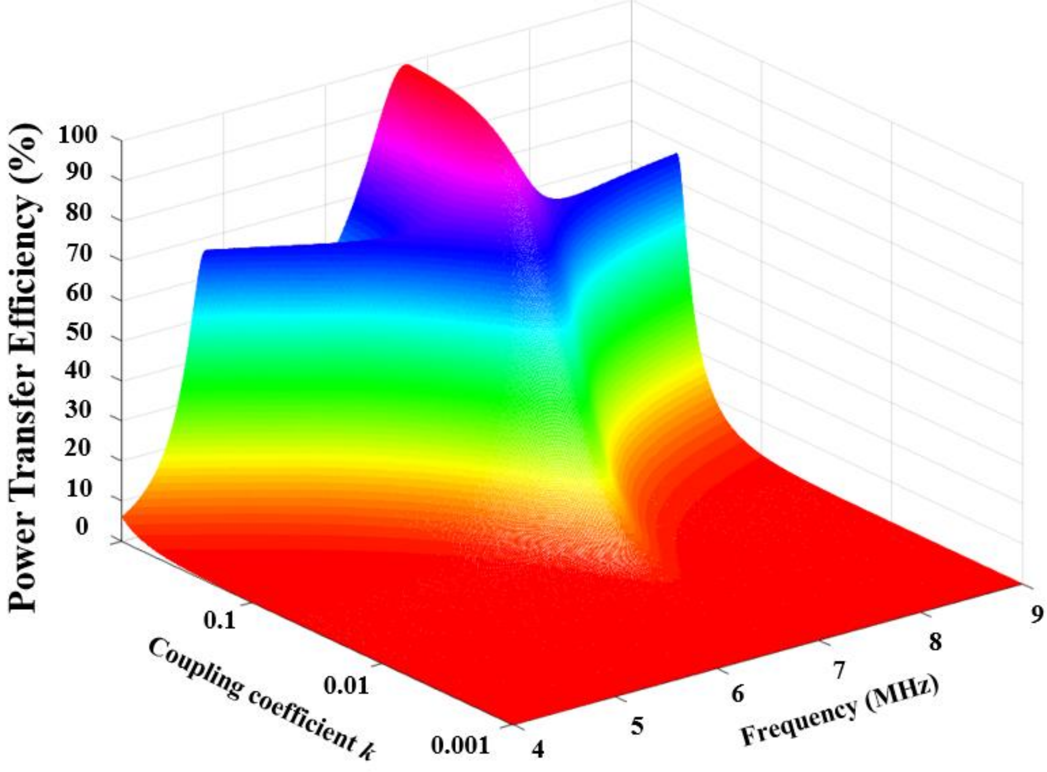

Fig. 3-7. Theoretical PTE against coupling coefficient and frequency.

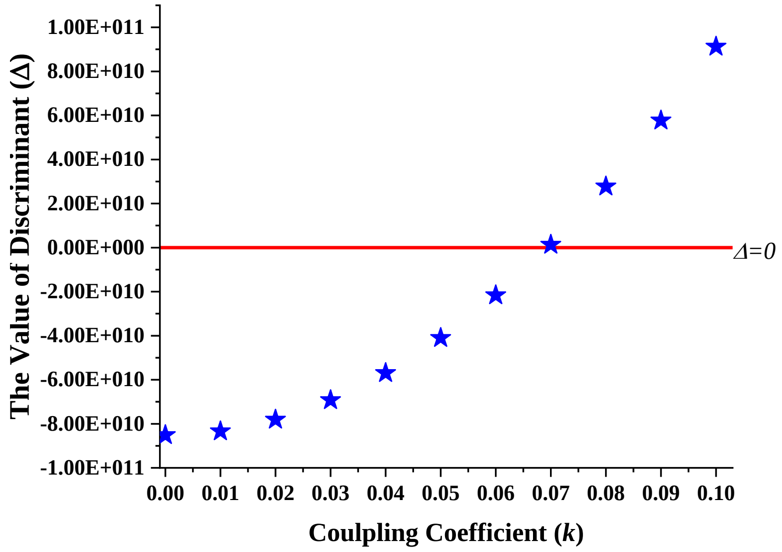

Fig. 3-8. Value of Δ against coupling coefficient.

When the load impedance is 100 Ω, equation (3.15) is satisfied, and the value of Δ varies with the coupling coefficient as shown in Fig. 3-8. The coefficient of mutual inductance is 0.084 when the distance between the two coils is 5 cm. In this case, the value of Δ is greater than 0, which means there are three resonant frequencies.

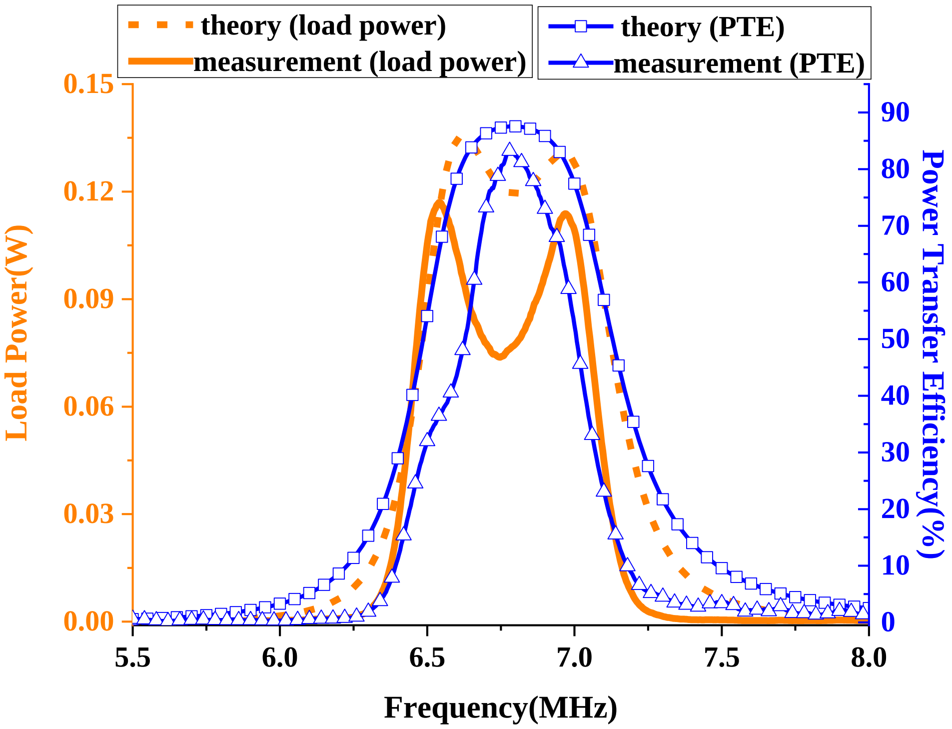

Fig. 3-9. Theoretical and measured load power and the PTE against frequency showing the phenomenon of frequency splitting.

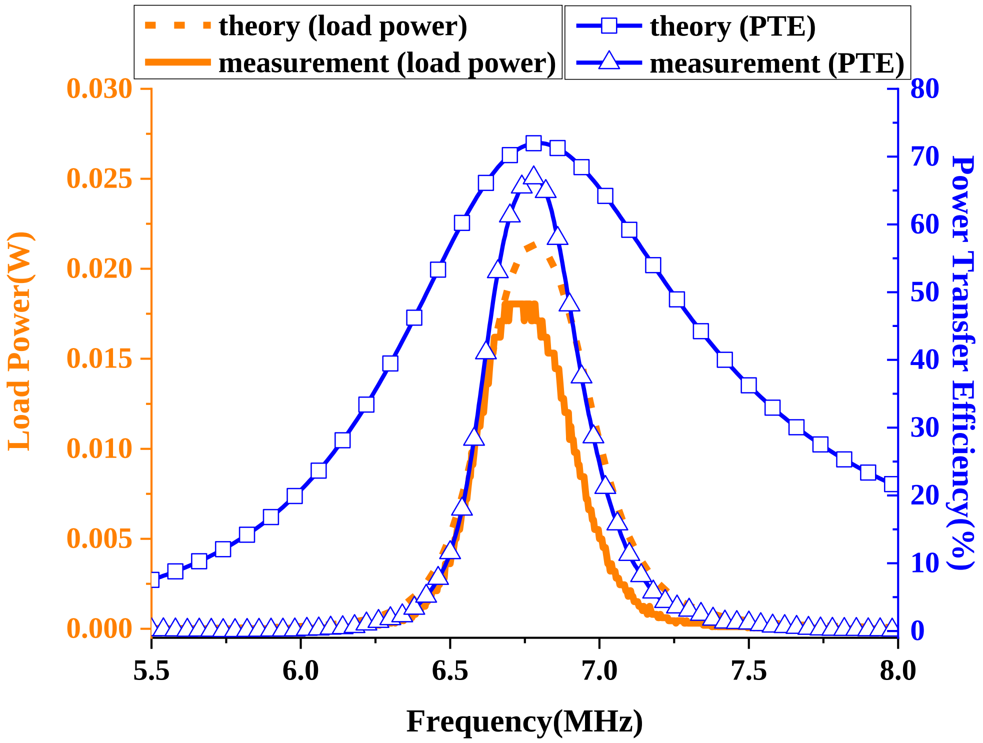

Fig. 3-10. Theoretical and measured load power and PTE against frequency without the phenomenon of frequency splitting by increasing transfer distance.

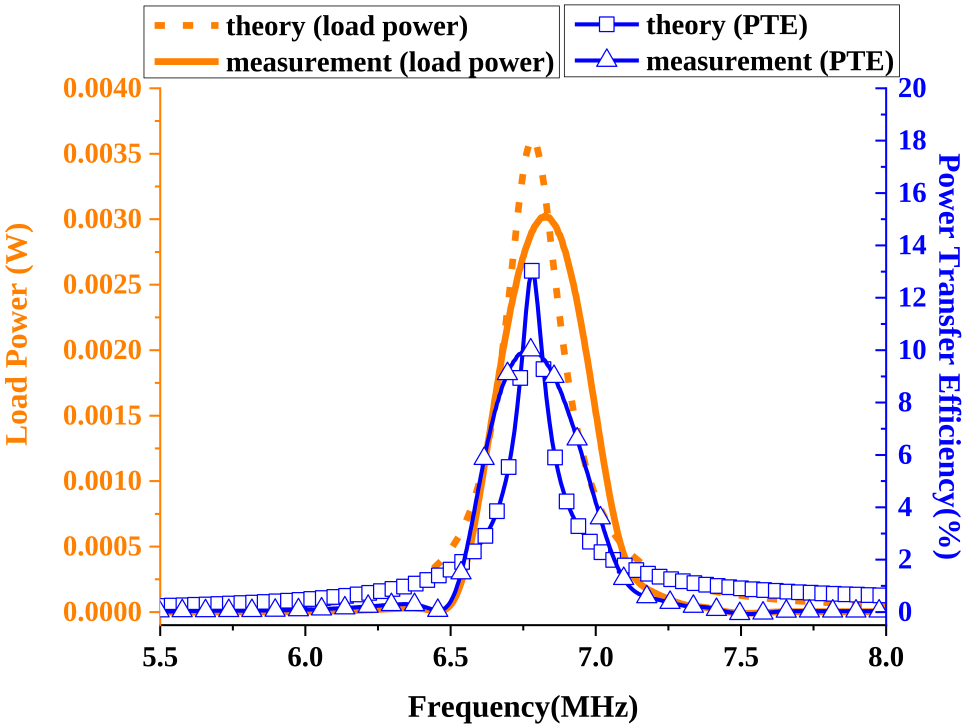

Fig. 3-11. Theoretical and measured load power and PTE against frequency without the phenomenon of frequency splitting by changing load impedance.

Trends of load power and PTE against frequency are shown in Fig. 3-9. The load power reaches two peaks at two of the resonant frequencies, however the PTE is not maximum in either case, which is the phenomenon of frequency splitting. Conversely, the PTE reaches a peak where the load power drops into the valley point between the peaks.

When the distance between the two coils reaches 8 cm, the coupling coefficient is 0.05, in this case, the value of Δ is less than 0 and there is only one resonant frequency. Trends of load power and PTE against frequency by enlarging the transfer distance to avoid the phenomenon of frequency splitting are shown in Fig. 3-10. Both the load power and PTE reach their peak at this one resonant frequency.

When the load impedance is 5 k**Ω**, equation (3.15) is not satisfied, and hence there is only one resonant frequency as well. The trends of load power and PTE with varying frequency by increasing the load impedance to avoid the phenomenon of frequency splitting are shown in Fig. 3-11. Both the load power and PTE reach their peak at the one resonant frequency.

Although SS topologies are suitable for small loads, they often lead to the phenomenon of frequency splitting, especially, when the distance between coils is small. To avoid this phenomenon, the distance could be made larger, however, the load power and the PTE will decrease. Consequently, there is a trade-off between load power, load and distance.

3.3 Summary

An investigation of the four possible system topologies for MRC for WPT has been presented in terms of both theoretical analysis and experimental verification. Application of a series secondary circuit was shown to be suitable for power transfer to small loads, conversely, if the load impedance is large then the parallel secondary circuit is more appropriate. For the primary circuit the parallel topology looks like an open circuit at resonance, which means a low current will be supplied to the inductor. Consequently, the power transferred to the secondary circuit will be low making it inappropriate for use in WPT applications.

The resonance frequency is affected by mutual inductance which is itself affected as the distance and/or environment between the coils changes. As the distance or environment changes the resonance frequency will shift, resulting in reductions in load power and PTE.

For the SS topology, the phenomenon of frequency splitting should be avoided to maintain maximum load power and PTE at resonance. Only when the load impedance and transfer distance are carefully chosen, can the load power and PTE maintain their maximums at resonance, but in this case, the PTE is not very high.

Finally, the SP topology is shown to be the most suitable candidate for use in WPT. Inductances, capacitances and the load impedances need to be optimised in order to gain maximum load power and transfer efficiency over the optimal transfer distance.

3.4 References

[1] G. Lerosey, "Wireless power on the move," *Nature,* vol. 546, p. 354, 06/14/online 2017, doi: 10.1038/546354a.

[2] A. Kurs, A. Karalis, R. Moffatt, J. D. Joannopoulos, P. Fisher, and M. Soljacic, "Wireless power transfer via strongly coupled magnetic resonances," *Science,* vol. 317, no. 5834, pp. 83-6, Jul 6 2007, doi: 10.1126/science.1143254.

[3] S. Assawaworrarit, X. Yu, and S. Fan, "Robust wireless power transfer using a nonlinear parity–time-symmetric circuit," *Nature,* vol. 546, p. 387, 06/14/online 2017, doi: 10.1038/nature22404 https://www.nature.com/articles/nature22404#supplementary-information.

[4] F. Tan, T. Lv, and P. Huang, "Global Energy Efficiency Optimization for Wireless-Powered Massive MIMO Aided Multiway AF Relay Networks," *IEEE Transactions on Signal Processing,* vol. 66, no. 9, pp. 2384-2398, 2018, doi: 10.1109/TSP.2018.2811732.

[5] X. Chen, D. W. K. Ng, and H. Chen, "Secrecy wireless information and power transfer: challenges and opportunities," *IEEE Wireless Communications,* vol. 23, no. 2, pp. 54-61, 2016, doi: 10.1109/MWC.2016.7462485.

[6] M. Song, P. Belov, and P. Kapitanova, "Wireless power transfer inspired by the modern trends in electromagnetics," *Applied Physics Reviews,* vol. 4, no. 2,

2017, doi: 10.1063/1.4981396.

[7] X. Wei, Z. Wang, and H. Dai, "A Critical Review of Wireless Power Transfer via Strongly Coupled Magnetic Resonances," *Energies,* vol. 7, no. 7, pp. 4316-4341, 2014, doi: 10.3390/en7074316.

[8] R. Jegadeesan and Y. Guo, "Topology Selection and Efficiency Improvement of Inductive Power Links," *IEEE Transactions on Antennas and Propagation,* vol. 60, no. 10, pp. 4846-4854, 2012, doi: 10.1109/TAP.2012.2207325.

[9] W. Zhang, S. Wong, C. K. Tse, and Q. Chen, "Analysis and Comparison of Secondary Series- and Parallel-Compensated Inductive Power Transfer Systems Operating for Optimal Efficiency and Load-Independent Voltage-Transfer Ratio," *IEEE Transactions on Power Electronics,* vol. 29, no. 6, pp. 2979-2990, 2014, doi: 10.1109/TPEL.2013.2273364.

[10] Y. Zhang, T. Kan, Z. Yan, Y. Mao, Z. Wu, and C. C. Mi, "Modeling and Analysis of Series-None Compensation for Wireless Power Transfer Systems With a Strong Coupling," *IEEE Transactions on Power Electronics,* vol. 34, no. 2, pp. 1209-1215, 2019, doi: 10.1109/TPEL.2018.2835307.

[11] C. Xiao, K. Wei, F. Liu, and Y. Ma, "Matching capacitance and transfer efficiency of four wireless power transfer systems via magnetic coupling resonance," *International Journal of Circuit Theory and Applications,* vol. 45, no. 6, pp. 811-831, 2017, doi: 10.1002/cta.2247.

[12] C. Jiang, K. T. Chau, C. Liu, and C. H. T. Lee, "An Overview of Resonant Circuits for Wireless Power Transfer," *Energies,* vol. 10, no. 7, 2017, doi: 10.3390/en10070894.

[13] Z. Bi, T. Kan, C. C. Mi, Y. Zhang, Z. Zhao, and G. A. Keoleian, "A review of wireless power transfer for electric vehicles: Prospects to enhance sustainable mobility," *Applied Energy,* vol. 179, pp. 413-425, 2016, doi: 10.1016/j.apenergy.2016.07.003.

[14] Y. Yi, U. Buttner, Y. Fan, and I. G. Foulds, "Design and optimization of a 3-coil resonance-based wireless power transfer system for biomedical implants," *International Journal of Circuit Theory and Applications,* vol. 43, no. 10, pp. 1379-1390, 2015, doi: 10.1002/cta.2024.

[15] C. Huang, C. Lin, and Y. Wu, "Simultaneous Wireless Power/Data Transfer for Electric Vehicle Charging," *IEEE Transactions on Industrial Electronics,* vol. 64, no. 1, pp. 682-690, 2017, doi: 10.1109/TIE.2016.2608765.

[16] J. Kim and J. Jeong, "Range-Adaptive Wireless Power Transfer Using Multiloop and Tunable Matching Techniques," *IEEE Transactions on Industrial Electronics,* vol. 62, no. 10, pp. 6233-6241, 2015, doi: 10.1109/TIE.2015.2420041.

[17] W. Lu, M. Zhao, L. Zhou, H. H. C. Iu, and J. Zhao, "Modeling and analysis of magnetically coupled resonant wireless power transfer system with rectifier bridge LED load," *International Journal of Circuit Theory and Applications,* vol. 43, no. 12, pp. 1914-1924, 2015, doi: 10.1002/cta.2053.

[18] H. Feng, T. Cai, S. Duan, X. Zhang, H. Hu, and J. Niu, "A Dual-Side-Detuned Series–Series Compensated Resonant Converter for Wide Charging Region in a Wireless Power Transfer System," *IEEE Transactions on Industrial Electronics,* vol. 65, no. 3, pp. 2177-2188, 2018, doi: 10.1109/TIE.2017.2745455.

[19] Y. Lyu *et al.*, "A Method of Using Nonidentical Resonant Coils for Frequency Splitting Elimination in Wireless Power Transfer," *IEEE Transactions on Power Electronics,* vol. 30, no. 11, pp. 6097-6107, 2015, doi: 10.1109/TPEL.2014.2387835.

[20] N. Kuo, B. Zhao, and A. M. Niknejad, "Bifurcation Analysis in Weakly-Coupled Inductive Power Transfer Systems," *IEEE Transactions on Circuits and Systems I: Regular Papers,* vol. 63, no. 5, pp. 727-738, 2016, doi: 10.1109/TCSI.2016.2529283.

[21] W. Choi, C. Park, and K. Lee, "Circuit Analysis of Achievable Transmission Efficiency in an Overcoupled Region for Wireless Power Transfer Systems," *IEEE Systems Journal,* vol. 12, no. 4, pp. 3873-3876, 2018, doi: 10.1109/JSYST.2017.2767060.

[22] N. Inagaki, "Theory of Image Impedance Matching for Inductively Coupled Power Transfer Systems," *IEEE Transactions on Microwave Theory and Techniques,* vol. 62, no. 4, pp. 901-908, 2014, doi: 10.1109/TMTT.2014.2300033.

[23] Y. Lim, H. Tang, S. Lim, and J. Park, "An Adaptive Impedance-Matching Network Based on a Novel Capacitor Matrix for Wireless Power Transfer," *IEEE Transactions on Power Electronics,* vol. 29, no. 8, pp. 4403-4413, 2014, doi: 10.1109/TPEL.2013.2292596.

[24] A. A. M. Bahar, Z. Zakaria, S. R. A. Rashid, A. A. M. Isa, and R. A. Alahnomi,

"High-Efficiency Microwave Planar Resonator Sensor Based on Bridge Split Ring Topology," *IEEE Microwave and Wireless Components Letters,* vol. 27, no. 6, pp. 545-547, 2017, doi: 10.1109/LMWC.2017.2701338.

[25] N. Sekiya and Y. Monjugawa, "A Novel REBCO Wire Structure That Improves Coil Quality Factor in MHz Range and its Effect on Wireless Power Transfer Systems," *IEEE Transactions on Applied Superconductivity,* vol. 27, no. 4, pp. 1-5, 2017, doi: 10.1109/TASC.2017.2660058.

[26] Y. Su, L. Chen, X. Wu, A. P. Hu, C. Tang, and X. Dai, "Load and Mutual Inductance Identification From the Primary Side of Inductive Power Transfer System With Parallel-Tuned Secondary Power Pickup," *IEEE Transactions on Power Electronics,* vol. 33, no. 11, pp. 9952-9962, 2018, doi: 10.1109/TPEL.2018.2793854.

[27] L. Sun, M. Sun, D. Ma, and H. Tang, "Detecting Load Resistance and Mutual Inductance in Series-Parallel Compensated Wireless Power Transfer System Based on Input-Side Measurement," *International Journal of Antennas and Propagation,* vol. 2018, pp. 1-6, 2018, doi: 10.1155/2018/2094637.

[28] Z. Chunbo, L. Kai, Y. Chunlai, M. Rui, and C. Hexiao, "Simulation and experimental analysis on wireless energy transfer based on magnetic resonances," in *2008 IEEE Vehicle Power and Propulsion Conference*, 3-5 Sept. 2008 2008, pp. 1-4, doi: 10.1109/VPPC.2008.4677400.

[29] L. Xie, Y. Shi, Y. T. Hou, and A. Lou, "Wireless power transfer and applications to sensor networks," *IEEE Wireless Communications,* vol. 20, no. 4, pp. 140-145, 2013, doi: 10.1109/MWC.2013.6590061.

[30] Z. Zhang, H. Pang, A. Georgiadis, and C. Cecati, "Wireless Power Transfer—An Overview," *IEEE Transactions on Industrial Electronics,* vol. 66, no. 2, pp. 1044-1058, 2019, doi: 10.1109/TIE.2018.2835378.

[31] M. Kiani and M. Ghovanloo, "The Circuit Theory Behind Coupled-Mode Magnetic Resonance-Based Wireless Power Transmission," *IEEE Transactions on Circuits and Systems I: Regular Papers,* vol. 59, no. 9, pp. 2065-2074, 2012, doi: 10.1109/TCSI.2011.2180446.

[32] Y. Yao, X. Liu, Y. Wang, and D. Xu, "LC/CL compensation topology and efficiency-based optimisation method for wireless power transfer," *IET Power Electronics,* vol. 11, no. 6, pp. 1029-1037, 2018, doi: 10.1049/iet-pel.2017.0875.

[33] S. D. Barman, A. W. Reza, N. Kumar, M. E. Karim, and A. B. Munir, "Wireless powering by magnetic resonant coupling: Recent trends in wireless power transfer system and its applications," *Renewable and Sustainable Energy Reviews,* vol. 51, pp. 1525-1552, 2015, doi: 10.1016/j.rser.2015.07.031.

[34] D. A. Borton, M. Yin, J. Aceros, and A. Nurmikko, "An implantable wireless neural interface for recording cortical circuit dynamics in moving primates," *J Neural Eng,* vol. 10, no. 2, p. 026010, Apr 2013, doi: 10.1088/1741-2560/10/2/026010.

[35] E. G. Kilinc, C. Dehollain, F. Maloberti,, *Remote Powering and Data Communication for Implanted Biomedical Systems* (Analog Circuits and Signal Processing). Springer, 2016.

Chapter 4 Printed Spiral Coils for Wireless Power Transfer

Wire coils are widely used in MRC based wireless power transfer (WPT) [1-3] due to their high Quality factor (*Q*-factor), however, they present technical difficulties in precise fabrication and mass production [4]. Furthermore, due to the typically large area occupied by wire coils, they are normally applicable for use in large electronic devices such as electric cars. They are not usually appropriate for use in small electronic devices such as implantable medical devices (IMDs), wireless sensors and devices with integrated circuit boards using micromachining technology. As an alternative, planar printed spiral coils (PSCs) are low-profile, low-cost and can have relatively small-dimensions. Additionally, planar PSCs offer higher geometrical manufacturing precision and have the potential to be integrated together with integrated circuits or within packages [5]. The ability to manufacture PSCs on flexible substrates means that they are suitable for use in wearable devices. There have been many PSC designs proposed for magnetic resonance coupling (MRC) based WPT featuring various shapes including circular, square and rectangular spiral coils [6-8].

High frequency bands such as 0.3 MHz, 6.78 MHz and 13.56 MHz were considered in recent works for WPT [9-12]. At these frequencies, coils with large inductances, up to µH, can be created allowing high *Q*- factor to be achieved and power transfer distances to be increased into the centimetres or meter ranges due to the longer wavelengths; typically more than 10 m. As electromagnetic energy absorption in human tissues increases with frequency, for implantable applications these high frequency bands are typically selected. However, as received power is proportional to the rate of change of the incident magnetic field, choosing a higher carrier frequency improves power transfer [13]. Therefore, a compromise between power transfer and field penetration into the human body must be made.

Few works related to coils printed on PCB in the sub-GHz region have been published, as standard spiral coils printed on PCB have low inductances (nH) and are therefore unable to realise high power transfer efficiencies or large transfer distances.

Also, matching networks for both the primary (transmitting) and secondary (receiving) circuits are essential in achieving a high PTE. Investigations on normal rectangular printed spiral coils for WPT are performed in this chapter. They explore the properties of PSCs for WPT and solutions for WPT operating in the sub-GHz region. This aims to offer a better understanding of the challenges of using PSCs for WPT at high frequencies.

4.1 Theoretical Modelling of Printed Spiral Coils

4.1.1 Inductance Modelling

The inductance of a planar rectangular spiral coil can be calculated by summing up the inductance of each segment and the positive mutual inductance and the negative mutual inductance between all pairs of segments. This is based on the Expanded Grover method [14]. The total inductance of a planar rectangular coil can be given by

$$L_T = L_S + M_{S+} - M_{S-} \tag{4.1}$$

where, L_S is the sum of the inductance of each segment, M_{S+} is the sum of positive mutual inductance between all pairs of segments and M_{S-} is the sum of negative mutual inductance between all pairs of segments.

The geometry and parameters for a *N*-turn planar rectangular spiral are shown in Fig. 4-1.

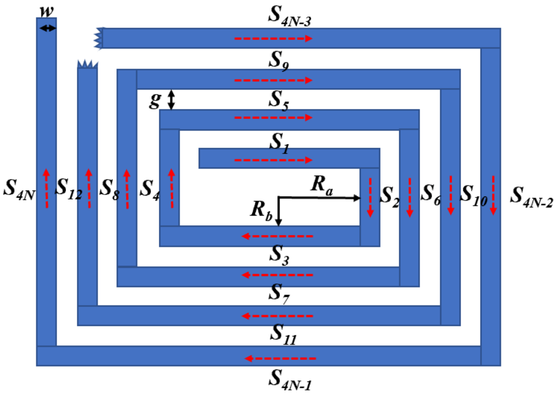

Fig. 4-1. Geometry of a rectangular PSC with *N* turns. (Red arrows represent current direction).

The inductance of each segment (S_i) can be calculated by

$$L_{S_i} = \frac{\mu_0}{2\pi}\ell_{S_i}\left[\ln\left(\frac{2\ell_{S_i}}{w+t}\right) + 0.50049 + \frac{w+t}{3\ell_{S_i}}\right] \tag{4.2}$$

where, μ_0 is the vacuum magnetic permeability $4\pi\times10^{-7}$ H/m, w is the width of the conductor track, ℓ_{S_i} is the length of each segment S_i and t is the thickness of the conductor material. Therefore, the sum of the inductance of each segment can be expressed as

$$L_S = \sum_{i=1}^{4N} L_{S_i} = \sum_{i=1}^{4N} \frac{\mu_0}{2\pi}\ell_{S_i}\left[\ln\left(\frac{2\ell_{S_i}}{w+t}\right) + 0.50049 + \frac{w+t}{3\ell_{S_i}}\right] \tag{4.3}$$

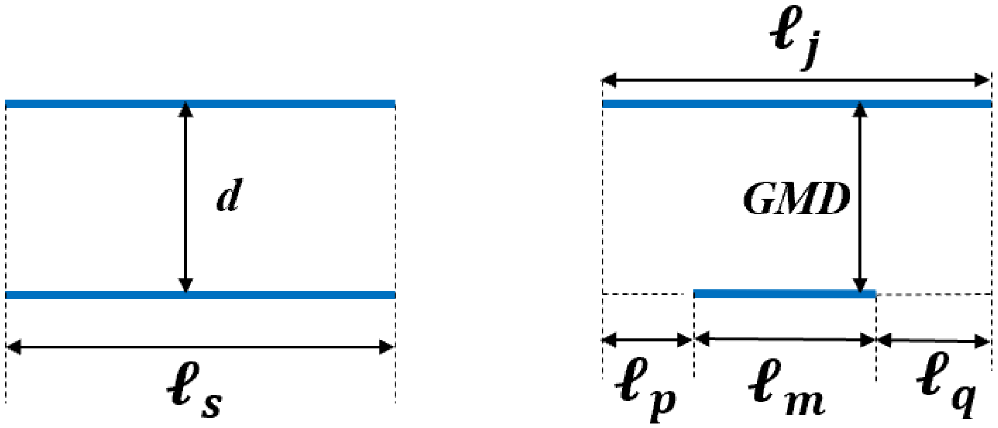

(a) **(b)**

Fig. 4-2. (a) Two equal infinitesimally thin parallel and straight filaments with same length separated by distance *d*. (b) Two parallel and straight filaments with different lengths separated by a distance *GMD*.

The current direction of the planar rectangular spiral coil is shown in Fig. 4-1 for a source port added to segment S_1. From Fig.4-1, the mutual inductance between two segments with the same current direction is positive and the mutual inductance between two segments with opposite current direction is negative. To obtain the positive and negative mutual inductances, the mutual inductance between two parallel segments needs to be calculated. If parallel segments have the same length (as shown in Fig. 4-2(a)), then ℓ_s the mutual inductance between those two segments can be calculated by

$$M_s = \frac{\mu_0}{2\pi}\ell_s\left[\ln\left(\frac{\ell_s}{d}+\sqrt{1+\left(\frac{\ell_s}{d}\right)^2}\right)-\sqrt{1+\left(\frac{\ell_s}{d}\right)^2}+\frac{d}{\ell_s}\right] \tag{4.4}$$

If two parallel segments S_j and S_m have different lengths of ℓ_j and ℓ_m, as described in Fig. 4-2(b), and the absent lengths of the segment on the bottom with respect to the segment on the top are defined as ℓ_p and ℓ_q. So the mutual inductance between these two parallel segments of different length can be expressed by

$$M_{S_j,S_m} = \frac{\left[M\left(\ell_m+\ell_p\right)+M\left(\ell_m+\ell_q\right)\right]-\left[M\left(\ell_p\right)+M\left(\ell_q\right)\right]}{2} \tag{4.5}$$

In this case, the distance *d* between two parallel segments should be replaced by the geometric mean distance (*GMD*) between two parallel segments which is approximately equal to the distance *d* between the segment centres. The exact value of *GMD* and the each mutual inductanc *M* can be calculated from the following equations.

$$GMD = \exp\left[\ln d - \left(\frac{w^2}{12d^2}+\frac{w^4}{60d^4}+\frac{w^6}{168d^6}+\frac{w^8}{360d^8}+\frac{w^{10}}{660d^{10}}+\cdots\right)\right] \tag{4.6}$$

$$M\left(\ell_{S_j}\right) = \ln\left(\frac{\ell_{s_j}}{GMD}+\sqrt{1+\left(\frac{\ell_{s_j}}{GMD}\right)^2}\right)-\sqrt{1+\left(\frac{\ell_{s_j}}{GMD}\right)^2}+\frac{GMD}{\ell_{s_j}} \tag{4.7}$$

When thinking of these elements as any pair of segments from the exemplary coil in Fig.4-1, the lengths ℓ_p and ℓ_q can be equal (such as the length of segment S_2 and S_6) . Then the mutual inductance can be obtained by

$$M_{S_j,S_m} = M\left(\ell_m+\ell_p\right)-M\left(\ell_p\right), \qquad \ell_p=\ell_q \tag{4.8}$$

Additionally, the lengths of ℓ_p and ℓ_q can be zero (such as for the length of segments S_4 and S_6) and the mutual inductance can be obtained by

$$M_{S_j,S_m} = \frac{\left[M\left(\ell_j\right)+M\left(\ell_m\right)\right]-M\left(\ell_q\right)}{2}, \qquad \ell_p=0 \tag{4.9}$$

The mutual inductance in different cases can be summarised as

$$M_{S_j,S_m}=\begin{cases}\dfrac{\left[M\left(\ell_j\right)+M\left(\ell_m\right)\right]-M\left(\ell_q\right)}{2}, & \ell_p=0\\ M\left(\ell_m+\ell_p\right)-M\left(\ell_p\right), & \ell_p=\ell_q\\ \dfrac{\left[M\left(\ell_m+\ell_p\right)+M\left(\ell_m+\ell_q\right)\right]-\left[M\left(\ell_p\right)+M\left(\ell_q\right)\right]}{2}, & \ell_p\neq\ell_q\neq 0\end{cases} \tag{4.10}$$

Consequently, the sum of the positive mutual inductance between two parallel segments can be calculated by

$$M_{S+}=2\sum_{i=1}^{N-1}\sum_{j=i+1}^{N}\sum_{k=1}^{4}M_{S_{4(i-1)+k},S_{4(j-1)+k}} \tag{4.11}$$

Conversely the sum of the negative mutual inductance between two parallel segments can be calculated by

$$M_{S-}=2\sum_{i=1}^{N}\sum_{j=1}^{N}\sum_{k=1}^{2}M_{S_{4(i-1)+k},S_{4(j-1)+k+2}} \tag{4.12}$$

Eventually, the total inductance of the planar rectangular coil with *N* turns can be obtained by

$$\begin{aligned}L_T&=L_S+M_{S+}-M_{S-}\\&=\sum_{i=1}^{4N}\frac{\mu_0}{2\pi}\ell_{S_i}\left[\ln(\frac{2\ell_{S_i}}{w+t})+0.50049+\frac{w+t}{3\ell_{S_i}}\right]\\&+2\sum_{i=1}^{N-1}\sum_{j=i+1}^{N}\sum_{k=1}^{4}M_{S_{4(i-1)+k},S_{4(j-1)+k}}\\&-2\sum_{i=1}^{N}\sum_{j=1}^{N}\sum_{k=1}^{2}M_{S_{4(i-1)+k},S_{4(j-1)+k+2}}\end{aligned} \tag{4.13}$$

4.1.2 Mutual Inductance

The net mutual inductance between two coaxial planar rectangular coils (as shown in Fig. 4-3) can be calculated by summing all mutual inductances between all pairs of parallel segments. The number of turns of the upper coil is N_1, and the number of turns of the lower coil is N_2. The distance between two rectangular coils is D. It can be seen from Fig.4-3 that segments in both coils with currents in the same direction would have a positive mutual inductance, and segments in the two coils with currents in the opposite direction would have a negative mutual inductance. Segments S_1, S_5, S_9 of the upper coil and segments P_1, P_5, P_9 of the lower coil would have positive mutual inductance. However, segments S_1, S_5, S_9 of the upper coil and segments P_3, P_7, P_{11} of the lower coil would have negative mutual inductance.

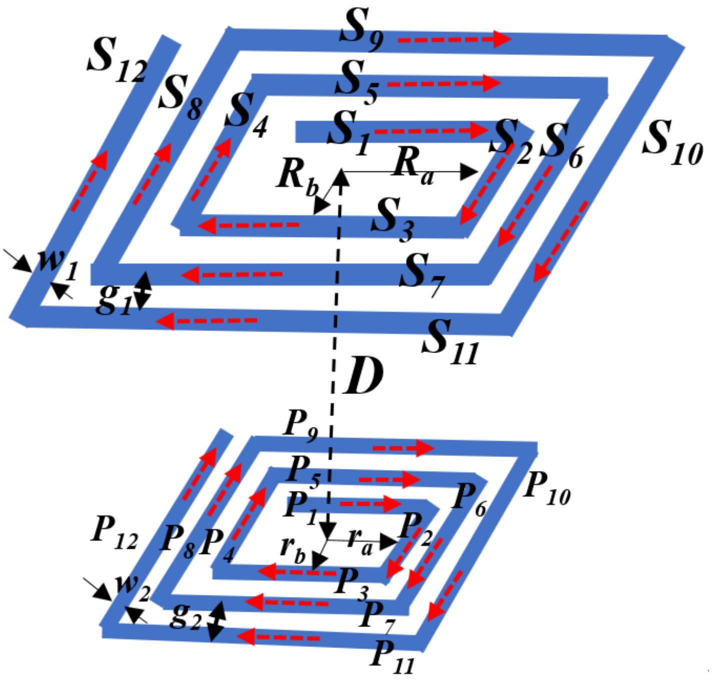

Fig. 4-3. Diagram of two coaxial rectangular PSCs with distance *D*. (Red arrows represent current direction).

The positive mutual inductance between the two coils is a sum of the mutual inductance between a pair of segments with currents in the same direction in both coils. The expression of positive mutual inductance [15] is given by

$$M_{+} = \sum_{i=1}^{N_1}\sum_{j=1}^{N_2}\sum_{k=1}^{4} M_{S_{4(i-1)+k},P_{4(j-1)+k}} \tag{4.14}$$

From equation (4.4), to obtain positive mutual inductance, it is necessary to calculate the distance between the segments in the upper and lower coils that have currents flowing in the same direction. Firstly, the distance between one segment and the centre of the upper rectangular coil can be obtained by

$$d_{S_i} = \frac{R_a + R_b + (-1)^i (R_a + R_b)}{2} + \left\lceil \frac{i}{4} - 1 \right\rceil (w_1 + g_1) \tag{4.15}$$

where, R_a and R_b represent the horizontal and vertical inner radii of the upper coil respectively, w_1 denotes the width of each segment and g_1 represents the gap between two adjacent segments.

Similarly, the distance between one segment and the centre of the lower rectangular coil can be obtained by

$$d_{P_i} = \frac{r_a + r_b + (-1)^i (r_a + r_b)}{2} + \left\lceil \frac{i}{4} - 1 \right\rceil (w_2 + g_2) \tag{4.16}$$

where, r_a and r_b represent the horizontal and vertical inner radii of the lower coil respectively, w_2 denotes the width of each segment and g_2 represents the gap between two adjacent segments.

Therefore, the distance between two segments with currents in the same direction in both coils can be calculated by

$$d_+ = \sqrt{\left(d_{S_i} - d_{P_i}\right)^2 + D^2} \tag{4.17}$$

The negative mutual inductance between the two coils is a sum of mutual inductance between pairs of segments with currents in the opposite direction in each coil. The expression of negative mutual inductance is given by

$$M_- = \sum_{i=1}^{N_1} \sum_{j=1}^{N_2} \sum_{k=1}^{4} M_{S_{4(i-1)+k}, P_{4(j-1)-k+(-1)^k+5}} \tag{4.18}$$

The distance between two segments with currents flowing in the opposite direction in each of the coils can be calculated by

$$d_- = \sqrt{\left(d_{S_i} + d_{P_i}\right)^2 + D^2} \tag{4.19}$$

If the length of the segments is different, irrespective of current direction, equation (4.9) can be used to calculate the positive or negative mutual inductance. Therefore, the total mutual inductance can be expressed by

$$M_{total} = M_{+} - M_{-} \tag{4.20}$$

4.1.3 Parasitic Capacitance

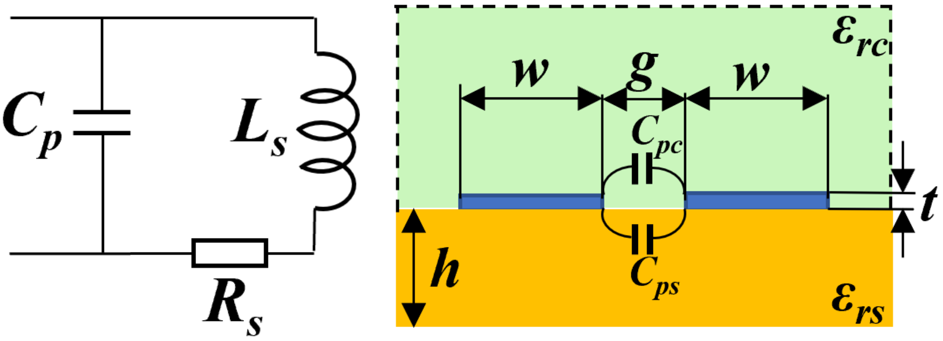

(a) **(b)**

Fig. 4-4. (a) Equivalent circuit of a rectangular PSC. (b) Cross section of a pair of parallel traces showing the parasitic capacitors within in the air and substrate materials.

PSCs can be self-resonant circuits, as shown in Fig. 4-4(a). Parasitic capacitance C_p is mainly determined by the spacing between the planar conductive traces and their surrounding materials. For PSCs in air, two parallel parasitic capacitors can be considered; the capacitance C_{pc} through air and the capacitance C_{ps} through the substrate material (such as FR-4, ceramic and polyimide), as shown in Fig. 4-4(b). The parasitic capacitance [16] can be calculated by

$$C_p = C_{pc} + C_{ps} \approx \left(\alpha\varepsilon_{rc} + \beta\varepsilon_{rs}\right)\varepsilon_0 \frac{t}{g}\ell_g \tag{4.21}$$

where ε_{rc} and ε_{rs} are the relative dielectric constants of air and the substrate materials, respectively and ε_0 is the vacuum dielectric constant (8.85×10^{12} F/m). α and β are empirically determined coefficients of the capacitance proportion. The values of α and β in the case of air and FR-4 are 0.9 and 0.1, respectively [17]. ℓ_g is the length of the gap between all segment sidewalls, which is given by [18]

$$\ell_g = \begin{cases} 4(N-1)(r_a + r_b) + (w-g) + \sum\limits_{n=3}^{N} 8(n-2)(w+g), & N \geq 3 \\ 4(N-1)(r_a + r_b) + (w-g), & N = 2 \end{cases} \tag{4.22}$$

4.1.4 Series Resistance

From Fig. 4-4(a), PSCs have a series resistance R_s. The series resistance R_s is generally caused by the skin effect and the proximity effect or current crowding effect. The DC resistance R_{DC} of each conductive trace of a PSC [19] is given by

$$R_{DC} = \rho_c \frac{\ell_{S_i}}{w \cdot t} \tag{4.23}$$

where ρ_c is the resistivity of the conductor, w and t are the width and thickness of each trace respectively and ℓ_{S_i} is the length of each trace.

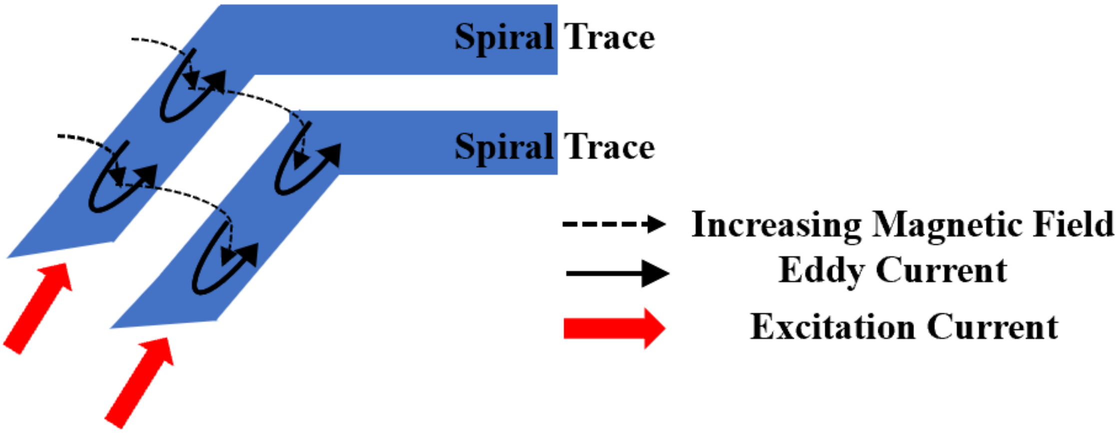

Fig. 4-5. Demonstration of the current crowding effect.

The skin effect [20] will increase the AC resistance of the PSC at high frequencies which can be calculated by

$$R_{skin} = R_{DC} \cdot \frac{t}{\delta(1-e^{-t/\delta})}, \delta = \sqrt{\frac{\rho_c}{\pi \mu_r \mu_0 f}} \tag{4.24}$$

where, δ is the skin depth, μ_0 is the permeability of free space ($4\pi \times 10^{-7}$ H/m) and μ_r is the relative permeability of the conductive material.

Current crowding caused by eddy currents should be taken into consideration above a critical frequency as they increase series resistance [21, 22]. These currents occur due to the magnetic fields external to the PSC or between adjacent traces of the

PSC. The direction of the eddy currents corresponds to an increasing magnetic field, which increases the effective resistance, as shown in Fig. 4-5. The series resistance including the effect of eddy currents [23] can be calculated by

$$R_{eddy} = \frac{1}{10} R_{DC} \left(\frac{\omega}{\omega_{crit}} \right)^2, \omega_{crit} = \frac{3.1}{\mu_0} \frac{w+g}{w^2} R_{sheet} \tag{4.25}$$

where, ω_{crit} is the angular frequency at which the current crowding begins to become significant and R_{sheet} is the conductive trace sheet resistance.

Consequently, if the eddy current needs to be considered, the total series resistance [24] can be given by

$$R_s = R_{skin} + R_{eddy} = \frac{\rho_c}{w \cdot t} \left[\frac{t}{\delta(1-e^{-t/\delta})} + \frac{1}{10} \left(\frac{\omega}{\omega_{crit}} \right)^2 \right] \sum_{i=1}^{4N} \ell_{S_i} \tag{4.26}$$

4.1.5 *Q*-Factor

The *Q*-factor, as an important parameter, is a measure of the loss of an inductor. According to the equivalent circuit, as shown in Fig. 4-4(a), the overall impedance (*Z*) and *Q*-factor [25] can be given by

$$Z = \frac{R_s + j\omega L_s}{1 - \omega^2 L_s C_p + j\omega R_s C_p} \tag{4.27}$$

$$\begin{aligned} Q = \frac{\mathrm{Im}(Z)}{\mathrm{Re}(Z)} &= \frac{\omega L_s - \omega C_p \left(\omega^2 L_s{}^2 - R_s{}^2 \right)}{R_s} \\ &\approx \frac{\omega L_s}{R_s} \quad \left(for\ small\ C_p\ or\ low\ \ frequency \right) \end{aligned} \tag{4.28}$$

Equation (4.28) shows that the *Q*-factor increases as R_s decreases, in other words lower loss implies a higher *Q*-factor. In order to obtain a PSC with high *Q*-factor, one of the techniques is to decrease resistance.

4.2 Design of a Rectangular Printed Spiral Coil

It is easy to design a PSC with a large inductance and high *Q*-factor at low frequencies (<100 MHz), however, few works are related to coils printed on PCB in the sub-GHz region (100 ~ 960 MHz). This is likely because a PSC becomes capacitive rather than inductive at higher frequencies. To design a rectangular PSC with inductive characteristics at high frequency, the effects of the parameters of the rectangular PSC need to be investigated.

4.2.1 Parameters Analysis

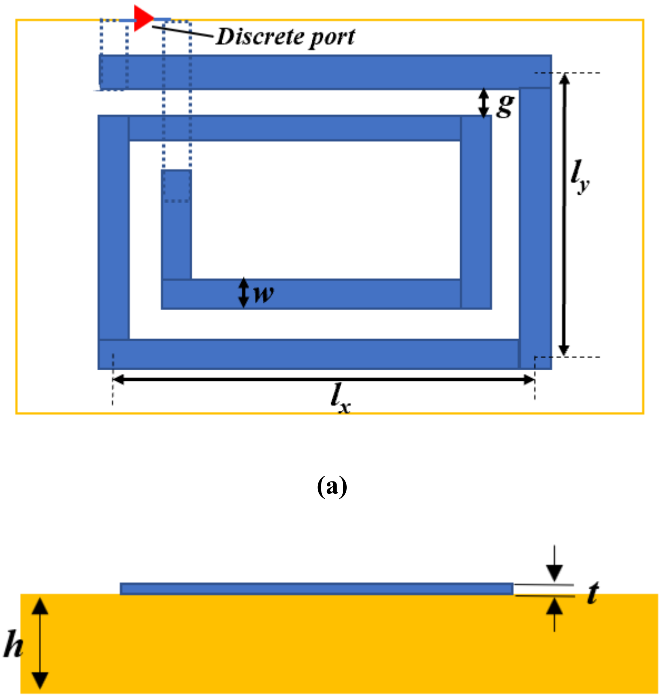

(a)

(b)

Fig. 4-6. Geometrical parameters of a rectangular PSC on the substrate (a) Top view (b) Side view.

The geometrical parameters of a rectangular planar coil printed on FR-4 substrate (ε_r=4.4) are shown in Fig. 4-6. Prior to any optimisation the initial parameters for the design were chosen as follows: the thickness of the copper trace t = 0.035 mm, the thickness of the substrate h = 1.5 mm, the width of the copper trace w = 1.0 mm, the gap between two copper traces g = 0.5 mm, the number of turns N = 2, length in the x-axis l_x = 20 mm and the length in the y-axis l_y = 15 mm. All optimisations were made by means of full-wave simulations performed using the transient solver of Computer Simulation Technology (CST) Microwave Studio.

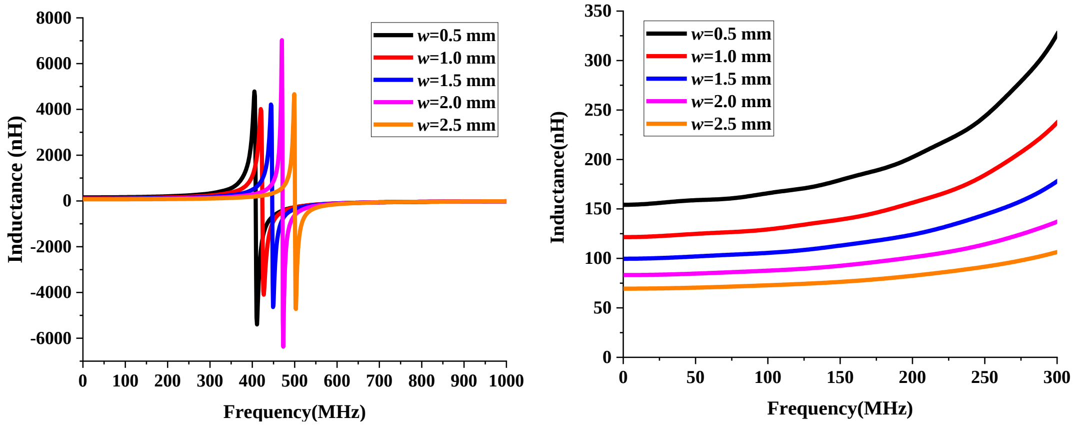

(a) **(b)**

Fig. 4-7. Simulated inductance of a rectangular PSC in different values of the parameter *w* (a) with the range of 1 GHz; (b) with the range of 0.3 GHz.

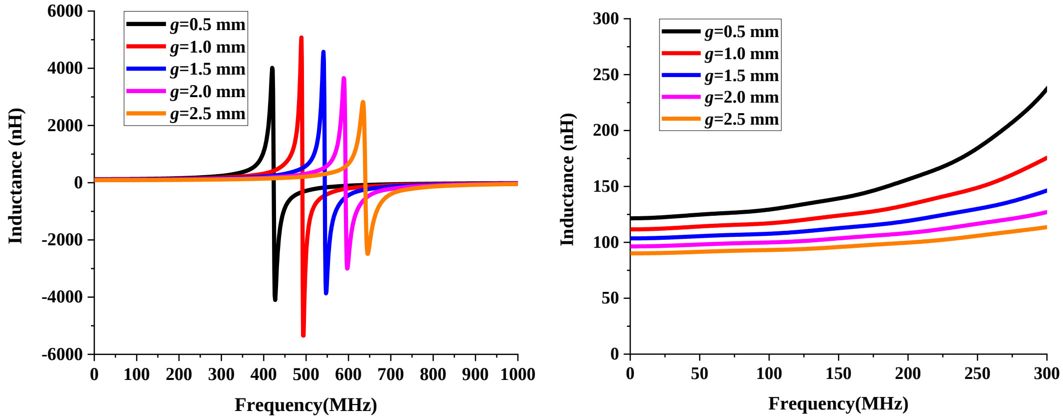

(a) **(b)**

Fig. 4-8. Simulated inductance of a rectangular PSC in different values of the parameter *g* (a) with the range of 1 GHz; (b) with the range of 0.3 GHz.

Firstly, the parameter *w* and *g* were individually swept as 0.5 mm, 1.0 mm, 1.5 mm, 2 mm and 2.5 mm to investigate their effects on the inductance of the PSC. The results of sweeping each parameter *w* and *g* on inductance are shown in Fig. 4-7 and Fig. 4-8, respectively.

In both cases looking at the inductance against frequency plots Fig. 4-7(a) and Fig. 4-8(a) the trend shows that the PSC begins as inductive (on the positive side of the *y*-axis) until it reaches the self-resonant point. Then the PSC becomes capacitive in nature (on the negative side of the *y*-axis).

It is worth noting from Fig. 4-7 that the inductance varies with frequency and the self-resonant frequency of the rectangular PSCs increases with the width of each conductive trace. The inductance changes gradually at lower frequencies and at a given frequency, the inductance is inversely proportional to the width of each conductive trace *w*.

Similarly, from Fig. 4-8 it can be seen that the self-resonant frequency is proportional to parameter *g*. Also, inductance increases as the values of the parameter *g* decrease, at a given frequency. Comparatively, parameter *g* is seen to have a greater influence on the self-resonant frequency than parameter *w* whereas parameter *g* has a smaller influence on inductance than parameter *w*.

Secondly, the parameters l_x and l_y were individually swept through 5 mm, 10 mm, 15 mm, 20 mm and 25 mm to investigate their effects on the inductance and self-resonance of the rectangular PSC. The plots of inductance against frequency for the sweep in l_x and l_y are shown in Fig. 4-9 and Fig. 4-10, respectively.

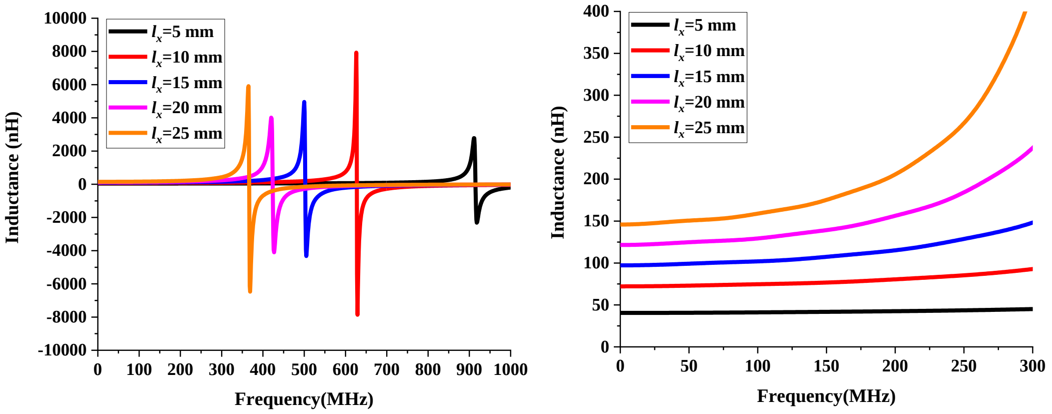

(a) **(b)**

Fig. 4-9. Simulated inductance of a rectangular PSC in different values of the parameter l_x (a) with the range of 1 GHz; (b) with the range of 0.3 GHz.

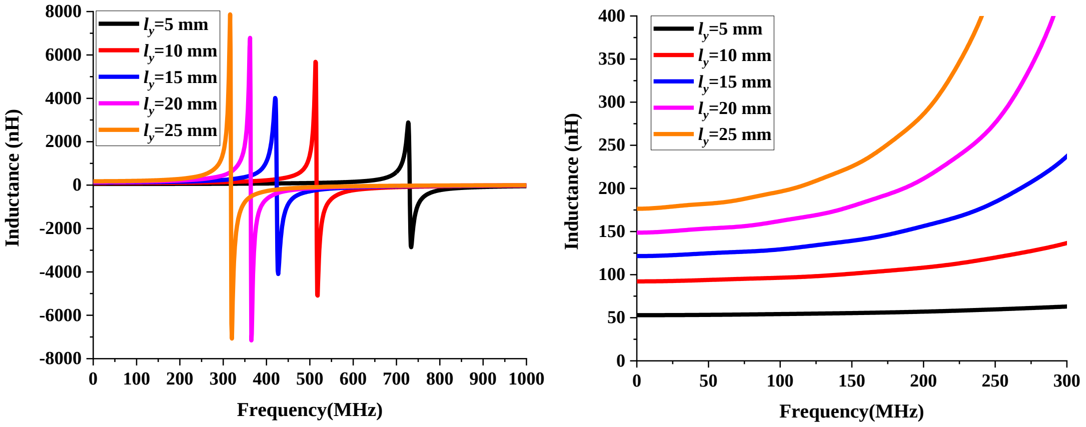

(a) **(b)**

Fig. 4-10. Simulated inductance of a rectangular PSC in different values of the parameter l_y (a) with the range of 1 GHz; (b) with the range of 0.3 GHz.

As can be seen in Fig. 4-9 and Fig. 4-10, the size of the rectangular PSC has a great influence on its inductance. Inductance increases at lower frequencies with increasing l_x and l_y, which also results in reducing self-resonant frequencies. Only when the parameter l_x is below 20 mm, can the PSC present as inductive around 400 MHz. Similarly, if the parameter l_y is bigger than 15 mm, the PSC presents as capacitive not inductive.

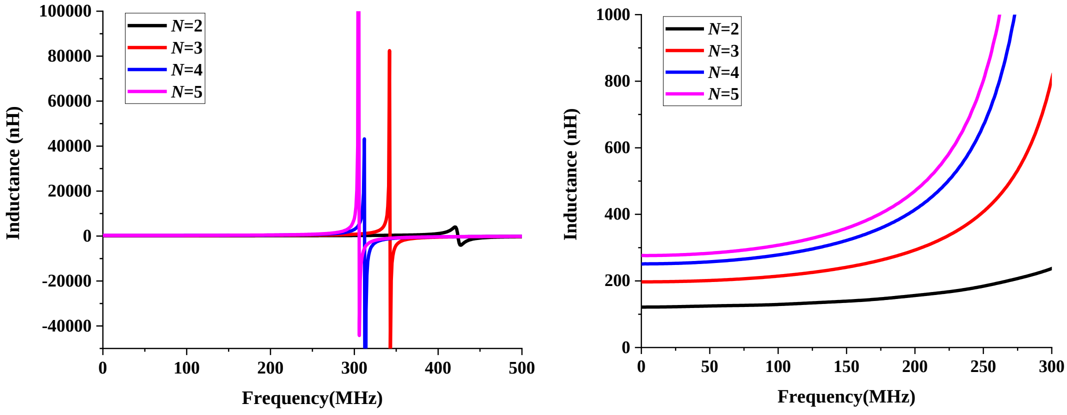

(a) **(b)**

Fig. 4- 11. Simulated inductance of a rectangular PSC in different turns N (a) with the range of 0.5 GHz; (b) with the range of 0.3 GHz.

Thirdly, the number of turns (N) was varied as 2, 3, 4, and 5 to investigate its effect on the inductance and self-resonance of the rectangular PSC. Fig. 4-11 shows the plots of inductance against frequency for varying turn number. It can be seen from Fig. 4-11 that the rate of change of inductance increases as the number of turns increases and the maximum inductance significantly increases as the number of turns increases from 3 to 5. The self-resonant frequencies become lower with the increasing turn number. Only when the number of turns is 2, does the PSC present as inductive around 400 MHz.

In summary, all parameters investigated have an influence on the inductance and self-resonant frequency. The parameters of w and g are inversely proportional to the inductance at frequencies lower than the self-resonant point and are proportional to the self-resonant frequency. However, the parameters l_x, l_y and N are proportional to the inductance at frequencies below the self-resonant point and inversely proportional to the self-resonant frequency. Importantly, increasing the number of turns is the most effective way of increasing the inductance of the PSC as long as the frequency is lower than the self-resonant frequency.

4.2.2 Design of a Rectangular PSC

Based on the parameteric analysis in the previous section and fabrication limitations, an optimised rectangular PSC with two turns working at 403 MHz was manufactured as shown in Fig. 4-5. The final values of the parameters are listed in Table 4-1. To minimise the dimensions of the rectangular PSC, the width of each conductive trace and the gap between two adjacent conductive traces were decreased to make the inductance increase. Also, the length of the outer conductive trace was decreased to increase the self-resonant frequency and make the rectangular PSC present as inductive at 403 MHz. This rectangular PSC was printed on FR-4 substrate with a size of 20 mm×18 mm×1.5 mm.

The trends of inductance, resistance and Q-factor of the optimised rectangular PSC are shown in Fig. 4-12 and Fig. 4-13. The inductance of the optimised rectangular PSC increases with frequency, gradually at first, then exponentially rises as to its maximum then suddenly drops as zero at the self-resonant frequency. Above this frequency the PSC presents as capacitive. Furthermore, the parasitic resistance changes are small at low frequencies and high frequencies, only becoming significant around the self-resonant frequency where it reaches its peak. The inductance, parasitic resistance and

Q-factor of the optimised rectangular PSC at 403 MHz are 106 nH, 1.91 Ω and 140 respectively. In this case, the optimised rectangular PSC can be used as an inductor in a WPT system operating at 403 MHz.

Table 4-1: Final parameter values of a rectangular PSC

Parameters	w	g	l_x	l_y	N
Values (mm)	0.48	0.17	10	8	2

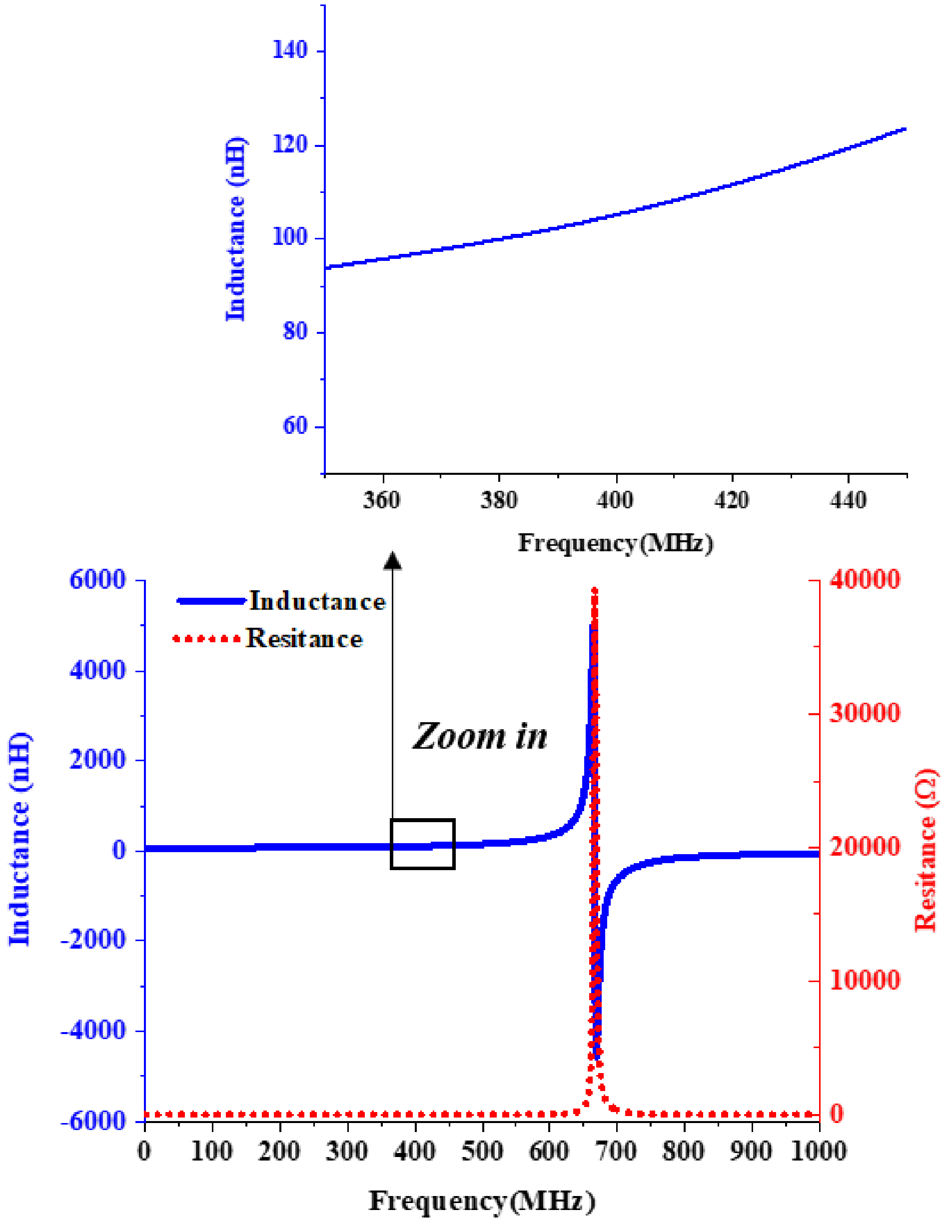

Fig. 4-12. Simulated inductance and resistance of the optimised rectangular PSC.

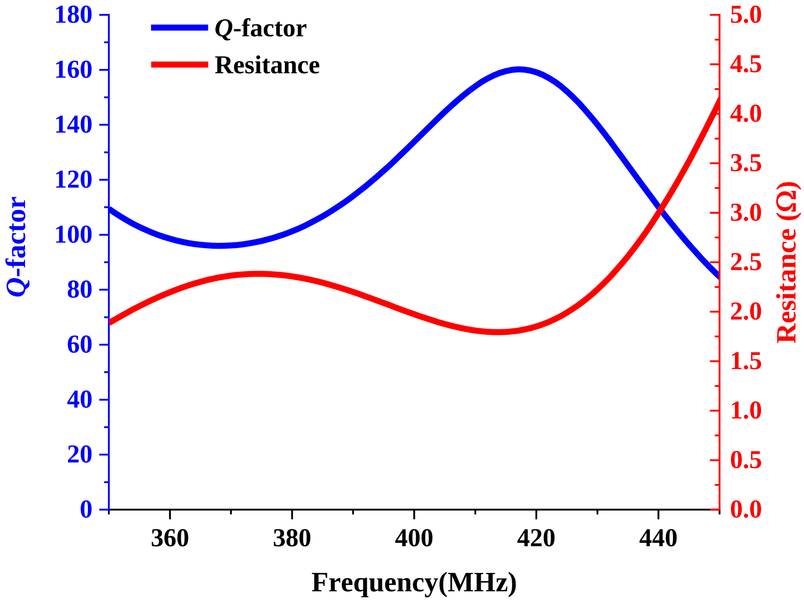

Fig. 4-13. Simulated *Q*-factor and resistance of the optimised rectangular PSC.

4.3 Performance of Rectangular Printed Spiral Coils for Wireless Power Transfer

4.3.1 Performance of Wireless Power Link

Based on the work in Chapter 3 the most practical WPT topology choice is to have a series primary circuit and select the secondary circuit dependent on the load impedance. In this chapter, the designed inductor has an inductance of 106 nH therefore to reach a resonance frequency of 403 MHz a 1.5 pF capacitance is required. Based on this, if the load impedance is larger than 270 Ω, a parallel secondary circuit for WPT should be used. The load impedance of a typical pacemaker is usually larger than 500 Ω [26]. Therefore, the choice of topology for MRC-WPT in this work is series-primary and parallel-secondary (SP). The schematic of the circuit is shown in Fig. 4-14(a). Inductors (L_s and L_p) represent two rectangular PSCs. Resistors (R_s and R_p) represent the parasitic resistances of the rectangular PSCs. Capacitors (C_s and C_p) represent compensation capacitors used to form resonators with the inductors. U_s represents the voltage source. R_{sc} and R_L represent the source resistance and the impedance of the load, respectively.

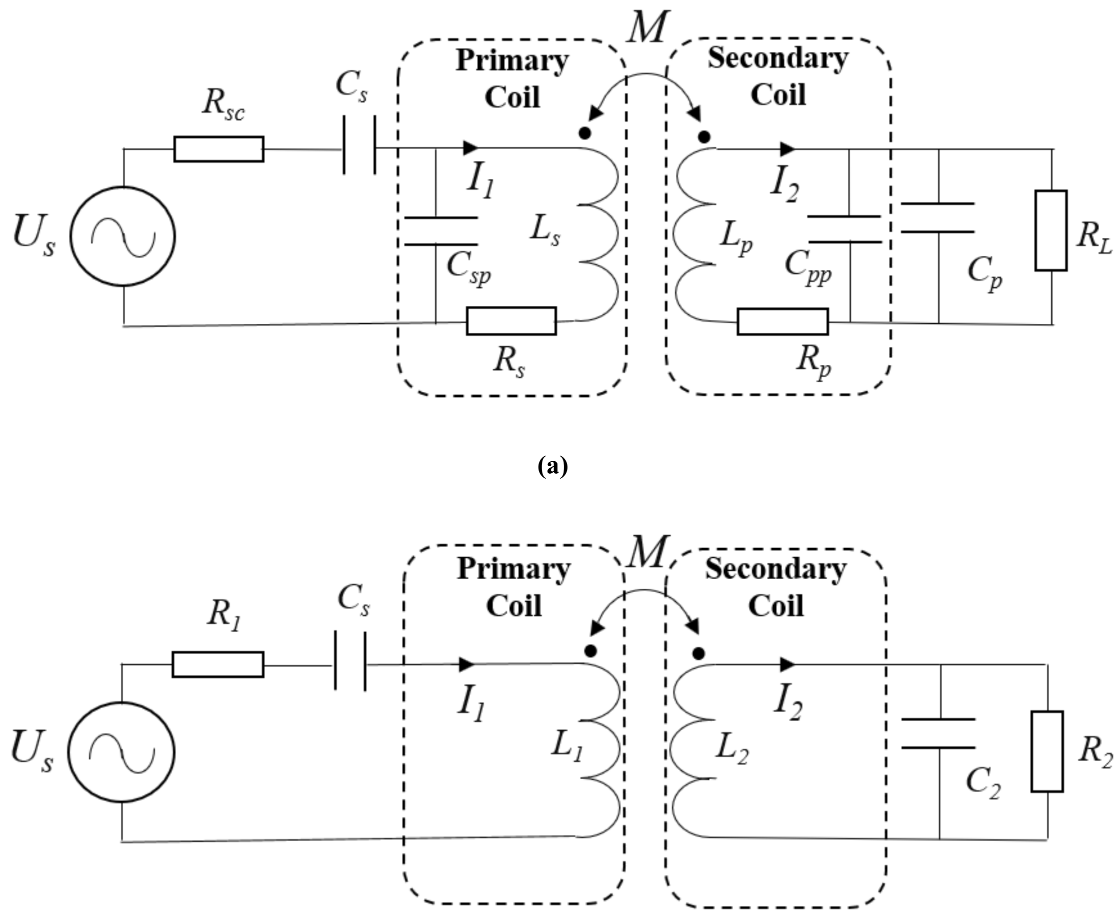

(a)

(b)

Fig. 4-14. (a) Original schematic series-primary and parallel-secondary circuit of MRC-WPT; (b) Schematic after equivalent transformation and parallel-to-series conversion.

The primary coil with a parallel parasitic capacitor and a series parasitic resistor can be transformed into an inductor (L_1) and a series resistor (R_e). In this case, the inductance and resistance [27] can be expressed by

$$L_1 = \frac{L_s - \omega^2 L_s C_{sp} - \omega^2 L_s^{\,2} C_{sp}}{1 + \omega^2 C_{sp}^{\,2}\left(R_s^{\,2} + \omega^2 L_s^{\,2}\right) - 2\omega^2 L_s C_{sp}} \tag{4.29}$$

$$R_e = \frac{R_s}{1 + \omega^2 C_{sp}^{\,2}\left(R_s^{\,2} + \omega^2 L_s^{\,2}\right) - 2\omega^2 L_s C_{sp}} \tag{4.30}$$

For the secondary coil, a narrowband approximation [28] can be used to make a parallel-to-series conversion from Fig. 4-14(a) to Fig. 4-14(b). The error caused by this approximation is negligible. According to [29]:

$$L_2 = L_p\left(1+\frac{1}{{Q_p}^2}\right) \approx L_p, \qquad Q_p = \frac{\omega L_p}{R_p} \tag{4.31}$$

$$R_{p2} = R_p\left(1+{Q_p}^2\right) \approx \frac{\omega^2 {L_p}^2}{R_p}, \qquad Q_p = \frac{\omega L_p}{R_p} \tag{4.32}$$

$$C_2 = C_{pp} + C_p \tag{4.33}$$

The equivalent resistance of the primary and secondary circuit can be calculated by

$$R_1 = R_{sc} + R_e \tag{4.34}$$

$$R_2 = R_L \| R_{p2} = \frac{R_L R_{p2}}{R_L + R_{p2}} \tag{4.35}$$

In Fig. 4-14(b), according to dot convention [30] between the primary coil and the secondary coil, two equations for the input voltage and current in the frequency domain can be written as

$$\left(R_1 + \frac{1}{j\omega C_s} + j\omega L_1\right)\mathbf{I}_1 - j\omega M\mathbf{I}_2 = \mathbf{U}_s \tag{4.36}$$

$$\left(j\omega L_2 + \frac{R_2}{1+j\omega C_2 R_2}\right)\mathbf{I}_2 - j\omega M\mathbf{I}_1 = 0 \tag{4.37}$$

If

$$Z_1 = R_1 + \frac{1}{j\omega C_s} + j\omega L_1 \tag{4.38}$$

$$Z_2 = j\omega L_2 + \frac{R_2}{1+j\omega C_2 R_2} \tag{4.39}$$

Then the equivalent input impedance of this WPT circuit can be expressed by

$$Z_{in} = Z_1 + \frac{\omega^2 M^2}{Z_2} \tag{4.40}$$

Therefore, the reflected resistance from secondary side to the primary side can be determined by

$$R_{reflect} = \mathrm{Re}\left(\frac{\omega^2 M^2}{Z_2}\right) = \frac{\omega^2 M^2 R_2}{\omega^2 L_2{}^2 + (1-\omega^2 L_2 C_2) R_2{}^2} \tag{4.41}$$

The PTE is defined as the power received by the load divided by the power provided by the source. Since reactive components do not dissipate power, the PTE can be expressed as

$$\begin{aligned} \eta &= \frac{R_{reflect}}{R_1 + R_{reflect}} \cdot \frac{R_{p2}}{R_L + R_{p2}} \\ &= \frac{\omega^2 M^2 R_2}{\omega^2 M^2 R_2 + \omega^2 L_2{}^2 R_1 + \left(1\text{-}\omega^2 L_2 C_2\right) R_1 R_2{}^2} \cdot \frac{R_{p2}}{R_L + R_{p2}} \end{aligned} \tag{4.42}$$

When ω reaches the resonance frequency $\omega_0 = 1\big/\sqrt{L_2 C_2} \approx 1\big/\sqrt{L_p C_2}$, the PTE reaches its maximum, which is expressed as

$$\eta = \frac{k^2 Q_1}{k^2 Q_1 + Q_2} \cdot \frac{R_{p2}}{R_L + R_{p2}} \tag{4.43}$$

where, *k* is the coupling coefficient of the coils [31], which is defined as

$$k = \frac{M}{\sqrt{L_1 L_2}} \tag{4.44}$$

Q_1 and Q_2 can be expressed as

$$Q_1 = \frac{\omega L_1}{R_1} \tag{4.45}$$

$$Q_2 = \frac{\omega L_2}{R_2} \tag{4.46}$$

Two identical optimised rectangular PSCs, as designed in Section 4.2, are applied as the transmit and receive coils in an MRC-WPT system. The transfer distance (*d*) between the PSCs is set at 10 mm. A relative position of the system is shown in Fig. 4-15. To obtain maximum PTE at the resonant frequency, 403 MHz, two compensation capacitors of 1.5 pF are used to constitute the WPT circuit. All simulations were made by means of full-wave simulations performed using the transient solver of Computer Simulation Technology (CST) Microwave Studio. The WPT circuit can be constructed in the schematic of CST allowing the performance of the WPT link to be simulated.

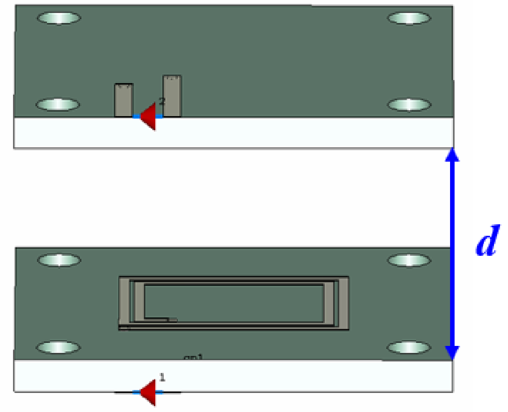

Fig. 4- 15. Relative position of two identical optimised rectangular PSC as TX and RX for WPT.

To find the optimal load for WPT in the SP topology, the PTE for different load impedances was simulated; the results are shown in Fig. 4-16. It can be seen that at the resonance frequency, the PTE increases and then drops off as the load impedance changes from 100 Ω to 3000 Ω. When the load impedance is lower than 1000 Ω, the PTE at the resonant point rises rapidly from 18.75% to 80.8%. Whereas, when the load impedance increases from 1000 Ω to 3000 Ω, the PTE decreases slowly from 80.8% to 65.96%. Therefore, a load impedance of 1000 Ω is used in this WPT circuit.

Furthermore, to investigate the effect of transfer distance on the performance of the wireless power link, the transfer distance was varied as 5 mm, 10 mm, 15 mm and 20 mm, the results of which are shown in Fig. 4-17. It is clear to see that the PTE at the resonant frequency decreases dramatically from 87.7% to 6.65% as the transfer distance increases from 5 mm to 20 mm. This is due to the relationship between distance and the coupling coefficient which is inversely proportional to the square of the transfer distance. Therefore, the transfer distance has a significant influence on the PTE.

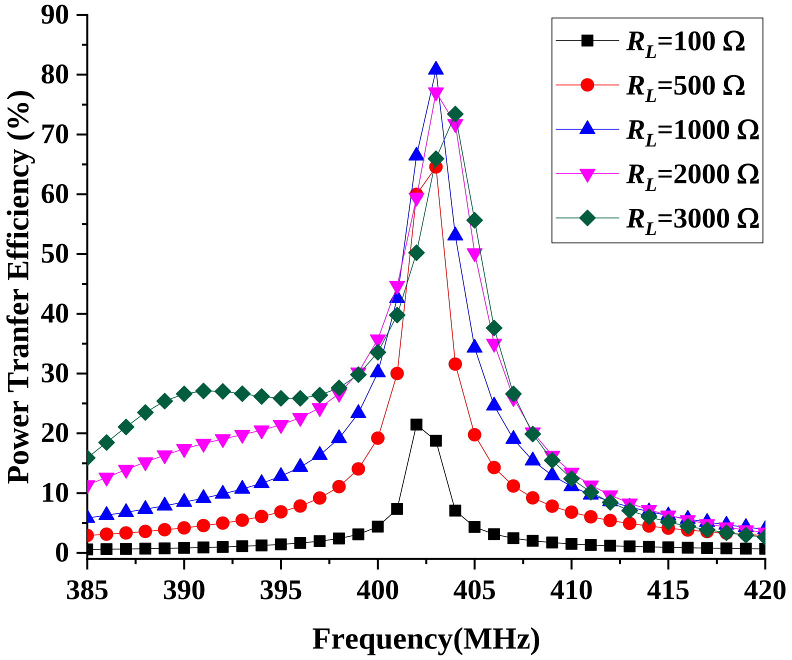

Fig. 4-16. Simulated PTE with difference load impedances.

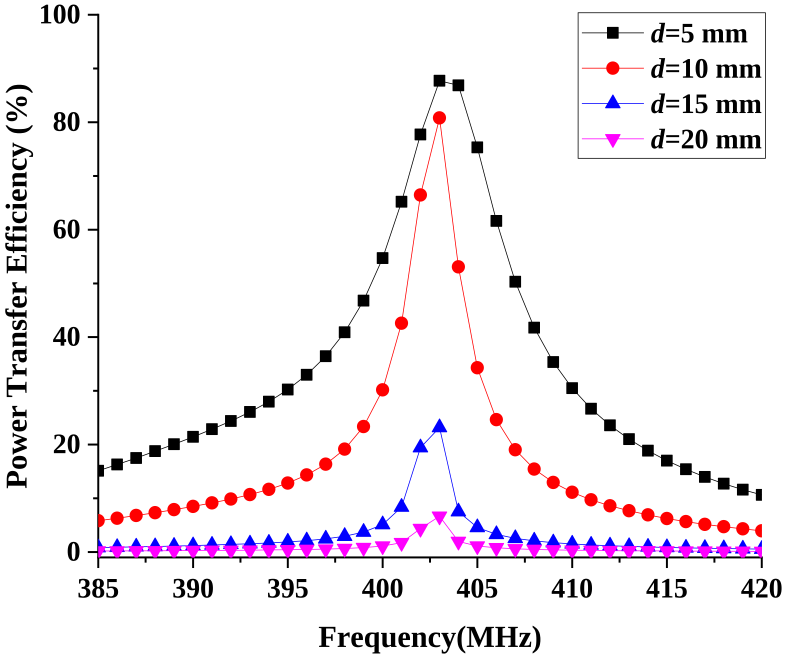

Fig. 4-17. Simulated PTE with difference transfer distances.

4.3.2 Measurement Results

The proposed wireless power link was fabricated on FR-4 substrate as shown in Fig. 4-18 using a PCB milling machine. The transmitting rectangular PSC with a series 1.5 pF chip capacitor was directly soldered with subminiature version A (SMA) connectors and then connected to a signal generator by using a circulator to mitigate reflection loss. The receiving rectangular PSC with a parallel 1.5 pF chip capacitor and parallel 1 kΩ chip resistor (load) was soldered directly to copper wire, to allow direct connection to an oscilloscope probe. It can be seen from the figure there are some holes at the corners of the substrate. These are used together with some plastic fixtures to support and separate the coupling PSCs during testing. The measurement setup includes an oscilloscope, a signal generator and a circulator, which can be seen from Fig. 4-19. The separation of this wireless power link is 5 mm.

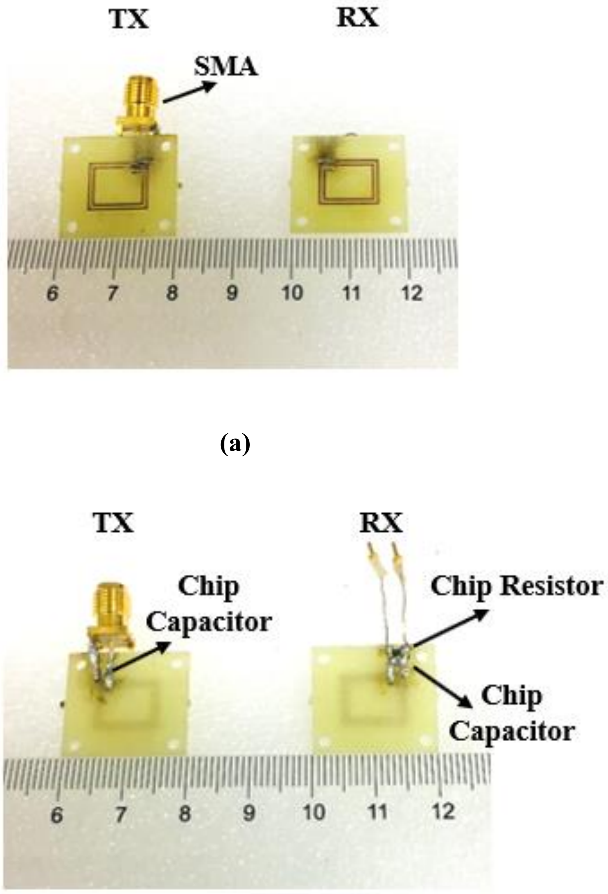

(a)

(b)

Fig. 4-18. Fabricated rectangular transmitting and receiving PSCs (a) Top view; (b) Back view.

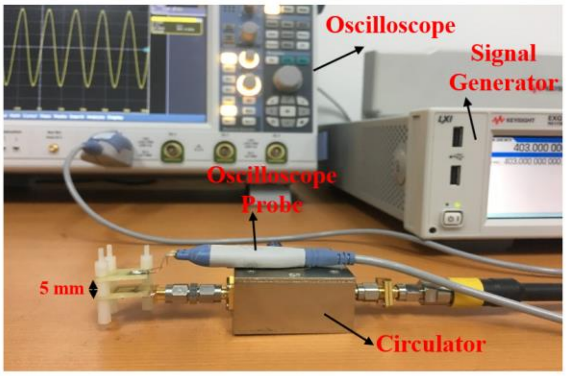

Fig. 4-19. Measurement setup of wireless power link with rectangular PSCs.

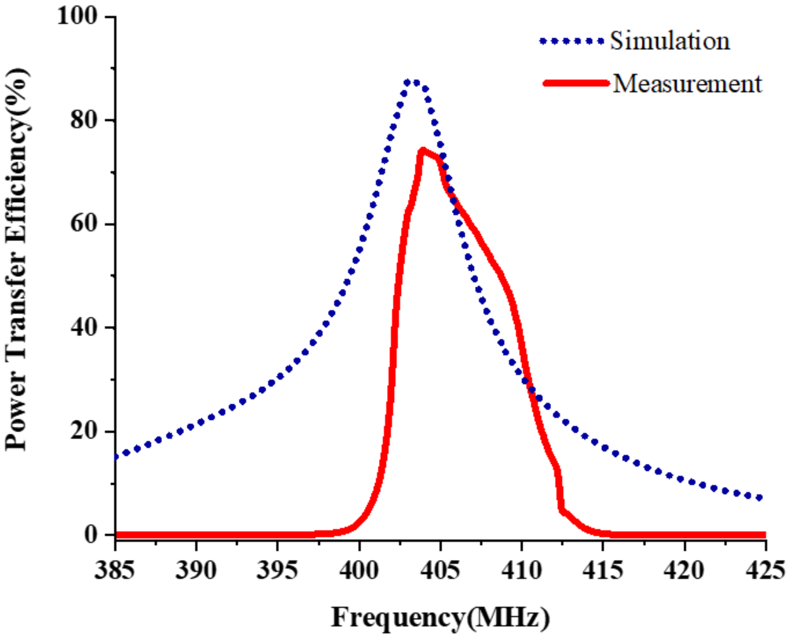

Fig. 4-20. Simulated and measured PTE of wireless power link with rectangular PSCs.

The signal generator has an internal resistance of 50 Ω and is set supply to 0 dBm (1 mW), the frequency was varied from 385 MHz to 425 MHz. The output voltage across the load can be measured directly by the RF oscilloscope. Then the measured PTE can be calculated using equation (3-27). The root mean square (RMS) of measured load voltage should be used to calculate the load power. The trend of measured PTE with as it varies with frequency is illustrated in Fig. 4-20. It is noticeable from Fig. 4-19 that the measured PTE reaches a peak of 74.4% at a transfer distance of 5 mm when the resonance frequency is 404 MHz, whereas the measured PTE is only 69.6% at 403 MHz. Compared with the simulation result, the resonant frequency in the measurement is shifted from 403 MHz to 404 MHz and the maximum PTE is lower than the simulated PTE of 87.7%. The reasons for this include the lower inductances of the PSCs caused by fabrication, chip capacitor tolerance, reduced coupling coefficient in a real environment and impedance losses incurred from the measurement equipment e.g. cable losses. Overall, the measured result shows agreement with the simulated result. The PTE climbs to a peak at the resonance frequency and deceases again.

4.4 Summary

In this chapter, the theoretical analysis of a normal rectangular PSC has been investigated including inductance, mutual inductance, parasitic capacitance, series resistance and Q-factor. The effect of varying the geometric parameters of a normal rectangular PSC (width of trace, gap between two adjacent traces, dimensions and turns) on the inductance and self-resonance frequency was investigated to obtain a good understanding of their limitations and challenges. To obtain a rectangular PSC with inductive characteristic at 403 MHz, the rectangular PSC was optimised and provided a simulated PTE of 87.7% at a transfer distance of 5 mm.

The challenge is that the width of the rectangular PSC and its number of turns should be small enough while maintaining an inductive property at high frequency. However, smaller dimensions and lower turn numbers results in a smaller inductance, which in turn decreases mutual inductance and inductive area, which results in low PTE and a short power transfer distance. It also leads to lower resonant frequencies limiting the choice of operating frequency. Therefore, there is a need to design planar coils with a high Q-factor and inductive properties for WPT that can operate at higher frequencies to achieve higher power transfer or larger transfer distances than the rectangular PSCs can.

4.5 References

[1] A. K. RamRakhyani, S. Mirabbasi, and M. Chiao, "Design and Optimization of Resonance-Based Efficient Wireless Power Delivery Systems for Biomedical Implants," *IEEE Transactions on Biomedical Circuits and Systems,* vol. 5, no. 1, pp. 48-63, 2011, doi: 10.1109/TBCAS.2010.2072782.

[2] H. Hu and S. V. Georgakopoulos, "Multiband and Broadband Wireless Power

Transfer Systems Using the Conformal Strongly Coupled Magnetic Resonance Method," *IEEE Transactions on Industrial Electronics,* vol. 64, no. 5, pp. 3595-3607, 2017, doi: 10.1109/TIE.2016.2569459.

[3] S. Mao, H. Wang, Z-H Mao, M. Sun, "A double-helix and cross-patterned solenoid used as a wirelessly powered receiver for medical implants " *AIP ADVANCES* 2018, doi: https://doi.org/10.1063/1.5007236

[4] F. Jolani, Y. Yu, and Z. Chen, "A Planar Magnetically Coupled Resonant Wireless Power Transfer System Using Printed Spiral Coils," *IEEE Antennas and Wireless Propagation Letters,* vol. 13, pp. 1648-1651, 2014, doi: 10.1109/LAWP.2014.2349481.

[5] X. Li, C. Tsui, and W. Ki, "A 13.56 MHz Wireless Power Transfer System With Reconfigurable Resonant Regulating Rectifier and Wireless Power Control for Implantable Medical Devices," *IEEE Journal of Solid-State Circuits,* vol. 50, no. 4, pp. 978-989, 2015, doi: 10.1109/JSSC.2014.2387832.

[6] S. Hekal *et al.*, "Compact Wireless Power Transfer System Using Defected Ground Bandstop Filters," *IEEE Microwave and Wireless Components Letters,* vol. 26, no. 10, pp. 849-851, 2016, doi: 10.1109/LMWC.2016.2601300.

[7] H. Huang and T. Li, "A Spiral Electrically Small Magnetic Antenna With High Radiation Efficiency for Wireless Power Transfer," *IEEE Antennas and Wireless Propagation Letters,* vol. 15, pp. 1495-1498, 2016, doi: 10.1109/LAWP.2016.2514534.

[8] G. Sun, B. Muneer, Y. Li, and Q. Zhu, "Ultracompact Implantable Design With Integrated Wireless Power Transfer and RF Transmission Capabilities," *IEEE Transactions on Biomedical Circuits and Systems,* vol. 12, no. 2, pp. 281-291, 2018, doi: 10.1109/TBCAS.2017.2787649.

[9] A. Christ, M. Douglas, J. Nadakuduti, and N. Kuster, "Assessing Human Exposure to Electromagnetic Fields From Wireless Power Transmission Systems," *Proceedings of the IEEE,* vol. 101, no. 6, pp. 1482-1493, 2013, doi: 10.1109/JPROC.2013.2245851.

[10] B. Lee, M. Kiani, and M. Ghovanloo, "A Triple-Loop Inductive Power Transmission System for Biomedical Applications," *IEEE Transactions on Biomedical Circuits and Systems,* vol. 10, no. 1, pp. 138-148, 2016, doi: 10.1109/TBCAS.2014.2376965.

[11] C. Xiao, K. Wei, D. Cheng, and Y. Liu, "Wireless Charging System

Considering Eddy Current in Cardiac Pacemaker Shell: Theoretical Modeling, Experiments, and Safety Simulations," *IEEE Transactions on Industrial Electronics,* vol. 64, no. 5, pp. 3978-3988, 2017, doi: 10.1109/TIE.2016.2645142.

[12] Y. Zeng, D. Qiu, X. Meng, B. Zhang, and S. C. Tang, "Optimized Design of Coils for Wireless Power Transfer in Implanted Medical Devices," *IEEE Journal of Electromagnetics, RF and Microwaves in Medicine and Biology,* vol. 2, no. 4, pp. 277-285, 2018, doi: 10.1109/JERM.2018.2863955.

[13] A. S. Y. Poon, S. O. Driscoll, and T. H. Meng, "Optimal Frequency for Wireless Power Transmission Into Dispersive Tissue," *IEEE Transactions on Antennas and Propagation,* vol. 58, no. 5, pp. 1739-1750, 2010, doi: 10.1109/TAP.2010.2044310.

[14] H. Greenhouse, "Design of Planar Rectangular Microelectronic Inductors," *IEEE Transactions on Parts, Hybrids, and Packaging,* vol. 10, no. 2, pp. 101-109, 1974, doi: 10.1109/TPHP.1974.1134841.

[15] F. S. Sandoval, A. Moazenzadeh, and U. Wallrabe, "Comprehensive Modeling of Magnetoinductive Wave Devices for Wireless Power Transfer," *IEEE Transactions on Power Electronics,* vol. 33, no. 10, pp. 8905-8915, 2018, doi: 10.1109/TPEL.2017.2779606.

[16] Z. Duan, Y. X. Guo, and D. L. Kwong, "Rectangular coils optimization for wireless power transmission," (in English), *Radio Sci,* vol. 47, Jun 27 2012, doi: Artn Rs301210.1029/2011rs004970.

[17] L. W. Ritchey, "A survey and tutorial of dielectric materials used in the manufacture of printed circuit boards," 1999. [Online]. Available: https://speedingedge.com/PDF-Files/tutorial.pdf.

[18] R. Garg and I. J. Bahl, "Characteristics of Coupled Microstriplines," *IEEE Transactions on Microwave Theory and Techniques,* vol. 27, no. 7, pp. 700-705, 1979, doi: 10.1109/TMTT.1979.1129704.

[19] Y. Eo and W. R. Eisenstadt, "High-speed VLSI interconnect modeling based on S-parameter measurements," *IEEE Transactions on Components, Hybrids, and Manufacturing Technology,* vol. 16, no. 5, pp. 555-562, 1993, doi: 10.1109/33.239889.

[20] H. A. Wheeler, "Formulas for the Skin Effect," *Proceedings of the IRE,* vol. 30, no. 9, pp. 412-424, 1942, doi: 10.1109/JRPROC.1942.232015.

[21] J. Craninckx and M. S. J. Steyaert, "A 1.8-GHz low-phase-noise CMOS VCO using optimized hollow spiral inductors," *IEEE Journal of Solid-State Circuits,* vol. 32, no. 5, pp. 736-744, 1997, doi: 10.1109/4.568844.

[22] T. Huan-Shang *et al.*, "Investigation of current crowding effect on spiral inductors," in *1997 IEEE MTT-S Symposium on Technologies for Wireless Applications Digest*, 23-26 Feb. 1997 1997, pp. 139-142, doi: 10.1109/MTTTWA.1997.595129.

[23] W. B. Kuhn and N. M. Ibrahim, "Analysis of current crowding effects in multiturn spiral inductors," *IEEE Transactions on Microwave Theory and Techniques,* vol. 49, no. 1, pp. 31-38, 2001, doi: 10.1109/22.899959.

[24] R. K. Ulrich and L. W. Schaper, *Integrated Passive Component Technology*. Wiley, 2003.

[25] U. Jow and M. Ghovanloo, "Design and Optimization of Printed Spiral Coils for Efficient Transcutaneous Inductive Power Transmission," *IEEE Transactions on Biomedical Circuits and Systems,* vol. 1, no. 3, pp. 193-202, 2007, doi: 10.1109/TBCAS.2007.913130.

[26] "Rega SR 7102." [Online]. Available: http://www.chuang-ling.com/product/pdf?id=25.

[27] W. H. Hayt, J. K. Kemmerly, S. M. Durbin,, *Engineerring circuit analysis*. McGraw-Hill, 2012.

[28] K. M. Silay, C. Dehollain, and M. Declercq, "Improvement of power efficiency of inductive links for implantable devices," in *2008 Ph.D. Research in Microelectronics and Electronics*, 22 June-25 April 2008 2008, pp. 229-232, doi: 10.1109/RME.2008.4595767.

[29] T. H. Lee, "The design of CMOS radio-frequency integrated circuits, 2nd edition," *Communications Engineer,* vol. 2, no. 4, pp. 47-47, 2004.

[30] W. Zhang and C. C. Mi, "Compensation Topologies of High-Power Wireless Power Transfer Systems," *IEEE Transactions on Vehicular Technology,* vol. 65, no. 6, pp. 4768-4778, 2016, doi: 10.1109/TVT.2015.2454292.

[31] Y. H. Sohn, B. H. Choi, E. S. Lee, G. C. Lim, G. Cho, and C. T. Rim, "General Unified Analyses of Two-Capacitor Inductive Power Transfer Systems: Equivalence of Current-Source SS and SP Compensations," *IEEE Transactions on Power Electronics,* vol. 30, no. 11, pp. 6030-6045, 2015, doi: 10.1109/TPEL.2015.2409734.

Chapter 5 Planar Split-ring Loops for Wireless Power Transfer

In Chapter 4, a conventional planar rectangular spiral coil operating in the sub-GHz region was utilised in a wireless power transfer (WPT) system. Simulation and practical results showed that this type of coil could only provide a low power transfer efficiency (PTE) and operate over a short transfer distance due to its low inductance and small magnetic field area. To improve the PTE capability of these coils one option is to increase the coil *Q*-factor by minimising the resistive effects [1-3]. Increases in transfer distance could be achieved by enlarging the coil and hence the area of the magnetic field. In this chapter, 4-turn planar split-ring loops are proposed which have a high *Q*-factor. Conventional printed spiral coils (PSC) have an equivalent circuit of a parallel inductor-capacitor (LC), which means they can exhibit self-resonance. However, based on the work in Chapter 3, a parallel LC resonator is not suitable for use in the primary (transmit) side of a WPT system as it appears as an open circuit at resonance resulting in low system power. The planar split-ring loop designed here has a series LC circuit characteristic, which can therefore be used to form a series-primary, series-secondary magnetic resonance (MRC)-WPT system. The loops are designed to operate at 433 MHz in the Industrial Scientific and Medical (ISM) band. This design enhances the PTE and allows for a greater transfer distance in the Ultra High Frequency (UHF) band than achieved in Chapter 4.

Section 5.1 develops a split-ring loop with equivalent inductance but increased *Q*-factor compared to the rectangular PSC. In Section 5.2 the split-ring loop is further developed to provide the desired series LC characteristic for WPT. Both investigations involve simulation and practical verification.

5.1 4-turn Planar Split-ring Loops for Wireless Power Transfer

5.1.1 Design of A 4-turn Planar Printed Loop

To increase the *Q*-factor obtained for the PSC there are two main avenues to explore, firstly inductance can be increased and secondly resistance can be decreased. Increasing the number of turns of the PSC can significantly enhance the inductance, as was presented in Chapter 4. However, that also decreases the self-resonance frequency and results in a capacitive characteristic at higher frequencies including in the desired design frequency band (i.e. the UHF band). Therefore, decreasing resistance compared with that of the PSC is the first target.

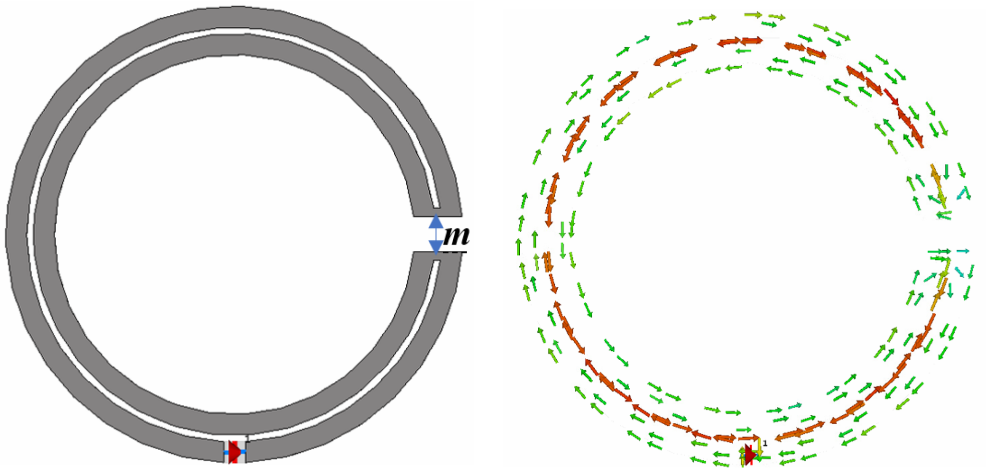

(a) **(b)**

Fig. 5-1. (a) Schematic of two connected split-ring loops; (b) Current distribution of the split-ring loop at 403 MHz.

In the PSC each conductive trace has the same current direction, which increases inductance but also increases the parasitic resistance due to eddy currents. Two split-ring loops with opposing current directions were connected to decrease the parasitic resistance, this is shown in Fig. 5-1(a). The split-ring loop was designed to operate at 403 MHz for direct comparison with the rectangular PSC and the following parameters used for the simulation: the width of each trace is 0.48 mm, the gap between the two conductive traces is 0.15 mm, the inner radius is 4.13 mm and the notch m = 1 mm. The substrate is FR-4 and has a thickness of 1.5 mm and overall size of 20 mm×20 mm.

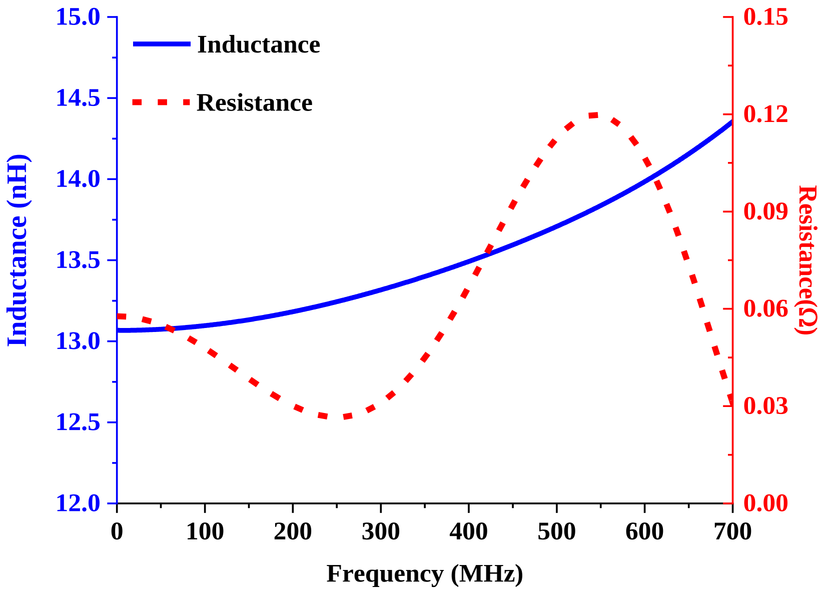

(a)

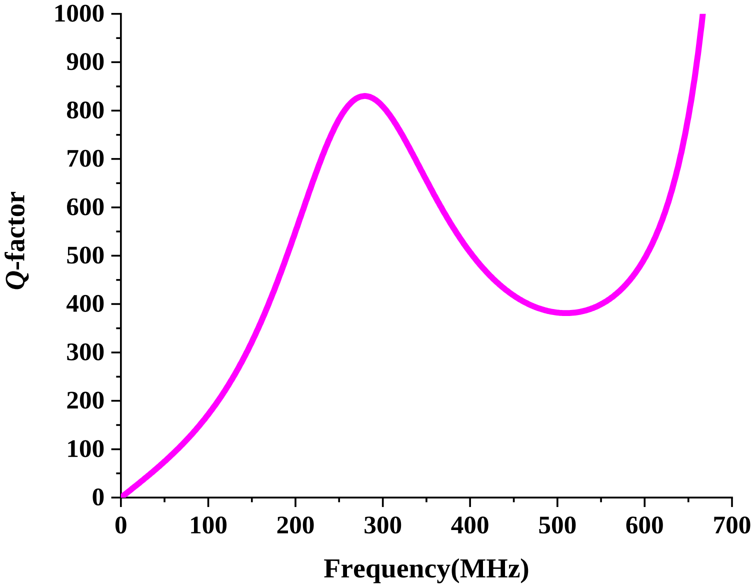

(b)

Fig. 5-2. Simulated (a) inductance and resistance and (b) *Q*-factor of this 2-turn split-ring loops.

The current distribution of this design is shown in Fig.5-1(b). It can be seen that the inner split-ring loop has an anti-clockwise current distribution, whilst the outer split-ring loop has a clockwise current distribution at 403 MHz.

The inductance and resistance of this design are shown in Fig.5-2(a) and the trend of the *Q*-factor with the varying frequency is presented in Fig. 5-2(b). From Fig. 5-

2(a), the inductance is 13.5 nH at 403 MHz, which is much lower than that of the rectangular PSC with 2 turns. However, the parasitic resistance is only 0.07 Ω as the eddy current effect has been reduced. This is significantly lower than that of the rectangular PSC. Consequently, the *Q*-factor increases significantly to 500, almost four times higher than that of the rectangular PSC.

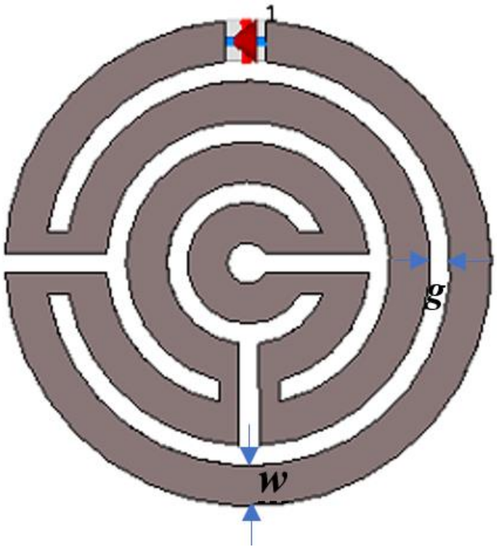

Fig. 5-3. Geometric schematic of 4-turn split-ring loop.

Now that the general split-ring loop design is shown to significantly reduce resistance and increase the *Q*-factor the aim is to increase the loop inductance again to match that of the rectangular PSC in Chapter 4, so that the effect of increasing the *Q*-factor on PTE can be seen directly. The increase in inductance is achieved by increasing the number of split-ring turns. A new design with 4 turns is shown in Fig. 5-3. The inner radius of the design is set at 1 mm. Design parameters have been swept with the aim of matching the inductance of the rectangular PSC (106 nH) at the design frequency.

Parameter *w* has been varied as 2 mm, 3 mm, 4 mm, and 5 mm (with the gap *g* = 1 mm). The parameter *g* has been varied as 0.5 mm, 1 mm, 1.5mm and 2 mm (with the width *w* = 2 mm). The inductance obtained for each sweep is shown in Fig. 5-4.

From both Fig. 5-4(a) and (b), the self-resonance frequency of the design decreases as either parameter *w* or parameter *g* increases. That said for all parameter values observed the loop presents as inductive at 403 MHz. Only when parameter *w* is 3 mm is the inductance of this design close to that of the rectangular PSC at 403 MHz, 106 nH.

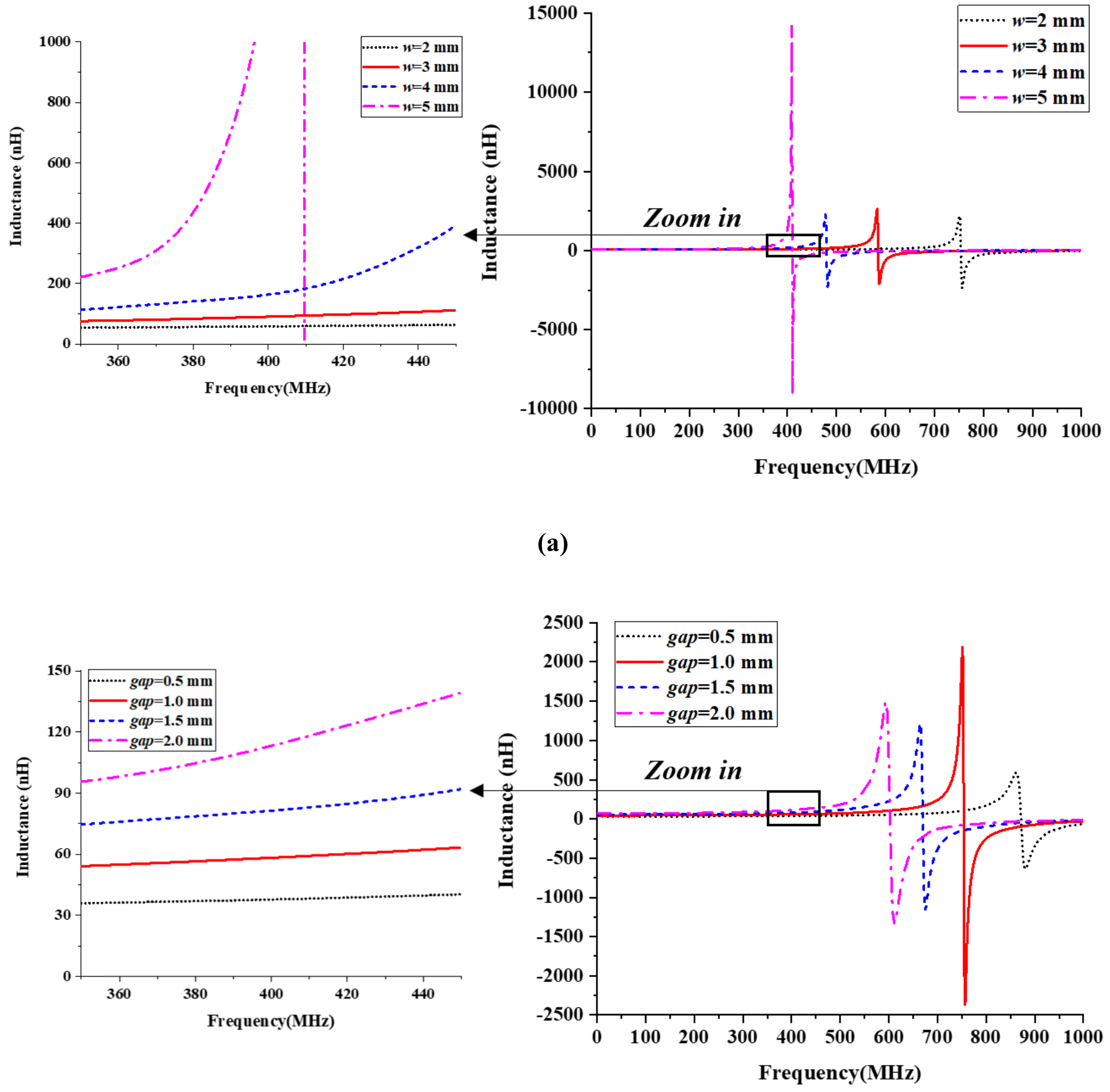

(a)

(b)

Fig. 5-4. Simulated inductance of 4-turn split-ring loops with (a) swept parameter *w* (with the gap *g*=1 mm); (b) swept parameter *g* (with the width *w*=2 mm).

Table 5-1: Final dimensions of the optimised proposed split-ring loops

Parameters	*w1*	*w2*	*w3*	*w4*	*g1*	*g2*	*g3*	*m*
Value(mm)	3.8	3.4	3.4	5.0	0.8	0.8	0.5	1.0

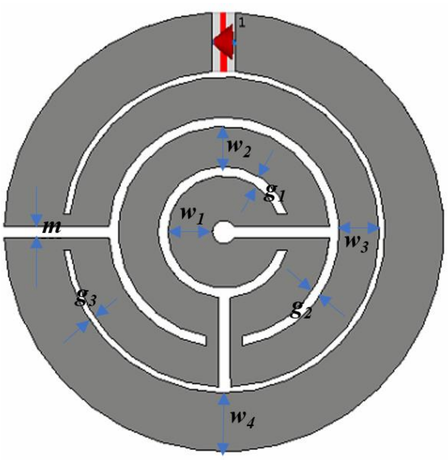

Fig. 5-5. Geometric layout model of the optimised 4-turn split-ring loop.

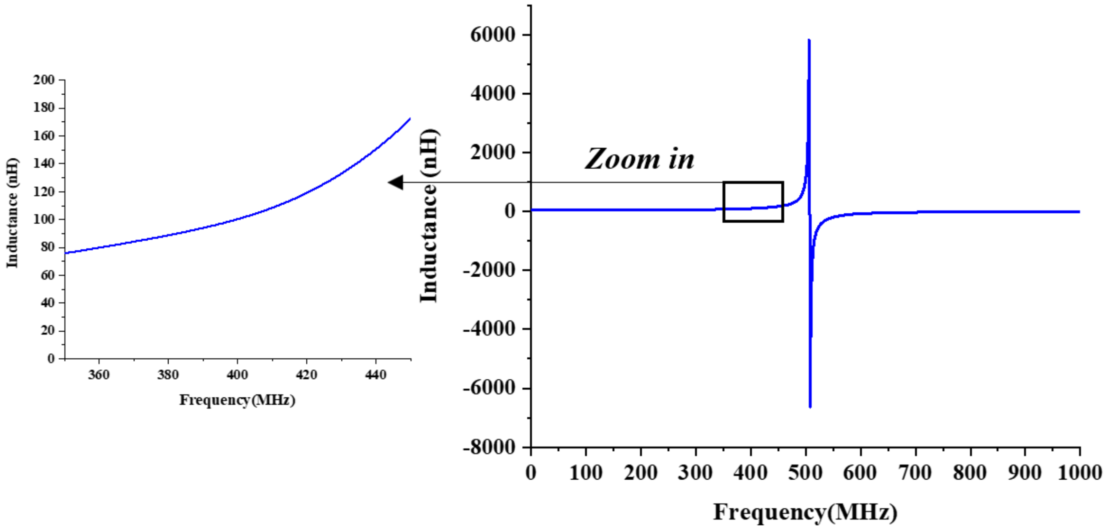

Fig. 5-6. Simulated inductance of the optimised 4-turn split-ring loop.

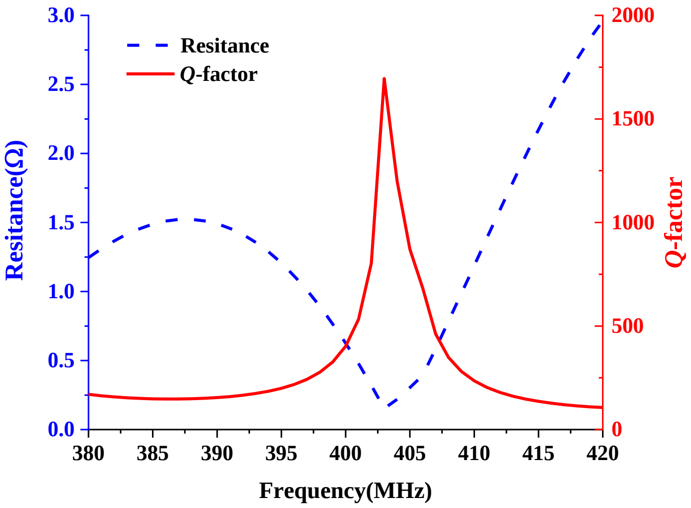

Fig. 5-7. Simulated parasitic resistance and *Q*-factor of the optimised 4-turn split-ring loop.

To obtain an inductance closer to 106 nH, the width of each conductive split-ring loop and each gap have been further optimised. The geometric layout model of this proposed 4-turn split-ring loop is illustrated in Fig. 5-5. The split-ring loop is printed on 1.5 mm FR-4 substrate with an area of 43 mm×43 mm. Details of the final optimised parameters are provided in Table 5-1. All optimisations were made by means of full-wave simulations performed using the transient solver of Computer Simulation Technology (CST) Microwave Studio.

From Fig. 5-6 and Fig. 5-7 the self-resonance frequency is around 500 MHz and the inductance and resistance at 403 MHz are 103 nH and 0.16 Ω respectively. The Q-factor of this loop is 1630 at 403 MHz, which is much greater than that of the rectangular PSC.

5.1.2 Performance of 4-turn Planar Split-ring Loops for Wireless Power Transfer

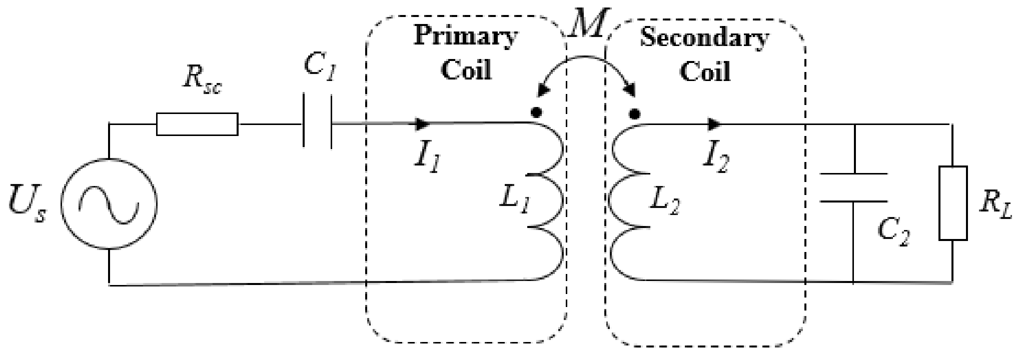

Fig. 5-8. Equivalent WPT circuit by using 4-turn split-ring loops.

To investigate the performance of a wireless power link between two of the proposed 4-turn planar split-ring loops, two compensation capacitors are necessary to match the WPT circuit between source and load. The SP topology for MRC-WPT is used, as shown in Fig. 5-8. Inductors (L_1 and L_2) represent two identical split-ring loops. Parasitic resistance and capacitance are considered negligible in this case for the simplicity of simulation and measurement. Capacitors (C_1 and C_2) are chosen to be 1.52 pF to obtain a resonance frequency of 403 MHz. U_s represents the voltage source. R_{sc} and R_L represent the source resistance and the load impedance of 1 kΩ, respectively. All simulations were made by means of full-wave simulations performed using the transient solver of Computer Simulation Technology (CST) Microwave Studio. The WPT circuit can be constructed in the schematic of CST allowing the performance of the WPT link to be simulated.

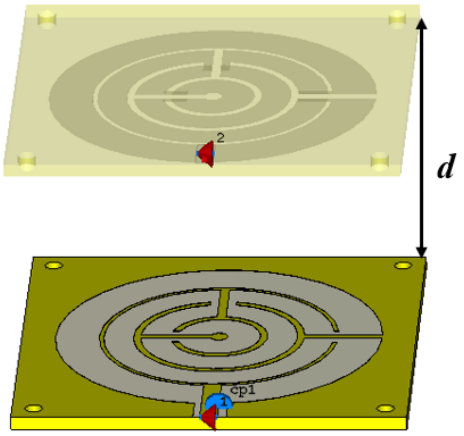

Fig. 5-9. Schematic of wireless power link with proposed 4-turn split-ring loops.

An overview of the transmit and receive loops is shown in Fig. 5-9 and the transfer distance (*d*) between the loops is varied as 5 mm, 10 mm, 15 mm, 20 mm, 25 mm and 30 mm. The trends of PTE at different transfer distances are depicted in Fig. 5-10.

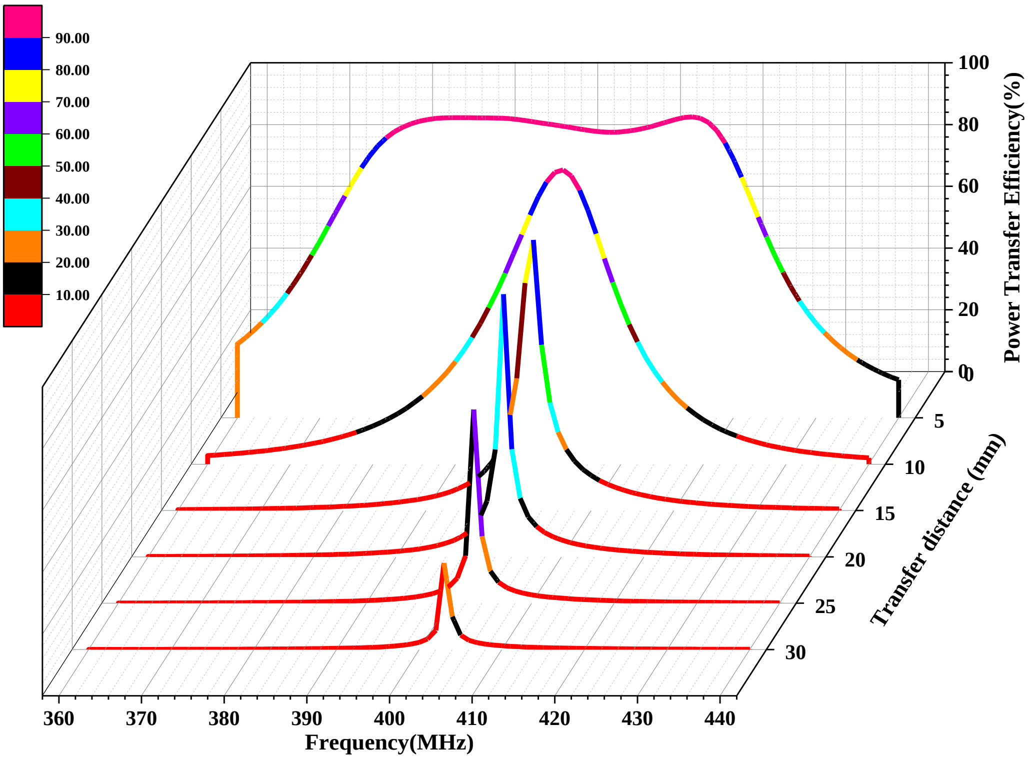

Fig. 5-10. Simulated PTE at different transfer distance by using 4-turn planar split-ring loops.

It is can be seen from Fig. 5-10 that the PTE at the resonance frequency of 403 MHz decreases as the transfer distance enlarges. At a transfer distance of 5 mm, the PTE is over 90% from 377 MHz to 419 MHz since the magnitude of the equivalent input impedance is close to 50 Ω over this range. However, the resonance frequency, where the imaginary part of the input impedance is equal to zero, is not 403 MHz, which means the transfer distance of 5 mm is not the optimal transfer distance. As the transfer distance becomes larger, only one resonance frequency appears, located at 403 MHz, where the PTE reaches its peak. The maximum PTE is 95.3% at a transfer distance of 10 mm and then decreases dramatically to 28% at a transfer distance of 30 mm. Importantly, the PTE is 85.1% at a transfer distance of 20 mm, which is similar to that obtained in Chapter 4 for the WPT link using traditional rectangular PSCs at a transfer distance of 5 mm. This means the performance of the WPT link with 4-turn planar split-ring loops can operate over a larger distance with the same efficiency, due to the significantly improved *Q*-factor. However, it is also important to highlight that the operating bandwidth is narrower than that of the traditional rectangular PSC again as a result of the increased *Q*-factor. Therefore, there exists a trade-off between bandwidth and power transfer distance through manipulation of the *Q*-factor.

5.1.3 Measurements

The proposed wireless power link was fabricated on FR-4 substrate as shown in Fig. 5-11 using a PCB milling machine. The transmitting split-ring loop with a series chip capacitor (1.52 pF) is directly soldered with a subminiature version A (SMA) connector. This is connected to an RF signal generator via a circulator to mitigate reflection loss. The receiving split-ring loop with parallel chip capacitor (1.52 pF) and parallel chip resistor (1 kΩ load) is soldered directly to copper wire, to allow direct connection to the probe of an RF oscilloscope. The holes at the corners of the substrate are to allow for plastic support fixtures to hold the boards in place during measurement. The measurement setup can be seen in Fig. 5-12. The separation of the wireless power link is 20 mm.

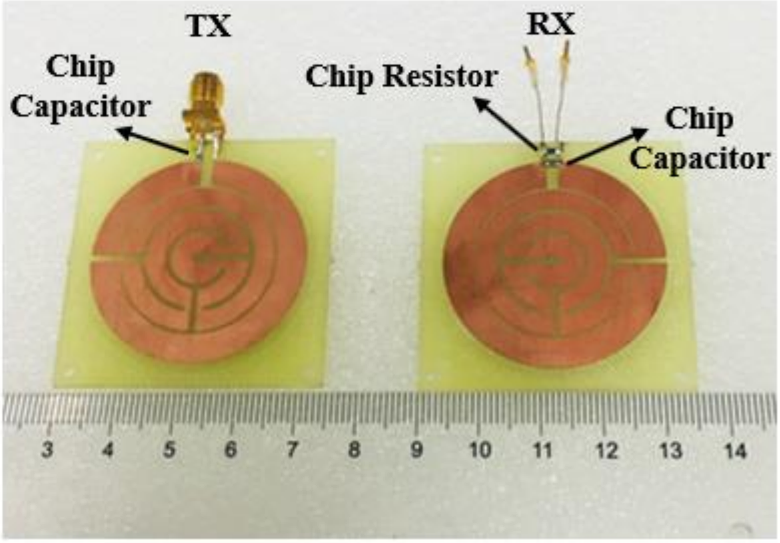

Fig. 5-11. Fabricated wireless power link with proposed 4-turn split-ring loops.

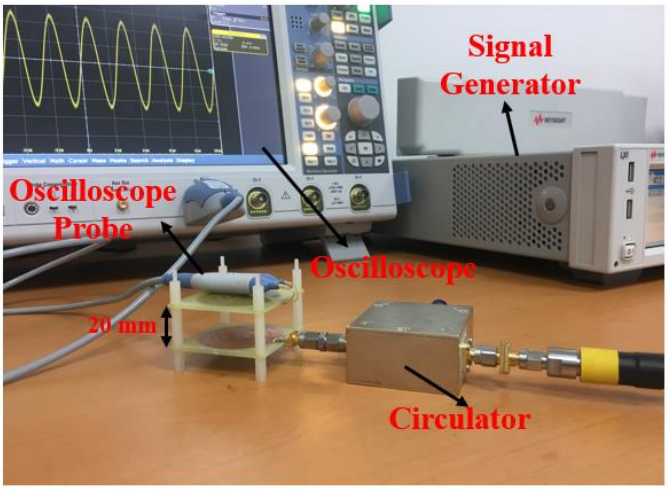

Fig. 5-12. Measurement setup of wireless power link with proposed 4-turn split-ring loops.

The signal generator was set to 0 dBm (1 mW) and varied over the frequency range 385 MHz ~ 420 MHz. The output voltage across the load was measured using the RF oscilloscope in 1 MHz increments, as shown in Fig. 5-12. PTE could then be calculated using the root-mean-square (RMS) of the voltage across the load (V_L) and input power as expressed in the equation (5.1).

$$\eta=\frac{P_{out}}{P_{in}}\times 100\%=\frac{V_L{}^2}{R_L\bullet P_{in}}\times 100\% \tag{5.1}$$

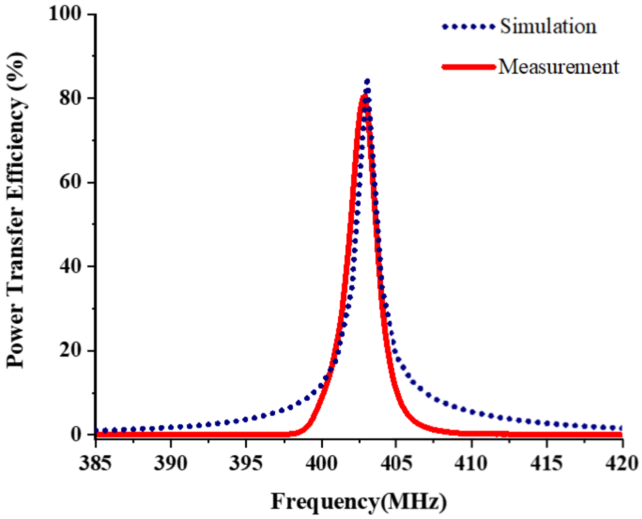

Fig. 5-13. Comparisons of simulated and measured PTE against frequency.

The measured PTE against frequency is shown in Fig. 5-13. It can be seen that the measured PTE reaches a peak of 80.5% at a transfer distance of 20 mm when the resonance frequency is 403 MHz. The power loss between signal generator and the primary circuit and the decreased mutual inductance caused by the practical environment, results in the measured PTE being lower than the simulated PTE.

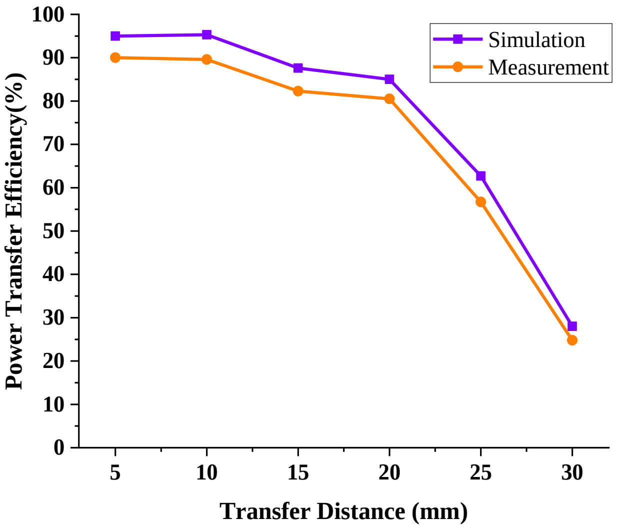

Fig. 5-14. Simulated and measured PTEs of the WPT link with 4-turn split-ring loops at different transfer distances.

The measured PTE at 403 MHz over different transfer distances is shown in Fig. 5-14. It is clear to see that the measured PTE remains stable between 5 mm and 10 mm and then decreases from 89% to 25% as the transfer distance increases to 30 mm, which is similar to the simulated results.

The measured PTE shows good agreement with the simulated PTE and shows that the proposed 4-turn split-ring loop offers better performance for a WPT system than a traditional rectangular PSC.

5.2 Improved 6-turn Planar Split-ring Loops for Wireless Power Transfer

The equivalent circuit of a conventional PSC is a parallel LC network hence using a pair as self-resonators to form a WPT system would constitute a parallel-primary and parallel-secondary system. However, the parallel-parallel topology offers poor power transfer performance, as discussed in Chapter 3, since the input voltage source would be loaded by an open circuit at resonance if directly connected [4-6]. The series-primary, series-secondary and series-primary, parallel-secondary topologies are most typically used for WPT to avoid this issue. In this section, a conformal planar split-ring loop is proposed with the characteristic of a series LC circuit. Importantly, this planar split-ring loop can be regarded as a self-resonator and is designed for use at 433 MHz in the Industrial Scientific and Medical (ISM) band [7-9]. The proposed loop is a good candidate for WPT in applications such as Ultra High Frequency Radio Frequency Identification (UHF-RFID) [10], where only the addition of the loop would be needed in a mobile device.

5.2.1 Design of 6-turn Planar Split-ring Loops

A conventional PSC with 6 turns on FR-4 substrate (ε_r=4.4) with a thickness of 1.5 mm, is shown in Fig. 5-15(a). The width of each track is 2 mm and the gap between the two tracks is 0.5 mm. A discrete 50 Ω port was used for simulations. The equivalent circuit of the PSC [11] is shown in Fig. 5-15(b). The real and imaginary parts of the impedance (Z) are shown in Fig. 5-16. This conventional PSC is inductive at lower frequencies and becomes capacitive at higher frequencies, characterising a parallel LC circuit. At the self-resonant frequency, the parallel LC circuit becomes open circuit (termed parallel self-resonance from this point), which as mentioned is not suitable for the primary side of the WPT system.

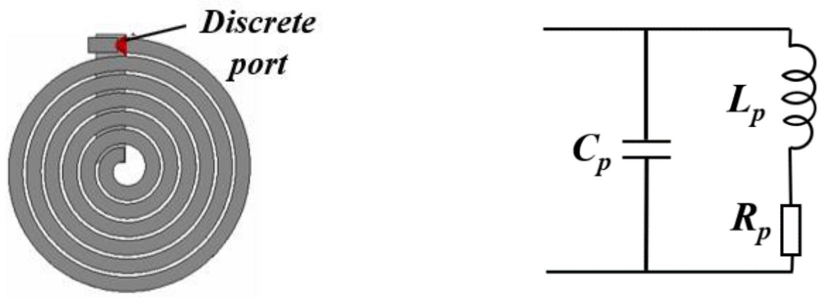

(a) (b)

Fig. 5-15. (a) Physical layout model of conventional 6-turn PSC (b) The equivalent circuit of conventional 6-turn PSC.

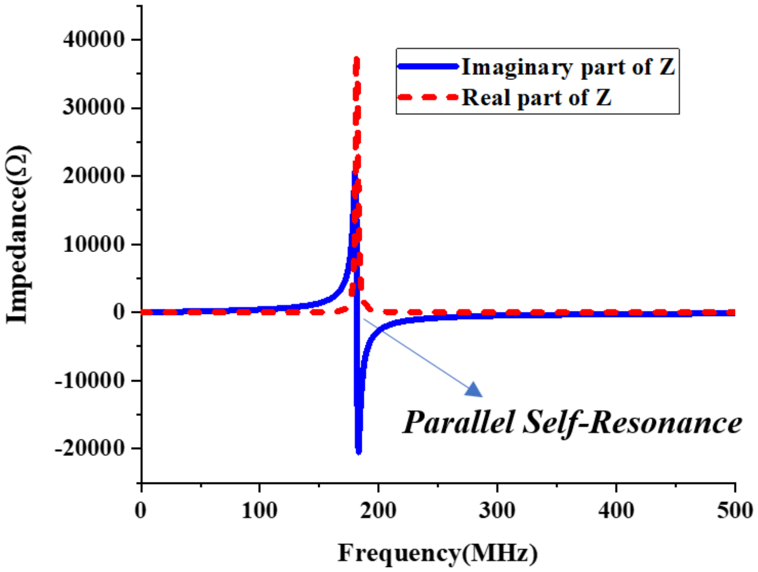

Fig. 5-16 Equivalent circuit of conventional 6-turn PSC.

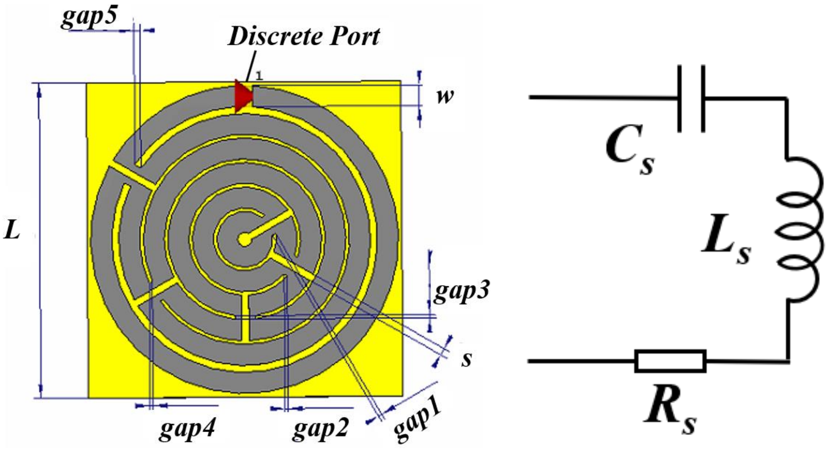

(a) (b)

Fig. 5-17. (a) Physical layout model of designed loop; (b) The equivalent circuit of designed sprit-ring loop at resonance frequency.

A conformal split-ring loop with small dimensions was designed in this work using the roundabout technique, as shown in Fig. 5-17(a), in order to realise the characteristics of a series LC circuit at the desired frequency. The loop impedance was optimised by forcing **Im**(*Z*) to zero and minimising **Re**(*Z*) at 433 MHz. This was achieved by setting *gap5* to 0.5 mm and then sweeping parameter *w* from 2 mm to 3.5 mm. A second optimisation stage then swept *gap5* from 0.5 mm to 2 mm, as shown in Fig. 5-18 and Fig. 5-19 respectively.

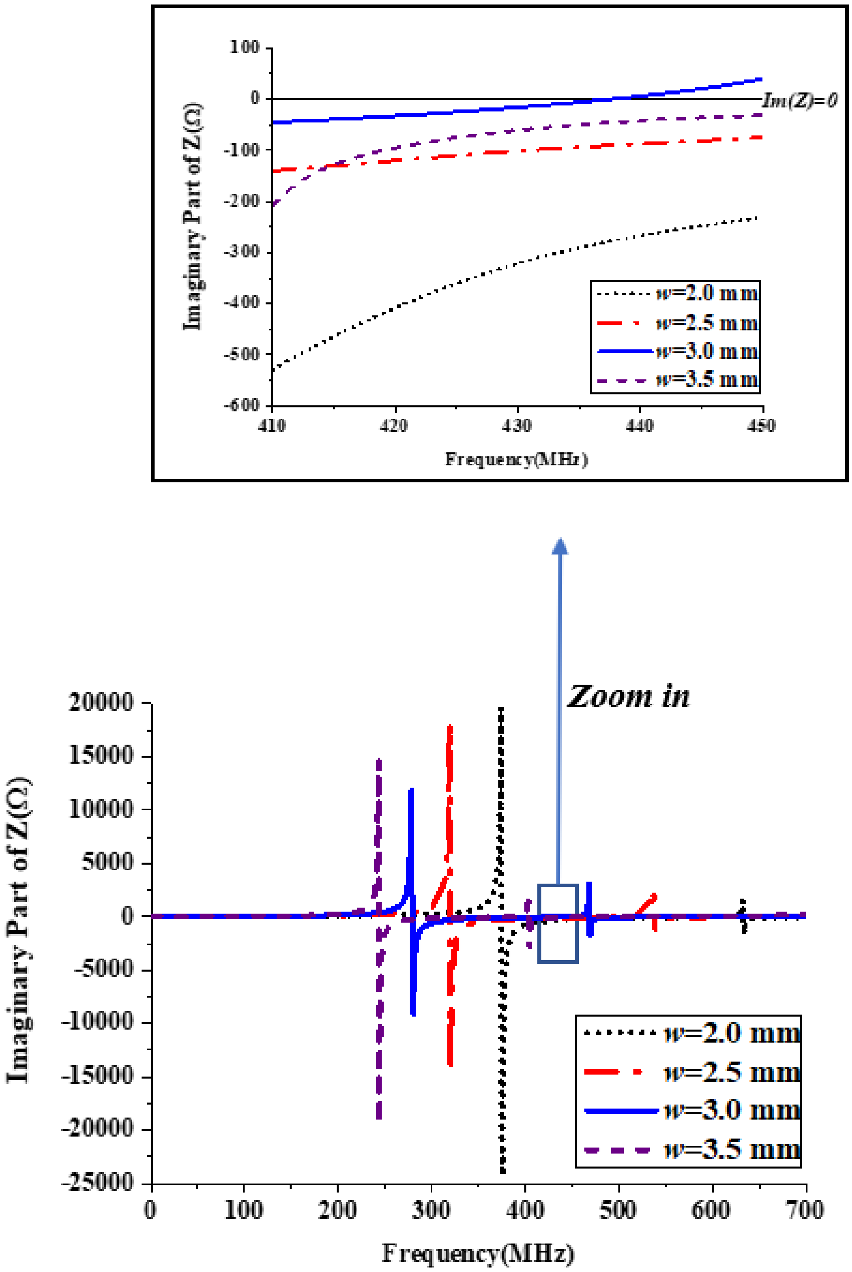

Fig. 5-18. Imaginary part of impedance of designed loop antenna against frequency by changing the width of each track.

It can be seen in Fig. 5-18 that each curve has two parallel self-resonances and an additional point exists between these two where the loop acts as a series LC circuit (as shown in Fig. 5-16(b)), indicated by the impedance changing from capacitive to inductive with increasing frequency (termed series self-resonance from this point). Only when the parameter *w* is 3 mm, does the series self-resonant point exist around 433 MHz.

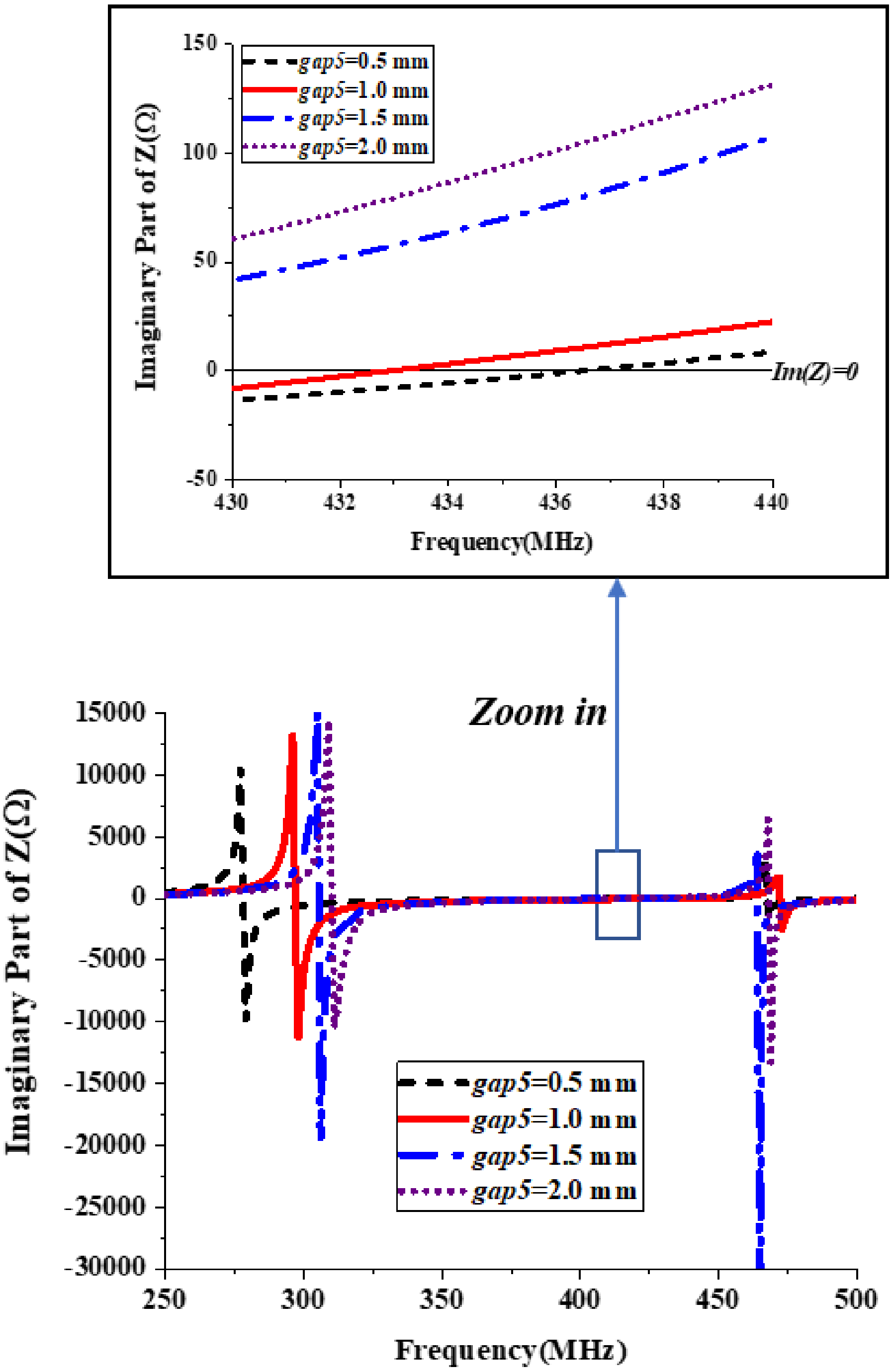

Fig. 5-19. Equivalent impedance of designed loop antenna against frequency by changing the parameter of *gap5*.

The parameter *gap5* was optimised by varying as 0.5 mm, 1 mm, 1.5 mm and 2 mm to bring the series self-resonant point closer to 433 MHz. From Fig. 5-19, it is noteworthy that varying *gap5* results in a shifting of the parallel self-resonances, they shift closer together as *gap5* increases.

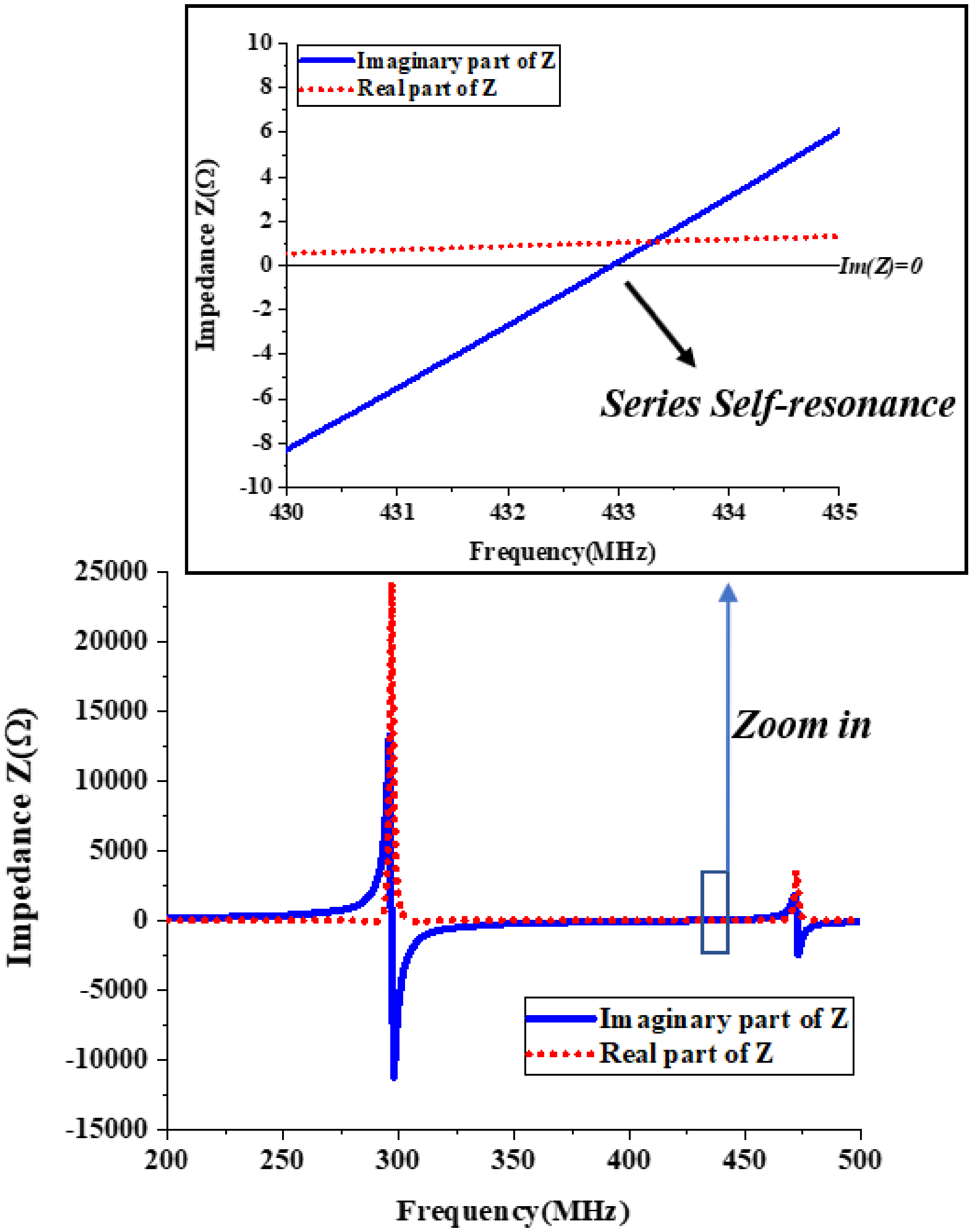

Fig. 5-20. Equivalent impedance of designed split-ring loop against frequency.

The imaginary part of the impedance of this split-ring loop is greater than zero in the frequency range of interest when the parameter *gap5* is 1.5 mm and 2.0 mm. When *gap5* = 1.0 mm the imaginary part of the impedance at 433 MHz is closest to zero.

Table 5-2: Dimensions of the proposed 6-turn split-ring loops

Parameters	*w*	*gap1*	*gap2*	*gap3*	*gap4*	*gap5*	*L*	*s*
Value(mm)	3.8	3.4	3.4	5.0	0.8	0.8	45	1.0

The details of the final optimised parameters for this split-ring loop are provided in Table 5-2. The thickness of the FR-4 substrate is 1.5 mm. The equivalent impedance of the designed split-ring loop is shown in Fig. 5-20. It can be seen from Fig. 5-20 that the simulated imaginary part of the impedance is almost zero at 433 MHz. Therefore, this proposed split-ring loop can be considered as a self-resonator with one series self-resonant frequency of 433 MHz. In this case, *Q*-factor is not included because *Q*-factor is a factor of an inductor not a resonator. The real part of the impedance of the proposed split-ring loop is very large at the two parallel self-resonances, whereas the real part of the impedance is only 1.04 Ω at the series self-resonance point. All optimisations were made by means of full-wave simulations performed using the transient solver of Computer Simulation Technology (CST) Microwave Studio.

5.2.2 Performance of 6-turn Planar Split-ring Loops for Wireless Power Transfer

Two of the proposed split-ring loops with the same series self-resonant frequency can now be used to constitute a WPT system of series-primary and series-secondary circuits. A 3-D view of the loop as applied in WPT is shown in Fig. 5-21. The distance between the transmit and receive loops is initially fixed at 25 mm.

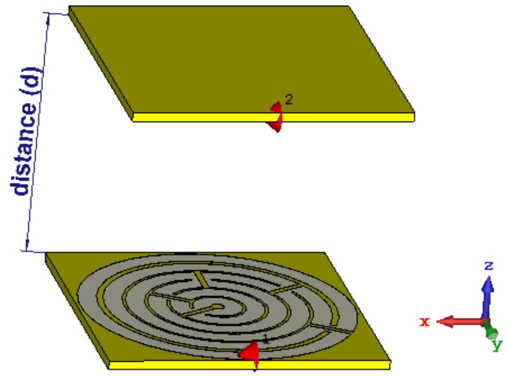

Fig. 5-21. 3-D view of WPT link between two identical 6-turn planar split-ring loops.

The simulated *S*-parameters of the final loop design are shown in Fig. 5-22. A reference impedance of 50 Ω has been assumed at both ports. It can be seen from Fig. 5-22 that the proposed antenna operates at 433 MHz covering a bandwidth of at least 27 MHz (421-448 MHz) for $S_{11} < -10$ dB, which covers the 433-434 MHz ISM (Industrial Scientific Medical) band. Additionally, at 433 MHz, the scattering parameters are $|S_{11}| = -24.04$ dB, $|S_{21}| = -0.74$ dB, and $|S_{22}| = -23.9$ dB.

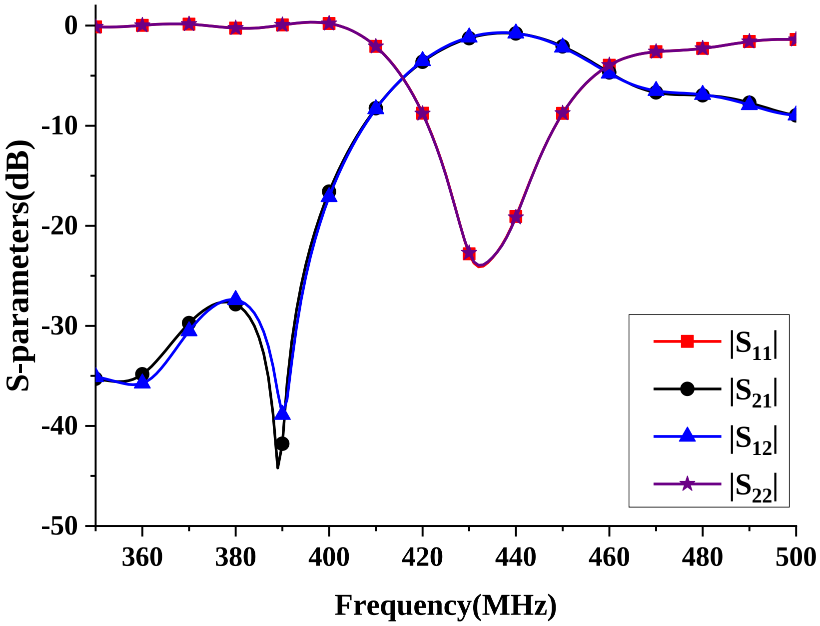

Fig. 5-22. Simulated scattering parameters of proposed antennas for WPT.

Both source impedance (Z_{in}) and load impedance (Z_{Load}) are designed to be 50 Ω, to allow practical measurements of the PTE (η) between the split-ring loops obtained using [12-14]:

$$\eta = \frac{Power\ delivered\ to\ the\ load\ Z_{load}}{Available\ power\ from\ the\ source} = |S_{21}|^2 \times 100\% \qquad (5.2)$$

The trend of simulated PTE against frequency is shown in Fig. 5-23. It can be seen that the peak of the PTE is 84.33% at 433 MHz. The PTE is over 80% over the frequency band 430 MHz to 440 MHz, and hence is not highly sensitive to operating frequency shift. However, the PTE dramatically decreases to 40% within narrow bands from 417 MHz to 430 MHz and from 440 MHz to 455 MHz. The imaginary part of the impedance of the proposed antenna around 433 MHz is approximately zero, therefore power is being transferred from transmitter to receiver by MRC.

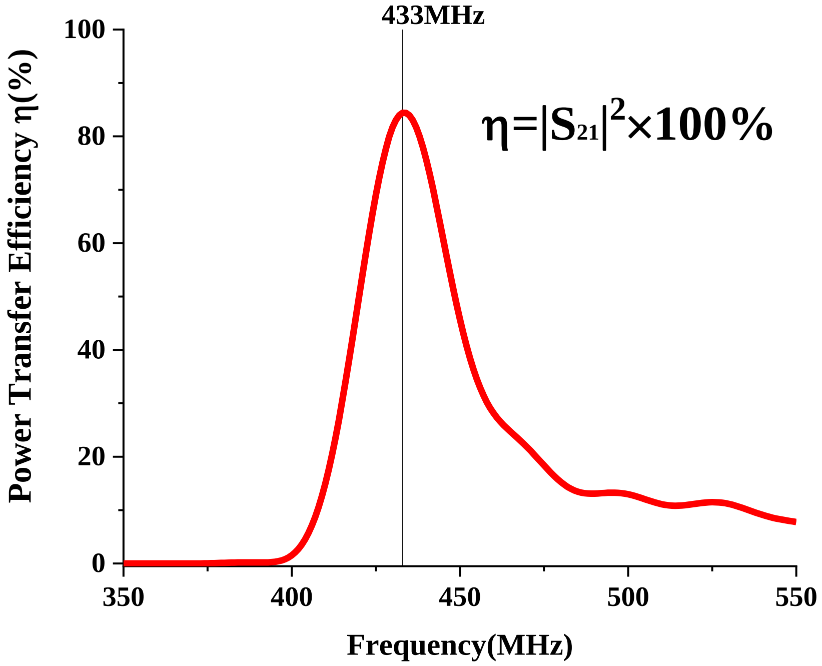

Fig. 5-23. Simulated PTE between two proposed antennas for WPT with the distance of 25 mm.

5.2.3 Sensitivity Analysis

In practical applications and measurements, misalignments due to shifts in the *xy* plane of the two antennas or due to a rotation of the transmitter or receiver can occur due to movements or displacements during charging. It is necessary to investigate the sensitivity of the proposed WPT system to misalignment. In this work, different transfer distances, horizontal or vertical shifts and angular displacements are varied in the CST simulation to conduct the sensitivity analysis.

5.2.3.1 Effect of Transfer Distance

The effect of transfer distance on WPT performance should be considered in taking measurements and in designing practical applications. The transfer distance *d* relates to the distance between the transmitter and receiver, as shown in Fig. 5-21. The transfer distances investigated by simulation are 15 mm, 22 mm, 25 mm, 30 mm, 35 mm, 45 mm and 55 mm. The PTE can be calculated by equation (5-2) in each case, as shown in Fig. 5-24.

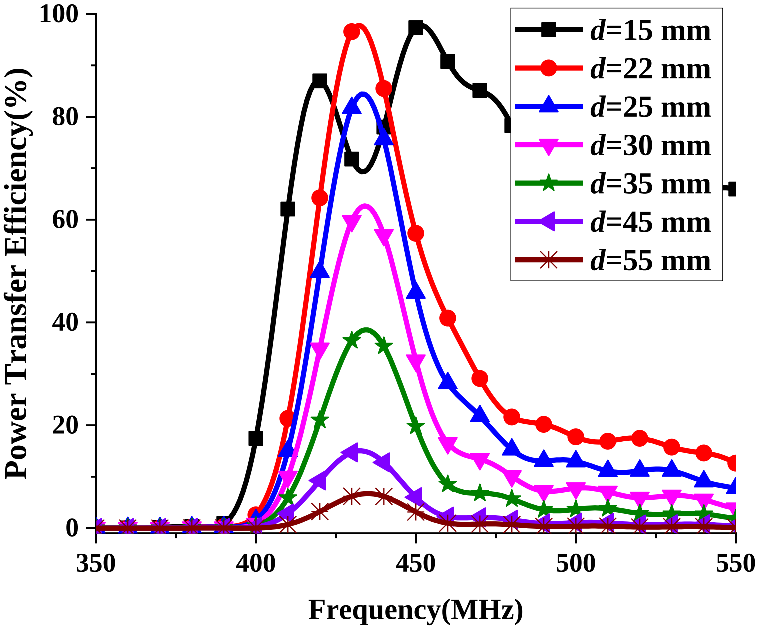

Fig. 5-24. Simulated PTE for different transfer distances.

The simulated PTE reaches its peak of 95.7% at a transfer distance of 22 mm. The PTE decreases significantly from 95.7% to 5% as the transfer distance increases from 22 mm to 55 mm, which results from an exponential decrease in coupling coefficient with increasing transfer distance. The PTE remains at over 50% up to transfer distances of less than 30 mm. When the transfer distance is 15 mm, the PTE has two peaks, one at 420 MHz and another at 452 MHz, respectively, which results from the frequency splitting phenomena [21]. The PTE is 66.33% at 433 MHz, which is not at a peak and is less than that at the transfer distance of 25 mm. Therefore, it is clear that smaller distances do not necessarily lead to higher power transfer efficiencies due to the coupling effects between the loops.

5.2.3.2 Effect of Plane Misalignment

The effect of displacement needs to be investigated since there is clear potential for misalignment in practical applications. The proposed transmit loop is shifted in the horizontal and vertical planes in the simulation with respect to the receive loop, as shown in Fig. 5-25. In this case, the transfer distance between transmitter and receiver is 22 mm and the displacement distance (*dx* or *dy*) is varied from -30 mm to 30 mm along either of the principal planes. Fig. 5-26 illustrates the performance of PTE at 433 MHz along the principal *x*- and *y*-axis.

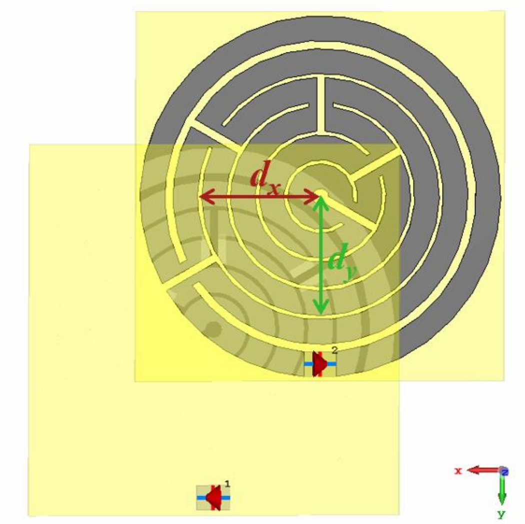

Fig. 5-25. Misalignment due to a shift on the horizontal plane.

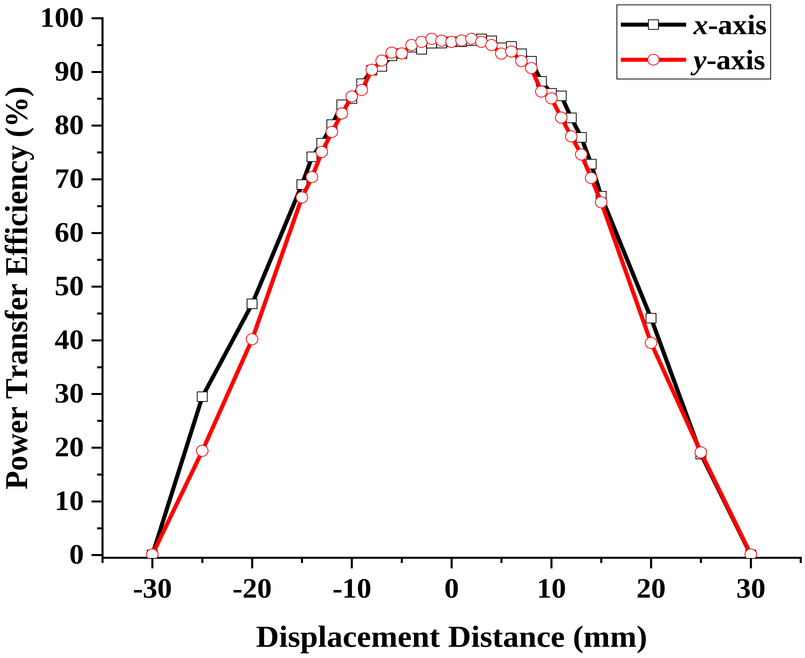

Fig. 5-26: Simulated PTE with shift distance along with *x*-axis and *y*-axis.

The trends for displacement in either *x* or *y* axis are the same. As the displacement increases in both the *x*-axis and *y*-axis a clear influence on the PTE can be seen. The simulated PTE remains over 90% for shifts from -8 mm to 8 mm and over 80% from -12 mm to 12 mm. However, as the shift values become larger, the PTE declines rapidly towards almost 0 at ±30 mm.

5.2.4 Measurements

The proposed loop was fabricated on FR-4 substrate as shown in Fig. 5-27(a) using a PCB milling machine. Fig. 5-27(b) shows the measurement setup, where a Vector Network Analyser (VNA) is used with a reference impedance of 50 Ω. The two identical loops were directly soldered with SMA connectors and then connected to the two VNA ports, respectively.

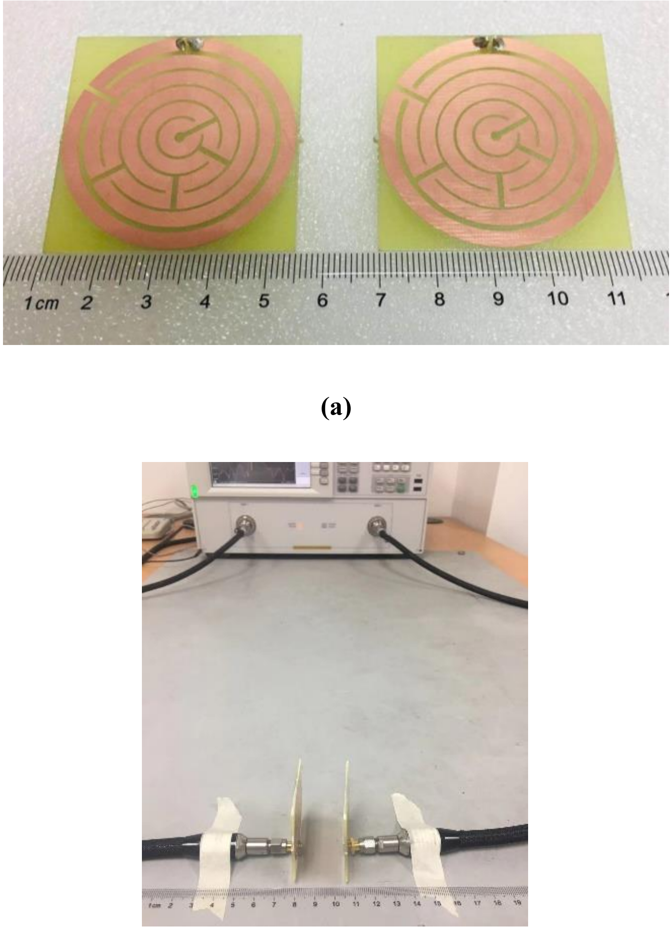

(a)

(b)

Fig. 5-27. (a) Fabricated antennas; (b) Measurement of proposed antennas for WPT.

The measured *S*-parameters are shown in Fig. 5-28, in which a slight frequency shift is seen to exist between the simulation and measurement results. The value of S_{11} drops below -10 dB over a smaller frequency range, from 425 MHz to 445 MHz, but still has enough bandwidth to cover the 433-434 MHz ISM band. At 433 MHz, the values of measured $|S_{11}|$, $|S_{21}|$, $|S_{22}|$ are -16.2 dB, -1.03 dB and -17.9 dB, respectively. Overall, the measured results show good agreement with the simulated results.

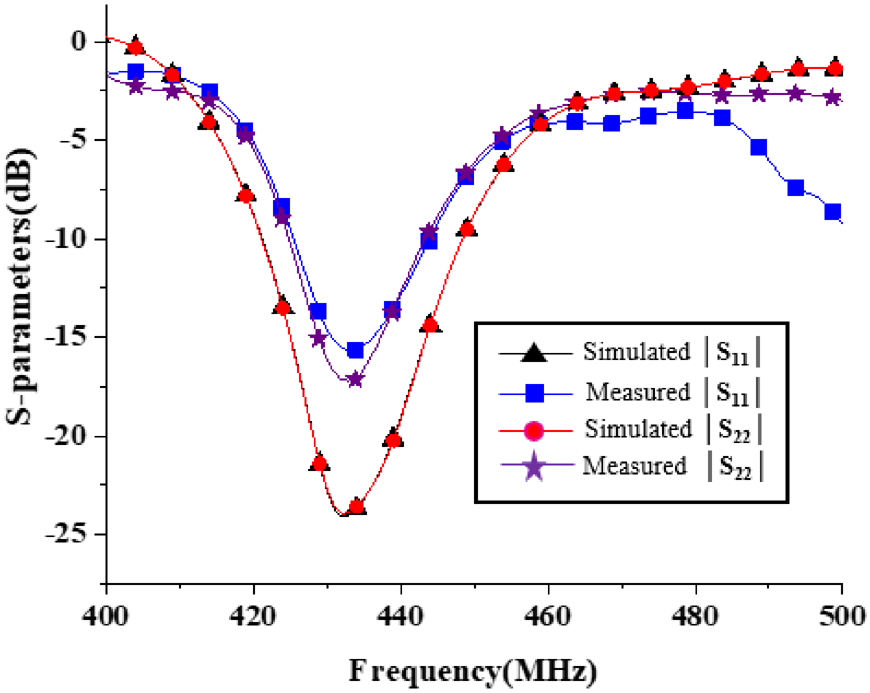

(a)

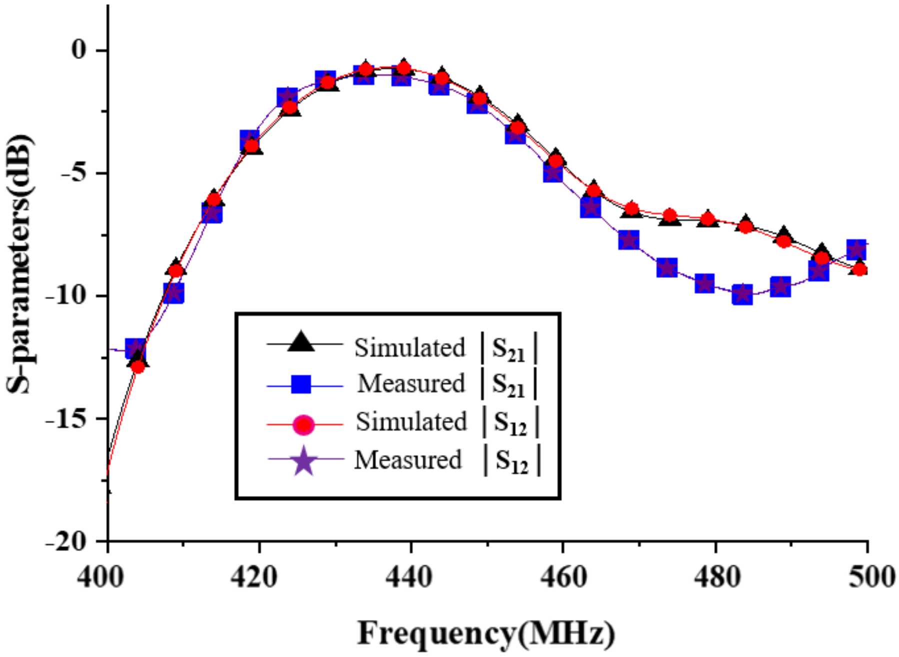

(b)

Fig. 5-28. Simulated and measured scattering parameters of proposed antennas for WPT (a) reflection coefficient in dB; (b) transmission coefficient in dB.

The self-resonance of the loop relies on the parasitic capacitance formed between the conductive tracks of the loop; therefore, it is necessary to consider possible effects of surrounding mediums on the capacitance value that would lead to a shift in resonance frequency. Practical scenarios in which non-metallic mediums such as plastic, foam and paper are placed in the direct vicinity of, as well as in between, the transmit and receive resonators have been investigated. The performance of the WPT link is not visibly affected by the presence of these external objects. A similar process was followed using metal materials such as copper sheet, which was also seen to have no visible influence on performance even within several millimetres of the resonators.

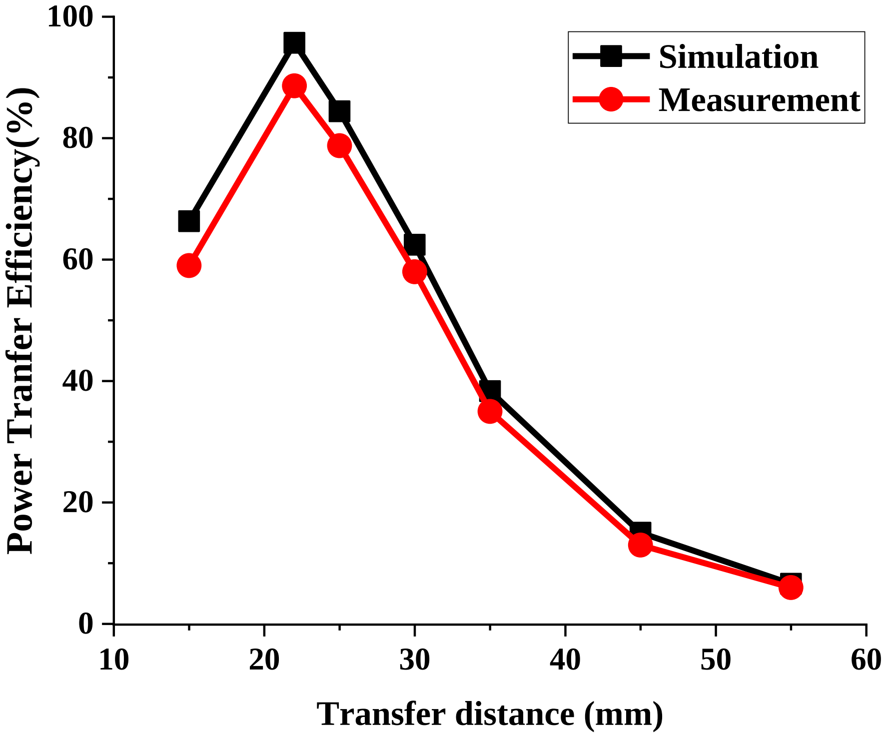

Fig. 5-29. Simulated and measured PTE of proposed antennas for WPT against transfer distance.

The trends of numerical and experimental PTE against transfer distance are shown in Fig. 5-29. It can be observed from Fig. 5-29 that the numerical and experimental PTE at 433 MHz first increases and then decreases rapidly as the transfer distance rises from 15 mm to 55 mm. This initially lower efficiency over shorter distances is due to the frequency splitting phenomenon [15, 16].

The measured PTE is seen to be lower than in the simulation results. One reason for this is due to the practical axis or angular misalignment of the transmitter with respect to the receiver during the experiments. Also, the parasitic resistance of the fabricated loop (which is typically larger) is different to that of the simulation due to material tolerances and fabrication errors. This extra resistance results in additional losses. Even though the measured PTE is not as high as in the simulated results, it attains 78.77% over a transfer distance of 25 mm and 87.9% over a transfer distance of 22 mm.

Table 5-3: Comparisons of this proposed 6-turn split-ring loops with other work

Ref.	Types	f_0 (MHz)	TX Size (mm)	RX Size (mm)	Transfer Distance (mm)	Simulated PTE	Measured PTE
[17]	Rectangular coils on PCB	110	10×10	10×10	3 (0.0011λ)	30%	/
[18]	Square Printed Spiral Coils	50.25	120×120	120×120	100 (0.01675λ)	/	43.62%
[19]	H-slot Resonators	1450	20×20	20×20	3.5 (0.01692λ)	90%	85%
This work	**Planar Split-ring Resonators**	**433**	**45×45**	**45×45**	**22** **(0.03175λ)**	**95.7%**	**87.9%**

Comparisons of this design with other works are summarised in Table 5-3. This proposed split-ring loop can be used for WPT in the UHF band. Despite the relatively large size, the split-ring loop can achieve higher PTE over a larger transfer distance at a higher frequency than in other works. Additionally, the PTE remains at over 30% when the transfer distance increases to 35 mm, which is also better performance than in the other published works, especially at 433 MHz.

5.3 Summary

A 4-turn split-ring loop was proposed in this chapter to increase the *Q*-factor by decreasing ohmic loss in comparison to the rectangular PSC in Chapter 4. Then two identical 4-turn split-ring loops with inductances equivalent to the rectangular PSCs were used to form an MRC-WPT link to allow direct comparison of the two systems and evaluate the effect of increasing the *Q*-factor on PTE. To form series and parallel resonators at the desired frequency (403 MHz) from the transmit and receive loops, series and parallel lumped capacitors had to be added respectively. The split-ring loops showed better WPT performance than the rectangular PSCs maintaining a higher PTE over at over 4 times the distance.

A second series self-resonant split-ring loop has also been proposed and investigated in this chapter. The loop was shown to have a series LC characteristic at one of its self-resonant frequencies, indicated by the imaginary part of the impedance curve changing from capacitive to inductive with increasing frequency. The loop was designed to resonate at 433 MHz (UHF band) without the need for additional matching circuits, which makes the system simpler, more compact and easily adaptable for use in WPT applications where space is restricted and complexity needs to be avoided. The performance of the WPT system, was measured, resulting in a PTE reaching 87.9% at a transfer distance of 22 mm. In comparison with existing literature, this proposed design has advantages of easy fabrication, smaller size, and longer transmission distances at similar efficiencies. The measured results show good agreement with the simulated results and demonstrate that the proposed split-ring loop is a good candidate for WPT as a self-resonant structure for applications such as portable or mobile devices with RFID functions.

5.4 References

[1] F. J. N and M. Nymand, "A New Method for Measuring Winding AC Resistance of High-Efficiency Power Inductors," *IEEE Transactions on Power Electronics,* vol. 33, no. 12, pp. 10736-10747, 2018, doi: 10.1109/TPEL.2018.2805867.

[2] J. Sathyasree, V. Vanukuru, D. Nair, and A. Chakravorty, "Compact Modeling of Proximity Effect in High- ${Q}$ Tapered Spiral Inductors," *IEEE Electron Device Letters,* vol. 39, no. 4, pp. 588-590, 2018, doi: 10.1109/LED.2018.2809787.

[3] J. Lawson, D. C. Yates, and P. D. Mitcheson, "High Q Coil Measurement for Inductive Power Transfer," *IEEE Transactions on Microwave Theory and Techniques,* vol. 67, no. 5, pp. 1962-1973, 2019, doi: 10.1109/TMTT.2019.2901442.

[4] Y. Zhang, Z. Yan, T. Kan, X. Zeng, S. Chen, and C. C. Mi, "Modeling and

Analysis of a Strongly Coupled Series–Parallel-Compensated Wireless Power Transfer System," *IEEE Journal of Emerging and Selected Topics in Power Electronics,* vol. 7, no. 2, pp. 1364-1370, 2019, doi: 10.1109/JESTPE.2018.2860935.

[5] Y. H. Sohn, B. H. Choi, E. S. Lee, G. C. Lim, G. Cho, and C. T. Rim, "General Unified Analyses of Two-Capacitor Inductive Power Transfer Systems: Equivalence of Current-Source SS and SP Compensations," *IEEE Transactions on Power Electronics,* vol. 30, no. 11, pp. 6030-6045, 2015, doi: 10.1109/TPEL.2015.2409734.

[6] J. Sallan, J. L. Villa, A. Llombart, and J. F. Sanz, "Optimal Design of ICPT Systems Applied to Electric Vehicle Battery Charge," *IEEE Transactions on Industrial Electronics,* vol. 56, no. 6, pp. 2140-2149, 2009, doi: 10.1109/TIE.2009.2015359.

[7] C. Liu, Y. Guo, and S. Xiao, "Capacitively Loaded Circularly Polarized Implantable Patch Antenna for ISM Band Biomedical Applications," *IEEE Transactions on Antennas and Propagation,* vol. 62, no. 5, pp. 2407-2417, 2014, doi: 10.1109/TAP.2014.2307341.

[8] A. Kiourti and K. S. Nikita, "Miniature Scalp-Implantable Antennas for Telemetry in the MICS and ISM Bands: Design, Safety Considerations and Link Budget Analysis," *IEEE Transactions on Antennas and Propagation,* vol. 60, no. 8, pp. 3568-3575, 2012, doi: 10.1109/TAP.2012.2201078.

[9] M. D. Weiss, J. L. Smith, and J. Bach, "RF Coupling in a 433-MHz Biotelemetry System for an Artificial Hip," *IEEE Antennas and Wireless Propagation Letters,* vol. 8, pp. 916-919, 2009, doi: 10.1109/LAWP.2009.2028906.

[10] H. Li, Y. Chen, Z. Xing, and S. Yang, "A Novel Printed Dual-Log-Periodic Array Antenna for UHF Near-Field RFID Applications," *IEEE Transactions on Antennas and Propagation,* vol. 66, no. 12, pp. 7418-7423, 2018, doi: 10.1109/TAP.2018.2874202.

[11] S. S. Mohan, M. d. M. Hershenson, S. P. Boyd, and T. H. Lee, "Simple accurate expressions for planar spiral inductances," *IEEE Journal of Solid-State Circuits,* vol. 34, no. 10, pp. 1419-1424, 1999, doi: 10.1109/4.792620.

[12] V. Talla and J. R. Smith, "An experimental technique for design of practical Wireless Power Transfer systems," in *2014 IEEE International Symposium on*

Circuits and Systems (ISCAS), 1-5 June 2014 2014, pp. 2041-2044, doi: 10.1109/ISCAS.2014.6865566.

[13] S. A. Mirbozorgi, P. Yeon, and M. Ghovanloo, "Robust Wireless Power Transmission to mm-Sized Free-Floating Distributed Implants," *IEEE Transactions on Biomedical Circuits and Systems,* vol. 11, no. 3, pp. 692-702, 2017, doi: 10.1109/TBCAS.2017.2663358.

[14] D. M. Pozar, *Microwave Engineering*. New York: Wiley, 2011.

[15] R. Huang, B. Zhang, D. Qiu, and Y. Zhang, "Frequency Splitting Phenomena of Magnetic Resonant Coupling Wireless Power Transfer," *IEEE Transactions on Magnetics,* vol. 50, no. 11, pp. 1-4, 2014, doi: 10.1109/TMAG.2014.2331143.

[16] Y. Zhang, Z. Zhao, and K. Chen, "Frequency-Splitting Analysis of Four-Coil Resonant Wireless Power Transfer," *IEEE Transactions on Industry Applications,* vol. 50, no. 4, pp. 2436-2445, 2014, doi: 10.1109/TIA.2013.2295007.

[17] S. Kim, B. Bae, S. Kong, D. H. Jung, J. J. Kim, and J. Kim, "Design, implementation and measurement of board-to-board wireless power transfer (WPT) for low voltage applications," in *2013 IEEE 22nd Conference on Electrical Performance of Electronic Packaging and Systems*, 27-30 Oct. 2013 2013, pp. 91-95, doi: 10.1109/EPEPS.2013.6703474.

[18] M. M. Falavarjani, M. Shahabadi, and J. Rashed-Mohassel, "Design and implementation of compact WPT system using printed spiral resonators," *Electronics Letters,* vol. 50, no. 2, pp. 110-111, 2014, doi: 10.1049/el.2013.3032.

[19] S. Hekal, A. B. Abdel-Rahman, H. Jia, A. Allam, R. K. Pokharel, and H. Kanaya, "Strong resonant coupling for short-range wireless power transfer applications using defected ground structures," in *2015 IEEE Wireless Power Transfer Conference (WPTC)*, 13-15 May 2015 2015, pp. 1-4, doi: 10.1109/WPT.2015.7140185.

Chapter 6 A Novel Wireless Power Transfer System for Implantable Applications

For implantable medical devices (IMDs) [1-3], a reliable and convenient method of supplying energy or replenishing depleted implanted power sources is vital to their future success. Traditional implanted electronic devices are battery-powered, typically designed to provide energy for no more than 12 years [4]. Wireless power transfer (WPT) technology represents an option that would allow a patient to avoid the need for additional surgeries to replace batteries, and hence avoid the obvious associated health risks, economic burden and patient inconvenience [5]. WPT for IMDs can be divided into far-field and near-field methods. Far-field WPT allows for a long transfer distance and a relaxed transmitter/receiver alignment tolerance. However, the overall power transfer efficiency (PTE) is low and the requirements on safety are high [6, 7]. In [8] a miniaturised implantable planar inverted-F antenna (PIFA) with a folded ground plane operating at 2.45 GHz in the far-field over a distance of 0.5 m was shown to receive -11 dBm of power. However, the high free space path loss at this frequency and low power density due to spreading of the radiated power over a large area, means there is low power transit and hence low transfer efficiency. In [9] the RF-to-DC conversion efficiency achieved was 15.7% at an input power of -20 dBm. In view of the low PTE and low RF-DC conversion efficiency, for a far-field system to supply sufficient power to a device the transmit power needs to be increased. However, there are limits on the maximum radiated power for an implanted antenna set by the Federal Communications Commission (FCC) [10]. Therefore, although far-field WPT can operate over a longer transfer distance than other WPT methods, the power received by the implanted antenna would be limited due to the low power density, low transit efficiency and restrictions on the transmit power.

Magnetic resonance coupling (MRC), a type of near-field WPT technology, has attracted researchers for implantable applications as it offers a higher PTE and larger transfer distance than inductive or capacitive coupling methods [11, 12]. Examples of this have been published working at 0.3 MHz [13], 6.78 MHz [14] and 13.56 MHz [15], chosen due to the low specific absorption by body tissues at these frequencies. Circular printed spiral coils (PSCs) are proposed in [16] and tested using a beef muscle tissue environment over a transfer distance of 10 mm. The measured PTE was 35.4% with a resonance frequency of 13.56 MHz. An operating frequency of 60 MHz was used for WPT with a mm-sized implant over a transfer distance of 16 mm, and the measured PTE was only 2.4% [17]. For a biomedical capsule endoscope, an improved wearable multi-coil resonance WPT system operating at 0.25 MHz achieved a PTE of 5.4% [18]. However, the optimal frequency for WPT into dispersive tissue is in the GHz-range for a mm-sized transmit antenna and shifts to the sub-GHz range for cm-sized transmit antennas [19] when considering size and PTE. The optimisation of such a system is still to be obtained.

This chapter presents an efficient WPT system for implantable applications working at an operating frequency of 403 MHz, which belongs to the Medical Implants Communication Service (MICS) band. The PTE of the proposed WPT system is not sensitive to detuning of the operating frequency due to environmental conditions or manufacturing tolerances. The system is designed to maximise transfer efficiency at the maximum transmit power allowable by the SAR regulations, which in turn maximises power delivery and hence could shorten charging time for a battery.

6.1 Implantable Loops for in-vivo Wireless Power Transfer

6.1.1 Design of Planar Split-ring Loops for Transmitters and Receivers

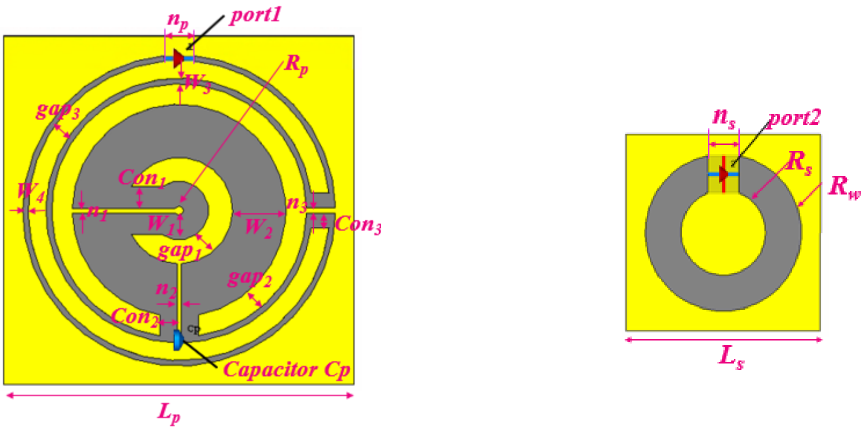

(a) **(b)**

Fig. 6-1. Physical layout models of (a) TX loops; (b) RX loops.

Table 6-1: Dimensions of the proposed wireless power link (Units: mm)

Parameter	Value	Parameter	Value	Parameter	Value	Parameter	Value
Lp	39.6	*gap1*	2.72	*Ls*	25.5	*dgap*	1
np	3.3	*gap2*	2.34	*Ns*	4.08	*dskin*	2
W1	2.84	*gap3*	2.02	*Rs*	5.56	*dfat*	2
W2	6.04	*Con1*	2.47	*Rw*	4.67	*dmuscle*	1
W3	0.64	*Con2*	1.91	*N*	0.55	*d*	6
W4	0.6	*Con3*	1.67	*Rp*	0.5	*t*	1.5

The impedance characteristic of a parallel self-resonating circuit changes from inductive to capacitive, whereas for a series self-resonating circuit the change is from capacitive to inductive; this was illustrated in Chapter 5. The desired characteristic for a series self-resonating loop to be used on the primary side (transmitting side) of the WPT system should therefore be for the imaginary part of the impedance to, change from negative to positive (i.e. from capacitive to inductive) and to be zero at the required resonance frequency (403 GHz). The transmit loop to be located outside of the body, shown in Fig. 6-1 (a), is designed using the roundabout technique on FR-4 substrate (with a relative dielectric constant ε_r=4.4).

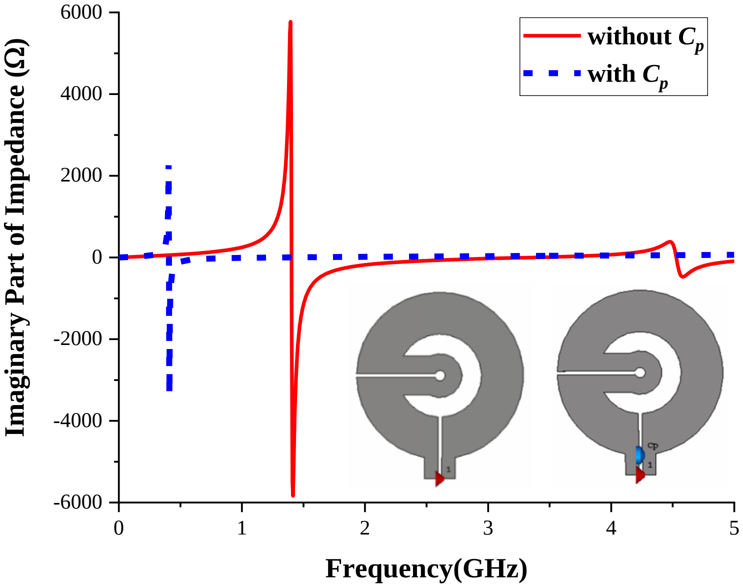

(a)

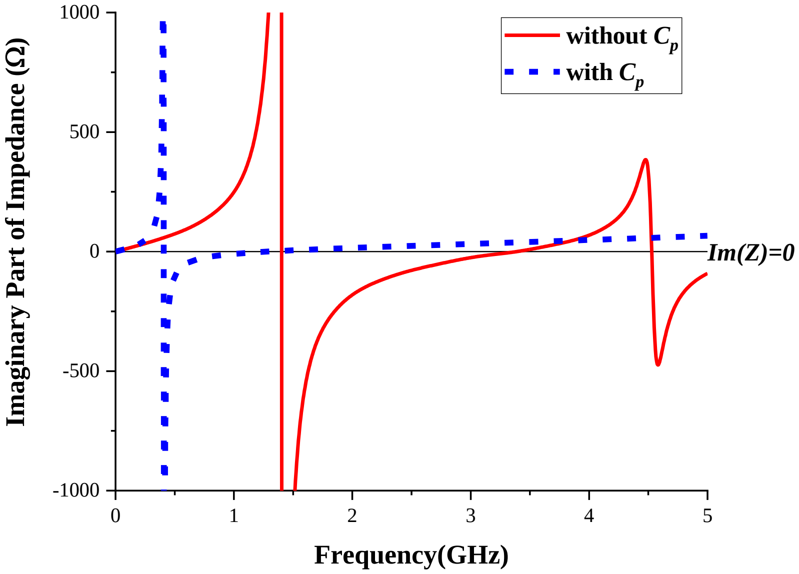

(b)

Fig. 6-2. Imaginary part of impedance of loops without a capacitor and with a capacitor (a) Originally (b) After zooming in.

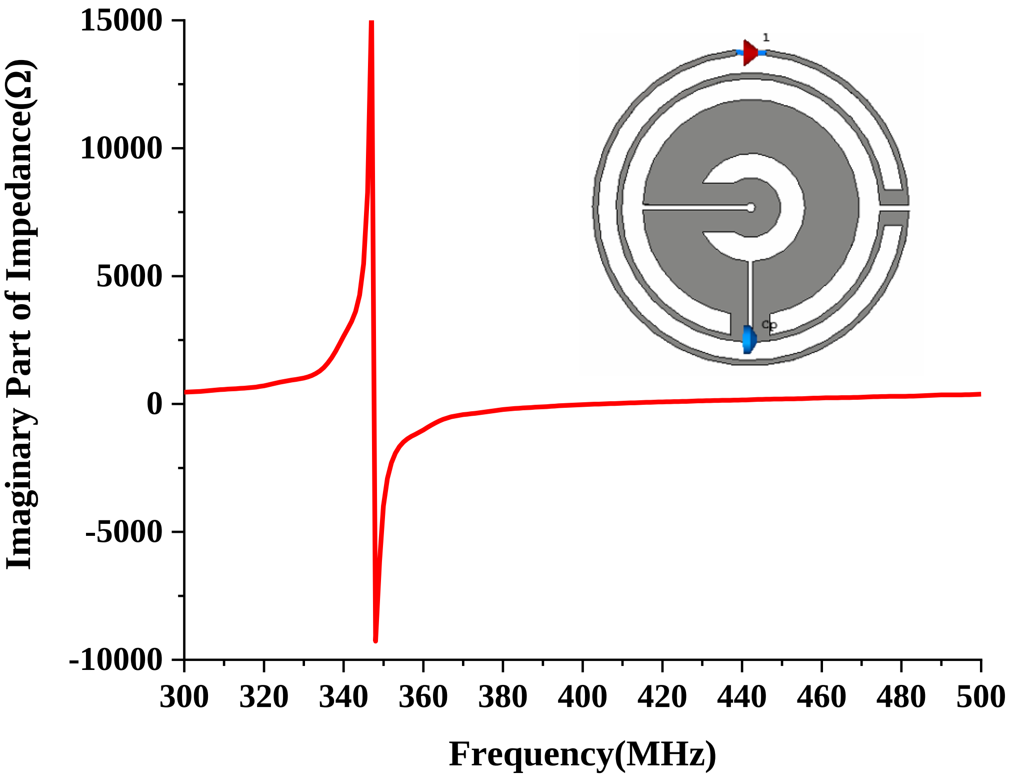

(a)

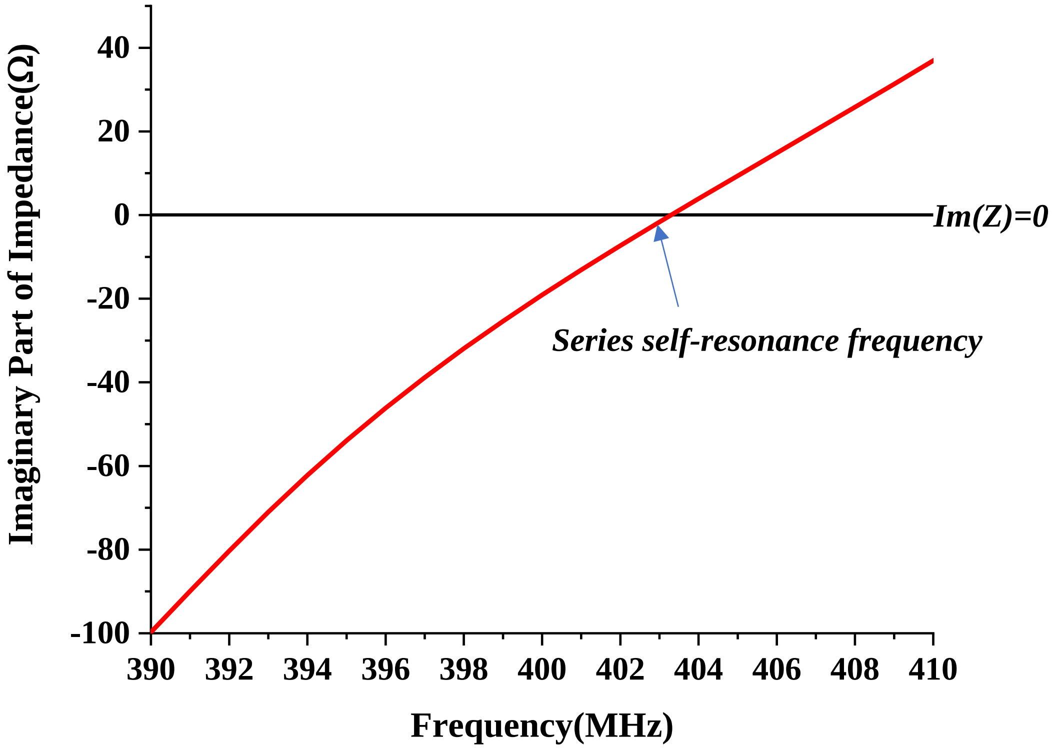

(b)

Fig. 6-3. Imaginary part of impedance of final proposed primary loop.

The trends of the imaginary part of the impedance with and without the compensation capacitor are illustrated in Fig. 6-2 and Fig. 6-3. Firstly, the two inner split-ring loops have a series self-resonance of around 3.39 GHz, which is much larger than the desired frequency of 403 MHz. Secondly, a parallel lumped element capacitor is introduced to increase the equivalent overall capacitance together with that of the two inner loops. The optimised capacitance of the lumped capacitor is 7.9 pF. In this case, the series self-resonance frequency decreases to 1.3 GHz. Finally, to realise series self-resonance at 403 MHz, two extra loops were added outside, as shown in Fig. 6-1(a). The imaginary part of the impedance of this proposed transmitter is shown in Fig. 6-3. The parallel self-resonance frequency is seen to be around 348 MHz. As frequency increases beyond this point the impedance increases to a capacitive maximum and then gradually decreases again. At 403 MHz, the impedance changes from capacitive to inductive, characterising a series self-resonant frequency and the loop looks like a series LC circuit, suitable for use as the primary WPT circuit.

To realise miniaturisation and simplification, the receive loop, to be located inside the body, as shown in Fig. 6-1(b), only has one conductive loop with the characteristic of a parallel LC circuit printed on FR-4 25.5 mm^2. This aims to constitute a WPT system of a series-primary and parallel-secondary topology. The receiver is small enough to be housed within most standard pacemakers which are on the order of 41.2 mm×41.5 mm [20]. The details of the optimised parameters for the transmit and receive loops are provided in Table 6-1.

6.1.2 Performance of Wireless Power Link

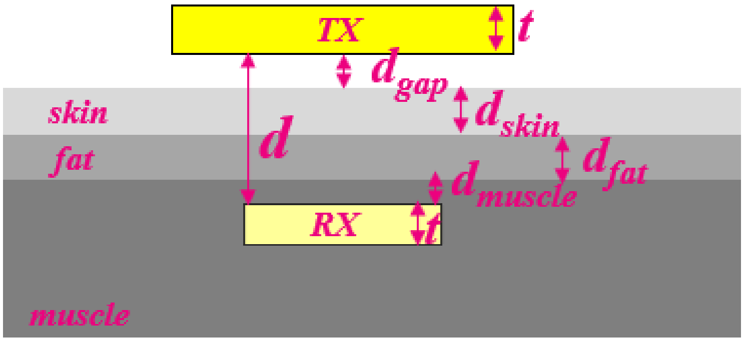

Fig. 6-4. Configuration of the WPT Link between TX and RX loops.

The placement of the loops with respect to the body tissues are shown in Fig. 6-4. Localised body tissues at a pacemaker implant site consist of skin, fat and muscle with a volume of 100 mm×100 mm×150 mm. The distance between transmitter and receiver is considered to be 6 mm, which is structured as an air gap of 1 mm and then skin, fat and muscle at 2 mm, 2 mm and 1 mm respectively.

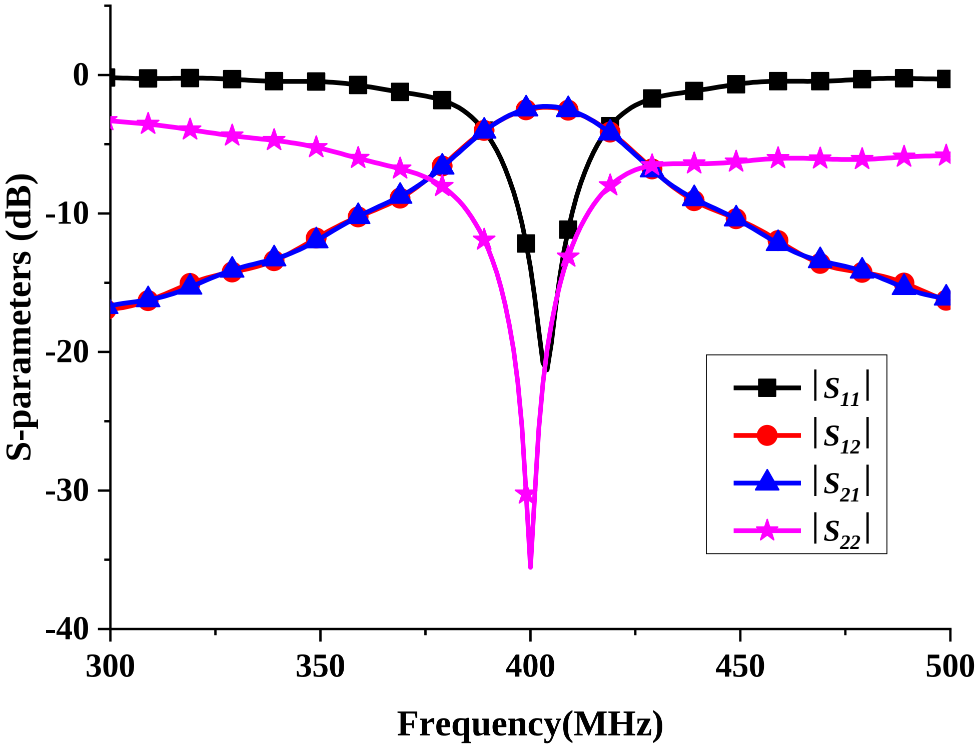

Fig. 6-5. Simulated scattering parameters of proposed antennas for WPT.

According to the IT'IS Foundation database [21], the relative permittivity and conductivity of skin, fat and muscle at 403 MHz are 46.7 and 0.689 S/m, 11.6 and 0.0808 S/m, and 57.1 and 0.797 S/m, respectively. All parameters of the transmit and receive loops have been optimised in terms of internal loss by means of full-wave simulations performed using the transient solver of CST Microwave Studio.

Fig. 6-5 shows the *S*-parameters obtained through simulation of the structures in Fig. 6-1. A reference impedance of 50 Ω has been assumed at both ports. It can be seen from Fig. 6-5 that the proposed loop operates at 403 MHz with a bandwidth of at least 13 MHz (397-410 MHz) for S_{11}<-10 dB, which covers the 402-405 MHz MICS band. Additionally, at 403 MHz, the scattering parameters are $|S_{11}|$=-20.8 dB, $|S_{21}|$=-2.27 dB, $|S_{12}|$=-2.34 dB, and $|S_{22}|$=-22.24 dB.

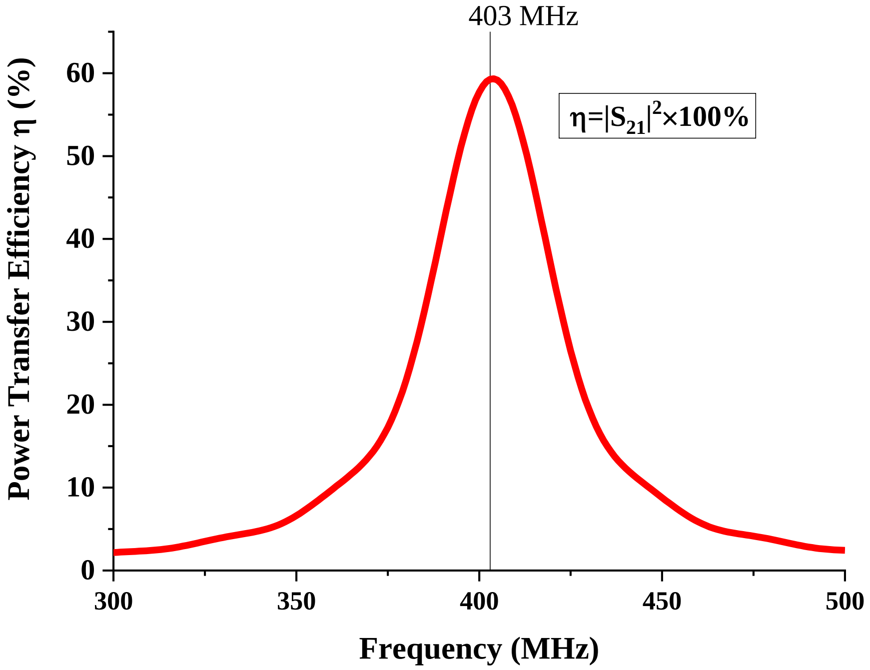

Fig. 6-6. Simulated PTE of proposed antennas for WPT.

To conduct practical measurements of power transmission, assuming that both source impedance (R_{in}) and load impedance (R_L) are 50 Ω, then the PTE (η) between the proposed loops can be defined as [22]:

$$\eta = \frac{\mathit{Power\ delivered\ to\ the\ load}\ R_L}{\mathit{Available\ power\ from\ the\ source}} = |S_{21}|^2 \times 100\% \tag{6.1}$$

The simulated PTE reaches a peak of 59.28% at 403 MHz, as seen from Fig. 6-4. Furthermore, the PTE remains over 50% from 395 MHz to 413 MHz, and hence is not highly sensitive to operating frequency shift. However, the PTE dramatically decreases to 20% from 50% within narrow bands from 378 MHz to 395 MHz and from 413 MHz to 429 MHz.

Considering the different physiques of men, women and children, the amount of body tissues at the pacemaker implant site are different. Therefore, simulations for different body tissue sizes are performed; the size is varied as 60 mm×60 mm, 100 mm×100 mm and 140mm×140mm, as described by Fig. 6-7. The PTE related to the change in size of the body tissues is shown in Fig. 6-8.

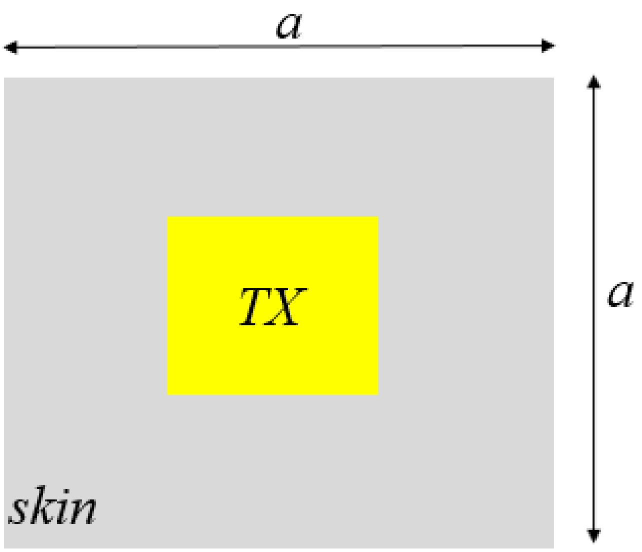

Fig. 6-7. Placement of transmit loop on the surface of the body tissues.

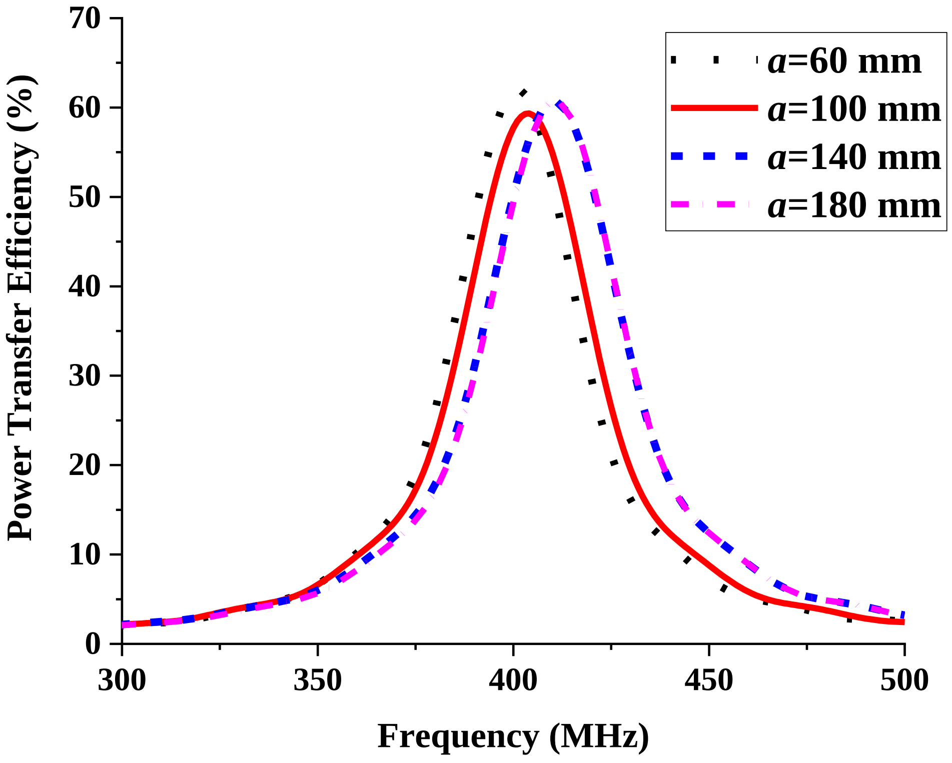

Fig. 6-8. Simulated PTE with different size of body tissues.

It can be seen from Fig. 6-8 that varying the size of the body tissue has little influence on the PTE. As the size of body tissues increases, the resonating frequency shifts up the spectrum a little, whereas, the PTE at 403 MHz remains over 55%. Therefore, for the remaining simulations a body tissue size of 100 mm×100 mm is applied.

6.1.3 Sensitivity Analysis

The influence of positioning sensitivity on the PTE of this WPT link is investigated in terms of power transfer distance, lateral misalignment and angular misalignment.

6.1.3.1 Effect of Transfer Distance

To investigate the effect of receiver depth, and hence transfer distance on the PTE, the implanted loop is varied in depth from 4.5 mm to 19 mm. A fixed air gap outside of the body of 1 mm is maintained in all cases to represent the likely practical scenario i.e. the transfer distance is varied from 5.5 mm to 20 mm. The trends of PTE and transmission parameter (S_{21}) against the power transfer distance are shown in Fig. 6-9.

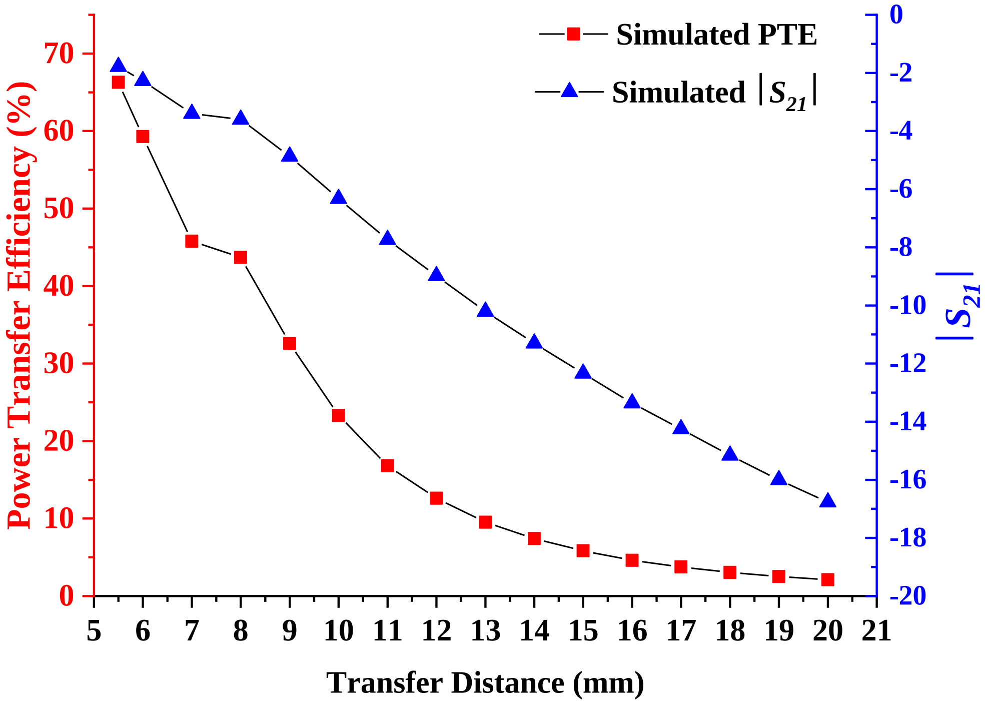

Fig. 6-9. Simulated transmission parameter and PTE between two proposed antennas against the transfer distance.

It can be seen from Fig. 6-9 that the PTE decreases as the implanted depth increases. The PTE is 66.28% ($|S_{21}|$=-1.786 dB) when the transfer distance is 5.5 mm whereas the PTE decreases to 2.03% ($|S_{21}|$=-16.93 dB) when the transfer distance reaches 20 mm. The PTE remains over 40% for transfer distances from 5.5 mm to 8 mm.

6.1.3.2 Effect of Plane Misalignment

In practical scenarios, the receive loop would be implanted in the muscle and the transmit loop located on the body surface; so without any visual cues it is likely they will not be perfectly aligned. Therefore, it is necessary to investigate the effect of plane misalignment on PTE. Misalignment along the two principal axis (*x* and *y*) due to a shift on the plane are shown in Fig. 6-10.

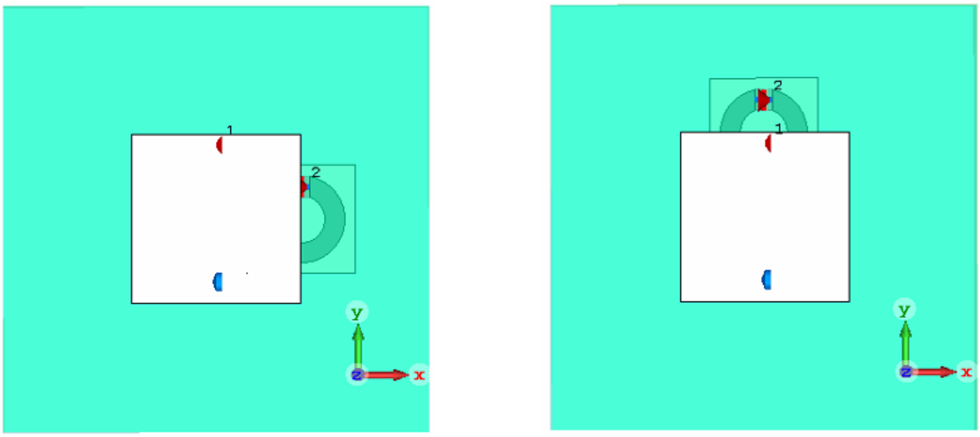

(a) **(b)**

Fig. 6-10. Misalignment due to a shift along (a) *x*-axis and (b) *y*-axis.

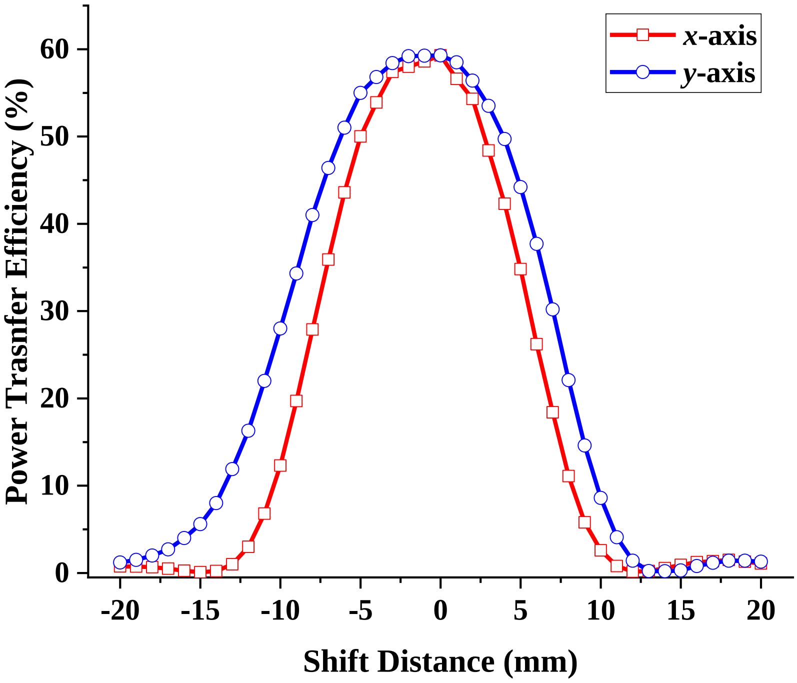

Fig. 6-11. Simulated PTE against a shift distance along *x*- and *y*-axis.

Trends of PTE against shift distance along the *x*- and *y*-axis are depicted in Fig. 6-11. It can be seen that misalignment due to a shift on the plane within 3 mm along either axis has little influence on the PTE. However, the PTE declines rapidly as the shift value becomes larger than 5 mm. The PTE remains over 50% for shifts in the *x*-axis between -5 mm and 3 mm and in the *y*-axis from -6 mm to 4 mm. Therefore, the PTE is affected by small plane misalignments.

6.1.3.3 Effect of Angular Misalignment

Practically, misalignment due to a rotation of the receive loop may happen during its placement in surgery. If the receive loop is implanted in the muscle at a depth of 1 mm then the maximum angle of rotation is only ±4°. The possible misalignments considered are described by Fig. 6-12. The trends of PTE against rotation angles of up to ±4° in each plane are illustrated in Fig. 6-13.

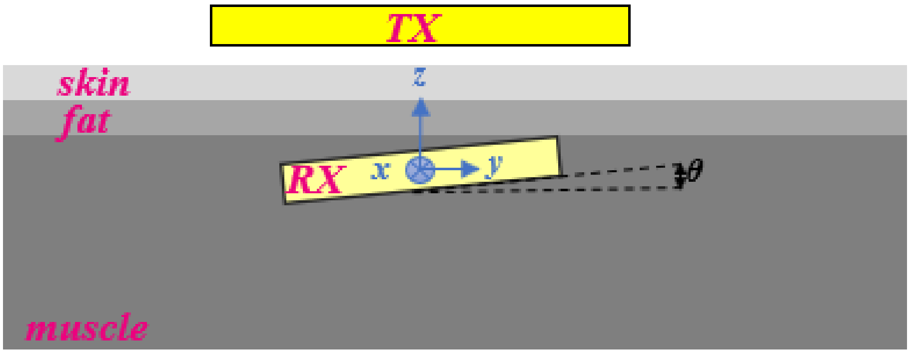

(a)

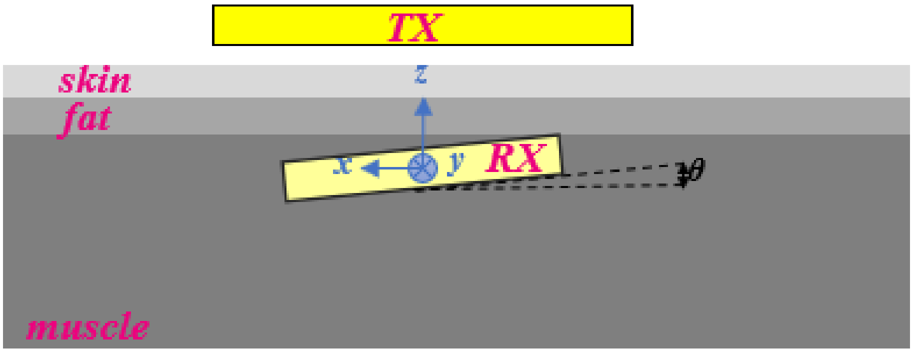

(b)

Fig. 6-12. Misalignments due to a rotation of the receive loop in the (a) *yz*-plane and (b) *xz*-plane.

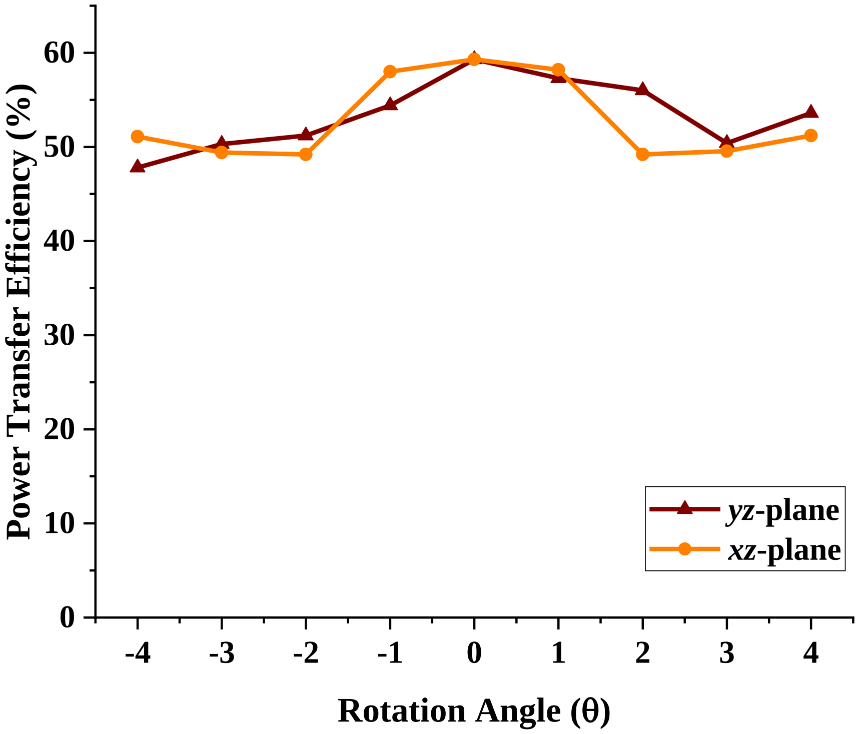

Fig. 6-13. Simulated PTE against rotation angle in the *yz*-plane and *xz*-plane.

It can be seen from Fig. 6-13 that PTE decreases gradually from 59.3% to a minimum 47.8% as the value of rotation angle in each plane varies from 0° to ±4°. The receive port is located on the positive *y* axis and therefore in the *yz*-plane, the distance between the two discrete ports decreases as the rotation angle increases from -4° to 4°, which is why the PTE shows a greater decrease for negative rotations and is not symmetrical about 0°. In the *xz*-plane, however, the relative distance between the two discrete ports is independent of rotation angle, which results in a symmetrical trend for PTE against angle. In either case rotation angles of this magnitude have little influence on the performance of the WPT link. Considering that when the absolute value of rotation angle is 4° the receive loop is almost located in the fat tissue, which has a lower permittivity and conductivity, the PTE becomes a litter larger than that at a rotation angle of ±2°.

6.1.4 Specific Absorption Rate Results

There has been increasing public concern about the possibility of biological hazards arising from human exposure to electromagnetic radiation (EMR) emitted by wearable/implantable sensors or devices, in response to their increased usage over recent years. The current basic safety limits applicable to wireless devices are defined in terms of specific absorption rate (SAR), which is defined as the rate at which a person absorbs electromagnetic energy per unit mass; where SAR averaged over X grams of tissue can be denoted by X-g SAR. The SAR in a biological body exposed to a radio frequency (RF) field depends on a number of factors, including tissue geometry and dielectric properties as well as the orientation of the body relative to the source [23]. There exist three different limits defined by: 1) a whole-body average SAR; 2) a local peak SAR; and 3) a specific absorption (SA), which limits the power of short pulses. 1) and 2) must be averaged over a defined period of time. In wireless devices at frequencies above 300 MHz, the absorption affects only parts of the body which are close to the device. Hence, the most critical value is the local peak SAR limit. Localised SAR averaged over 10-g and 1g of tissue i.e. peak 10-g SAR and peak 1-g SAR must not exceed 2.0 W/kg and 1.6 W/kg respectively, as recommended by the IEEE/ANSI/FCC as the upper safety limit [24].

Evaluating the SAR distributions associated with electronic devices is a complex task, usually accomplished by measurement techniques or numerical modelling. Two experimental methods to evaluate compliance with specific SAR requirements use measurement of either, the electric field (E-field) strength or, the rate of temperature increase in a tissue-equivalent liquid using anthropomorphic models of the human head or other body part [25].

Firstly, the electric-field probe method, as a rapid and non-invasive SAR measurement solution, is based on utilising automatic positioning systems to move an E-Field measuring probe in a liquid phantom to assess SAR values [26]. The specific absorption rate (SAR) is usually used as the primary dosimetric parameter of EM wave exposure for standardisation [27], expressed as:

$$\text{SAR}=\frac{\sigma|\text{E}|^2}{\rho}\left[W/kg\right] \tag{6.2}$$

Where, σ [S/m] is the conductivity of the tissue, ρ [kg/m^3] is the density of the tissue, and E [V/m] is the electric field intensity within the tissue.

Secondly, temperature distributions produced by energy absorption in phantom models after exposure to radiating fields can be measured. The model is first disassembled along a plane where SAR is to be determined and a thermographic-temperature scan is made over the plane. The model is then reassembled and exposed to a high power density signal for a short time; followed by disassembly and another thermographic scan. Thermographic experiments [28, 29] are carried out using brain and skull-equivalent solid phantom models to estimate the SAR distribution in human heads. If heat diffusion is negligibly small during the exposure period, the SAR at an arbitrary point is given by

$$\text{SAR}=\text{c}\frac{\Delta T}{\Delta t}\left[W/kg\right] \tag{6.3}$$

where, c [J/kg·K] is the specific heat of the phantom, ΔT [K] is the temperature rise at the point, and Δt [second] is the exposure time. Hence, the temperature rise profile is proportional to the SAR distribution. The specific heat of the brain and skull-equivalent phantom are 3750 and 2850 J/kg K, respectively. This equation describes that the SAR distribution is proportional to the temperature rise.

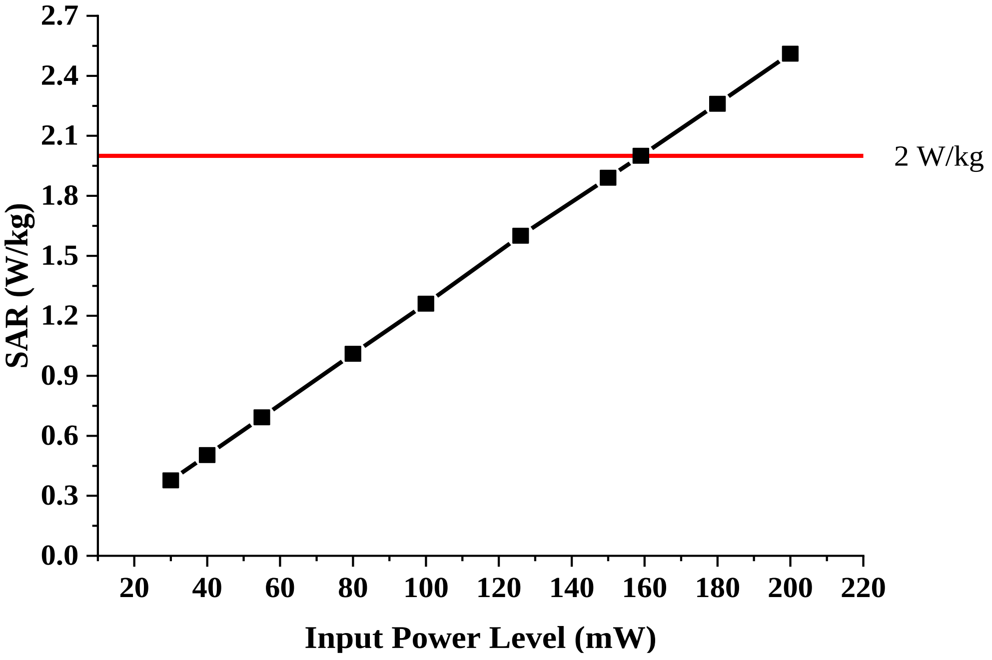

Fig. 6-14: Calculated 10-g average SAR value with different input power level. The SAR limit (2 W/kg) is plotted as the horizontal line.

According to the IEEE C95.1-2005 standards on human safety considerations, the 10-g average SAR should be less than 2 W/kg [30]. Full-wave simulations were performed as shown in Fig. 6-4 by CST Microwave Studio to determine how much power can be provided to the primary resonator of the proposed WPT link based on these safety regulations. The trend of the SAR value against primary resonator input power is shown in Fig. 6-14. The horizontal line represents the 10-g average SAR limitation of 2 W/kg and the other curve shows the trend of the calculated SAR value for this WPT link in body tissue. The calculated SAR value is directly proportional to the input power delivered to the primary resonator. To satisfy the IEEE SAR regulations (2 W/kg), the input power delivered to the primary antenna should be less than 159 mW (22dBm) at 403 MHz.

6.1.5 Measurement Results

The proposed transmit and receive loops were fabricated on FR-4 substrate as shown in Fig. 6-15. The two loops were directly soldered with subminiature version A (SMA) connectors and then connected to the two VNA ports. Fig. 6-16 shows the measurement setup, where a Vector Network Analyser (VNA) is used with a reference impedance of 50 Ω. The receive antenna is placed inside some minced pork, used to simulate the body tissue, and the transmit antenna is placed on the surface of the minced pork. Both antennas and connectors were protected by a thin layer of plastic wrap.

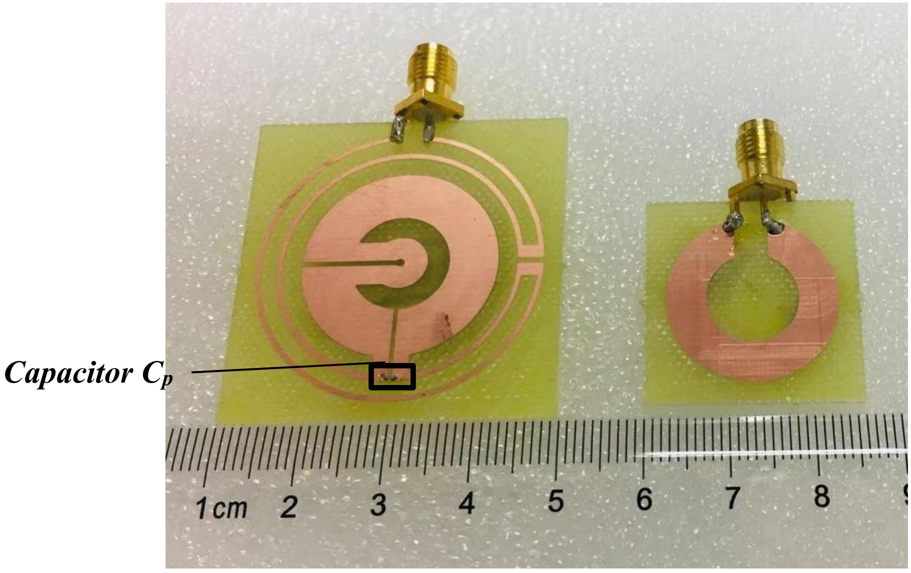

Fig. 6-15. Fabricated transmit and receive antennas with soldered SMA.

Fig. 6-16. Measurement of proposed loops for WPT.

Comparisons of the measured *S*-parameters with the simulations are shown in Fig. 6-17. A small frequency shift is seen to exist between the simulation and measurement results. The value of S_{11} drops below -10 dB over the frequency range 394 MHz to 406 MHz, covering the Medical Implants Communication Service (MICS) band. At 403 MHz, the values of measured $|S_{11}|$, $|S_{21}|$, $|S_{22}|$ are -12.4 dB, -2.37 dB and -10.8 dB, respectively. Overall, the measured results show good agreement with the simulated results.

The simulated and measured PTE of this proposed WPT link are shown in Fig. 6-18. Good agreement between the simulated and measured power transfer efficiencies can be seen despite the slight frequency shift. The maximum simulated PTE reaches a peak of 59.3% at 403 MHz, whereas the maximum measured PTE of 60.7% occurs at 400 MHz. The measured PTE remains over 50% over a bandwidth of 17 MHz (from 390 MHz to 407 MHz). That means the receiving loop can receive more than half of the transmit power despite any potential shifts in resonating frequency. However, the PTE dramatically decreases to 20% from 50% within narrow bands from 371 MHz to 394 MHz and from 413 MHz to 420 MHz. The possible reasons for shifts in the resonant frequency of the system are capacitance tolerance, the depth of the secondary resonator, manufacturing tolerances and variation in environmental conditions.

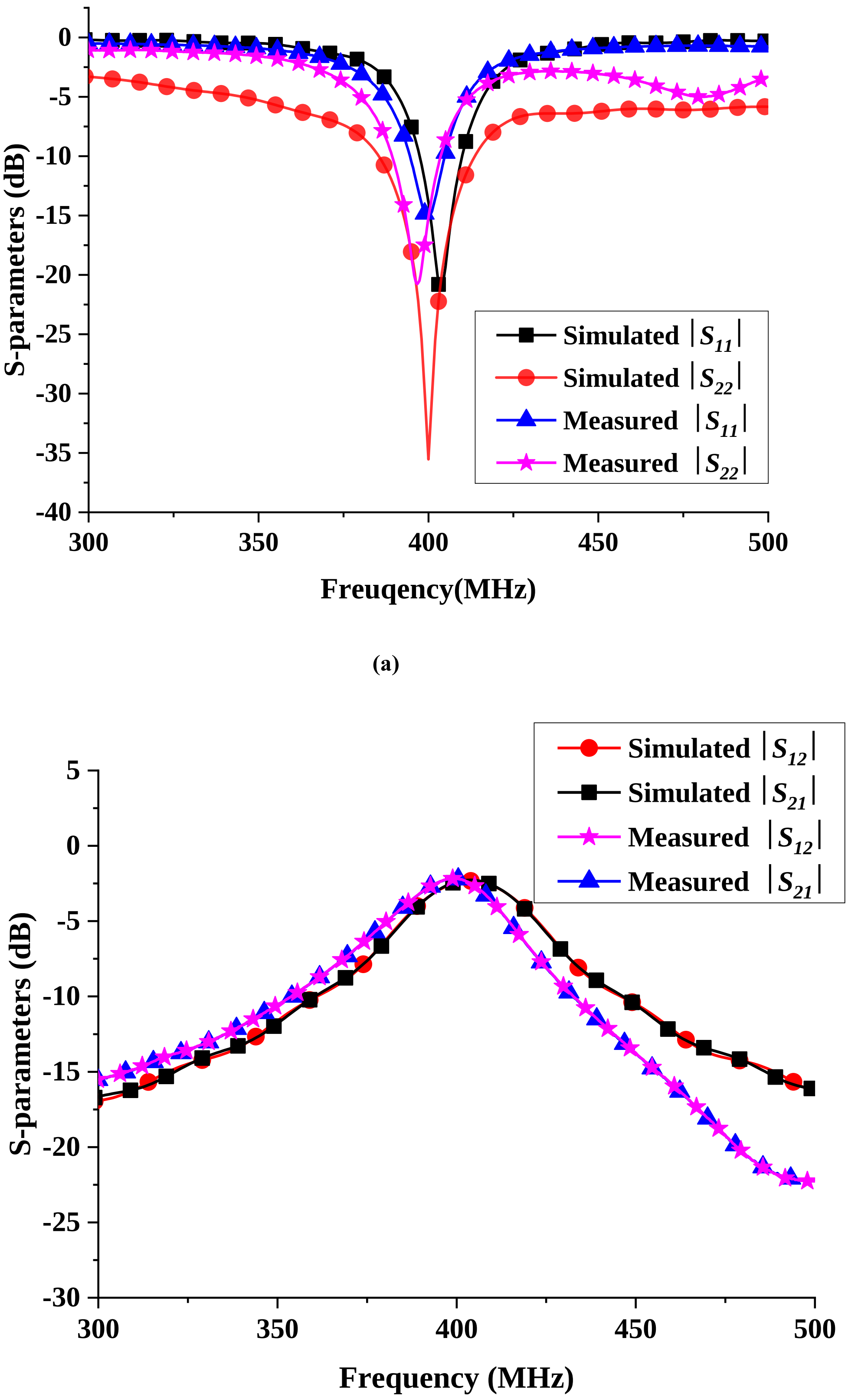

(a)

(b)

Fig. 6-17. Simulated and measured scattering parameters of proposed loops for WPT (a) reflection coefficient in dB (b) transmission coefficient in dB.

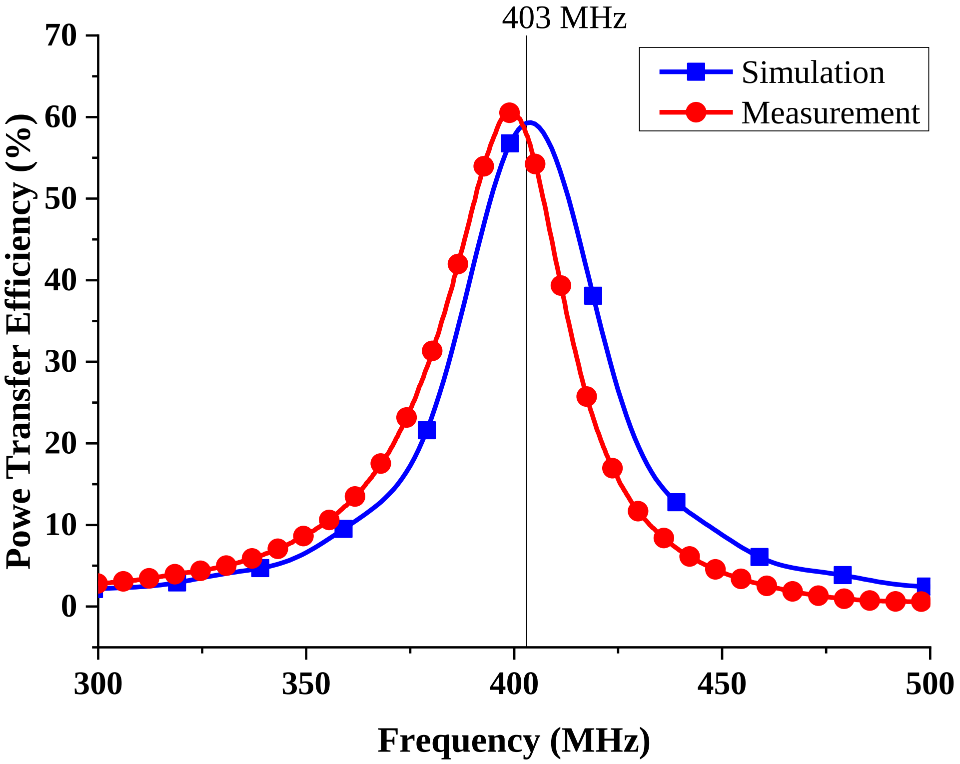

Fig. 6-18. Simulated and measured PTE over the WPT link.

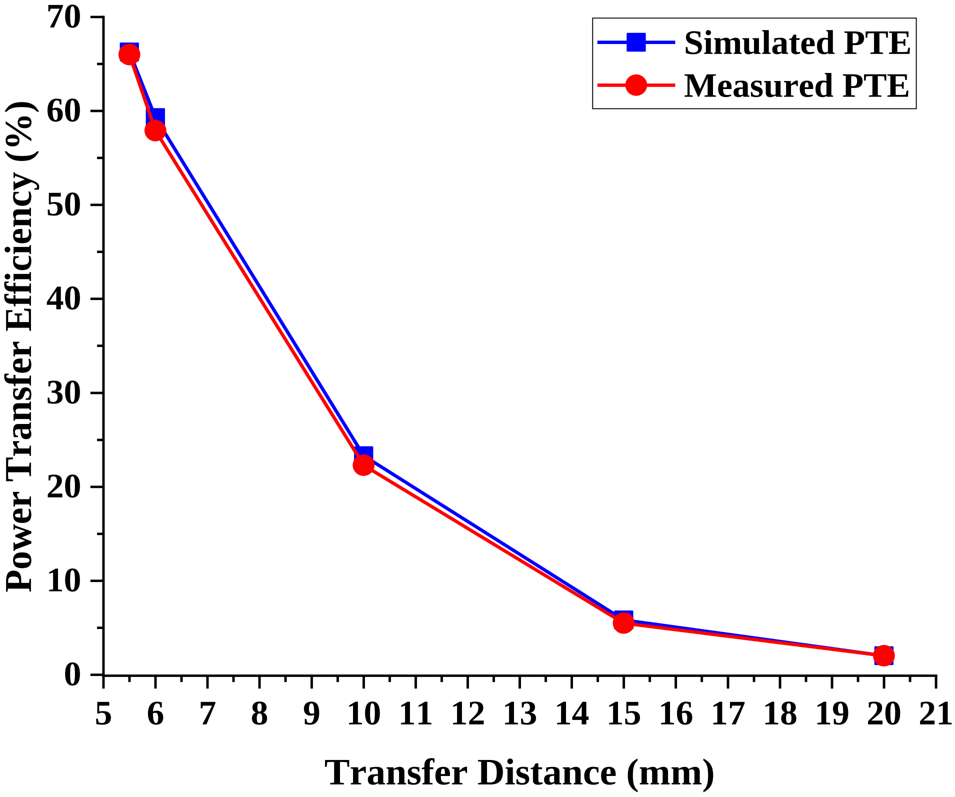

Fig. 6-19. Simulated and measured PTE against transfer distance over the WPT link at 403 MHz.

The simulated and measured PTE at 403 MHz against transfer distance between transmit and receive loops are compared in Fig. 6-18. The transfer distance between the antennas is varied as 5.5 mm, 6 mm, 10 mm, 15 mm and 20mm including a 1 mm air gap between the transmitter and the body tissues. From Fig. 6-19 is can be seen that both simulated and measured PTE show good agreement. The measured PTE at 403 MHz decreases dramatically from 66% at a transfer distance of 5.5 mm to 2% at a transfer distance of 20 mm. This is due to the coupling coefficient between the antennas decreasing exponentially with increasing transfer distance.

Table 6-2: Comparisons of this proposed implantable WPT link with other work

Ref.	[31]	[32]	[33]	**This work**
Types	Dual-band Antenna	Square Coils with Metamaterials	Planar Ring Resonator	**Planar Split-ring loops**
f_0 (MHz)	13.56	430	403	**403**
RX Size (mm)	24×24	10×10	9.87×9.87	**20.46×20.46**
Transfer Distance (mm)	16	20	5	**6**
Simulated PTE	/	2.88%	20.75%	**59.3%**
Measured PTE	17%	2.51%	20.54%	**57.9%**
Maximum Input Power (mW)	100	/	38	**159**
Maximum Receiving Power (mW)	17	/	7.8	**92**

Comparisons of this design with other works are shown in TABLE II. Maximum source power represents the maximum power that can be supplied to the transmitting loop in consideration of the SAR regulations. The table shows that in this work, the PTE has been significantly improved at 403 MHz, achieved partially by slightly enlarging the dimensions of the receive loop, though its dimensions remain small enough to fit within a typical pacemaker. Additionally, the maximum source power available within safe use limits is significantly larger than in other works, which means the battery in the pacemaker can be charged faster using this proposed WPT link. Importantly, the maximum receive power of this proposed WPT link can reach 92 mW, which is more than ten times as much as that in [35]. That will significantly reduce battery charging time.

6.2 Rectifier Design

6.2.1 Rectifier Configuration

To realise the RF-DC conversion at the receiver side a rectifying circuit is required. Generally, a rectifying circuit consists of an impedance matching network to ensure maximum converted power is delivered, a rectifying element (diode) to perform RF-to-DC conversion and a DC-pass filter to smooth any ripple on the DC output delivered to the load (resistor). The voltage doubler rectifier is used for RF-to-DC conversion in this work since it has a high efficiency and high output voltage compared to a single series half-wave rectifier [34].

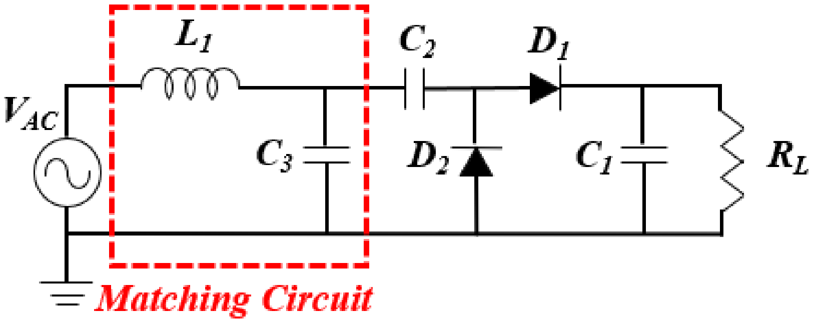

Fig. 6-20. Schematic of the voltage doubler rectifier.

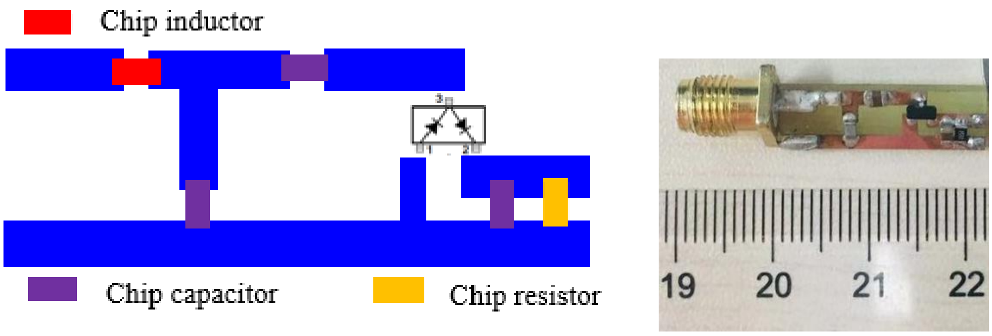

(a) **(b)**

Fig. 6-21. (a) Topology of the proposed rectifying circuit; (b) Fabricated rectifying circuit.

The schematic of the voltage doubler rectifier is shown in Fig. 6-20. Schottky detector diodes HSMS-286c are selected for the rectifier due to their low-cost. In consideration of the human safety requirements as detailed in Fig. 6-14, when the power provided to the primary resonator is 55 mW, the calculated SAR value is only

0.692 W/kg, which fully satisfies the safety regulations. In this case, the secondary resonator can receive up to 31.8 mW (≈15 dBm), which can be considered as the source power of the rectifier. A matching circuit is designed to match the load (R_L=1.5 kΩ) to the 50 Ω source impedance (since the designed secondary resonator is matched for a 50 Ω) when the input power to the rectifier circuit is 15 dBm.

The rectifier circuit has been simulated and optimised using the Advanced Design System (ADS) software. The inductance of the chip inductor (L_1) is 27 nH and the chip capacitances C_1, C_2 and C_3 are 4.7 µF, 4.7 µF and 2.7 pF, respectively. The circuit has been fabricated on FR-4 substrate and soldered with an SMA connector between input and ground to allow measurements to be made, as shown in Fig. 6-21.

6.2.2 Rectifier Performance

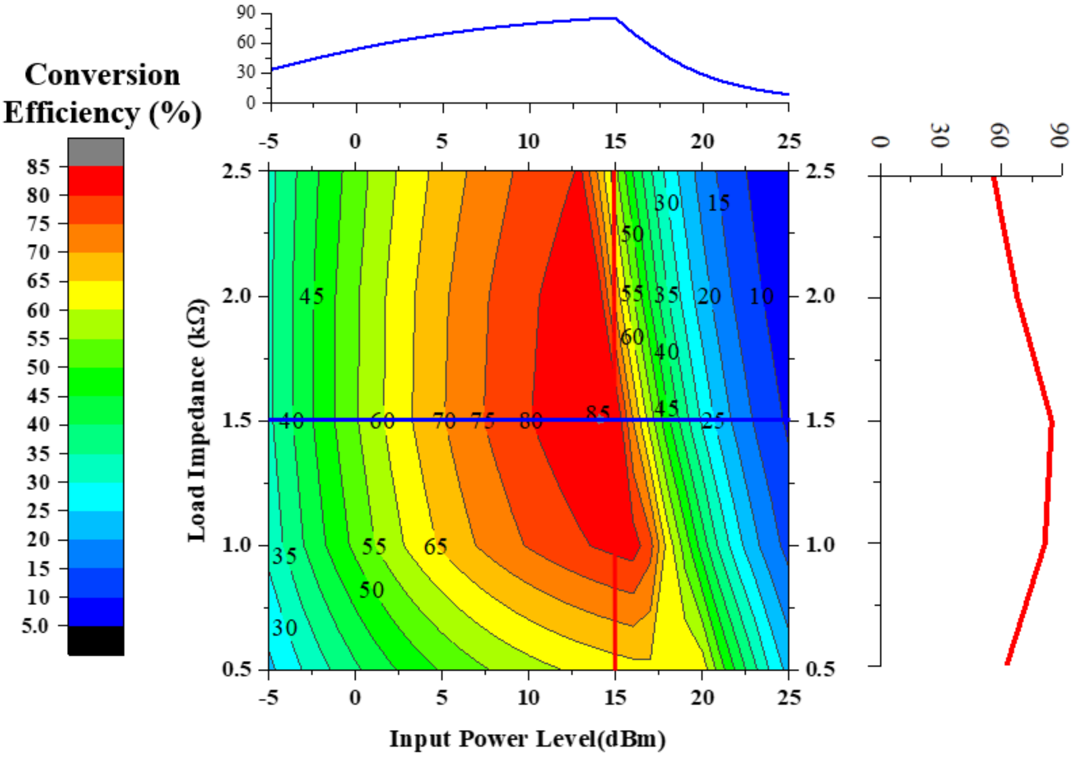

Fig. 6-22. Simulated RF-to-DC conversion efficiency of the proposed rectifier versus input power level and load impedances. The operating frequency is 403 MHz.

The simulated RF-DC conversion efficiency versus input power level for different load resistances is depicted in Fig. 6-22 at 403 MHz. It can be seen that for load values from 1 to 2.5 kΩ, the maximum conversion efficiency can reach 80% for various input power levels. When the input power level is 15 dBm, the RF-to-DC conversion efficiency reaches a peak of 85% with a load impedance of 1.5 kΩ, which can be seen from the red curve in Fig. 6-22. When the load impedance is 1.5 kΩ, the trend of output DC voltage for varying input power levels is shown by the blue curve of Fig. 6-22. For different load resistances, all component parameters of the matching network for the rectifier need to be optimised to reach a peak at one input power level. In this work, the circuit is optimised for a 1.5 kΩ.

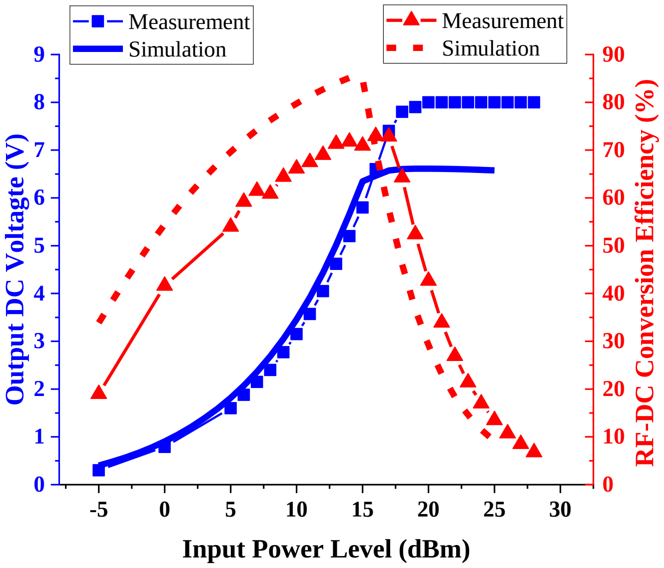

Fig. 6-23. Measured and simulated RF-DC conversion efficiency and output voltage of the rectifier against input power.

The measured and simulated conversion efficiency and output voltages on the 1.5k Ω load at 403 MHz are shown in Fig. 6-23. The measurements were made by connecting an RF signal generator to the rectifier circuit input and varying the signal generator output power while measuring the voltage on the load using a digital multimeter. The measured maximum conversion efficiency was 73.2% at 403 MHz when the input power to the rectifier was 16 dBm. The simulated maximum conversion efficiency was 84% when the input power to the rectifier was 15 dBm, however the measurement results still satisfy safety regulations and power delivery requirements for medical devices implanted in the human body. The main reason for this difference is the tolerance of the chip components. The measured conversion efficiency is maintained at over 60% for a variation in rectifier input power from 8 dBm to 18 dBm which is sufficient for low power devices and safe for the human body. Overall, the measured conversion efficiency and output voltage on the load show good agreement with the simulated results.

The total system PTE can be found by cascading the two sets of two-port network parameters [35], The theoretical overall WPT system efficiency should be approximately 42.4%.

6.3 Measurements of a WPT System for Implantable Applications

6.3.1 Measurement Setup

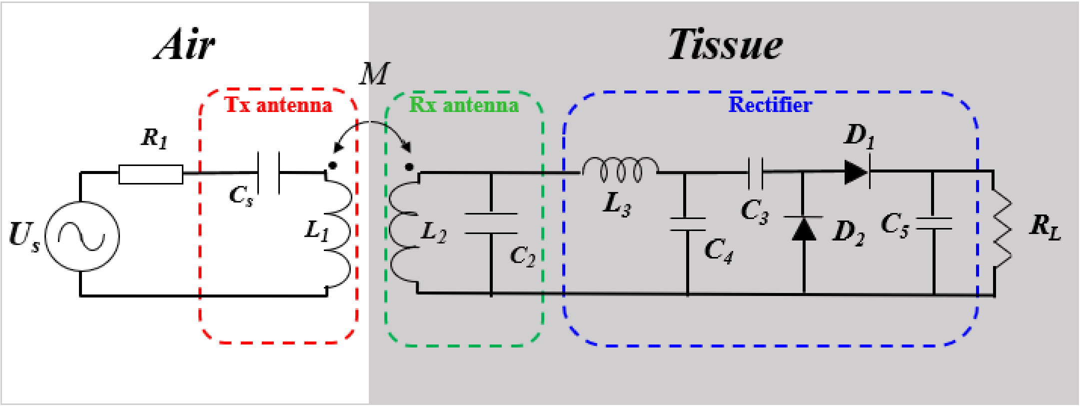

Fig. 6-24. Equivalent schematic of this proposed WPT system.

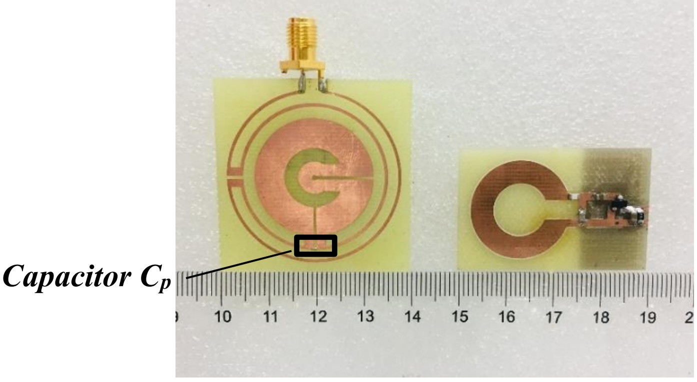

Fig. 6-25. Fabricated primary loop and secondary loop with integrated rectifying circuit.

A simplified equivalent schematic diagram of this proposed WPT system is shown in Fig. 6-24. To validate the overall PTE of this proposed WPT system from the source power to DC power on the load, the designed rectifying circuit is integrated with the receiving loop, as shown in Fig. 6-25. The values of all parameters for the transmit and receiving loops and the rectifying circuit are same as in previous sections.

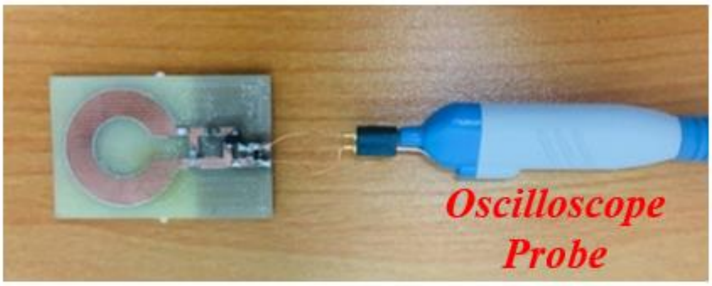

(a)

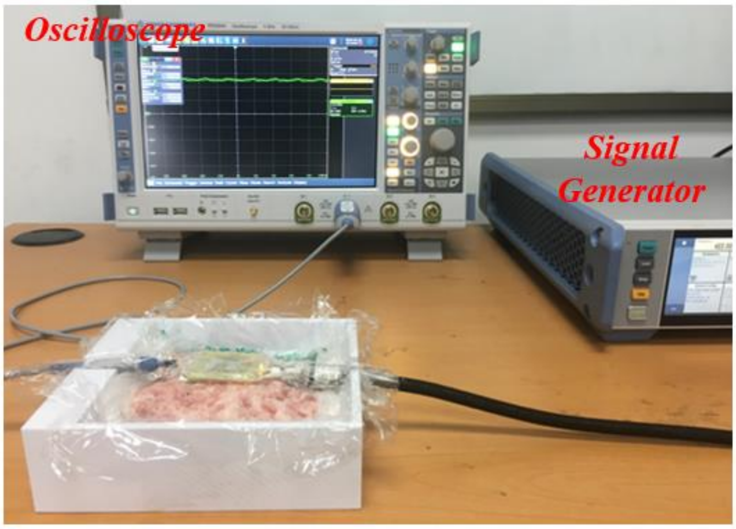

(b)

Fig. 6-26. (a) Connection between receive antenna integrated with the rectifying circuit and measurement oscilloscope probe; (b) Measurement setups.

The measurement setup is illustrated in Fig. 6-26. The SMA100B signal generator from Rohde & Schwarz is used during experiments, which can provide over 25 dBm of input power from 9 kHz to 3 GHz. The transmit loop is directly soldered with an SMA connector and then connected to the signal generator. The RTO2044 oscilloscope from Rohde & Schwarz is used to measure the DC voltage across the load clearly and accurately. The receive loop with integrated rectifying circuit is directly soldered to the oscilloscope probe for measurement convenience. Both transmit and receive loop with integrated rectifying circuit were protected by a thin layer of plastic wrap and located appropriately on and within the pork mince.

6.3.2 Measurement Results

At 403 MHz, the measured DC voltage (VDC) across the load (1.5 kΩ) and the measured overall PTE between source power and load power are depicted in Fig. 6-27. As can be seen, the measured DC voltage increases gradually to 8 V as the input power rises from -5 dBm (0.32 mW) to 20.5 dBm (112.2 mW) and is then maintained at 8 V for continuing increases in input power from 20.5 dBm to 25 dBm (316.2 mW). The measured overall PTE climbs slightly from 14% at an input power of -5 dBm to a maximum of 42.4% at an input power of 19 dBm (79.4 mW) and then declines rapidly to 13.5% as the input power rises from 19 dBm to 25 dBm. The overall PTE is maintained at over 40% in the input power range from 14 dBm (25 mW) to 20 dBm (100 mW). The input power of 20 dBm still satisfies the requirements of the IEEE SAR regulations for the safety of the human body.

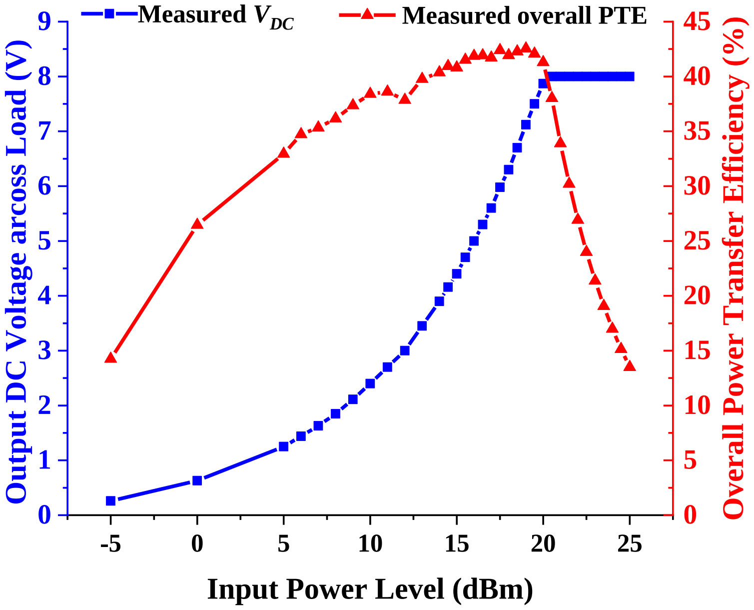

Fig. 6-27. Measured DC output voltage across loads and overall PTE of this proposed WPT system.

The trend of measured load power against input power level is presented in Fig. 6-28. The measured load power rises from 0.045 mW to 42.7 mW as the input power increases from -5 dBm to 20.5 dBm and is then maintained at 42.7 mW no matter how much extra input power is delivered, which is similar to the trend of the DC load voltage. When input power is 19 dBm, load power is 33.7 mW, which is sufficient to charge a pacemaker.

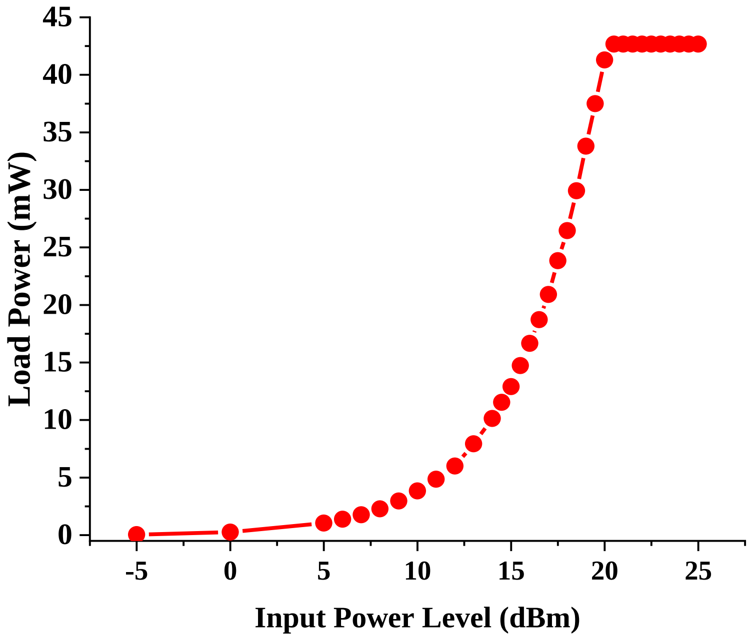

Fig. 6-28. Measured load power against input power level.

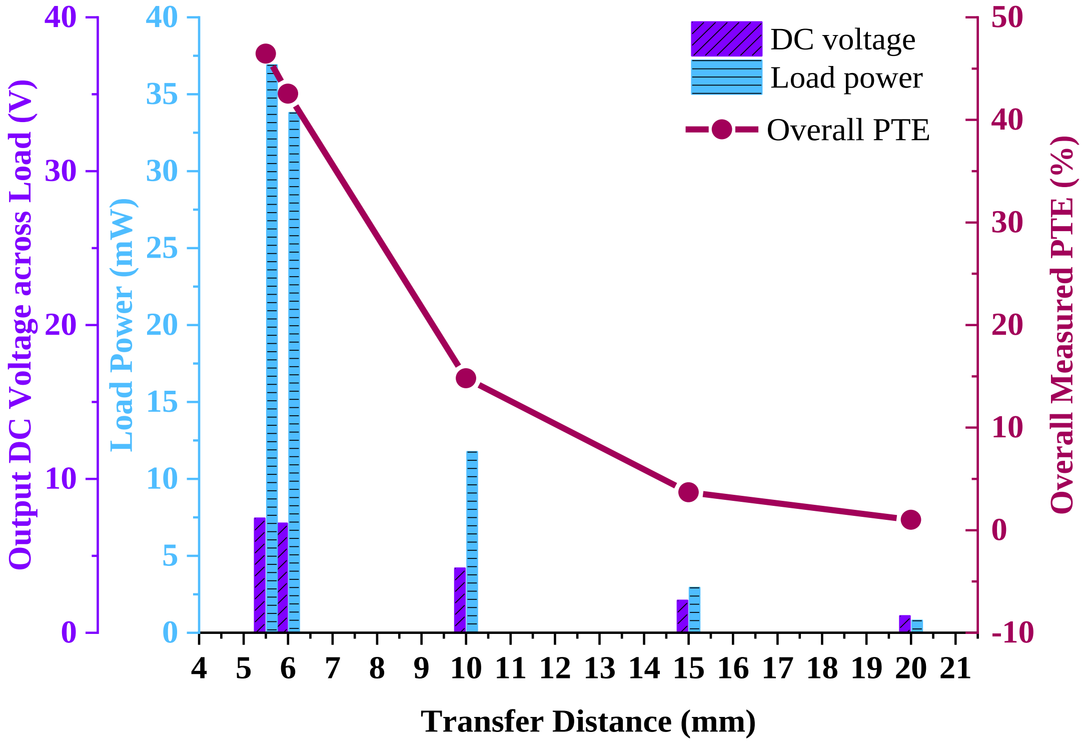

Fig. 6-29. Measured DC voltage, load power and overall PTE against transfer distance with input power of 19 dBm.

Furthermore, to investigate the influence of power transfer distance on the overall PTE of this system, the trends of measured DC voltage, overall PTE and load power against transfer distance are shown in Fig. 6-29. The transfer distance between antennas is varied as 5.5 mm, 6 mm, 10 mm, 15 mm and 20 mm including a 1 mm air gap between the transmit loop and the surface of the minced pork. The input power is set to 19 dBm at 403 MHz. It is clear that the measured DC voltage, overall PTE and load power fall dramatically as the transfer distance increases. The measured maximum overall PTE is 46.4% at a transfer distance of 5.5 mm with a DC voltage of 7.44 V and load power of 36.9 mW.

Consequently, the measured overall PTE shows good agreement with the calculated efficiency, which is equal to the measured PTE of the wireless power link multiplied by the measured conversation efficiency of the rectifying circuit. At 403 MHz, the overall PTE is 42.4% and the DC output voltage is 7.12 V. The obtained load power is 33.7 mW, which is enough to be a good candidate for charging pacemakers.

6.4 Summary

A near-field WPT system for implantable devices has been presented in this chapter. It offers good performance in terms of PTE at 403 MHz.

Firstly, a near-field wireless power link was proposed including transmit and receive loops. For the transmitter, split-ring loops are used to achieve the characteristic of a series LC circuit and a lumped capacitor is added to decrease the series self-resonance frequency to the operating frequency of 403 MHz. The measured PTE of this WPT link can reach 57.9% at a transfer distance of 6 mm including a 1 mm air gap and 5 mm of body tissues. The PTE decreased as power transfer distance increases. The measured results show good agreement with the simulated results. To satisfy SAR regulations, the maximum transmit power was found to be 159 mW, which is significantly larger than in other works, potentially reducing charging time for pacemaker batteries.

Secondly, a voltage-doubler rectifier was designed for this WPT link to perform RF-DC conversion. The rectifier was measured to have a maximum conversion efficiency of 73.2% at an input power level of 17 dBm which produced a DC voltage across a 1.5 kΩ load of 7.4 V. This result in combination with the results for the PTE of the antennas leads to a theoretical overall system PTE of 42.4%.

Thirdly, a near-field WPT system with integrated rectifier was fabricated and measured. The measured maximum overall system efficiency at 403 MHz was 42.3%. The measured load power was 33.7 mW and the measured output DC voltage across the load was 7.12 V when the input power was 79.4 mW, which satisfies the SAR regulations. Both the load power and output DC voltages decrease greatly as the transfer distance becomes larger, resulting from the inverse relationship between the coupling coefficient and distance between the loops.

In conclusion, even though this proposed WPT system has a relatively large receiver dimension, it offers good performance in terms of high PTE and allowable transmit power. Therefore, this proposed WPT system is a good candidate for the transference of power in applications involving the charging of implantable devices.

6.5 References

[1] R. Jegadeesan, S. Nag, K. Agarwal, N. V. Thakor, and Y. Guo, "Enabling Wireless Powering and Telemetry for Peripheral Nerve Implants," *IEEE Journal of Biomedical and Health Informatics,* vol. 19, no. 3, pp. 958-970, 2015, doi: 10.1109/JBHI.2015.2424985.

[2] K. Na, H. Jang, H. Ma, and F. Bien, "Tracking Optimal Efficiency of Magnetic Resonance Wireless Power Transfer System for Biomedical Capsule Endoscopy," *IEEE Transactions on Microwave Theory and Techniques,* vol. 63, no. 1, pp. 295-304, 2015, doi: 10.1109/TMTT.2014.2365475.

[3] Y. Cheng, G. Wang, and M. Ghovanloo, "Analytical Modeling and Optimization of Small Solenoid Coils for Millimeter-Sized Biomedical Implants," *IEEE Transactions on Microwave Theory and Techniques,* vol. 65, no. 3, pp. 1024-1035, 2017, doi: 10.1109/TMTT.2016.2627564.

[4] R. Xue, K. Cheng, and M. Je, "High-Efficiency Wireless Power Transfer for Biomedical Implants by Optimal Resonant Load Transformation," *IEEE Transactions on Circuits and Systems I: Regular Papers,* vol. 60, no. 4, pp. 867-874, 2013, doi: 10.1109/TCSI.2012.2209297.

[5] H. Dinis, I. Colmiais, and P. M. Mendes, "Extending the Limits of Wireless

Power Transfer to Miniaturized Implantable Electronic Devices," *Micromachines (Basel),* vol. 8, no. 12, Dec 12 2017, doi: 10.3390/mi8120359.

[6] K. N. Bocan, M. H. Mickle, and E. Sejdić, "Multi-Disciplinary Challenges in Tissue Modeling for Wireless Electromagnetic Powering: A Review," *IEEE Sensors Journal,* vol. 17, no. 20, pp. 6498-6509, 2017, doi: 10.1109/JSEN.2017.2748338.

[7] F. Huang, C. Lee, C. Chang, L. Chen, T. Yo, and C. Luo, "Rectenna Application of Miniaturized Implantable Antenna Design for Triple-Band Biotelemetry Communication," *IEEE Transactions on Antennas and Propagation,* vol. 59, no. 7, pp. 2646-2653, 2011, doi: 10.1109/TAP.2011.2152317.

[8] C. Liu, Y. Guo, H. Sun, and S. Xiao, "Design and Safety Considerations of an Implantable Rectenna for Far-Field Wireless Power Transfer," *IEEE Transactions on Antennas and Propagation,* vol. 62, no. 11, pp. 5798-5806, 2014, doi: 10.1109/TAP.2014.2352363.

[9] G. A. Vera, A. Georgiadis, A. Collado, and S. Via, "Design of a 2.45 GHz rectenna for electromagnetic (EM) energy scavenging," in *2010 IEEE Radio and Wireless Symposium (RWS)*, 10-14 Jan. 2010 2010, pp. 61-64, doi: 10.1109/RWS.2010.5434266.

[10] *Evaluating Compliance with FCC Guidelines for Human Exposure to Radiofrequency Electromagnetic Fields*, F. C. C. O. o. E. Technology, 1997.

[11] H. Kim, H. Hirayama, S. Kim, K. J. Han, R. Zhang, and J. Choi, "Review of Near-Field Wireless Power and Communication for Biomedical Applications," *IEEE Access,* vol. 5, pp. 21264-21285, 2017, doi: 10.1109/ACCESS.2017.2757267.

[12] K. Agarwal, R. Jegadeesan, Y. Guo, and N. V. Thakor, "Wireless Power Transfer Strategies for Implantable Bioelectronics," *IEEE Reviews in Biomedical Engineering,* vol. 10, pp. 136-161, 2017, doi: 10.1109/RBME.2017.2683520.

[13] C. Xiao, D. Cheng, and K. Wei, "An LCC-C Compensated Wireless Charging System for Implantable Cardiac Pacemakers: Theory, Experiment, and Safety Evaluation," *IEEE Transactions on Power Electronics,* vol. 33, no. 6, pp. 4894-4905, 2018, doi: 10.1109/TPEL.2017.2735441.

[14] S. C. Tang, T. L. T. Lun, Z. Guo, K. Kwok, and N. J. McDannold, "Intermediate Range Wireless Power Transfer With Segmented Coil Transmitters for

Implantable Heart Pumps," *IEEE Transactions on Power Electronics,* vol. 32, no. 5, pp. 3844-3857, 2017, doi: 10.1109/TPEL.2016.2584558.

[15] S. Stoecklin, A. Yousaf, T. Volk, and L. Reindl, "Efficient Wireless Powering of Biomedical Sensor Systems for Multichannel Brain Implants," *IEEE Transactions on Instrumentation and Measurement,* vol. 65, no. 4, pp. 754-764, 2016, doi: 10.1109/TIM.2015.2482278.

[16] S. R. Khan and G. Choi, "Analysis and Optimization of Four-Coil Planar Magnetically Coupled Printed Spiral Resonators," *Sensors (Basel),* vol. 16, no. 8, Aug 3 2016, doi: 10.3390/s16081219.

[17] S. A. Mirbozorgi, P. Yeon, and M. Ghovanloo, "Robust Wireless Power Transmission to mm-Sized Free-Floating Distributed Implants," *IEEE Transactions on Biomedical Circuits and Systems,* vol. 11, no. 3, pp. 692-702, 2017, doi: 10.1109/TBCAS.2017.2663358.

[18] M. R. Basar, M. Y. Ahmad, J. Cho, and F. Ibrahim, "An Improved Wearable Resonant Wireless Power Transfer System for Biomedical Capsule Endoscope," *IEEE Transactions on Industrial Electronics,* vol. 65, no. 10, pp. 7772-7781, 2018, doi: 10.1109/TIE.2018.2801781.

[19] A. S. Y. Poon, S. O. Driscoll, and T. H. Meng, "Optimal Frequency for Wireless Power Transmission Into Dispersive Tissue," *IEEE Transactions on Antennas and Propagation,* vol. 58, no. 5, pp. 1739-1750, 2010, doi: 10.1109/TAP.2010.2044310.

[20] "Datasheet of pacemakers in Chuang-ling Company." [Online]. Available: http://www.chuang-ling.com/product/pdf?id=16.

[21] "IT'IS Foundation – Database at a Glance." [Online]. Available: http://www.itis.ethz.ch/itis-for-health/tissue-properties/database/.

[22] G. Monti, M. V. De Paolis, L. Corchia, M. Mongiardo, and L. Tarricone, "Inductive link for power and data transfer to a medical implant," *Wireless Power Transfer,* vol. 4, no. 2, pp. 98-112, 2017, doi: 10.1017/wpt.2017.6.

[23] C. K. Chou *et al.*, "Radio frequency electromagnetic exposure: tutorial review on experimental dosimetry," *Bioelectromagnetics,* vol. 17, no. 3, pp. 195-208, 1996, doi: 10.1002/(SICI)1521-186X(1996)17:3<195::AID-BEM5>3.0.CO;2-Z.

[24] M. S. Mahmud, F. J. J. Jabri, and B. Mahjabeen, "Compact UWB Wearable antenna on leather material for wireless applications," in *2013 IEEE Antennas*

and Propagation Society International Symposium (APSURSI), 7-13 July 2013 2013, pp. 2191-2192, doi: 10.1109/APS.2013.6711754.

[25] Y. Okano, K. Ito, I. Ida, and M. Takahashi, "The SAR evaluation method by a combination of thermographic experiments and biological tissue-equivalent phantoms," *IEEE Transactions on Microwave Theory and Techniques,* vol. 48, no. 11, pp. 2094-2103, 2000, doi: 10.1109/22.884200.

[26] O. Merckel, G. Fleury, and J. Bolomey, "Propagation model choice for rapid SAR measurement," in *2002 11th European Signal Processing Conference*, 3-6 Sept. 2002 2002, pp. 1-4.

[27] "IEEE Standard for Safety Levels with Respect to Human Exposure to Radio Frequency Electromagnetic Fields, 3 kHz to 300 GHz Amendment 1: Specifies Ceiling Limits for Induced and Contact Current, Clarifies Distinctions between Localized Exposure and Spatial Peak Power Density," *IEEE Std C95.1a-2010 (Amendment to IEEE Std C95.1-2005),* pp. 1-9, 2010, doi: 10.1109/IEEESTD.2010.5433227.

[28] Q. Balzano, O. Garay, and F. R. Steel, "Energy deposition in simulated human operators of 800-MHz portable transmitters," *IEEE Transactions on Vehicular Technology,* vol. 27, no. 4, pp. 174-181, 1978, doi: 10.1109/T-VT.1978.23746.

[29] A. W. Guy and C. Chung-Kwang, "Specific Absorption Rates of Energy in Man Models Exposed to Cellular UHF Mobile-Antenna Fields," *IEEE Transactions on Microwave Theory and Techniques,* vol. 34, no. 6, pp. 671-680, 1986, doi: 10.1109/TMTT.1986.1133416.

[30] "IEEE Draft Standard for Safety Levels with Respect to Human Exposure to Electric, Magnetic and Electromagnetic Fields, 0 Hz to 300 GHz," *IEEE PC95.1/D3.5, October 2018,* pp. 1-312, 2018.

[31] A. Sharma, E. Kampianakis, and M. S. Reynolds, "A Dual-Band HF and UHF Antenna System for Implanted Neural Recording and Stimulation Devices," *IEEE Antennas and Wireless Propagation Letters,* vol. 16, pp. 493-496, 2017, doi: 10.1109/LAWP.2016.2585650.

[32] L. Li, H. Liu, H. Zhang, and W. Xue, "Efficient Wireless Power Transfer System Integrating With Metasurface for Biological Applications," *IEEE Transactions on Industrial Electronics,* vol. 65, no. 4, pp. 3230-3239, 2018, doi: 10.1109/TIE.2017.2756580.

[33] G. Monti, M. V. D. Paolis, L. Corchia, and L. Tarricone, "Wireless resonant

energy link for pulse generators implanted in the chest," *IET Microwaves, Antennas & Propagation,* vol. 11, no. 15, pp. 2201-2210, 2017, doi: 10.1049/iet-map.2017.0250.

[34] C. Song, Y. Huang, P. Carter, J. Zhou, S. D. Joseph, and G. Li, "Novel Compact and Broadband Frequency-Selectable Rectennas for a Wide Input-Power and Load Impedance Range," *IEEE Transactions on Antennas and Propagation,* vol. 66, no. 7, pp. 3306-3316, 2018, doi: 10.1109/TAP.2018.2826568.

[35] R. E. Collin, *Foundations for Microwave Engineering*. New York: IEEE, 2001.

Chapter 7 Conclusions and Future Work

7.1 Conclusions

Motivated by the potential to eliminate the inconvenience caused by the finite battery lifetime of implantable devices and the associated discomfort and cost of surgeries to replace batteries, wireless power transfer (WPT) technology has become an important target of medical implant device development. The main constraints on practicability and applicability of WPT technology for implantable applications are the low power transfer efficiency (PTE) caused by the lossy effects of body tissues and the low received power due to specific absorption rate (SAR) regulations on human safety. Consequently, not only patients but also researchers are eager to make a breakthrough by realising the use of WPT technologies for medical implants.

This thesis has focused on the development of an efficient near-field WPT system for pacemakers, with the goal of addressing the aforementioned research challenges. Several novel techniques have been developed in the design of a wireless power link that has a simple structure and that can operate at high frequency while meeting requirements on human safety. The system developed not only increases the available transmit power but is also comparatively efficient and practically realisable.

A brief history of the development of WPT technology was provided in Chapter 1, along with a detailed comparison of the various methods available for WPT i.e. far-field and near-field methods. Theoretical knowledge relating to the different approaches used for WPT was introduced in Chapter 2 along with an overview of research cases of WPT through free space and the human body. Examples of current achievements were also offered in Chapter 2 which helped to highlight the existing challenges facing the research community.

Owing to the extremely low PTE and low receivable power of far-field WPT systems when applied for implantable devices, the near-field magnetic resonance coupling (MRC) method is seen as a more viable WPT choice for medical applications. Chapter 3 investigated the four possible topologies of MRC-WPT circuits (SS, SP, PP and PS) in regard to the amount of available received power and the effect of loading on PTE. Solutions for avoiding the phenomena of frequency splitting, which can lead to a reduction in system performance were also considered. It was found that use of a parallel resonator on the transmit side of the system would result in very small receivable power, as due to its open circuit resonating characteristic very little power would be drawn from the signal source. Series primary resonance circuits have short circuit characteristics hence drawing large currents from the source, which is suitable for MRC-WPT as it relies on formation of a strong magnetic field.

On the secondary side of the WPT system it was found that series circuits are suitable for power delivery to small load impedances due to their short circuit resonating characteristic. By contrast, parallel secondary circuits which resonate open circuit, leading to higher voltages and are suitable for applications with large load impedances. It is important to clarify that the load here will consist of the requisite RF-to-DC and DC-to-DC conversion circuits between the resonator and the actual application load.

It was shown in Chapter 3 that the phenomena of frequency splitting may easily occur in SS topologies due to over coupling between resonators. Frequency splitting occurs when the resonators are too close and results in reduced PTE. Therefore the peak in PTE does not necessarily occur at the shortest distance, it occurs a distance beyond the effects of frequency splitting. These effects can be avoided by ensuring the transfer distance is large enough or by increasing the load. Alternatively, the inductance and capacitance parameters of the resonators can be re-optimised to realise efficient power transmission at the desired distance.

The licensed frequency bands for medical implant devices are from 402 MHz to 405 MHz, which is a much higher operating frequency than those used in recently published works. It is prohibitively difficult to form inductors made of wire coils at such high frequencies, because the values of inductance and capacitance need to be unrealisably small. However, printed spiral coils (PSCs) offer a feasible manufacturing solution for such resonators. Chapter 4 presents the necessary theoretical knowledge relating to the modelling of inductance, mutual inductance, parasitic capacitance, parasitic resistance and Quality factor (*Q*-factor). Additionally, the design procedure for a rectangular PSC and investigations of the effects of PSC parameters on inductance were provided.

A rectangular PSC with dimensions of 20 mm×18 mm, inductance of 106 nH, resistance of 1.91 Ω and a *Q*-factor of 140 was developed. Two of these were combined with series 1.5 pF chip capacitors to constitute a pair of 403 MHz series resonators for WPT. The PTE performance of this WPT link with a load impedance of 1 kΩ over a transfer distance of 5 mm was 87.7%.

The need for the proposed rectangular PSCs to present as inductive at 403 MHz restricts any further optimisation of track width or turn number to enhance PTE or power transfer distance. Therefore, planar split-ring loops were proposed in Chapter 5 as inductors aimed at decreasing parasitic resistance in comparison to the rectangular PSC and hence enhance *Q*-factor. Loops with comparable inductance to the rectangular PSC (103 nH) were developed and again combined with series 1.5 pF capacitors to constitute a pair of series resonators. With an improved *Q*-factor of 1069 (from 140) the WPT system PTE reached 83% at a transfer distance of 20 mm.

To simplify the resonance circuit, an improved planar split-ring loop was developed as a self-resonator with series resonance characteristics, ensuring suitability for the primary side of the WPT system. This proposed novel planar split-ring resonator has a size of 45 mm×45 mm and does not require additional capacitance or a matching circuit making its integration into systems easier. It is proposed that these resonators could be used in applications requiring simple circuit configurations, such as RFID applications with WPT functions. The WPT link formed which operates at 433 MHz in the industrial, scientific and medical (ISM) band and obtained a PTE of 87.9% at a transfer distance of 22 mm.

Chapter 6 develops an efficient WPT system operating at 403 MHz for pacemakers by extending the split-ring loop work of Chapter 5. This proposed WPT system constitutes a transmitting loop, a receiving loop and a rectifying circuit. The transmitting loop with the dimensions of 39.6 mm×39.6 mm was designed using multiple split-ring loops and a lumped capacitor to obtain a series self-resonance frequency of 403 MHz. A one-turn 20.46 mm×20.46mm receiving parallel self-resonating loop was designed for implant within body tissue (muscle). The transmit and receiving resonators constitute a series-primary and parallel-secondary WPT link. The simulated and measured results of the system show good agreement in terms of

PTE (57.9%) over a transfer distance of 6 mm. The maximum allowable transmit power is 159 mW in view of satisfying SAR regulations, which is much higher than that available in other recent works.

A rectifying circuit optimised for a load impedance of 1.5 kΩ was designed to perform RF-to-DC conversion with a measured efficiency of 73%. The measured output voltage across load was 7.1 V and hence a load power of 33.6 mW for a transmit power of 19 dBm (79.4 mW) was achieved.

The overall system PTE was measured to be 42% over a transfer distance of 6 mm with the receiving circuit implanted under 5 mm of minced pork. Even though this proposed WPT system did not have a small size compared to other published work, it offers improvements in PTE and available transmit power which would potentially decrease implant charging time while staying within SAR regulations.

7.2 Key Contributions

This work has provided a thorough study of MRC based WPT and developed techniques to overcome some of the most challenging aspects related to this topic of research. As an outcome, there are two published journal papers and one published conference paper, as listed in the preface of this thesis on page VII.

The key contributions to knowledge are detailed as follows.

1) A topological investigation of MRC-WPT including theoretical analysis and experimental verification which lead to guidelines for the selection of a suitable configuration for a given application. A flow chart is provided in this regard to aid in the design of an MRC-WPT circuit with optimised application specific parameters. Also, solutions are offered for the avoidance of frequency splitting in terms of making a trade-off between PTE, power transfer distance and receivable power.

2) The idea of using split-ring loops in place of PSCs as resonators for WPT at high frequencies has been developed. Chapter 5 showed that the split-ring loop can decrease the comparative parasitic resistance and hence increase the comparative *Q*-factor, which was shown to offer higher PTE.

3) The development of a split-ring loop series self-resonator in the desired medical frequency band. Conventional coil self-resonators have parallel self-resonant characteristics, which are not suitable for MRC-WPT systems. To obtain this series self-resonator characteristic multiple split-ring loops were proposed in Chapter 5 attaining a self-resonance frequency of 433 MHz. A pair of these resonators was used to form a WPT system with a maximum measured PTE of 87.9% in free space over a transfer distance of 22 mm at 433 MHz.

4) In Chapter 6 a fully realised WPT system including rectifier was developed for use with implantable devices. The split-ring loop of Chapter 5 was combined with a chip capacitor to provide series resonance at 403 MHz on the system transmit side. A single loop with parallel self-resonance was designed for the receiver implant. The transmit receive pair provided a PTE of 57.9% over a distance of 6 mm through an air gap and 5 mm of body tissues. The transmitter can provide up to 159 mW of power while remaining within the SAR safety requirements, which could potentially reduce the required device charging time. The addition of a rectifying circuit with measured conversion efficiency of 73% provided a measured system PTE of 42.3%

The design developments are shown in Fig. 7-1, which is a profile of this research work.

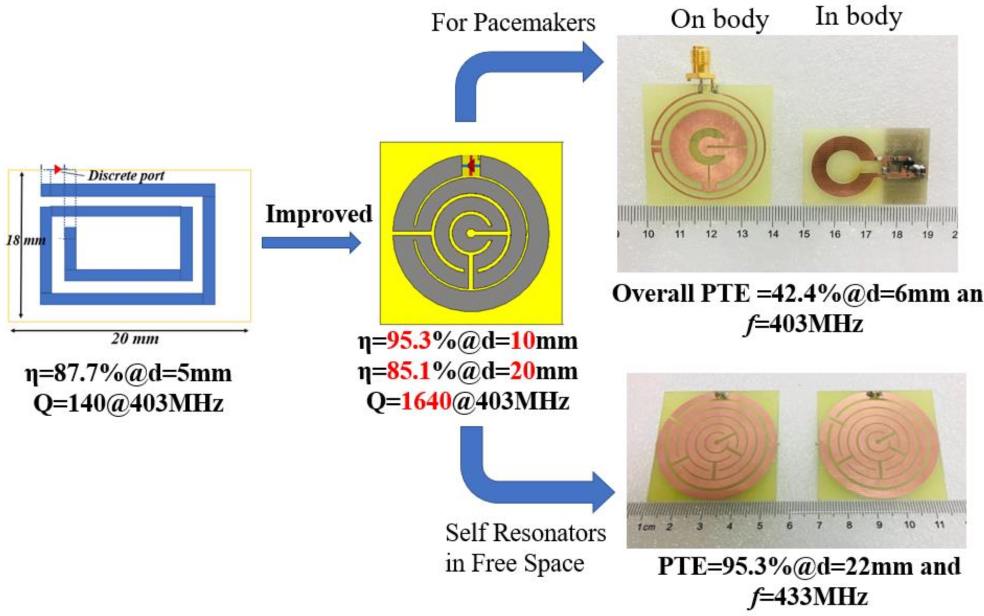

Fig. 7-1. A profile of design procedure for this research work.

7.3 Future work

According to the above conclusions and considering the limitations of the existing work, some future avenues that could be explored are given in the following:

1) Consideration of the pacemaker case – The case of a pacemaker is typically metal. Metallic materials will affect the performance of MRC-WPT if placed between primary secondary resonators. In this case, the receiver should be located on the surface of pacemaker not inside. Therefore, further investigation is required using an actual pacemaker as part of the experimental design.

2) Robust power transfer efficiency for varied relative positions - PTE degradation is caused by variations in distance, angle and axial misalignment. Methods of reducing the sensitivity of PTE to such practically common displacements should be further investigated.

3) Use of multiple implanted resonators to allow increased implant depth - For pacemakers, a gap of 6 mm between the primary and secondary circuits is sufficient. However, for other implantable devices (e.g. wireless capsule endoscopes, brain stimulators and nerve implants), the transfer distance could be larger, however that results in a low PTE. A possible solution would be to place additional resonators between the transmit and receive resonators. This would effectively allow energy to be stored and passed on along the power transfer route.

4) Addition of a superstrate layer to further decrease SAR - The proposed WPT link leads to exposure of body tissues to RF energy and hence power levels are limited. Superstrates can be used to prevent electromagnetic power from being absorbed into surrounding tissues, which would be conducive to reducing SAR values allowing larger transmit power to be provided. Both the transmitting and receiving resonators could have a layer of superstrate added, however this will require an investigation of the dielectric characteristics of potential superstrates and how these would impact on WPT performance.